Improving Acoustic Measurements with Cavities in Closed Test Section Wind Tunnels

VanDercreek, Colin

Citation (APA)
VanDercreek, C. (2022). *Improving Acoustic Measurements with Cavities in Closed Test Section Wind Tunnels*. [Dissertation (TU Delft), Delft University of Technology]. https://doi.org/10.4233/uuid:fccd4c49-9e04-4d57-b949-cb86153257a5

Important note
To cite this publication, please use the final published version (if applicable).
Please check the document version above.

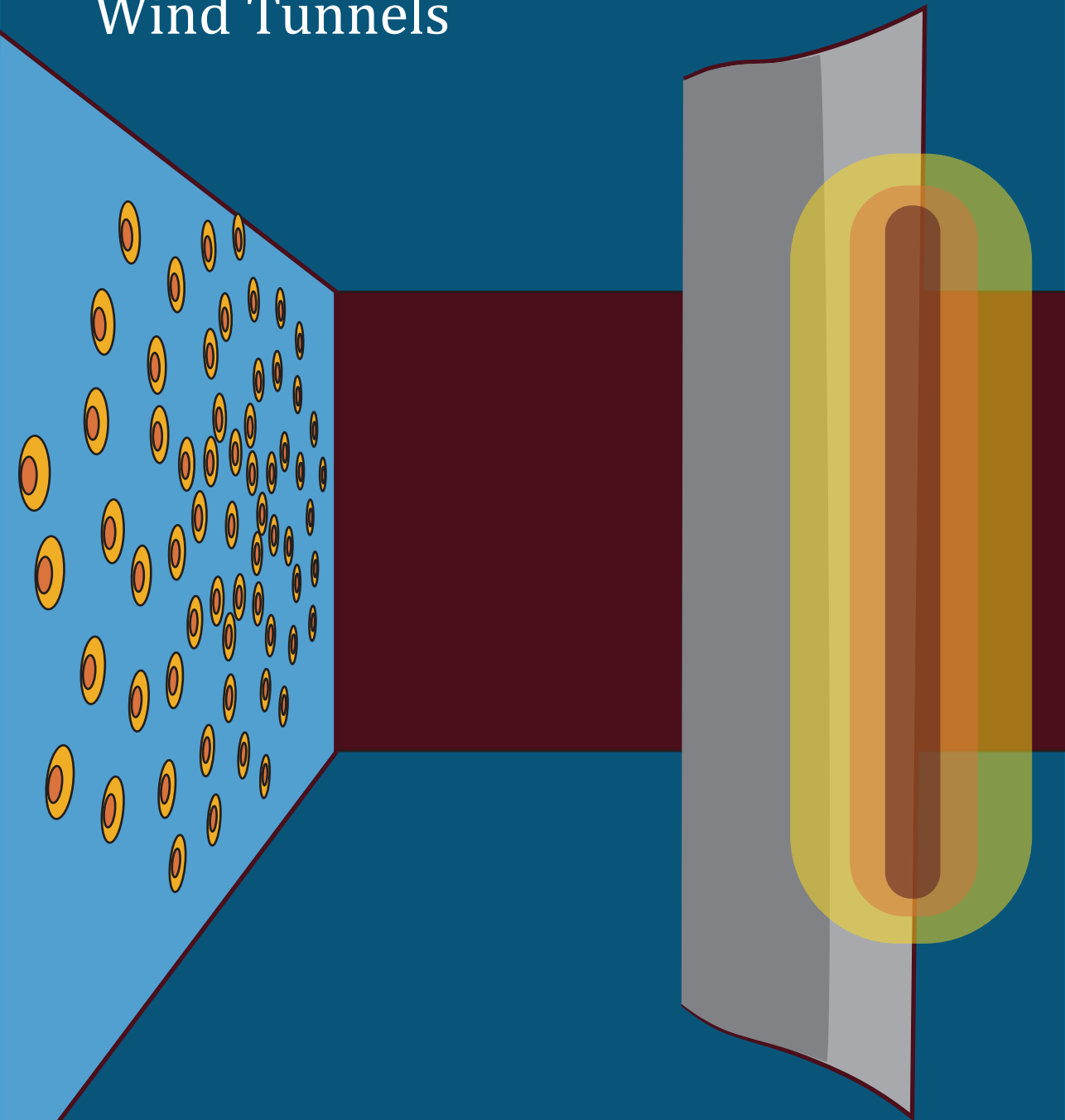# Improving Acoustic Measurements with Cavities in Closed Test Section Wind Tunnels

Colin van Dercreek

Improving Acoustic Measurements with Cavities in Closed Test Section Wind Tunnels

Improving Acoustic Measurements with Cavities in Closed Test Section Wind Tunnels

Proefschrift

ter verkrijging van de graad van doctor
aan de Technische Universiteit Delft,
op gezag van de Rector Magnificus Prof. dr. ir. T.H.J.J. van der Hagen,
voorzitter van het College voor Promoties,
in het openbaar te verdedigen
op Maandag 26 September 2022 om 15:00 uur

door

Colin Paul VAN DERCREEK

Master of Science in Aerospace Engineering,
University of Maryland, College Park, USA
geboren te Portsmouth, Virginia USA.

Dit proefschrift is goedgekeurd door de promotoren

promotor: Prof. dr. ir. M. Snellen
promotor: Dr. D. Ragni
copromotor: Dr. F. Avallone

Samenstelling promotiecommissie:

Rector Magnificus,	voorzitter
Prof. dr. ir. M. Snellen,	Technische Universiteit Delft, promotor
Dr. D. Ragni,	Technische Universiteit Delft, promotor
Dr. F. Avallone	Technische Universiteit Delft, copromotor
Onafhankelijke leden:	
Prof. dr. ing. E. Sarradj,	Technische Universität Berlin, Duitsland
Prof. dr. ir. C.H. Venner,	Universiteit Twente
Prof. dr. S.J. Watson,	Technische Universiteit Delft
Dr. ir. M.I. Gerritsma,	Technische Universiteit Delft
Prof. dr. D.A. von Terzi	Technische Universiteit Delft, reservelid

To Sara, Otto, and Majken.

Contents

Nomenclature

Abbreviations

A/D	Analog–to–digital
AIC	Akaike information criterion
BPM	Brooks, Pope, and Marcolini
CFD	Computational fluid dynamics
CFL	Courant-Friedrichs-Lewy number
CSM	Cross–spectral matrix
DAQ	Data acquisition system
DoE	Design of experiments
FEM	Finite element method
GAM	Generalized additive model
GLMM	Generalized linear mixed model
HWA	Hot–Wire anemometry
LTT	Low turbulence tunnel
MEMS	Micro–electromechanical systems
MSL	Maximum side lobe level, dB
NI	National Instruments
OASPL	Overall A-weighted sound pressure level
OFAT	One–factor–at–a–time
OSPL	Overall sound pressure level
PSD	Power spectral density
PWL	Sound power level
RMS	Root mean square
ROI	Region of integration

SNR	Signal–to–noise ratio
SPI	Sound power integration
SPL	Sound pressure level
TBL	Turbulent boundary layer
TBL–TE	Turbulent boundary layer – trailing edge
TI	Turbulence intensity
TKE	Turbulent kinetic energy
VLES	Very large eddy simulation
VR	Variable resolution region within a CFD simulation

Greek Symbols

α	Constant
$\alpha_{m\mu}$	Radial wavenumber
$\boldsymbol{\beta}$	Vector containing the linear model coefficients
β_0	GAM model intercept
δ	Cavity depth correction term, m
Δ	Difference notation
$\delta^\star$	Boundary layer displacement thickness, m
δ_{99}	Boundary layer thickness, m
δ_{ij}	Kronecker delta
$\boldsymbol{\epsilon}$	Vector containing the model error residuals
ϵ_p	Porosity,
γ	Length of the conical sidewall, m
κ	Equivalent bulk modulus, $\mathrm{kg\,m^{-1}\,s^{-2}}$
λ	Constant
$\boldsymbol{\Lambda}$	SVD matrix of $\mathbf{K}$
Λ_x	Streamwise coherence length of the TBL pressure, m
Λ_z	Spanwise coherence length of the TBL pressure, m

μ_0 Dynamic viscosity of the fluid, $\mathrm{Pa\,s}$

ν Kinematic viscosity of the fluid, $\mathrm{m^2\,s^{-1}}$

ω Angular frequency, $\mathrm{rad\,s^{-1}}$

$\tilde{\omega}$ Normalized angular frequency, $\frac{\omega a}{c_0}$

ω_n Angular harmonic frequency, $\mathrm{rad\,s^{-1}}$

$\boldsymbol{\Phi}$ Spatial POD mode matrix

$\boldsymbol{\phi_r}$ Spatial structure of POD mode r, and is the column vector of $\boldsymbol{\Phi}$

ϕ_i Parameter obtained from the simulation with grid i

$\phi_{m\mu}$ Acoustic azimuthal and radial mode shape for mode $m\mu$

Φ_{xx} Power spectra of the wall pressure fluctuations, $\mathrm{Pa^2}$

$\boldsymbol{\Psi}$ Eigenvalue of the temporal correlation matrix $\mathbf{K}$

$\boldsymbol{\psi_r}$ Temporal base of POD mode r, and is the column vector of $\boldsymbol{\Psi}$

ρ Density of the fluid, $\mathrm{kg\,m^{-3}}$

$\tilde{\rho}$ Normalized density, $\frac{\rho}{\rho_0}$

ρ_0 Ambient density of the fluid, $\mathrm{kg\,m^{-3}}$

ρ_{rig} Equivalent rigid density, $\mathrm{kg\,m^{-3}}$

$\boldsymbol{\Sigma}$ Diagonal matrix containing the energy of each POD mode σ_r

σ_r Energy content of POD mode r

τ Lattice Boltzmann viscosity–dependent, collision relaxation time

τ_w Wall shear stress, Pa

τ_∞ Tortuosity factor,

Θ Boundary layer momentum thickness, m

Θ_{min} Rayleigh distance between two acoustic sources, m

$\boldsymbol{\xi}_p$ Location of a point in the scan plane

ζ Eigenfrequency

Latin Symbols

A	Cross–sectional area, m^2
a	Cavity radius, m
$A_{m\mu}$	Amplitude of inward propagating acoustic mode $m\mu$
B	Source power matrix beamforming output
b	Cavity bottom radius, m
$B_{m\mu}$	Amplitude of outward propagating acoustic mode $m\mu$
C	Form drag coefficient of a porous material, m^{-1}
C	Cross–spectral matrix of microphone array measurements
C_i	Lattice Boltzmann collision operator
c_0	Speed of sound of the fluid, $m\,s^{-1}$
D	POD data matrix of spatially distributed temporal data
$\tilde{D}$	Normalized cavity depth, $\tilde{D} = \frac{D}{a}$
D	Cavity depth, m
D_{array}	Diameter of the microphone array, m
d_c	Countersink depth, m
D_{eff}	Effective cavity depth, m
$\mathbf{e_k}$	Wave direction unit vector
E_w	Measured hot–wire voltage, V
$E_{w,r}$	Temperature corrected hot–wire voltage, V
F_i	Particle distribution function with respect to the ith lattice direction
F_{sol}	Solution to the radial ordinary differential equation
$F_i^{eq}(\boldsymbol{x},t)$	Lattice Boltzmann equilibrium distribution function
f_l	Lower frequency at the half–power location, Hz
f_m	GAM model splines
f_n	Harmonic frequency of the acoustic mode, Hz
f_u	Upper frequency at the half–power location, Hz
g	Beamforming steering vector

G_{sol}	Solution to the azimuthal ordinary differential equation
H	Number of chunks used in Welch's method
H_{sol}	Solution to the axial ordinary differential equation
$H_{m\mu}$	Cumulative amplitude of the inward and outward propagating acoustic mode $m\mu$
h_i	Minimum voxel size, m
i	$\sqrt{-1}$
J_m	Bessel function of the first kind, order m
K	Permeability of a porous material, m^{-2}
k	Wavenumber, m^{-1}
$\mathbf{K}$	POD temporal correlation matrix
$k_{m\mu}$	Axial wavenumber corresponding to acoustic mode $m\mu$
k_0	Acoustic wavenumber, m^{-1}
k_c	Convective wavenumber, m s^{-1}
$k_{m\mu}$	Axial wave number of mode $m\mu$
L	Cavity length in the streamwise direction, m
L_v	Viscous characteristic length, m
L_{th}	Thermal characteristic length, m
M	Mach number, U_∞/c_0
N	Number of temporal samples contained within a signal
$N_{m\mu}$	Normalization factor for acoustic mode $m\mu$
N_{fft}	Number samples used in a chunk with Welch's method.
N_x	Number of spatially sampled points
n_x	Lengthwise rectangular cavity mode number
n_y	Depthwise rectangular cavity mode number
n_z	Spanwise rectangular cavity mode number
o	Order of convergence
$\tilde{p}$	Normalized pressure, $\dfrac{p}{\rho_0 c_0^2}$

p	Pressure of the fluid, Pa
p_0	Incident wave pressure amplitude, Pa
P_{bot}	Integrated energy at the bottom of the cavity
P_{top}	Integrated energy at the top of the cavity
P_{xx}	Power spectral density, $\text{Pa}^2\,\text{Hz}^{-1}$
P_{xy}	Cross power spectral density, $\text{Pa}^2\,\text{Hz}^{-1}$
Q	Quality factor
$\tilde{r}$	Normalized radius variable, $\frac{r}{a}$
R	Dimensionless acoustic resistance across porous cloth
r	Radius variable
R_T	Ratio of outer boundary layer region and inner boundary layer region time scales
R_{refl}	Reflection coefficient
R^2	Proportion of the variation in the dependent variable that is predicted by the independent variable
R_f	Flow resistivity, $\text{Pa}\,\text{s}\,\text{m}^{-2}$
R_i	Inertial resistivity of a porous medium, m^{-1}
R_v	Viscous resistivity of a porous medium, s^{-1}
Re	Reynolds number, $\text{Re} = \frac{\rho U_\infty x}{\mu_0}$
Re_Θ	Reynolds number with respect to the boundary layer momentum thickness
S	Window correction coefficient
St	Strouhal number
T	Temporal duration of a signal, s
t	Time, s
$\tilde{t}$	Normalized time, $\frac{t c_0}{a}$
T_a	Wind tunnel ambient temperature, $^\circ\text{K}$
t_c	Thickness of stainless steel cloth, m
T_r	Reference temperature for the hot−wire probe, $^\circ\text{K}$

T_w	Temperature of the hot–wire probe, °K
$\bar{\mathbf{u}}$	Mean velocity vector, $\mathrm{m\,s^{-1}}$
$\mathbf{u}$	Velocity vector, $\mathrm{m\,s^{-1}}$
$\mathbf{u}'$	Velocity fluctuations, $\mathrm{m\,s^{-1}}$
$u^\star$	Boundary layer friction velocity, $\mathrm{m\,s^{-1}}$
U_c	Boundary layer convective velocity, $\mathrm{m\,s^{-1}}$
U_∞	Free–stream velocity, $\mathrm{m\,s^{-1}}$
v	Acoustic velocity, $\mathrm{m\,s^{-1}}$
$\dot{V}$	Volumetric flow through a material, $\mathrm{m^3\,s^{-1}}$
$\tilde{v}$	Normalized acoustic velocity, $\frac{v}{c_0}$
V_i	Discrete particle velocity with respect to the ith lattice direction
v_d	Darcy velocity within a porous medium, $\mathrm{m\,s^{-1}}$
W	Cavity width, m
$\hat{X}(f)$	Discrete Fourier transform of a discrete signal $\hat{x}(t)$
$\hat{x}(t)$	Signal consisting of discrete samples in time
$\mathbf{X}$	Design matrix of a statistical model
$\mathbf{x}_k$	Location of microphone k
$\tilde{x}(t)$	Signal which varies continuously with respect to time
x	Streamwise coordinate
$X(f)$	Fourier transform of a continuous signal $\tilde{x}(t)$
x_0	Distance between the bottom frustum and conical vertex within a conical cavity, m
x_{im}	GAM experimental factor i for spline m
y	Vertical coordinate
y_{array}	Distance from the microphone array to the scan plane, m
y^+	Non-dimensional wall distance,
y_i	Response variable, i, of a statistical model
$\mathbf{Z}$	Design matrix of known sources of error

$\tilde{z}$	Normalized propagation distance, $\frac{z}{a}$
Z	Acoustic impedance, normalized by $\rho_0 c_0^2$
z	Spanwise coordinate
Z_c	Normalized cavity impedance
Z_r	Normalized radiation impedance

Superscripts

$+$	Above cavity
$-$	Within cavity
$\tilde{\ }$	Normalized

Subscripts

∞	Free stream
μ	Radial mode number
m	Azimuthal mode index
n	Iteration index

Summary

Aerodynamic noise produced by aircraft, wind turbines, and other objects subjected to airflow contribute to environmental noise pollution, which adversely affects human and animal health. Consequently, governments impose restrictions on aircraft and wind turbine noise levels. These restrictions can have an economic impact by limiting aircraft traffic and reducing wind turbine energy production. Accordingly, improving the design of aerodynamic surfaces to reduce their noise levels benefits health while enabling improved operational efficiency. Therefore, aeroacoustic research focuses on identifying and understanding the physical mechanisms behind aerodynamic noise to improve noise mitigation technologies. This research relies on acoustic wind tunnel measurements to validate simulations, theories, and design improvements.

Closed test section wind tunnels are widely used for aerodynamic testing but are less suitable for acoustic measurements because microphones must be installed in the wall. This location subjects the microphones to pressure fluctuations from the turbulent boundary layer (TBL), which contaminates acoustic measurements and reduces the signal–to–noise ratio (SNR). The impact of the TBL can be mitigated by recessing microphones within cavities and covering them with an acoustically transparent material. Modifying existing wind tunnel walls by installing cavity–mounted microphones is a straightforward and cost-effective improvement that enables combined aerodynamic and acoustic measurement campaigns.

The cavity geometry, i.e., depth, aperture size, wall angle, and presence of a covering determines the amount of TBL attenuation and consequently the improvement to SNR. While several studies have shown empirically that these parameters have an effect, few studies focus on identifying the physical mechanisms that explain the relationship between geometry and the reduction in TBL pressure fluctuations at the microphone. Thus, this thesis aims to identify these physical mechanisms through experiments and different modeling approaches to better explain the relationship between cavity geometry, the amount of TBL attenuation, and the subsequent impact on the measured acoustic signal.

Experimental data were collected to develop an empirical model to quantify how varying cavity geometry affects the measured pressure spectra. Moreover, experiments were also performed to validate simulation results and to quantify the SNR improvement when applying a beamforming algorithm to microphone array data. The modeling and simulation efforts focus on explaining the trends and phenomena identified in the experimental data. Initially, a physical model was developed that assumed acoustic propagation into an axisymmetric cavity with a constant cross–section. This model decomposes a pressure field, resulting from a TBL, into circular duct modes and was used to evaluate the relationship between cavity geometry and the propagation of these acoustic modes into the cavity. This model was followed up with a finite element method (FEM) simulation to study the influence of different cavity geometric parameters and wall materials on the acoustic response of the cavity when subjected to an acoustic wave.

The FEM simulation showed that the cavity's acoustic response is determined by the presence of standing waves in the form of acoustic depth modes. This simulation showed that cavities with angled walls have depth modes with lower amplitude waves and thus distort the acoustic signal less. Furthermore, it is shown that the acoustic responses of cavities formed out of sound-absorbing foam are driven by the shape of the foam holder and not the cavity shapes within the foam. Thus, the holder can be optimized to minimize the acoustic response, while the cavity itself can be optimized to reduce the influence of the TBL. Building upon these simulations, a Lattice Boltzmann based computational fluid dynamics (CFD) method was used to simulate the pressure and flow fields within three uncovered cavities and covered cavities resulting from the presence of a turbulent boundary layer.

The CFD simulations confirmed a significant finding of the physical model, that the amount of TBL attenuation increases as the cavity aperture size increases relative to the TBL streamwise coherence length. This is due to the resulting modal decomposition of the pressure field above larger cavities having more energy distributed across higher-order modes than for smaller cavities. These higher–order modes decay exponentially into the cavity, resulting in increased attenuation of the TBL. Smaller cavities have most of their energy in their first mode, which does not decay with increasing cavity depth. Furthermore, these simulations showed that the pressure field within covered cavities is primarily acoustic and can be decomposed into acoustic circular duct modes. Since the propagation of TBL pressure fluctuations into covered cavities is primarily acoustic, the shape of future cavities can be efficiently optimized using FEM simulations.

Finally, beamforming used with cavities improved the acoustic measurement SNR. Analysis shows that the improvements due to beamforming are independent of those attributed to the cavity geometry. Thus, combining the two approaches improves the SNR of acoustic measurements in closed test section wind tunnels.

Samenvatting

Aerodynamisch geluid, geproduceerd door vliegtuigen, windmolens, voertuigen en andere objecten, verhoogt het omgevingsgeluid. Dit geluid kan de gezondheid en het welzijn van mens en dieren schaden. Als gevolg hiervan beperken regeringen het toegestane geluidsniveau ten gevolge van vliegtuigen en windmolens. Deze beperkingen kunnen een negatieve economische invloed hebben door beperkingen op de operaties van vliegtuigen en verlaging van de energie productie door windmolens. Daarom richt aeroakoestische onderzoek zich op het identificeren en begrijpen van de mechanismen die aerodynamisch geluid veroorzaken om geluidsreductie technieken te verbeteren. Dit onderzoek maakt gebruik van akoestische windtunnel afmetingen om simulaties, theorieën, en ontwerpverbeteringen te bevestigen.

Gesloten windtunnels worden veel gebruikt voor aerodynamische metingen, maar zijn minder geschikt voor akoestische metingen omdat de microfoons in de tunnel muur moeten worden geïnstalleerd. Deze locatie ondergaat de stevige fluctuerende druk van de turbulente grenslaag (TBL) die de akoestische metingen beïnvloedt en de signaal–ruisverhouding (SNR) te verlaagt. Terwijl signaalverwerking door akoestische beeldvormingsmethoden de invloed van de TBL kan verlagen, beperkt de TBL nog steeds de SNR. De invloed van de TBL kan verder worden verminderd door het gebruik van "cavities". Microfoons die in cavities met een akoestische doorlatende afdekking worden geplaatst meten minder ruis van de TBL. Het aanpassen van bestaande windtunnels met de installatie van microfoons in cavities, is een relatief eenvoudige en goedkope oplossing die aeroakoestische metingen mogelijk maakt.

De cavity geometrie, bijvoorbeeld de diepte, de grootte van de opening, de hoek, het materiaal en aanwezigheid van een afdekking, bepaalt de vermindering van de TBL bijdrage en dus de verbetering van de SNR. Terwijl verschillende onderzoeken de invloed van deze geometrische parameters hebben aangetoond, hebben weinig onderzoeken zich gericht op het begrijpen van de relatie tussen cavity geometrie en de vermindering van TBL ruis. Daarom is het doel van dit proefschrift om deze relatie, en de relatie tussen cavity geometrie en het door de microfoon ontvangen akoestische signaal, beter te begrijpen middels experimenten en simulaties.

Experimenten met verschillende cavity geometrieën zijn gedaan om trends van eerder onderzoek te verifiëren en om een empirisch model te creëren. Bovendien, zijn experimenten uitgevoerd om simulaties te valideren en om de verbetering van de SNR te meten bij het gebruik van akoestische beeldvormingsmethoden. Het doel van de modellering en simulaties is om de relatie tussen de cavity geometrie, de TBL, en de akoestische respons te begrijpen. Als eerste is een fysisch model ontwikkeld waarbij is aangenomen dat de propagatie van de TBL geinduceerde fluctuerende druk akoestische beschreven kan worden. Ook zijn de cavities in dit model alleen cilindrisch en is hun dwarsdoorsnede constant. Dit model ontleedt het drukveld in modes, waarna de relatie tussen de voortplanting van deze modes en de cavity geometrie Bestudeerd kan worden. Ten tweede is een empirisch

model gecreëerd om de relaties tussen de cavity geometrie, de vermindering van de TBL bijdrage aan de metingen, en het invloed op de SNR te identificeren. Als volgende stap is een eindige–elementenmethode (FEM) simulatie om de invloed van verschillende cavity geometrie parameters op de akoestisch response van de holten te bestuderen opgezet. Als laatste stap is een Lattice Boltzmann method numerieke stromingsleer (CFD) simulatie gebruikt om de drukvelden en het stromingsveld in de drie cavities zonder en met een akoestische afdekking te evalueren.

De FEM simulatie toonde aan dat de akoestische respons van de cavities door de aanwezigheid van staande golven in de vorm van akoestische diepte modes wordt veroorzaakt. Deze simulatie liet zien dat cavities met schuine zijden lagere amplitude staande golven hebben. Dus vervormen ze het signaal minder. Bovendien wordt aangetoond dat de akoestische respons van cavities gevormd uit geluidsabsorberend schuim wordt aangedreven door de houder van de cavity en niet de holte geometrie zichzelf. Als gevolg daarvan kan de houder worden geoptimaliseerd om de akoestische respons te optimaliseren en kan de cavity zelf worden geoptimaliseerd om de invloed van de TBL te verminderen.

Een andere bevinding van dit proefschrift is dat de hoeveelheid demping van de TBL drukveld toeneemt naarmate de grootte van de holte opening groter wordt in verhouding tot de stroomwijze TBL coherentie lengte. Het fysische model verklaart deze relatie als de afhankelijkheid van de verdeling van energie over modes van hogere orde. Groter cavities hebben meer energie verspreid over hogere orde modes, terwijl kleiner cavities de meeste van de energie in de eerste mode hebben. De energie van de hogere orde modes neemt binnen de cavities exponentieel af, terwijl de eerste mode niet vervalt. Dus wordt de TBL verminderd in cavities met grotere opening. De CFD simulatie bevestigde dit resultaat en heeft aangetoond dat het drukveld onder de afdekking akoestisch is en kan worden ontleed in cirkelvormige 'duct' modes. Omdat de voortplanting van de TBL geinduceerde druk in afgedekte cavities voornamelijk akoestisch is, kan de geometrie van toekomstige cavities efficiënt geoptimaliseerd worden door FEM simulaties.

Uiteindelijk heeft het gebruik van akoestische beeldvorming met microfoons in cavities de SNR van akoestische afmetingen verbeterd. Analyse toont aan dat de verbeteringen door akoestische beeldvorming onafhankelijk zijn van die van de cavitie geometrie. Daarom verbetert de combinatie van de twee oplossingen de SNR van akoestische afmetingen in gesloten windtunnels meer dan het toepassen van een van de oplossingen.

1

Introduction

1.1 Motivation

Noise pollution negatively affects our health, natural ecosystems, and economic productivity. Aircraft and wind turbine noise are two anthropogenic noise sources that contribute to increased noise pollution levels. The impact of elevated noise pollution ranges from annoyance to more severe health problems including, but not limited to, hypertension [1, 2] and sleep deprivation [3]. Furthermore, animal behavior, such as communication, is altered by the continuous presence of noise [4, 5] in the animal habitats surrounding airports and wind farms. To reduce noise, regulations are applied to both aircraft and wind turbines to manage their respective contributions to noise levels.

Aviation noise affects the well-being of communities located near airports [6]. To address this problem, airport operations are often restricted in densely populated areas. These restrictions include limitations on the size and type of aircraft, as well as limits on the number of flights. Reducing the number of flights reduces noise levels within the surrounding communities but constricts aviation traffic. Given that aviation passenger and cargo traffic are expected to grow between 2.6% and 4.2% annually over the next 30 years [7], limitations on air traffic levels have a potential economic impact.

New wind turbine farms, in terms of installed power, are expected to grow between 12% and 17% annually according to industry estimates [8]. Onshore wind turbines, whose noise affects people and animals living nearby, are expected to constitute a significant portion of these installations due to their lower installation and maintenance costs [9]. Government regulations often limit the noise levels produced by these wind turbines to lessen the impact on surrounding areas. For example, in The Netherlands, the daytime restriction on overall sound pressure level (OSPL) is 47 dB, which falls to 41 dB at night [10]. These restrictions reduce the power generated by wind turbines as they must operate at lower power production levels to comply with these noise limits. This means that quieter wind turbines can produce more electricity. Specifically, a 1 dB improvement (reduction) in OSPL corresponds to a 2–4% increase in electricity production [11].

Improving the acoustic signature of aircraft and wind turbines, by reducing the aerodynamic noise, requires computational [12] and experimental investigations [13] of the noise–producing mechanisms. Experimental studies often involve acoustic measurements

1

in wind tunnels. In these experiments, the noise produced by test articles, e.g., an aircraft model or wind turbine blade, is measured to study the noise generating mechanisms and to develop noise prediction models [14]. The results of these experiments are used by engineers and scientists to improve the designs of aircraft and turbine blades. However, as design improvements lower the noise levels, quantifying the noise reduction becomes challenging as the noise levels approach the background noise levels of the wind tunnel. This is particularly an issue for closed test section wind tunnels [15], where acoustic measurements are affected by several tunnel background noise sources. These sources include fan noise, noise produced by protrusions into the free-stream, e.g., instrumentation and guide vanes, reflections within the tunnel circuit, and the turbulent boundary layer (TBL) present along the tunnel walls. When the amplitudes of the pressure fluctuations due to the TBL are greater than or equal to the acoustic pressure waves emitted by the test article, separating the acoustic signal from the TBL pressure fluctuations can be problematic. Other wind tunnel types, such as open–jet wind tunnels, are more suitable for acoustic measurements because the microphones can be placed outside of the free-stream in an anechoic chamber designed to reduce the effect of the tunnel background noise. However, closed test section wind tunnels are widely used for aerodynamic research because the test section walls improve the uniformity of the flow by bounding the free-stream flow, which results in more consistent and accurate aerodynamic measurements. Due to ubiquity of these wind tunnels, it is desirable to also use them for aeroacoustic research.

Acoustic measurements in closed test section wind tunnels can be improved by placing microphones within cavities. Cavities reduce the amplitude of the TBL pressure fluctuations at the microphone, thus improving the signal–to–noise ratio (SNR) of the measurements. Modifying existing wind tunnels by installing cavities is a straightforward and cost–effective solution to improve the SNR of the microphones [16]. This improvement is advantageous because measuring acoustic and aerodynamic data can occur in the same test campaign, which reduces testing time and cost. The amount of improvement has been shown to be dependent on the cavity geometry, however, prior research into using cavities has been primarily empirical with minimal focus on understanding the physical mechanisms that influence cavity performance. The research presented in this thesis identifies specific cavity parameters that reduce the influence of the TBL and describes different modeling and simulation approaches that provide a physical explanation for this reduction. Using this work, cavities can be designed to attenuate the TBL pressure fluctuations at the microphone, while minimizing the effect of the cavity on the acoustic signal of interest.

1.2 Aerodynamic Noise Sources and Mitigations

Aeroacoustic experiments in wind tunnels typically measure the aerodynamic noise produced by the aircraft landing gear, the airframe (wings, fuselage, and lifting devices) [17], wind turbine blades, and so forth [18]. Examples of aerodynamic phenomena that generate noise include vortex shedding and the interaction between the turbulent boundary layer and the airfoil trailing edge. The noise produced by vortex shedding can occur at the landing gear, the leading edge slats, as well as the wings and wingtips. Landing gear shed vortices, which are also referred to as von Kármán vortex sheets [19], from the wheels and struts [20]. This shedding produces tonal bluff body noise. The vortices shed by the
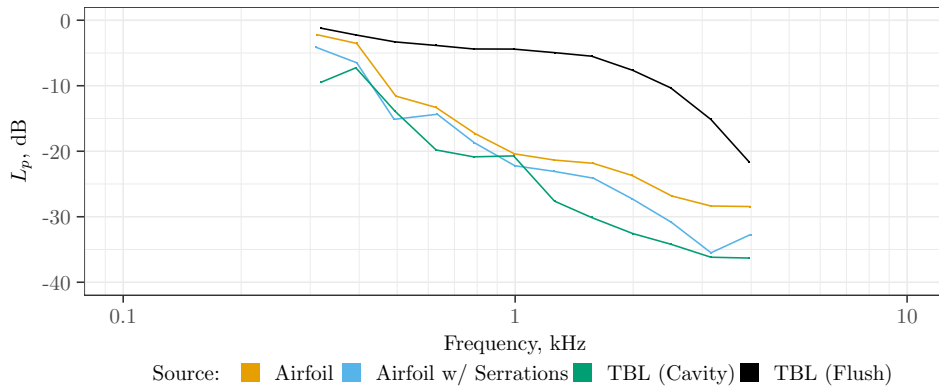
1

Figure 1.1: Illustrative comparison between the sound pressure level L_p from an airfoil, the same airfoil with trailing edge serrations, L_p of the TBL pressure fluctuations at the tunnel wall, and the TBL L_p as measured from a cavity.

leading edge slats can impinge on the main wing [21] and produce broadband acoustic scattering. Furthermore, depending on the attitude of the aircraft, vortex shedding and re-circulation can be induced by large angles of attack, which also produce noise [22]. Flow separation at the wingtips, as well as the generation of tip vortices also contribute to air-frame noise [22]. Another phenomenon that results in aerodynamic noise is turbulent boundary layer trailing edge (TBL-TE) noise, which radiates from the trailing edge of air-craft wings and flaps [23]. This noise is also the primary aerodynamic noise source for wind turbine blades [24]. This phenomenon is characterized by the randomly fluctuating eddies, within the TBL, that advect over the wing. When these eddies reach the wing's or turbine blade's trailing edge, the sudden change in acoustic impedance results in broad-band acoustic noise radiating into the far–field.

Reducing the amount of aerodynamic noise requires modifying the trailing edge and other lifting surfaces. These modifications include optimizing the shape of the trailing edge to minimize the boundary layer velocity fluctuations and to suppress the vortex shedding [25]. Adding serrations to the trailing edge is another effective modification that reduces the radiated sound [26, 27]. These serrations are typically v-shaped, e.g., a sawtooth pattern but can also include slits or sinusoidal profiles [28]. Serrations reduce the amount of radiated sound by promoting destructive interference [29] in the acoustic pressure field. Experiments have shown serrations can reduce the OSPL by 2–6 dB [30]. Modifying the construction of the trailing edges with the use of porous materials is another noise reduction approach. Using a porous material reduces the boundary layer velocity fluctuations compared to a solid trailing edge, which results in reduced radiated noise levels [31]. Typically this porous material consists of a metallic foam [31, 32]. Revell showed that porous wing flaps can reduce the radiated sound pressure level (L_p) by approximately 5 dB [33]. Another study [31] showed that replacing the last 5% of the airfoil, with respect to the chord length, with porous materials reduces the radiated TBL-TE noise by as much as 5 dB. Additionally, the complementary approach of forming serrations out of porous materials also has been shown to reduce noise levels [34].

As these innovations reduce the acoustic signature of aircraft and wind turbine blades, acoustic measurements in closed test section wind tunnels become increasingly challenging. An illustrative example is plotted in Fig. 1.1, which shows the reduction in the measured radiated L_p from an airfoil due to adding serrations. Furthermore, this figure shows that for a closed test section wind tunnel, the measured L_p of the airfoils are lower than the TBL pressure fluctuations measured by a flush–mounted microphone and only with a cavity can these airfoils be measured. Therefore, the use of cavities can improve the SNR of acoustic measurements in existing wind tunnels to enable aeroacoustic research applications.

1.3 Comparison of Wind Tunnel Configurations

Wind tunnels can be broadly characterized by the configuration of their test section. They typical feature either an open–jet, a closed test section, or a test section enclosed with acoustically transparent walls that combines the features of open–jet and closed test section wind tunnels. This section describes the typical layout of these tunnels, their sources of background noise, and their relative advantages and disadvantages for aerodynamic and acoustic testing.

1.3.1 Open–Jet Wind Tunnels
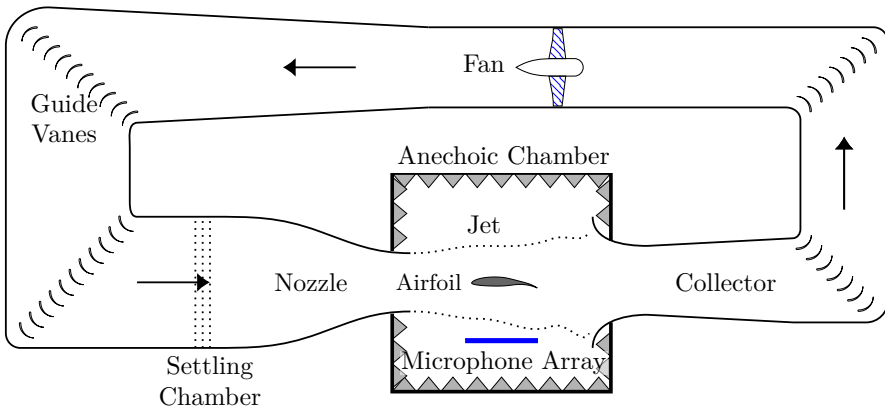
Figure 1.2: Configuration of a typical open–jet wind tunnel with a microphone array placed outside the jet in an anechoic chamber.

Open–jet wind tunnels, as their name suggests, are wind tunnels that exhaust the airflow directly into a room, as illustrated in Fig. 1.2. These tunnels are driven by one or more fans, which propel the air through a tunnel circuit. Downstream of the fans, there is a settling chamber with anti-turbulence screens [35–37] to reduce the noise generated by the fan blades and to decrease the free-stream turbulence [35]. The exit-nozzle is located after the settling chamber and accelerates the flow while keeping the velocity of the jet uniform across its cross–section as it is exhausted into the test chamber. The test article,

1

e.g., a wing or wind turbine blade, is placed in the jet so that aerodynamic and acoustic data can be measured. Finally, the jet flows into a collector. The collected flow can either be exhausted outside the chamber or recirculated through a closed circuit using guide vanes. These guide vanes reduce the pressure loss caused by redirecting the flow [38].

The open–jet wind tunnel configuration is well suited for acoustic measurements [37] because the microphone array can be placed outside of the jet flow [35]. This placement prevents the jet from grazing the microphone array, eliminating contamination from hydrodynamic noise. Furthermore, the test section can be placed in an anechoic chamber, which reduces acoustic reflections that contribute to the background noise. Figure 1.2 illustrates a typical open–jet wind tunnel configuration for acoustic measurements. The anechoic chamber is lined with wedges made of sound-absorbing foam or fiber-glass [35]. This chamber is designed to have as low as possible cut-off frequency, typically around 150 Hz [35, 39]. Above this cut-off frequency, acoustic reflections from the tunnel and test article are attenuated, reducing their impact on the acoustic measurements.

When wind tunnels are optimized for acoustic testing, the layout and the components are designed to minimize the production and propagation of background noise. The fans, guide vanes (if present), nozzle trailing edge, and the jet flow impinging on the collector contribute to this noise. The fan noise is higher at low frequencies due to the low fan blade passage frequency and is characterized as being tonal. Typically, the fan rotational speed is minimized to improve the tunnel efficiency and reduce the amount of noise generated by the fan [35]. Fan noise can also be lowered by decreasing the number of stators relative to the number of fan blades and by optimizing the blade geometry [37]. The guide vanes are also sources of aerodynamic noise due to the phenomena described in the previous section. Acoustic reflections occur at these guide vanes and contribute to the tunnel background noise. Thicker guide vanes with integrated acoustic absorbing materials can reduce these reflections [37]. Another source of tunnel noise are the vortices shed by the trailing edge of the exit nozzle, which can result in buffeting. This phenomenon occurs at low frequencies and affects both aerodynamic and acoustic measurements. Reducing this source of noise is a challenge and requires the use of exit vanes [40] or vortex generators. However, these solutions also produce unwanted noise [37]. Finally, the fluctuating jet shear layer impinging on the collector also contributes to the background noise. The fluctuation shear layer can be mitigated by lining the collector with acoustic absorbing materials and ensuring the opening is larger than the incoming jet [37]. An open–jet tunnel, that is acoustically optimized, can have a background A-weighted OSPL (OASPL) as low as 42 dBA at 30 m s^{-1} and 62 dBA at 55 m s^{-1} with louder tunnels having background noise levels of up to 66 dBA and 78 dBA for the same tunnel velocities [41].

The disadvantage of open–jet wind tunnels is that they are less suitable for aerodynamic measurements compared to closed test section wind tunnels. The buffeting and fluctuating shear layer both contribute to instability in the flow field. This instability affects both pressure measurements and velocity measurements [42]. Concurrently, the jet expands between the nozzle and the collector, decelerating the flow. This deceleration increases the static pressure in the streamwise direction [37], which affects the aerodynamic pressure measurements used to calculate lift and drag. Another source of measurement error occurs when the test article deflects the jet and alters the flow pattern in the test section. This alteration in the flow affects the accuracy of the test article's measured lift

1

and drag characteristics [43]. Acoustic measurements are also affected by the open jet. While this configuration reduces background noise, the jet's shear layer refracts acoustic waves as they pass through it. However, this refraction can be accounted for during post–processing [44]. Additionally, the shear layer can cause the acoustic signal to become decorrelated over the microphone array [45] as well the spectrum to become broader [46].
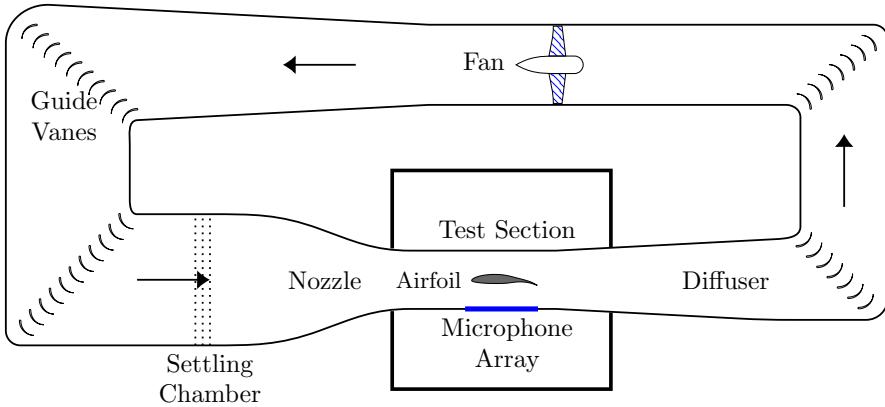
1.3.2 Closed Test Section Wind Tunnels

Figure 1.3: Configuration of a typical closed test section wind tunnel with a microphone array mounted on the test section wall.

Closed test section wind tunnels have a similar design as open–jet tunnels, as shown in Fig 1.3. The primary difference is that the test section is enclosed, which improves the uniformity of the flow. Because the jet is enclosed, a diffuser is used downstream of the test section instead of a collector.

As with the open–jet tunnel, the sources of background noise include the fans, guide vanes, and protrusions into the flow from instrumentation. Enclosing the test section and eliminating the anechoic chamber results in two additional sources of noise. First, acoustic reflections from the walls are a considerable contributor to the background noise levels. These reflections create a reverberant sound field within the tunnel [47]. Reducing the noise produced by the fans and guide vanes relies on the same approach as for open–jet wind tunnels. The background noise levels due to reflections can be reduced by installing sound-absorbing materials along the tunnel walls [41]. Second, the TBL which forms along the test section walls results in surface pressure fluctuations occurring at the microphones placed along the wall. These fluctuations are the primary noise source that affects acoustic measurements [48], and they affect acoustic measurements in two ways. First, the pressure fluctuations radiate sound into the test section [49] and second, the fluctuations impinge on wall flush-mounted microphones [50]. This hinders acoustic measurements when the acoustic signal being measured is equal to or lower than the TBL pressure fluctuations [16].

Closed test section wind tunnels are better suited for aerodynamic measurements due to test section walls bounding the free stream [50]. This configuration eliminates the buffeting and oscillating shear layer seen in open–jet wind tunnels and thus the flow is more stable. Furthermore, the test section walls can be instrumented with pressure taps to measure the aerodynamic properties of a test article [39]. However, the test section walls constrain the flow moving past the test article, which results in the flow moving faster than it would if no walls were present. This phenomenon is referred to as a blockage effect and thus must be accounted for when computing the aerodynamic characteristics [51].

1.3.3 Wind Tunnels with Acoustically Transparent Walls
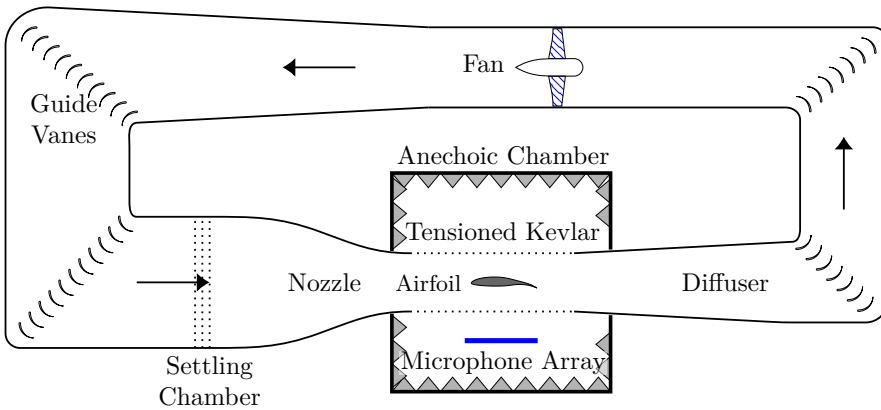

Figure 1.4: Configuration of a wind tunnel with an acoustically transparent tensioned Kevlar sheet replacing the test section walls.

A wind tunnel with acoustically transparent walls combines the acoustic testing advantages of an open–jet wind tunnel with the aerodynamic testing advantages of a closed test section wind tunnel. Figure 1.4 illustrates the layout of an example wind tunnel with Kevlar walls. The Virginia Tech Anechoic Wind Tunnel [52] is an example of this design. This wind tunnel uses Kevlar 120 sheets to replace the walls of a closed test section wind tunnel. The Kevlar confines the tunnel flow while allowing for the transmission of the acoustic waves from the test article into the anechoic chamber with approximately 1 dB of transmission loss. The sidewalls are Kevlar sheets that are held in tension and extend from the exit nozzle to the diffuser. The top and bottom of the test section, where the test article is attached, are Kevlar–covered metal perforated plates. As with an anechoic open–jet tunnel, the test section is located in an anechoic chamber. The microphone array is placed at a distance from the Kevlar sidewall, which eliminates the grazing TBL pressure fluctuations as a noise source. The Virginia Tech design resulted in a 24 dB (OSPL) reduction in background noise compared to their previous closed test section configuration [43].

This design maintains most of the aerodynamic testing advantages of a closed test

1

section tunnel. However, the absence of solid walls results in deflections in the Kevlar due to blockage effects and lift interference from the test article. These phenomena deflect the tunnel flow towards the Kevlar, which deforms the sheet. For the Virginia Tech tunnel, deflections of approximately 2 cm were measured when testing a NACA0012 airfoil at 0° angle of attack at 30 m s^{-1} and up to 4 cm when testing it at 8° angle of attack. These deflections alter the aerodynamic characteristics and require additional corrections to the lift and drag calculations [52]. Another disadvantage of this design is that the Kevlar must be held in tension across a 4.13 m span [43], which introduces mechanical complexity and affects tunnel operations. Replacing the walls of a preexisting closed test section wind tunnel with tensioned Kevlar sheets requires extensive modifications to the tunnel and surrounding test chamber. Additionally, extensive follow−on tunnel calibration is required to account for the effect of the Kevlar walls on the aerodynamic measurements.

1.4 Acoustic Array Measurements and the TBL

Acoustic measurements in wind tunnels are conducted with either individual microphones [53] or more commonly with an array of microphones [35]. As discussed previously, when testing in closed test section wind tunnels, placing microphones flush with the tunnel wall results in the grazing TBL reducing the acoustic measurement SNR. However, the amount of noise due to the TBL can be reduced by post−processing the measurement data using beamforming algorithms. This is referred to as acoustic imaging, which applies beamforming algorithms to localize and estimate the sound pressure level (L_p) of the noise sources located in a pre−defined scan plane [54]. When a noise source within this scan plane is coherent (at the microphone array), it appears as a source in the resulting acoustic image. Typically this scan plane is chosen to contain the test article or other expected sources of sound. The noise levels of sources outside of this scan plane, e.g., from the tunnel or the TBL present over the microphones, will be reduced relative to the sources within the scan plane. This is known as spatial filtering [55]. The amount of background noise suppression is dependent on the number of microphones and their relative positions [56]. The resulting acoustic source maps are then used to identify components or regions on a wing or turbine blade, which produce the most noise. However, poor SNR due to the TBL can result in acoustic maps with no identifiable noise sources.

Figure 1.5a is an illustrative example of an acoustic source map of a wing for an array with sufficient SNR. Two distinct acoustic sources are visible in this map. First, a source with a higher L_p at the trailing edge flap near the tip and second, a slightly weaker source along the leading edge slat. An acoustic map such as this one would inform the engineer that these two components are the dominant source of noise from the wing. However, if the SNR of the microphone array is low due to the TBL, the resulting source map is difficult to interpret. This is illustrated in Fig. 1.5b, where random noise sources are present on the map with no dominant source. This figure is representative of measurements where the incoherent TBL pressure fluctuations dominate the acoustic signal being measured.
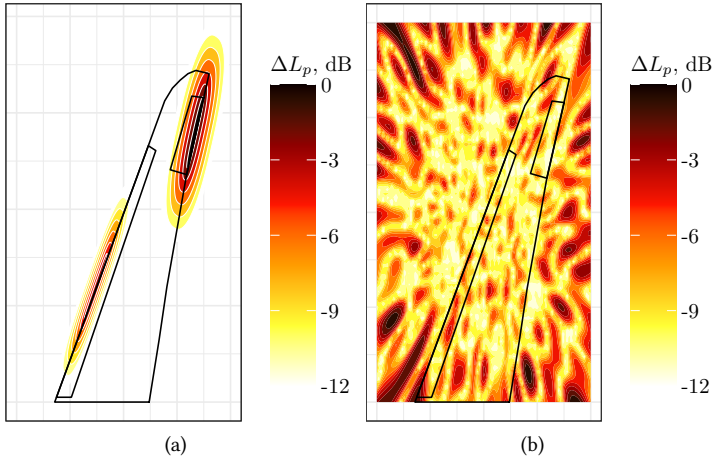
Figure 1.5: Illustrative acoustic source maps of a notional wing. a) Clean map with sufficient SNR. b) Noisy map with insufficient SNR.

1.5 Improving Wind Tunnel Acoustic Measurements

Several complementary approaches can improve the array SNR. First, increasing the number of microphones reduces the background noise levels when using beamforming algorithms because for every doubling of the number of microphones, the background noise levels are reduced by 3 dB [56]. However, this increases the array and processing costs due to the increase in microphones and thus the number of data acquisition channels. Second, longer measurement times improve the SNR [50], however, this increases the required testing time and thus testing costs. Third, post–processing with different acoustic imaging algorithms or other signal–processing methods can improve the effective SNR of the array. Finally, the microphones can be placed in cavities to reduce the TBL pressure fluctuations at the microphone. Recessing the microphones from the tunnel wall attenuates this noise source and increases the SNR [16]. The last approach is the focus of this research.

Increasing the number of microphones in an array improves the SNR by improving the spatial filtering of the TBL noise. Horne and James [50] estimated the relationship between the number of array microphones and the array SNR. This analysis showed that a 70 microphone array has an SNR threshold of −12.4 dB compared to a single microphone. In other words, a 70 microphone array can detect a noise source 12.4 dB lower than the noise floor imposed by the TBL pressure fluctuations, of a single microphone. Moreover, they showed that recessing a microphone 3.8 cm behind a metallic porous screen can reduce the pressure fluctuations at the microphone by an additional 20 dB at 4 kHz and by 5 dB at 10 kHz. The authors estimated the theoretical attenuation with respect to recession depth by modeling the TBL disturbances as waves propagating at their convective velocity. However, this explanation over-predicted the amount of attenuation.

Jaeger *et al.* expanded on the work of Horne and James by recessing a microphone array behind a Kevlar sheet [16]. The researchers studied three types of Kevlar: Kevlar 120 "thin weave" ($7.9\,\mathrm{g\,cm^{-2}}$), Kevlar 124 "crow's foot weave" ($7.9\,\mathrm{g\,cm^{-2}}$), and Kevlar 500
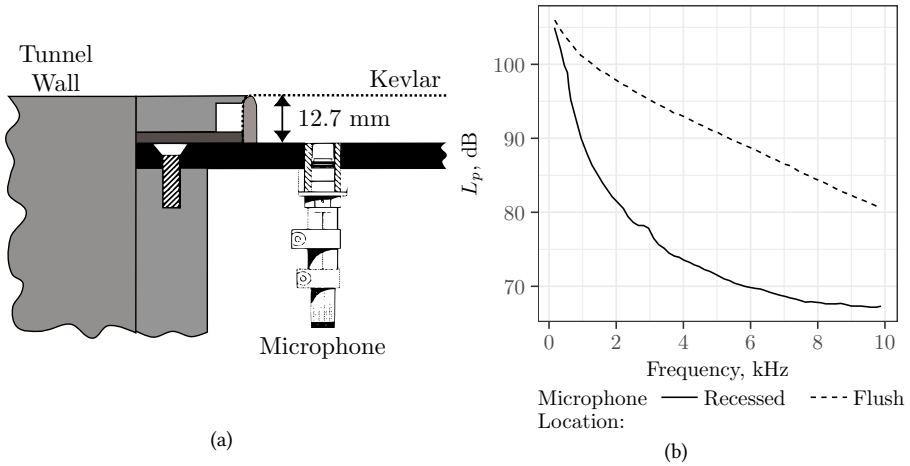
Figure 1.6: Jaeger et al. recessed array design. a) Diagram of the array recessed behind a tensioned Kevlar sheet. b) Single microphone results showing reduction in TBL noise due to recessing the microphone. Diagram and data taken from [16].

"thick weave" ($22\,\mathrm{g\,cm^{-2}}$). The authors chose thin weave Kevlar because it attenuated the acoustic signal of interest by only 1 dB in contrast to the thick weave Kevlar, which attenuated the signal by as much as 15 dB. Figure 1.6a shows the cross-section of their array design. This design holds the Kevlar sheet in tension, flush with the tunnel wall, above an array of microphones which are recessed 12.7 mm. This configuration reduced the TBL noise at the microphone by as much as 20 dB, as shown by the comparison between the flush and recessed microphone in Fig. 1.6b. This improvement enabled the authors to measure the noise generated by a wing flap beginning at 2 kHz where previously the TBL noise prevented acoustic measurements below 10 kHz.

Shin *et al.* [57] tested different recessed microphone array configurations based upon the approach of Jaeger *et al.* [16]. These arrays contained 100 microphones and were mounted either flush to the wind tunnel wall or recessed to depths of 2, 5, 10, or 20 mm. The authors experimented with both Kevlar and stainless-steel mesh cloth coverings. The TBL noise was attenuated by approximately 10 dB when the microphones were recessed by 10 mm with a free stream velocity of $30\,\mathrm{m\,s^{-1}}$. They showed that there were marginal improvements to the amount of TBL attenuation for recessed arrays deeper than 10 mm.

Koop and Ehrenfried used 45° countersunk cavities to form a microphone array consisting of 135 microphones [58]. This array was uncovered, which exposed the cavities directly to the grazing TBL. This work compared the effect of E-DAMAS2 and CLEAN-SC beamforming algorithms on improving the source localization of the acoustic map. However, the reduction of the TBL noise due to the cavities was not quantified.

Carballo-Crespo and Takeda compared 16 microphone mounting configurations, which varied the cavity depth, countersink angle, as well as placing cavities in a recessed plate, similar to the design of Jaeger [59]. These cavities were covered with either Kevlar type 1, type 2, or Taffeta silk cloth. Furthermore, the gap between the cover and the cavities was

either void or filled with acoustic foam. The results of this experiment showed that recessing the microphones improve the SNR but there was little improvement due to increasing the cavity depth beyond the cavity diameter. The author measured a 5 dB improvement through the usage of the type 1 Kevlar and the silk cloth. This improvement is smaller than observed by Jaeger. Finally, the use of foam within the recessed plate improved the SNR by an additional 5 dB.

Fleury *et al.* [60, 61] investigated the impact on reducing the influence of the TBL by placing microphones within individual cavities in addition to recessing the entire array. The authors also compared the efficacy of three stainless-steel mesh cloths with different weave densities and patterns. Stainless–steel was chosen instead of Kevlar because it has been observed that the flow over Kevlar generates high-frequency self-noise. Figure 1.7a compares the effect of three stainless-steel cloths compared to a flush microphone. The cloths tested are as follows: W1 (square weave, 0.4 mm thread spacing), W2 (square weave, 0.2 mm thread spacing), and W3 (triangular weave, 0.1 mm thread spacing). As this figure shows, the finely woven W3 cloth attenuates the TBL noise by as much as 20 dB while the coarser cloths had increased low–frequency noise at frequencies < 1 kHz and attenuated the TBL by at most 10 dB. The signal attenuation due to the cloth was measured to be between 1 and 2 dB, comparable to the Kevlar.
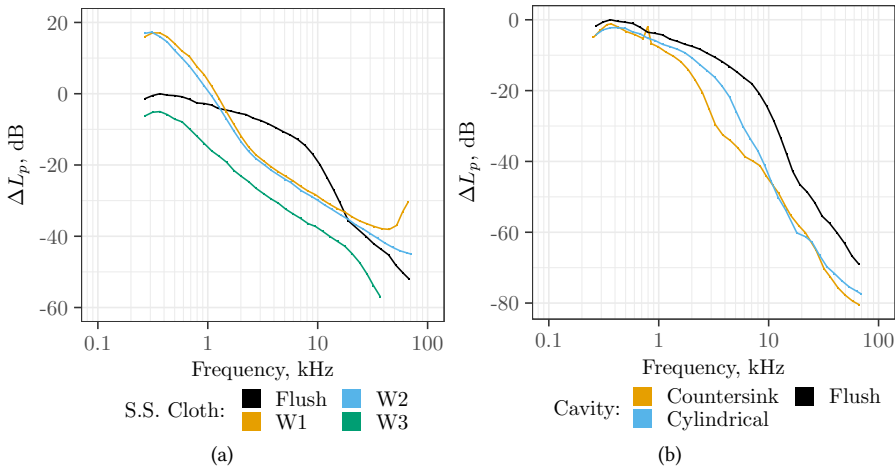
Figure 1.7: Key findings from Fleury et al. a) Effect of stainless–steel cloth with different weaves over a recessed plate. b) Effect of cylindrical and countersunk cavities on TBL noise. The data were extracted from [61].

This study also compared cavities placed within a wind tunnel wall with cavities placed in a plate that was recessed from the wall, similar to the one studied by Jaeger *et al.* [16]. Using individual cavities can be advantageous for large arrays because the covering can be attached to the wall between the cavities. This design makes it easier to maintain tension in the material covering the array. Furthermore, cavities isolate the microphones from each other. These experiments compared cylindrical cavities of different depths with and without a 45° countersink. The recessed plate depth ranged between 0 and 20 mm, while the cavity depths ranged from 3 to 6 mm. The recessed plate was lined with sound-

1

absorbing foam to reduce acoustic reflections between the plate and the covering. Recessing the plate by 2 mm reduced the TBL noise by 15 dB. Increasing the plate's recession depth, attenuated the TBL noise by an additional 5 dB for the 20 mm case. Figure 1.7b shows the change in TBL attenuation for two cavities placed in the wall compared with a flush–mounted microphone. An important finding is that a covered countersunk cavity attenuates the TBL noise better than a cylindrical cavity of the same depth.

1.6 Research Objectives

The studies discussed in the previous section empirically quantify the overall reduction in TBL noise using different covering materials, recession depths, and cavity shapes. Their research focus is not on providing physical explanations as to why certain geometries improve the SNR over others. This thesis builds upon this prior work by relating cavity geometric parameters such as aperture size, wall angle, presence of a covering, and depth to the physical phenomena induced by TBL pressure fluctuations. Furthermore, this thesis addresses the effect of cavity geometry on the measured acoustic signal. The cumulative response to the TBL and the acoustic signal determines the SNR of the microphone in a cavity. In order to understand and quantify these relationships, this thesis has the following research objectives:

1. Develop modeling techniques to identify the cavity geometric parameters that influence the attenuation of the turbulent boundary layer noise and affect the acoustic response of the cavities.

2. Quantify the impact of the relationship between cavity acoustic response and different geometric parameters and their effect on the acoustic measurements and the amount of TBL attenuation, quantified by the change in SPL in dB with respect to the flush–mounted microphone SPL.

3. Identify the acoustic and hydrodynamic phenomena present in the cavities due to the presence of the turbulent boundary layer and how these phenomena are influenced by different cavity geometries.

4. Quantify the impact of cavities on the SNR combined with using acoustic imaging post-processing on a microphone array, quantified by change in SNR in dB with respect to an array of flush mounted microphones.

1.6.1 Thesis Organization

This thesis uses different modeling approaches to accomplish the research objectives. Chapters 3–6 each describe different modeling or simulation approaches to identify which geometric parameters affect the cavity response as well their relationship with the physical phenomena that determine the response. Table 1.1 identifies which modeling approach is used in each chapter and which phenomenon the model addresses.

Chapter 2 describes the background theory and analytical tools that form the foundation of the subsequent chapters. The first half of this chapter focuses on the propagation of an acoustic wave into a cavity as well as the resulting response of the cavity. This is followed by a description of the characteristics of a wall–bounded turbulent boundary layer,

Table 1.1: Modeling approaches used to evaluate the effect of cavity geometry on the acoustic response and the attenuation of TBL pressure fluctuations.

Modeling Approach	Acoustic Response of Cavities	Propagation of TBL Pressure Fluctuations
Physical		Chapter 3
Empirical	Chapter 4	Chapter 4
Finite Element	Chapter 5	
Lattice Boltzmann		Chapter 6

useful empirical models, and the phenomena that occur within a cavity subject to grazing flow. The second half of Chapter 2 describes the experimental methods used in this thesis and the analytical techniques used to analyze the experimental and numerical data in the subsequent chapters.

Chapter 3 introduces a physical acoustic model that explains how cavity depth, aperture size, and wall material affect the propagation of the pressure fluctuations induced by the TBL into the cavity. This model is based upon duct acoustics and modal decomposition of the TBL pressure field at the top of the cavity. The results of this model partially explain the trends later identified in Chapter 4 as well as aid in interpreting the Lattice Boltzmann CFD simulation in Chapter 6. This chapter partially fulfills research objectives 1 and 2.

Chapter 4 presents two empirical models that estimate the amount of TBL attenuation and the change in SNR with respect to cavity depth, presence of a countersink, aperture size, and presence of a covering. Instead of testing all possible combinations of cavity geometries, a design of experiments (DoE) methodology was applied to minimize the number of cavities tested while ensuring statistically significant data. These data were fit to generalized additive models for the TBL attenuation and SNR response variables. The outcome of this work influenced the subsequent choice of cavities used in the later simulations and experiments. This chapter partially addresses objectives 1 and 2.

Chapter 5 uses a finite element method (FEM) based model to simulate the acoustic response to quantify the impact of cavity geometry on the acoustic signal when no TBL is present. These results explain the acoustic phenomena seen experimentally in Chapters 4 and 7 as well as the acoustic modes seen in the simulations of Chapter 6. The output of this chapter is essential for correcting the measured levels in order to retrieve the source spectrum. This chapter partially addresses objectives 1 and 2.

Chapter 6 uses a Lattice–Boltzmann based computational fluid dynamics (CFD) method to simulate a turbulent boundary layer advecting over three cavity shapes, with and with-

1

out a covering. This chapter addresses the question of how cavity geometry affects the pressure fluctuations at the bottom of the cavities by identifying how hydrodynamic and acoustic phenomena are influenced by cavity geometry. This chapter shows that the TBL pressure fluctuations within a cavity can be modeled as acoustic modes for covered cavities, which supports some of the assumptions in Chapter 3. This chapter addresses research objectives 1, 2, and 3.

Chapter 7 quantifies the combined effect of using cavities and beamforming algorithms on the SNR. This chapter uses conventional frequency-domain beamforming (CFDBF) to post–process the data collected from three arrays, each featuring a different cavity. The performance of these arrays is compared with a flush–mounted microphone array. This chapter shows that improving the SNR through the use of cavities is enhanced by the use of acoustic imaging post–processing. This chapter addresses research objective 4.

Finally, Chapter 8 summarizes the key findings of this work, identifies suggested modeling approaches to optimize future cavity designs, and proposes improved cavity geometries to increase the SNR of acoustic array measurements.

2

Background

This chapter summarizes the background knowledge and theory that this thesis is built upon. The beginning of this chapter introduces the fundamentals of cavity acoustics that determine the acoustic response of a cavity when subject to either an incident acoustic wave or the pressure fluctuations from a turbulent boundary layer (TBL). These fundamentals include analytical expressions for predicting the harmonic frequency of acoustic modes in the form of standing waves as well as the propagation of acoustic waves into a circular cavity in terms of duct modes. In addition to defining the fundamentals of cavity acoustics, this chapter provides an overview of the relevant TBL characteristics that affect the cavity response. Specifically, semi–empirical models that estimate the auto–spectra levels of the TBL pressure fluctuations, the relative levels of the hydrodynamic and acoustic components of the spectrum, and the coherence length of the TBL pressure fluctuations are described. Additionally, phenomena such as Rossiter modes, vortex shedding, and cavity–driven recirculation due to the presence of the TBL on top of the cavity are introduced. Finally, this chapter concludes by describing the measurement and analysis techniques used in this thesis. These techniques include spectral analysis, the calculation of the coherence between two microphones, acoustic imaging using conventional frequency-domain beamforming, wavenumber-frequency spectral analysis, and proper orthogonal decomposition.

2.1 Cavity Acoustics

The cavity's acoustic response due to either an incident acoustic wave or the TBL pressure fluctuations affects acoustic measurements in wind tunnels. This response can distort the measurements by either reducing the SNR by attenuating the incident acoustic wave or the signal can be amplified by the presence of acoustic modes in the form of standing waves. These standing waves occur when two acoustic waves moving in opposite directions constructively interfere with one another, i.e., when the acoustic wave reflected off the cavity bottom meets an acoustic wave propagating into the cavity. This phenomenon occurs at specific harmonic frequencies, which can be predicted using analytical expressions that depend on the cavity geometry. Perturbations due to acoustic waves or other pressure fluctuations at or near the harmonic frequency will excite these standing waves. This excitation is identified by a peak in the pressure spectrum. The amplitude of this peak

is quantified in terms of its quality factor, Q. Q is defined as $Q = f_n / (f_u - f_l)$, where f_n is the harmonic frequency, f_l is the frequency at the lower half–power location and f_u is the frequency at the upper half–power location. The half–power location is defined as 3 dB below the amplitude of the harmonic peak. The definitions for f_l and f_u are illustrated in Fig. 2.1.
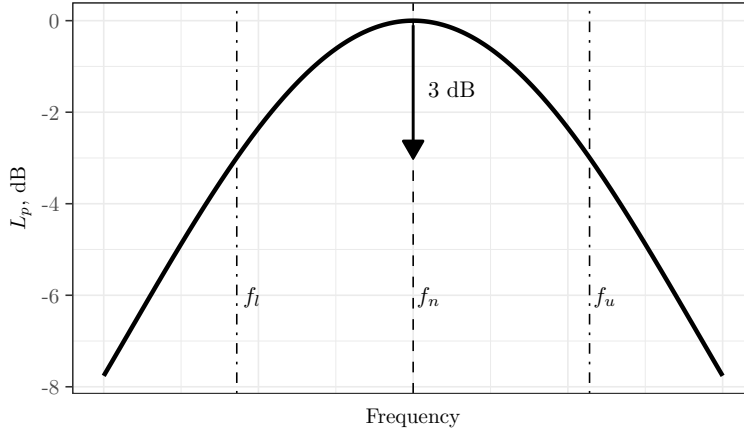

Figure 2.1: Half–power definition at which the lower f_l and upper f_u frequencies are defined, where f_n is the peak frequency.

Cavities can be characterized as either being rectangular or axisymmetric. Axisymmetric cavities include cylindrical, countersunk, and conical geometries. The expressions that predict the standing wave harmonic frequencies vary for rectangular, cylindrical, and conical cavities. These expressions are described in the following subsections.

2.1.1 Rectangular Cavity Acoustic Modes

Standing waves within rectangular cavities are also referred to as room acoustic modes. These modes can occur in the depth, longitudinal, and lateral directions. The frequency of these modes are predicted using the following expression [62, 63] :

$$f_{n_x n_y n_z} = c_0 \sqrt{\left(\frac{n_x}{2L}\right)^2 + \left(\frac{n_y}{4D}\right)^2 + \left(\frac{n_z}{2W}\right)^2} \tag{2.1}$$

In this equation, $f_{n_x n_y n_z}$ is the predicted harmonic frequency; n_x, n_y, and n_z are the integer mode numbers in the longitudinal, depth, and lateral directions. c_0 is the speed of sound, L is the cavity length, D is the cavity depth, and W is the width of the cavity. The physical interpretation of Eq. 2.1 is that for the lateral and longitudinal modes, the cavity is bounded by the cavity walls at a distance W and L. Since these directions are bounded by walls, the harmonic frequency occurs at the half–wavelength, which is $c_0/2L$. The frequency of the depth mode is determined by the quarter–wavelength with respect to the cavity depth, $c_0/4D$ due to the open top. Equation 2.1 states that increasing the cavity dimensions reduces the frequency at which these modes occur.
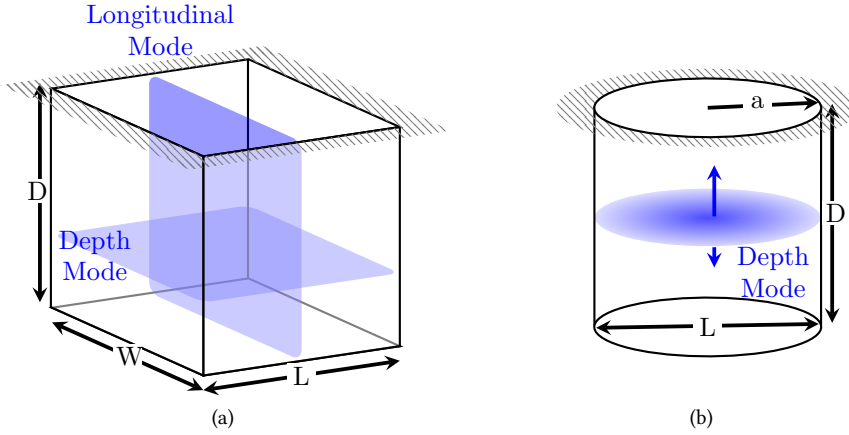
Figure 2.2: Illustrative acoustic modes within: a) a rectangular cavity and b) a cylindrical cavity.

2.1.2 Axisymmetric Cavity Acoustic Modes

Cylindrical Cavity Depth Modes

For cylindrical cavities, acoustic depth modes are typically the dominant acoustic mode. These depth modes are also referred to as quarter–wavelength modes due to the standing wave occurring at the quarter wavelength frequency associated with the cavity depth. Figure 2.2b shows the cylindrical cavity geometry with a depth mode present. The quarter–wavelength frequency is defined as,

$$f_n = \frac{(2n+1)c_0}{4(D+\delta)} \tag{2.2}$$

where f_n is the harmonic frequency of mode n and δ is the aperture correction term. The $2n+1$ term indicates that these depth modes occur at odd–numbered harmonics for open cavities. The aperture correction term, δ, depends on the cavity cross–sectional shape and whether not the cavity is flanged [64]. A flanged cavity is a cavity that features a solid wall that extends parallel to the cavity aperture. In the case of closed test section wind tunnels, the tunnel wall is considered to be an infinite flange, therefore, the depth correction term, δ, is defined as,

$$\delta = 0.8216a\left[1 + \frac{(0.77ka)^2}{1+0.77ka}\right]^{-1} \tag{2.3}$$

where k is the wavenumber corresponding to the harmonic frequency, f_n, and a is the cavity aperture radius [64]. For the cavities sizes used in this research, δ ranges between $0.597a$ and $0.707a$. As with rectangular cavities, the harmonic frequency decreases with increasing cavity depth. Additionally, the amplitude of the depth mode increases for deeper cavities. Equation 2.3 is applicable to cylindrical and countersink cavities.
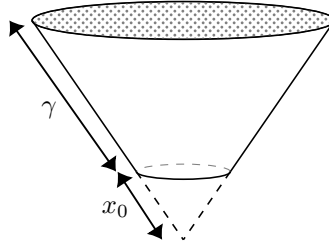
Figure 2.3: Definition of conical cavity geometric parameters.

Conical Cavity Depth Modes

The depth modes that occur within conical cavities do not directly depend on the cavity depth, D. Instead, the frequencies of these modes depend on the length of the cavity sidewall and the distance between the conical frustum, i.e., the location of the conical cavity bottom and vertex of the cone [65]. These geometric parameters are illustrated in Fig. 2.3. Using these parameters, the harmonic frequency is predicted using Eq. 2.4:

$$\tan(k\gamma) = -kx_0 \tag{2.4}$$

where x_0 is the distance between the bottom frustum and the conical vertex, k, is the wavenumber, and γ is the length of the cavity sidewall, i.e., the distance between the vertex and the aperture [65]. This equation is transcendental, therefore the resulting harmonic frequencies do not occur at integer values of the fundamental frequency but are spaced at monotonically increasing intervals, depending on x_0. This equation lacks a flanged correction term as the analytical solution for the conical waveguide is unknown [65]. Compared to the cylindrical cavities, the depth modes present in conical cavities typically have lower quality factors, thus have lower peaks. The reduced amplitude of the standing waves is caused by the radii of the cross-section decreasing with depth, which does not support high amplitude standing waves [65].

Azimuthal and Radial Modes

Within axisymmetric cavities, the standing waves can also include azimuthal and radial acoustic modes [66]. These modes are identified by their azimuthal mode number, m, and radial mode number, μ. The azimuthal mode number ranges between $-\infty$ and ∞ while the radial mode number ranges from 1 to ∞. This work uses the numbering convention where the radial mode number index begins at 1, per the Refs. 67. The normalized mode shape, $\phi_{m\mu}$ is defined in Eq. 2.5:

$$\phi_{m\mu}(\tilde{r},\theta) = N_{m\mu}J_m(\alpha_{m\mu}\tilde{r})e^{-im\theta} \tag{2.5}$$

where $\tilde{r}$ is the normalized radius (r/a), θ, is the azimuthal angle, $N_{m\mu}$ is the normalization factor, J_m is the Bessel function of the first kind, order m (azimuthal mode number), μ is the radial mode number and $\alpha_{m\mu}$ is the radial wavenumber [68]. The normalization factor,

$N_{m\mu}$, is defined in Eq. 2.6,

$$
N_{m\mu} = \begin{cases} \sqrt{2}, & \text{for } m = 0 \ \& \ \mu = 1 \\[2ex] \dfrac{\sqrt{2}}{J_m(\alpha_{m\mu})\sqrt{\left(1 - \dfrac{m^2}{\alpha_{m\mu}^2}\right)}}, & \text{all other values} \end{cases}
\tag{2.6}
$$

where $N_{m\mu}$ scales with the energy content of the corresponding mode [68]. The radial wavenumbers are the roots of the first derivative of the Bessel function of the first kind, $J'_m(\alpha_{m\mu})$. Table 2.1 lists these zeros for the first six azimuthal modes (m) and the first five radial modes (μ). J_m is symmetric, meaning $J_m(-x) = J_{-m}(x)$, therefore the values of $\alpha_{m\mu}$ for $m < 0$ are the same for $m > 0$.

Table 2.1: Zero's of $J'_m(\alpha_{m\mu})$ [69].

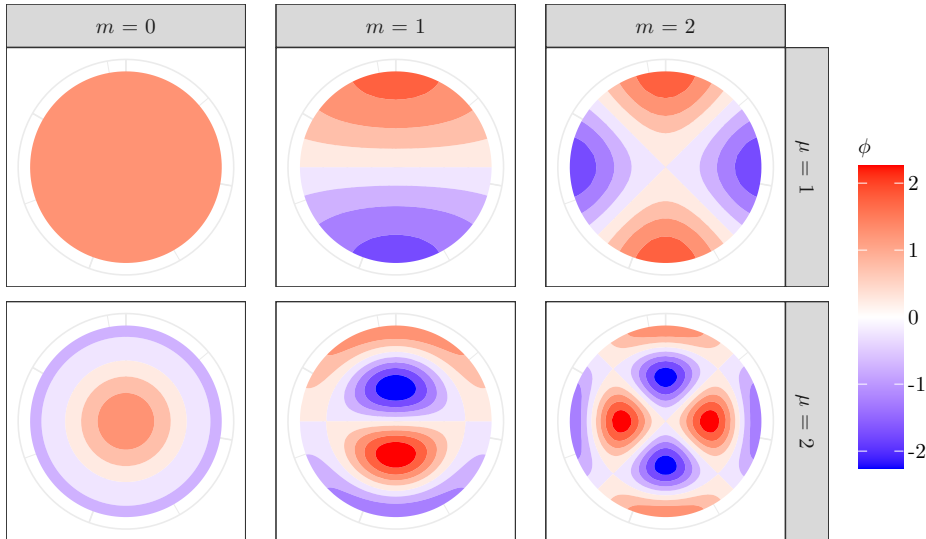|			m			
μ	0	1	2	3	4	5
1	0.000	1.8412	3.0542	4.2012	5.3175	6.4156
2	3.8317	5.3314	6.7061	8.0152	9.2824	10.5199
3	7.0156	8.5363	9.9695	11.3459	12.6819	13.9872
4	10.1735	11.7060	13.1704	14.5858	15.9641	17.3128
5	13.3237	14.8636	16.3475	17.7887	19.1960	20.5755

Figure 2.4: Mode shapes, $\phi_{m\mu}$, for a circular duct with hard walls. Calculated using Eq. 2.5.

Figure 2.4 shows the mode shapes for the first three azimuthal mode numbers and the first two radial mode numbers. The first mode, $m = 0$, $\mu = 1$ is the planar mode. These

modes can be excited at or above their cut–off frequencies, defined by Eq. 2.7.

$$\omega > \frac{\alpha_{m\mu} c_0}{a} \tag{2.7}$$

Note that for the planar mode, $\alpha_{m\mu} = 0.0$, and therefore this mode is cut–on for all frequencies. The standing wave associated with the planar mode manifests itself as a depth mode.

2.1.3 Propagation of Acoustic Waves Into a Cavity

The pressure field at the top of the cavity, which results from either an incident acoustic wave, the TBL pressure fluctuations, or a combination of the two, can be decomposed into azimuthal and radial acoustic modes defined by Eq. 2.5 and shown in Fig. 2.4. The acoustic energy in the pressure field is thus distributed across the resulting modes. The amplitude or energy content of each mode depends on the composition of the pressure field and the cavity aperture size and shape. This decomposition, for axisymmetric apertures, can be performed using the following integral [68]:

$$A_{m\mu} = \frac{1}{2\pi} \int_0^{2\pi} \int_0^1 p(\tilde{r}, \theta, \omega) \phi_{m\mu}(\tilde{r}, \theta) \tilde{r} d\tilde{r} d\theta \tag{2.8}$$

where $A_{m\mu}$ is the amplitude of the inward propagating mode with mode numbers: m and μ; $p(\tilde{r}, \theta, \omega)$ is the pressure field defined in terms of the normalized radial location, $\tilde{r} = r/a$, where a is the aperture radius. θ is the azimuthal location and ω is the angular frequency. $\phi_{m\mu}$ is the mode shape defined by Eq. 2.5. If the pressure field at the top is constant in the radial and azimuthal directions, the output of Eq. 2.8 will have all of the energy contained in the first mode, A_{01}. However, if the pressure field varies either or both the radial and azimuthal directions, the energy will be distributed across multiple modes. The resulting azimuthal and radial modes can therefore be summed together to reconstruct the original pressure field. The propagation of these modes into a cavity is defined by Eq. 2.9

$$H_{m\mu}(\tilde{z}) = A_{m\mu} e^{ik_{m\mu}\tilde{z}} + B_{m\mu} e^{-ik_{m\mu}\tilde{z}} \tag{2.9}$$

where $H_{m\mu}$ is the cumulative amplitude of the inward propagating acoustic mode, $A_{m\mu}$, and outward propagating mode, $B_{m\mu}$; $\tilde{z} = z/a$ is the normalized propagation distance from top to bottom, $k_{m\mu}$ is the axial wavenumber, and $i = \sqrt{-1}$. $k_{m\mu}$ is defined in Eq. 2.10:

$$k_{m\mu} = -\text{sgn}\left(\mathfrak{Im}\left(\sqrt{\tilde{\omega}^2 - \alpha_{m\mu}^2}\right)\right) \sqrt{\tilde{\omega}^2 - \alpha_{m\mu}^2} \tag{2.10}$$

where sgn is the sign function with extracts the sign of a real number, $\mathfrak{Im}$ is the imaginary component, and $\tilde{\omega} = \omega a/c_0$ is the normalized angular frequency, also known as the non–dimensional Helmholtz number. The amount of energy that propagates, $H_{m\mu}$, is dependent on $k_{m\mu}$ and normalized distance $\tilde{z}$. If $k_{m\mu}$ is complex, the mode is cut–off. Cut–off modes decay exponentially with distance into the cavity, per Eq. 2.9. Therefore, these modes have a negligible contribution to the acoustic energy at the bottom of the cavity.

Figure 2.5 plots the real component of the axial wavenumber with respect to normalized angular frequency for the first six azimuthal modes. This figure shows that the plane
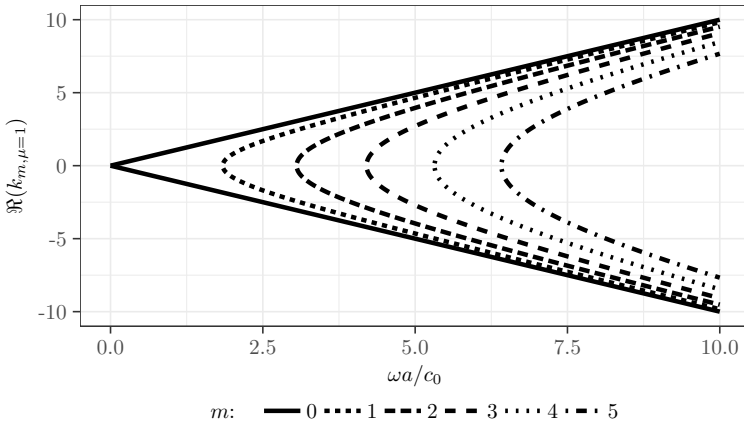
Figure 2.5: Real component of the axial wavenumber for the first six azimuthal modes with respect to normalized angular frequency, $\omega a/c_0$.

wave mode, ($m = 0$, $\mu = 1$) is cut–on for all frequencies. The higher–order modes become cut–on at specific frequencies, defined by Eq. 2.7 and this frequency increases with increasing mode number. At frequencies below this cut–off, the acoustic energy represented by these higher modes does not propagate into the cavity. Therefore, the amount of energy that propagates toward the bottom of the cavity depends on the distribution of energy across cut–on and cut–off modes. If the energy is concentrated in the cut–on modes, more energy will propagate toward the bottom while if the converse is true, the energy in the cut-off modes decay and thus the acoustic energy at the cavity bottom is reduced.

2.2 Wall and Cavity Noise Due to the TBL

The spectra levels of turbulent boundary layer pressure fluctuations that affect the wall–mounted microphone measurements. The spectra levels of these fluctuations can be estimated using different wall pressure spectra models, described in this section. These models are dependent on the boundary layer properties, e.g., its thickness, friction velocity, and scaling regions, which are also defined in this section. This section also introduces the noise–producing mechanisms caused by the interaction between the TBL and a cavity. These phenomena can generate additional noise, affecting the acoustic measurements.

2.2.1 Definition of Boundary Layer Properties

The turbulent boundary layer that forms at a wall is self–similar and can therefore be scaled using non–dimensional terms such as its Reynolds number, defined as $\mathrm{Re} = \frac{\rho_0 U_\infty x}{\mu_0}$. Where ρ_0 is the ambient density of the fluid (air), x is the position in the streamwise direction with respect to the origin, and μ_0 is the dynamic viscosity. The critical value of Re at which the boundary layer is considered turbulent depends on surface roughness, whether a favorable or adverse pressure gradient is present, and the turbulence of the free–stream [49]. In the case of a wind tunnel wall, the boundary layer is considered turbulent for $\mathrm{Re} > 1 \times 10^7$.
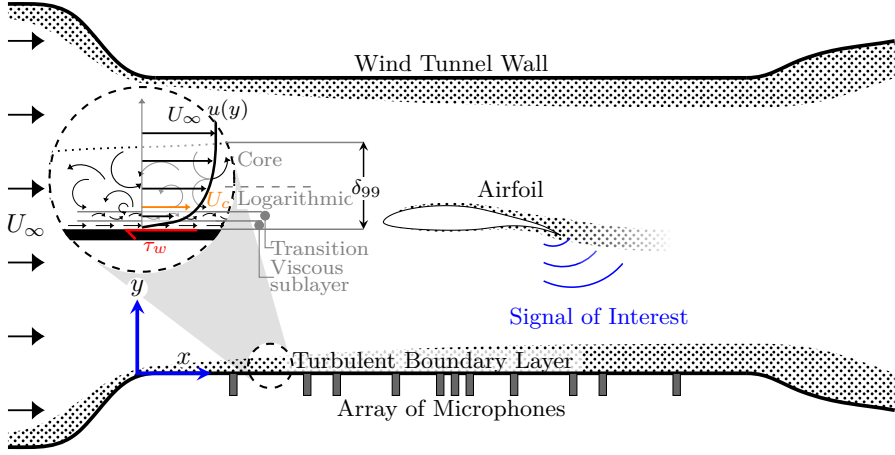
Figure 2.6: Diagram of a TBL present along a closed test section wind tunnel wall used for microphone array measurements. The detailed section view shows the velocity profile within the boundary layer, the presence of turbulent eddies, and the regions of the boundary layer [71].

The velocity profile of the TBL between the tunnel wall and the free–stream, U_∞, is assumed to be fully developed and in equilibrium. Therefore its mean velocity profile, $u(y)$, can be used to calculate the TBL thickness and other properties. This profile is illustrated in the detailed view of Fig. 2.6. The boundary layer velocity profile is asymptotic and varies from $0\,\mathrm{m\,s^{-1}}$ at the wall to 99% of the free–stream velocity, U_∞ at the boundary layer edge. The distance between the wall and $0.99U_\infty$ is the boundary layer thickness, δ_{99} [70]. The boundary layer is also described in terms of its displacement thickness, defined as follows:

$$\delta^\star = \int_0^{\delta_{99}} \left(1 - \frac{u}{U_\infty}\right)\mathrm{d}y \qquad (2.11)$$

where $\delta^\star$ is the displacement thickness, and u is the streamwise velocity profile as a function of y [70]. The boundary layer momentum thickness is another important property that is used to describe the TBL and is defined as follows:

$$\theta = \int_0^{\delta_{99}} \left(1 - \frac{u}{U_\infty}\right)\frac{u}{U_\infty}\mathrm{d}y \qquad (2.12)$$

where Θ is the boundary layer momentum thickness [70]. These three definitions of boundary layer thickness are used as dependent scaling variables in wall pressure spectra models [49].

In addition to the free–stream velocity, U_∞, the boundary layer can be described in terms of its friction velocity, $u^\star$ and its convective velocity, U_c. The friction velocity is

calculated as follows:

$$u^\star = \sqrt{\frac{\tau_w}{\rho_0}} = U_\infty \sqrt{\frac{C_f}{2}} \tag{2.13}$$

where τ_w is the boundary layer wall shear stress, shown in Fig. 2.6, and C_f is the coefficient of friction at the wall [70]. The convective velocity, U_c, is the velocity at which the eddies convect along the wall, within the boundary layer, which typically ranges between $0.55U_\infty$ and $0.85U_\infty$ [49].

2.2.2 Wall Bounded TBL Pressure Fluctuations

The boundary layer's turbulent structures subject wall–mounted microphones to pressure fluctuations and can be characterized by their spectra levels and their coherence lengths in the streamwise and spanwise directions. Several models that estimate the TBL spectra levels and coherence lengths are described in this sub–section.

Wall Spectra Models

Wall pressure spectra models are semi–empirical and are scaled using the boundary layer properties to estimate the spectra levels of the TBL near–field wall pressure fluctuations. These models are applicable to different turbulent boundary layers because the boundary layers are self–similar and therefore can be described in terms of non–dimensional variables [72]. One challenge with modeling the wall spectra is that the dominant TBL length, velocity, and pressure scales, vary depending on the region of the TBL. These regions are shown in the detailed view of Fig. 2.6 and include, starting from the wall, the viscous sublayer, a transition or buffer region, the logarithmic region, and the core region [49, 71]. The viscous sublayer and transition region are categorized together as the inner–region, while the logarithmic and the core region are referred to as the outer–region [71]. Many wall spectra models define separate length, velocity, and pressure scales for the inner and outer regions to properly model the contributions to the spectra levels from each region [72]. These models combine these different scaling parameters with empirical constants to estimate the spectrum levels across a range of angular frequencies, ω.

Example models include, but are not limited to, the Chase model [73], the Smol'yakov and Tkachenko model [49, 74], the Howe model [75], and the Goody model [72]. The Goody model has been shown to agree well with experimental data across the boundary layer inner and outer regions for values of Re_Θ between 1.4×10^3 and 2.34×10^4 [49], where Re_Θ is the Reynolds number with respect to the boundary layer momentum thickness. This model assumes no pressure gradient is present in the streamwise direction. Equation 2.14 defines the Goody model,

$$\frac{\Phi_{xx}(\omega)U_\infty}{\tau_w^2 \delta_{99}} = \frac{3\left(\omega\delta_{99}/U_\infty\right)^2}{\left[\left(\omega\delta_{99}/U_\infty\right)^{0.75} + 0.5\right]^{3.7} + \left[\left(1.1R_T^{-0.57}\right)^{0.75}\left(\omega\delta_{99}/U_\infty\right)\right]^7} \tag{2.14}$$

where Φ_{xx} is the wall pressure auto–spectra at a point, and R_T is the time scale ratio between the outer and inner boundary layer scaling regions. R_T is defined as $(u^\star \delta_{99}/v)(u^\star/U_\infty)$ where v is the kinematic viscosity of the fluid. The auto–spectra is normalized by the shear stress at the wall, τ_w and the time scale in the outer region, δ_{99}/U_∞. τ_w is used to normalize

the pressure fluctuations as it has been shown that using τ_w to normalize multiple experimental data sets collapses the pressure spectra across the widest range of frequencies [72]. The numerator of Eq. 2.14 varies the spectra with ω^2, which corresponds to the core region of the TBL. The largest coherent structures within the core region of the TBL are on the order of δ_{99}, thus δ_{99} is used as the length scaling term for this region. The first term in the denominator models the spectra in the transition region of the TBL, which varies with $\omega^{-0.7}$, according to Goody, or ω^{-1} in other literature [49]. The second term in the denominator accounts for the viscous inner layer, which at higher frequencies collapses using the inner layer time scale, $v/u^{\star 2}$. To account for the different time scales between the regions, this term is multiplied by $R_T^{-0.57}$. As R_T increases, the inner–layer frequency shifts away from the outer–layer scaled frequency range and the width of the transition region's frequency range increases, which accounts for the change in spectra due to increasing Reynolds number [72]. The inclusion of the term accounting for the inner–layer scaling increases the accuracy of the Goody model at higher frequencies.
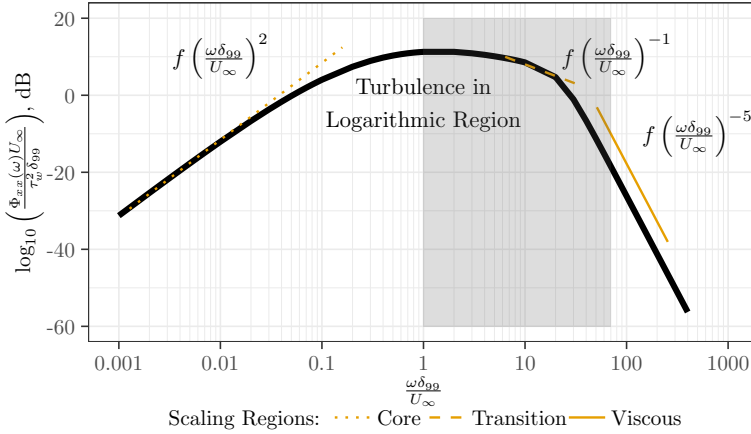

Figure 2.7: Wall pressure spectra (Φ_{xx}) as modeled by the Goody model (Eq. 2.14), where $\tau_w = 1.63\,\text{Pa}$, $U_\infty = 32\,\text{m}\,\text{s}^{-1}$, $\delta_{99} = 0.0324\,\text{m}$, and $R_T = 95.7$. The gray region represents the frequency range applicable to this work.

The Goody model is used to calculate the spectrum plotted in Fig. 2.7. This spectrum is representative of the variation of TBL pressure spectrum levels at the wall with respect to frequency. The trends in wall pressure variation with frequency for the different boundary layer regions [49], are shown in Fig. 2.7. The lower frequency range of the spectrum is due to boundary layer velocity fluctuations occurring in and near the edge of the boundary layer [76] and the spectrum varies with ω^2. Moving closer to the wall, the pressure fluctuations are associated with the eddies convecting along the wall [76]. This region corresponds to the logarithmic layer of the boundary layer, which is the region where the boundary layer velocity scales logarithmically [71]. The pressure spectrum due to turbulence is generally highest in this region [49]. In the transition region, the spectrum varies inversely proportional to ω. The inner scaling law applies to the viscous subregion [77], which is located close to the wall, $y < v/u^{\star}$ [71]. The pressure spectrum levels vary with frequency to the power of -5 in this region. The gray region is the frequency range that is the focus of this work and ranges from 0.25 kHz to 10 kHz. These frequencies were chosen

as they cover the frequencies of interest for aeroacoustic wind turbine blade studies, e.g., Oerlemans *et al.* [26] and Chong and Dubois [34]. In this region, the spectral levels of the TBL pressure fluctuations decrease with increasing frequency.

The Goody model accurately estimates the wall pressure spectra, however, it does not provide information on the acoustic and hydrodynamic components of the TBL pressure fluctuations. These components can be identified by calculating the wall pressure spectra with respect to wavenumber, k, instead of frequency. Wavenumbers are the spatial analog to frequency, where the wavenumber k, is the angular frequency ($\omega = 2\pi f$) divided by a velocity u, thus $k = \omega/u$. Wavenumber spectra are used to account for the propagation velocity of the pressure fluctuations. For example, acoustic pressure fluctuations will have a spectral peak at the acoustic wavenumber, $k_0 = \frac{\omega}{c_0}$ because they propagate at the speed of sound. In contrast, hydrodynamic pressure fluctuations along a wall typically have a spectral peak near the convective wavenumber, $k_c = \frac{\omega}{U_c}$ due to the transport velocity of the turbulent eddies being near the convective velocity, U_c [49].

The wall pressure model developed by Chase [73] accounts for both the hydrodynamic and acoustic components of the TBL spectrum. Chase built upon the work of Ffowcs Williams [78] to develop a wavenumber spectrum model for the TBL. Chase modeled the wall pressure spectrum as the combination of a turbulence–turbulence contribution and a turbulence–mean shear contribution [73]. The turbulence–mean shear component is the modeled contribution to the pressure fluctuations by the turbulent structures, i.e., the eddies, convecting at a constant mean convective velocity, U_c, [49]. The turbulence-turbulence component represents the unsteady convection of turbulence, i.e., the instantaneous velocity fluctuations deviating from the mean U_c. Chase's model is presented in Eq. 2.15:

$$\frac{\Phi_{xx}(\mathbf{k},\omega)U_\infty}{\tau_w^2\delta_{99}^3} = \frac{(U_\infty/u^\star)(1/\delta_{99}^3)}{\left[K_+^2 + (b\delta_{99})^{-2}\right]^{-5/2}}\left[C_M\left(\frac{|\mathbf{k}|}{|K_c|}\right)^2 k_x^2\right.$$
$$\left.+ \left[c_2\left(\frac{|K_c|}{|\mathbf{k}|}\right)^2 + c_3\left(\frac{|\mathbf{k}|}{|K_c|}\right)^2 + (1 - c_2 - c_3)\right]C_T|\mathbf{k}|^2\left[\frac{K_+^2 + (b\delta_{99})^{-2}}{|\mathbf{k}| + (b\delta_{99})^{-2}}\right]\right]$$

(2.15)

where $\mathbf{k}$ is the wavenumber vector in the streamwise and spanwise directions, and $|\mathbf{k}|$ is its magnitude. The empirical constants b, c_2, and c_3 are found experimentally, and their values are 0.37, 1/6, and 1/6 [49]. C_M and C_T are the empirical constants that scale the modeled mean–shear turbulence and the turbulence–turbulence contribution to the spectra. These constants are 0.155, and 0.0047. The expressions K_+ and K_c are defined in Eq. 2.16:

$$K_+^2 = \frac{(\omega - U_c k_x)^2}{h^2 u^{\star 2} + |\mathbf{k}|^2}$$

$$K_c = \sqrt{k_0 - |\mathbf{k}|^2}$$

(2.16)

where k_x is the streamwise wavenumber, and h is an empirical constant equal to 3.88. For Eq. 2.15, the mean–shear turbulence contribution increases as it approaches the convective wavenumber $k_c = \omega/U_c$, where the model has a maximum due to the term $\left(\frac{|\mathbf{k}|}{|K_c|}\right)$

approaching unity. For low wavenumbers, the turbulence–turbulence contribution, indicated by C_T is larger with a local maxima at the acoustic wave number, k_0. An interpretation of this model shows that the hydrodynamic component is dominant, especially at the wavenumber associated with the convection of eddies within the TBL. An example of the wall spectra calculated using Eq. 2.15 is shown in Fig. 2.8.
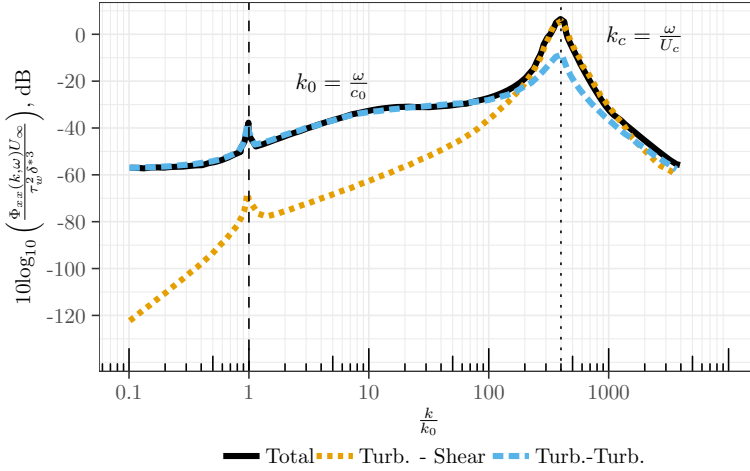

Figure 2.8: Illustrative example of the modeled turbulence–turbulence and turbulence–mean shear contributions to the total wall pressure spectral level, Φ_{xx}. Normalized spectra levels with respect to the normalized wavenumber, k/k_0, are calculating using the Chase model [73] using parameters from Blake [49]. The spectra are normalized with the free–stream velocity, U_∞, the TBL wall shear stress, τ_w, and the TBL displacement thickness, $\delta^\star$. The wavenumber is normalized by the acoustic wavenumber $k_0 = \omega/c_0$, where ω is the angular frequency and c_0 is the speed of sound. The long dashed vertical line is the acoustic wavenumber, k_0, and the dotted vertical line is the convective wavenumber k_c, where U_c is the TBL convective velocity.

Figure 2.8 plots the normalized wall pressure spectra level, Φ_{xx}, using Chase's model as well as the modeled turbulence-turbulence and turbulence-shear contributions as calculated using Eq. 2.15. This spectrum has two peaks. The smallest peak is at the acoustic wavenumber, where the acoustic pressure fluctuations from the turbulence–turbulence component are dominant. The larger peak, 45 dB higher, occurs at the convective velocity wavenumber, $k_c = \omega/U_c$. The spectral energy above the acoustic wavenumber is the hydrodynamic component of the TBL pressure fluctuations. Chase's model has been verified experimentally by Blake [49] and Ehrenfried and Koop [79]. Since the peak at k_c is highest, the wall–mounted microphones are thus primarily subjected to hydrodynamic pressure fluctuations due to the convecting TBL eddies. Given that the acoustic component is lower than the hydrodynamic component, typically the wall–pressure spectra models, such as the Goody model, only account for the hydrodynamic component of the TBL wall pressure spectrum.

TBL Coherence Length
The coherence length of the boundary layer pressure fluctuations is the distance at which the pressure fluctuations, p', at two points along the wall are correlated. Corcos [80] introduced a model for the TBL wall cross–spectra that modeled the change in coherence

length with increasing frequency as exponentially decaying. This model is shown in Eq. 2.17:

$$\Phi_p(\Delta x, \Delta z, \omega) = \Phi_{xx}(\omega) e^{\frac{-\alpha_z|\omega\Delta z|}{U_c}} e^{\frac{-\alpha_x|\omega\Delta x|}{U_c}} e^{\frac{i\omega\Delta x}{U_c}} \tag{2.17}$$

where $\Phi_p(\Delta x, \Delta z, \omega)$ is the cross–spectra; Δx and Δz are the separation distance between two points in the streamwise and spanwise directions; α_z and α_x are empirical constants equal to 0.116 and 0.7. For the wall pressure spectrum, Φ_{xx}, one can use experimental values or predicted values from one of the wall pressure spectra models described previously. The $\exp\left(\frac{-\alpha_z|\omega\Delta z|}{U_c}\right)$ term describes the spanwise decay of the pressure spectra, the $\exp\left(\frac{-\alpha_x|\omega\Delta x|}{U_c}\right)$ term represents the streamwise decay, and the $\exp\left(\frac{i\omega\Delta x}{U_c}\right)$ term is the streamwise convection of the pressure fluctuations. The coherence lengths, normalized by δ_{99} in the streamwise and spanwise directions are thus:

$$\begin{aligned}
\frac{\Lambda_x}{\delta_{99}} &= \left|\frac{U_c}{\omega\delta_{99}}\right|\frac{1}{\alpha_x} \\
\frac{\Lambda_z}{\delta_{99}} &= \left|\frac{U_c}{\omega\delta_{99}}\right|\frac{1}{\alpha_z}
\end{aligned} \tag{2.18}$$

where Λ_x and Λ_z, are the streamwise and spanwise coherence lengths, the inverse of these are used in the streamwise and spanwise exponential functions in Eq. 2.17.

Equation 2.17 was modified by Efimtsov [81] to improve the agreement between the Corcos cross–spectra model and experimental data. Efimtsov replaced Corcos' modeled coherence lengths in Eq. 2.18 with the following definitions provided in Eq. 2.19:

$$\begin{aligned}
\frac{\Lambda_x}{\delta_{99}} &= \left[\left(\frac{a_1\omega\delta_{99}/u^\star}{U_c/u^\star}\right)^2 + \frac{a_2^2}{(\omega\delta_{99}/u^\star)^2 + (a_2/a_3)^2}\right]^{-1/2} \\
\frac{\Lambda_z}{\delta_{99}} &= \left[\left(\frac{a_4\omega\delta_{99}/u^\star}{U_c/u^\star}\right)^2 + \frac{a_5^2}{(\omega\delta_{99}/u^\star)^2 + (a_5/a_6)^2}\right]^{-1/2}
\end{aligned} \tag{2.19}$$

where the empirical constants are defined as $a_1 = 0.1$, $a_2 = 72.8$, $a_3 = 1.54$, $a_4 = 0.77$, $a_5 = 548$, and $a_6 = 13.5$. Efimtsov's model is applicable for flows of $M < 0.75$ [81].

Figure 2.9 plots the streamwise and spanwise coherence lengths using Efimtsov's model, normalized by the boundary layer thickness, δ_{99}. This model shows that the coherence length within the TBL is longer in the streamwise direction than in the spanwise and both lengths decay with increasing frequency. Since the size of the TBL eddies can be inferred from the coherence length, this expression suggests that the eddy size decreases with increasing frequency. The coherence length and its frequency dependence partially explain the relationship between cavity geometry and the amount of TBL attenuation, which will be discussed in Chapters 3 and 6. Modeling the coherence length is also important to quantify the accuracy of wall pressure measurements. If the coherence length, i.e., the turbulent eddy, is smaller than the microphone transducer, multiple eddies will be present on the transducer. With multiple coherent sources present, the pressure fluctuations from these eddies will be spatially averaged by the transducer, due to the mean of the pressure
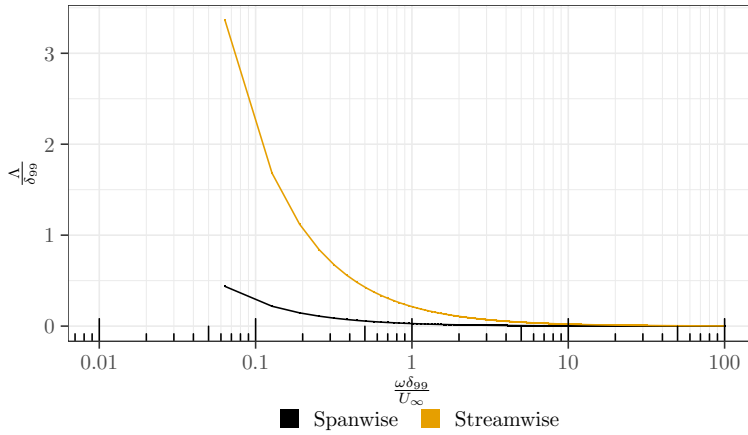
Figure 2.9: Coherence lengths in the streamwise and spanwise directions using the Efimtsov's model [81], where $u^\star = 1.19\,\mathrm{m\,s^{-1}}$, $U_c = 21\,\mathrm{m\,s^{-1}}$, and $\delta_{99} = 0.0324\,\mathrm{m}$.

fluctuations tending toward zero. This results in lower than actual measurements of the pressure fluctuation amplitudes at higher frequencies.

2.2.3 Cavity Noise

Chapter 1 introduced the concept of placing microphones at the bottom of cavities to reduced the amount of measured TBL pressure fluctuations. However, the interaction between the TBL and the cavity can also generate additional sources of hydrodynamic and acoustic noise. One source of noise is the interaction between the shear layer above the cavity, which forms when the flow separates from the cavity leading edge, and the cavity itself. This shear layer contains random turbulence and coherent vortices that are shed from the upstream cavity edge. The impingement of these vortices on the downstream wall generates acoustic pressure waves that radiate into and out of the cavity. Simultaneously, the flow above the cavity induces the formation of recirculation regions within the cavity. Recirculating flow produces hydrodynamic noise within cavities because it transports turbulence from the shear layer and cavity walls toward the cavity bottom. Finally, these sources of pressure fluctuations excite acoustic cavity modes that can become dominant at certain frequencies, as discussed in section 2.1. Figure 2.10 illustrates these phenomena for a typical cavity. The cavity length, also referred to as the aperture diameter, is defined as L, and the cavity depth is defined as D. The hydrodynamic and acoustic phenomena that produce noise are affected by the shape of the cavity, i.e., whether the cavity is a rectangular or axisymmetric cavity, and by its length to depth ratio L/D.

The shear layer above a cavity has a hyperbolic velocity profile, which is inherently unstable [82]. When perturbed, the shear layer oscillates, which results in periodic vortex shedding from the leading edge, as shown in Fig. 2.10. The impingement of these vortices generates pressure waves that propagate within and outside the cavity [83]. These pressure waves subsequently perturb the shear layer [84], resulting in additional vortex shedding. This phenomenon can create a feedback loop, which is referred to as a Rossiter mode [85]. Rossiter developed an empirical model to predict the Strouhal number at which
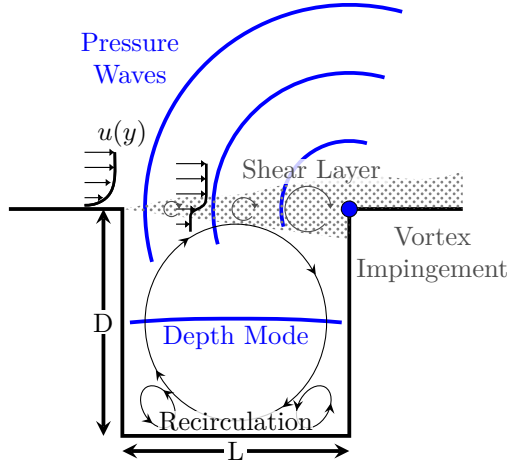
Figure 2.10: Acoustic and hydrodynamic phenomena due to the TBL above a cavity.

these modes occur in rectangular cavities, as described by Eq. 2.20,

$$\text{St}_L = \frac{fL}{U_\infty} = \frac{n - \zeta}{M + \frac{1}{\kappa}} \tag{2.20}$$

In Eq. 2.20, St_L is the Strouhal number, L is the cavity length (defined in Fig. 2.10), n is the mode number, ζ is an empirical constant equal to 0.25, M is the Mach number, and κ is the ratio between U_c and U_∞. When the ratio between cavity aperture length, L, and the TBL momentum thickness, Θ, is below 42, Rossiter modes are not typically seen [86]. For rectangular cavities, the pressure fluctuations due to these modes manifest themselves as narrowband spectral peaks [82, 85, 87]. However, this response changes for axisymmetric cavities, e.g., cylindrical, cylindrical with a countersink, and conical geometries. The feedback loop identified by Rossiter is also present in these cavities, however, these modes feature a broad peak with reduced spectral levels compared to the narrowband peaks seen in rectangular cavities [87]. This change in response is due to the difference in leading–edge geometry for rectangular and axisymmetric cavities. Rectangular cavities have a straight leading edge in the spanwise direction which sheds vortices that extend parallel to this edge. These vortices are thus parallel to the downstream rectangular cavity edge when they impinge, producing a stronger pressure wave at a specific frequency. In contrast, cylindrical cavities have upstream and downstream edges that vary in the spanwise direction. This results in smaller spanwise vortices that impinge at different points along the downstream edge, resulting in weaker pressure waves that are emitted at different frequencies. Rossiter modes affect microphone measurements in this application when the cavities are uncovered.

These pressure waves, as well as the pressure fluctuations within the shear layer, and recirculating flow, excite acoustic modes within the cavities. The frequency and type of acoustic mode depend on the cavity geometry, as discussed in section 2.1. Shallow cavities ($L/D > 1$) feature longitudinal acoustic modes [88–90] due to pressure waves emanating

from the downstream cavity wall, as illustrated in Fig. 2.2a. Rectangular cavities can also have spanwise modes present [91]. For deeper cavities ($L/D \leq 1$), these perturbations excite acoustic depth modes at the cavity quarter wavelength frequency [92, 93], as discussed previously in section 2.1. For axisymmetric cavities, radial and azimuthal modes, shown in Fig. 2.4, may also be excited, depending on the cavity geometry [63]. Very deep ($L/D \ll 1$) cylindrical cavities, often referred to as side-branches, have large amplitude acoustic depth modes [86]. For these very deep cylindrical cavities, the pressure fluctuations toward the cavity bottom are predominantly acoustic [94]. When the Rossiter mode and an acoustic cavity mode occur at or near the same harmonic frequency, these modes become locked–on. This locked–on phenomenon results in higher amplitude acoustic waves that radiates from the cavities into the far–field [63, 95].

Recirculation within the cavity transports turbulence to the bottom of uncovered cavities, which results in hydrodynamic pressure fluctuations [96]. Turbulence is also generated at the bottom of these cavities due to the increased amount of wall shear caused by the recirculating flow. This produces turbulent fluctuations as high as $\approx 35\%$ of the local velocity [97]. These fluctuations are highest between the downstream bottom corner and the cavity center [98]. The recirculation pattern within cavities depends on the cavity shape, as an example, shallow cavities ($L/D > 4$) feature multiple recirculation zones near the upstream and downstream walls of the cavity [99]. While deeper cavities ($L/D \leq 1$) behave like lid-driven cavities with a large recirculation region along the centerline of the cavity and smaller recirculation regions near the bottom corners [100], as illustrated in Fig. 2.10. For deep cylindrical cavities, the recirculating flow is symmetric with respect to the cavity centerline [101]. This recirculation results in high-pressure regions at the bottom corners aligned with the center streamline and a low-pressure region at the cavity center [101, 102]. Shallower axisymmetric cavities, feature unsteady and asymmetric recirculation patterns [103].

2.3 Measurement & Post–Processing Methodologies

2.3.1 Measurements
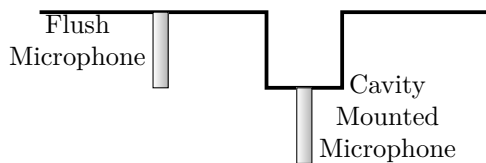
Individual Microphone Placement

Figure 2.11: Illustrated placement of microphones for flush–mounted and cavity–mounted positions.

In this thesis, the transfer function between the flush–mounted microphone and a microphone placed within a cavity is defined as:

$$\Delta L_{p,\text{TBL}} = L_{p,\text{TBL cavity}} - L_{p,\text{TBL flush}} \tag{2.21}$$
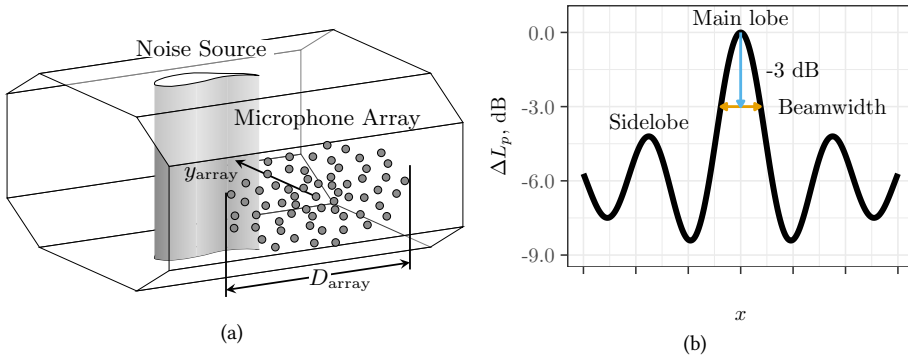
Figure 2.12: a) Illustration of a microphone array, placed on a tunnel wall, with the microphones distributed using the Underbrink distribution. b) Illustrated definitions of beamwidth and sidelobes from a 1D beam pattern.

where $\Delta L_{p,\text{TBL}}$ is the change in measured TBL spectrum, expressed in dB, between the TBL SPL measured at the bottom of the cavity, $L_{p,\text{TBL cavity}}$ and the flush–mounted microphone, $L_{p,\text{TBL flush}}$. Figure 2.11 illustrates the relative placement of these microphones.

Microphone Array Measurements

Acoustic measurements in wind tunnels are often performed with an array of microphones instead of a single microphone. The advantage of microphone arrays is that acoustic imaging, using beamforming, can be performed on the measurement data. When designing a microphone array, the placement and quantity of microphones in the array will affect the beamforming results. The microphone placement refers to both the size of the array as well as the relative placement of the microphones with respect to each other. The diameter of the array determines the minimum distance between which two acoustic sources can be distinguished from one another, which is referred to as the Rayleigh criterion. The Rayleigh criterion [104], is defined in Eq. 2.22:

$$\Theta_{\text{min}} = 1.22 c_0 \frac{y_{\text{array}}}{D_{\text{array}} f} \tag{2.22}$$

where Θ_{min} is the minimum separation distance between two sources for them to be identified as individual sources, y_{array} is the distance from the array to the scan plane, and D_{array} is the diameter of the array. This criterion states that the spatial resolution improves, i.e., Θ_{min} decreases, with increasing frequency and also with increasing array size. The parameters y_{array} and D_{array} are shown in Fig. 2.12a.

The relative placement of the microphones within an array affects the location and strength of side lobes. For example, a beamforming map of a single acoustic source will have a main lobe at the location of the source and several lower amplitude side lobes. This is illustrated in Fig. 2.12b. The difference between the main lobe peak and the highest sidelobe peak is defined as the maximum sidelobe level, MSL, [105]. The beamwidth of the beam pattern within the acoustic image is defined as the width of the main lobe 3 dB beneath the peak. Ideally, the side lobe levels should be as low as possible relative to

the main lobe. This can be achieved by irregularly spacing the microphones to maximize the MSL [105]. However, the distribution of microphones needs to be balanced as placing more microphones near the array center improves the MSL while placing them near the edge decreases the beamwidth [106]. Spiral-shaped arrays are commonly used in practice [105, 107] as the microphone placement is inherently irregular. Specifically, the Underbrink [108] spiral array design is often used, as illustrated in Fig. 2.12a. Another possible microphone distribution is the sunflower arrangement [107], which also ensures irregular spacing of the microphones. The minimum spacing of the microphones also affects the beamforming results. For linear arrays, this spacing must be less than $\lambda/2$, where λ is the wavelength of the frequency of interest, to avoid grating lobes [109]. Regardless of the array configuration type, the placement of the microphones can be further optimized using a genetic algorithm [110] such as Differential Evolution [111] or an extension of the HR CLEAN-SC method [112].
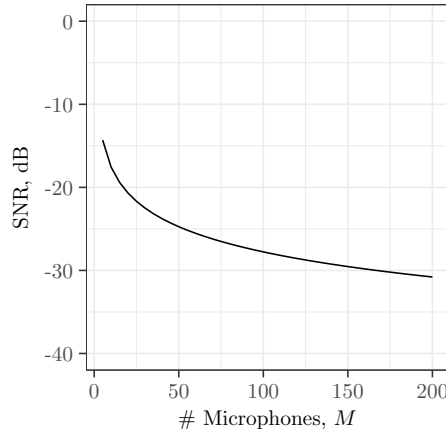

Figure 2.13: Illustrative change in SNR with increasing number of array microphones [56].

The number of microphones used within the array affects the SNR of the acoustic measurements. Since the beamforming algorithm identifies coherent (over the microphones) acoustic sources and the TBL pressure fluctuations are incoherent, thus beamforming intrinsically suppresses the amount of TBL noise [113]. This improves the SNR of acoustic measurements when compared to a single microphone measurement. Increasing the number of microphones further improves the array SNR, specifically for every doubling of the number of microphones, the SNR improves by 3 dB. Sijtsma [56] described a theoretical framework to estimate this improvement in SNR with increasing microphones. Figure 2.13 plots the predicted change in SNR with an increasing number of microphones. In Fig. 2.13, SNR is defined as the minimum L_p of a source below that of $L_{p,\text{TBL}}$, where the L_p is the identifiable source.

Data Acquisition
Both analog condenser and micro−electromechanical systems (MEMS) microphones are used in this work to measure the TBL pressure fluctuations and incident acoustic pressure waves. These measurement data are acquired by connecting the microphone(s) to a data

acquisition system (DAQ), which features an analog–to–digital (A/D) signal converter, an amplifier, and a low–pass filter [114]. The A/D converter used for measurements in this work has 24–bit resolution for obtaining adequate dynamic range for the microphone measurements. The microphone signal is sampled at a minimum of twice the maximum signal frequency of interest. This frequency is referred to as the Nyquist frequency [114]. A low–pass analog filter applied to the signal with the cut–off frequency set at the Nyquist frequency is used to avoid aliasing in the recorded signal.

2.3.2 Data Post–Processing Methodology

Fourier Transform

The Fourier Transform transforms time–varying signals, such as the pressure measured by a microphone, from the time domain to the frequency domain. Equation 2.23 defines the Fourier transform for a continuous signal,

$$X(f) = \int_{-\infty}^{\infty} \tilde{x}(t) e^{-2\pi i f t} \, \mathrm{d}t \tag{2.23}$$

where $\tilde{x}(t)$ is the continuously measured signal in the time domain, f is the frequency, $i = \sqrt{-1}$, and $X(f)$ is the continuous Fourier transformed signal in the frequency domain. However, when measuring the signal, the DAQ samples the signal discretely with a sampling rate f_s. Therefore, the discrete Fourier transform (DFT) is used. The DFT is defined in Eq. 2.24:

$$\hat{X}(f_m) = \Delta t \sum_{n=0}^{N-1} \hat{x}(n) e^{\frac{-2\pi i m n}{N}} \tag{2.24}$$

where $\hat{X}(f_m)$ is the discrete Fourier transformed signal in the frequency domain, $f_m = m\Delta f$, m is the frequency index which ranges from 0 to $N-1$, Δt is the temporal sampling interval, and Δf is the frequency resolution defined as f_s/N. N is the number of discrete samples, n is the sample index, and $\hat{x}(n)$ is the discretely sampled time signal [114]. Typically DFTs are calculated using the Fast Fourier Transform (FFT), which is a computationally efficient implementation of the Discrete Fourier Transform (DFT).

Power Spectral Density

The power spectral density (PSD) describes the power distribution of the measured signal in the frequency domain. The continuous PSD is defined in Eq. 2.25:

$$P_{xx}(f) = \frac{|X(f)|^2}{T} \tag{2.25}$$

where P_{xx} is the PSD and T is the duration of the time sample. In practice, the discrete form is used as defined in Eq. 2.26:

$$P_{xx}(f_m) = \frac{\left|\hat{X}(f_m)\right|^2}{N\Delta t} \tag{2.26}$$

where Δt is the sampling interval and N is the number of samples.
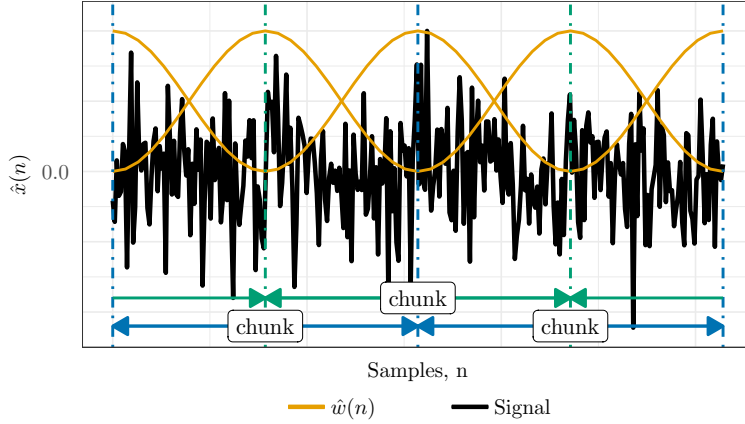
Figure 2.14: Example of Hanning windowing applied to a discrete time varying signal with 50% overlap.

Welch's Method

Welch's method is used to reduce the random noise in the spectrum when calculating the PSD of pressure fluctuations [115]. This method is implemented by dividing a signal, $\hat{x}(n)$, into a number H chunks as shown in Fig. 2.14. These chunks typically overlap each other by 50% to further reduce the random noise in the spectrum. Once the signal is divided into chunks, each chunk is multiplied by a windowing function, $\hat{w}(n)$. Windowing functions are used to reduce the sidelobes, i.e., spectral leakage [114] in the spectrum. Figure 2.14 shows the Hanning windowing function overlaid on top of each chunk. The Hanning window tapers the amplitude chunk so that the sampled data at the beginning and end of each chunk, i.e., $n = 0$ and $n = N_{\text{fft}-1}$ are equal to zero. The DFT for each chunk is then calculated using Eq. 2.27:

$$\hat{X}_h(f_m) = \Delta t \sum_{n=0}^{N_{\text{fft}}-1} \hat{w}(n)\hat{x}_h(n)e^{\frac{-2\pi imn}{N_{\text{fft}}}} \tag{2.27}$$

where $\hat{X}_h(f_m)$ is the DFT of the chunk with index h, N_{fft} is the number of samples in the chunk, $\hat{w}(n)$ is the window function, $\hat{x}_h(n)$ is the discretely sampled signal for chunk h, and n is the sample index within the chunk. The Welch's method is then used to calculate the PSD for each chunk and averages the resulting spectra as described by Eq. 2.28:

$$P_{xx}(f_m) = \frac{S}{N_{\text{fft}}^2 H \Delta f} \sum_{h=1}^{H} \hat{X}_h(f_m)\hat{X}_h^{\star}(f_m) \tag{2.28}$$

where $\hat{X}_h^{\star}(f_m)$ is the conjugate transpose of $\hat{X}_h(f_m)$ and S is the window correction term, which is defined as [114]:

$$S = \frac{N_{\text{fft}}}{\sum_{n=0}^{N_{\text{fft}-1}} \hat{w}^2(n)} \tag{2.29}$$

This term corrects the power levels of the spectra.

The resulting frequency resolution of the spectra calculated using Welch's method, i.e., the ability to resolve the signal at consecutive frequencies, is determined by the inverse of the length of the chunk in seconds. This resolution is calculated as follows: $\Delta f = f_s/N_{\text{fft}}$.

Coherence

Calculating the coherence between two simultaneously measured signals is used to quantify how the two signals are related to one another. The coherence, C_{xy}, ranges between zero and one where $C_{xy} = 1$ means the two signals are perfectly coherent. In the context of measuring the TBL pressure fluctuations, two microphones placed sufficiently far apart, e.g., greater than the TBL coherence length shown in Fig. 2.9, have a coherence approaching zero, while two microphones spaced by the TBL coherence length or less will have a coherence approaching one, depending on the frequency. For acoustic measurements, two microphones measuring the same acoustic wave at different locations will have a coherence near one. Equation 2.30 defines the coherence:

$$C_{xy}(f_m) = \frac{\left|P_{xy}(f_m)\right|^2}{P_{xx}(f_m)P_{yy}(f_m)} \tag{2.30}$$

where P_{xy} is the cross–power spectral density of signals $\hat{x}$ and $\hat{y}$; P_{xx} and P_{yy} are the power spectral densities of signals $\hat{x}$ and $\hat{y}$, which can be calculated with either Eq. 2.26 or Eq. 2.28. The cross–power spectral density is calculated as follows:

$$P_{xy}(f_m) = \frac{\hat{X}^\star(f_m)\hat{Y}(f_m)}{N\Delta t} \tag{2.31}$$

where $\hat{X}(f_m)$ and $\hat{Y}(f_m)$ are the discrete Fourier transform of signals $\hat{x}$ and $\hat{y}$.

Sound Pressure Level

The power spectral density of an acoustic signal is often expressed as the sound pressure level (L_p), which has a decibel (dB) scale. Equation 2.32 defines L_p in terms of dB, where p_{ref} is the reference pressure, 2×10^{-5} Pa.

$$L_p(f_m) = 10\log_{10}\left(\frac{P_{xx}(f_m)\Delta f}{p_{\text{ref}}^2}\right) \tag{2.32}$$

Signal-to-Noise Ratio

The signal–to–noise ratio is the ratio between the signal of interest and the TBL noise. This ratio is defined in Eq. 2.33:

$$\text{SNR} = L_{p,\text{signal}} - L_{p,\text{TBL}} \tag{2.33}$$

where $L_{p,\text{signal}}$ is the sound pressure level of the signal of interest and $L_{p,\text{TBL}}$ is the sound pressure level of the TBL, both at the microphone. Since L_p is expressed in dB, $L_{p,\text{TBL}}$ can be subtracted from $L_{p,\text{signal}}$, which is the equivalent of dividing the power spectral densities of the signal of interest by that of the TBL. This is only possible for spectra with the same Δf.

Acoustic Imaging

Acoustic imaging, using beamforming, is used to identify the location and estimate the L_p of acoustic noise sources. Several beamforming algorithms are used in practice, including but not limited to: conventional beamforming [55], functional beamforming [116], and orthogonal beamforming [117]. This work utilizes conventional beamforming, formally referred to as conventional frequency-domain beamforming (CFDBF).

When performing beamforming, a grid of points is defined where acoustics sources are expected to be present. These points form a plane, referred to as the scan plane, and for wind tunnel testing this plane is centered at the test article, as shown in Fig. 2.15. At each point in the scan plane, the L_p radiated from that point is estimated by correcting the measured pressure signals by shifting the signals to account for the time delay from the scan grid point to the microphone location. When the shifted signals are in phase, the resulting beamforming map shows a higher L_p, which indicates the presence of a potential acoustic source.
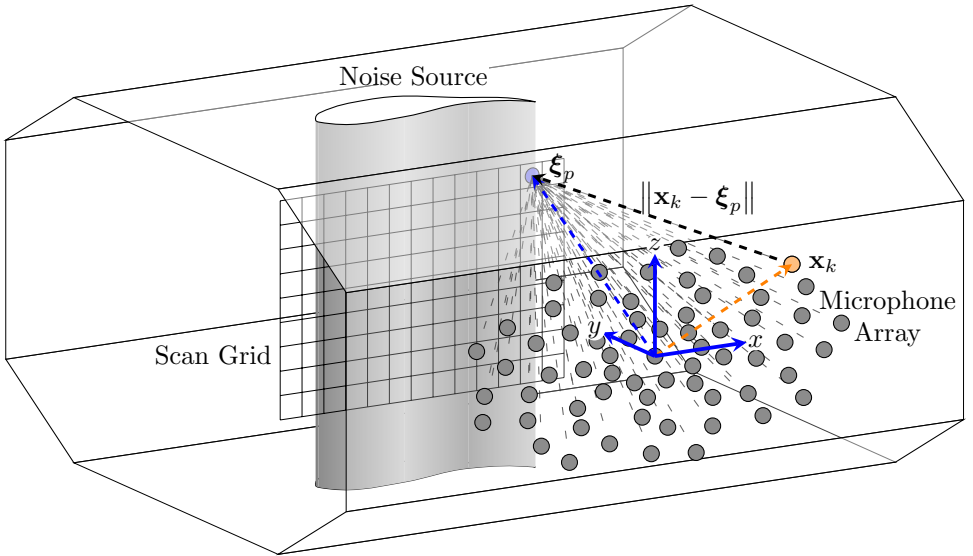

Figure 2.15: Illustration of beamforming using a microphone array to scan a grid of points across an airfoil.

The CFDBF beamforming algorithm is performed as follows: First, the microphone array measurements are expressed as $\hat{\mathbf{x}}(t) \in \mathbb{R}^{K \times 1}$, where $\hat{\mathbf{x}}(t)$ is a vector with components $\hat{x}_k(t)$ signals at time t, where $k = 1, \ldots, K$, and K is the number of microphones. Second, the time signal for each microphone is transformed to the frequency domain using a discrete Fourier transform, which results in $\hat{\mathbf{X}}(f_m)$, as described in the previous section. Third, the cross−spectral matrix (CSM) of these signals is calculated using Eq. 2.34:

$$\mathbf{C}(f_m) = \mathbb{E}\left[\hat{\mathbf{X}}(f_m)\hat{\mathbf{X}}^\star(f_m)\right] \tag{2.34}$$

where $\mathbf{C}(f_m)$ is the CSM at a frequency f_m, $\mathbb{E}$ is the expectation operator, $\hat{\mathbf{X}}(f_m)$ is the vector containing the Fourier coefficients for all K microphones at frequency f_m, and $\hat{\mathbf{X}}^\star(f_m)$

is the conjugate transpose of $\hat{\mathbf{X}}(f_m)$. Finally, the beamforming map is calculated using Eq. 2.35 for all grid points in the scan plane,

$$\mathbf{B}(\boldsymbol{\xi}_p) = \frac{\mathbf{g}^\star \mathbf{C}\mathbf{g}}{\|\mathbf{g}\|^4} \tag{2.35}$$

where $\mathbf{B}(\boldsymbol{\xi}_p)$ is the estimate of the auto-power at the grid point p, $\boldsymbol{\xi}_p$ is the location of the grid point p, and $\mathbf{g}$ is the steering vector to point $\boldsymbol{\xi}_p$, where $\mathbf{g} \in \mathbb{C}^{K \times 1}$. The elements, g_k, of the steering vector, $\mathbf{g}$, are defined in Eq. 2.36:

$$g_k(\boldsymbol{\xi}_p, f_m) = \frac{1}{\|\mathbf{x}_k - \boldsymbol{\xi}_p\|} e^{\frac{-2\pi i f_m \|\mathbf{x}_k - \boldsymbol{\xi}_p\|}{c_0}} \tag{2.36}$$

where $\mathbf{x}_k$ is the vector of the coordinates of the microphone locations, defined as $\mathbf{x}_k \in \mathbb{R}^{K \times 3}$ [117]. The term $\|\mathbf{x}_k - \boldsymbol{\xi}_p\|$ is illustrated in Fig. 2.15.

The beamforming algorithm identifies coherent (over the microphones) acoustic sources and because the TBL pressure fluctuations are incoherent the amount of TBL noise is intrinsically suppressed in the acoustic maps [113]. This improves the SNR of acoustic measurements when compared to a single microphone measurement. As discussed in section 2.3.1, the SNR can be improved by increasing the number of microphones, as illustrated by Fig. 2.13.

Applying beamforming post-processing techniques can further reduce the TBL noise levels, thus increasing the SNR. One such approach is to remove the diagonal of the cross-spectral matrix (CSM). The diagonal of the CSM contains the spectral energy of the incoherent sources. When the diagonal is set to zero, these sources are removed from the acoustic source map. Deconvolution methods such as DAMAS [118] and CLEAN-SC [119] can also further improve the beamforming maps. Another approach is to perform principal component analysis on the CSM to extract the acoustic signal from the TBL noise [120]. This approach allows for the extraction and identification of acoustic signals from measurements with poor SNR.

Wavenumber Analysis
Wavenumber-frequency spectral analysis can be used to identify the wave propagation speed of the pressure fluctuations, which is useful for identifying the acoustic and hydrodynamic components of the spectra [79, 121]. These components are identified by their wavenumbers, The acoustic component, also known as the compressible region, is the region of the wavenumber–frequency spectrum where the wavenumber, k, is between $-f/c_0$ and f/c_0. The hydrodynamic region is comprised of the wavenumbers outside this acoustic region, where the propagation velocity is lower than the sound speed. This region is also known as the incompressible region. In the case of the TBL along a wall, the spectral energy of the TBL pressure fluctuations is concentrated in the wavenumbers near the convective wavenumber, $k_c = f/U_c$.

The wavenumber-frequency spectra is calculated using either a 2D or 3D Fourier transform. The formulation of which is similar to Eq. 2.24, except the Fourier transform is also performed using data sampled in one or two spatial directions. A 2D DFT is used for the

wavenumber transform in one spatial direction and with respect to time, while the 3D DFT is applied to two spatial directions and the time domain. The pressure measurements used for this analysis can be microphones arranged in an array [121] or by sampling a transient CFD simulation [122]. Equation 2.37 describes the 2D DFT [123]:

$$\hat{X}(k_{xl}, f_m) = \Delta t \Delta x \sum_{n_x=0}^{N_x-1} \sum_{n=0}^{N-1} \hat{x}(n_x, n) e^{-2\pi i \left(\frac{n_x l}{N_x} + \frac{nm}{N} \right)} \tag{2.37}$$

where $\hat{X}(k_{xl}, f_m)$ is the wavenumber-frequency DFT. The wavenumber in the x direction is $k_{xl} = l\Delta k_x$, where l is the wavenumber index, Δk_x is the wavenumber spatial resolution, N_x is the number of spatially measured points in the x−direction, and n_x and is the index of the spatial measurements.

The wavenumber spectra can also be calculated using Welch's method. The expression for the DFT with a windowing function applied to the temporal samples is shown in Eq. 2.38:

$$\hat{X}_h(k_{xl}, f_m) = \Delta t \Delta x \sum_{n_x=0}^{N_x-1} \sum_{n=0}^{N_{\text{fft}}-1} \hat{w}(n) \hat{x}_h(n_x, n) e^{-2\pi i \left(\frac{n_x l}{N_x} + \frac{nm}{N_{\text{fft}}} \right)} \tag{2.38}$$

where the DFT in the spatial domain is the same as Eq. 2.37 and the DFT in the time domain being performed for a chunk of samples with a size of N_{fft}.

Equation 2.39 defines the wavenumber power spectral density,

$$\hat{P}_{xx}(k_{xl}, f_m) = \frac{S}{H \Delta f N_{\text{fft}}^2 N_x \Delta x} \sum_{h=1}^{H} \left| \hat{X}_h(k_{xl}, f_m) \right|^2 \tag{2.39}$$

where, S is the correction term for the window, as defined by Eq. 2.29, N_x is the number of spatially sampled points of the sample array in the x−direction, N_{fft} is the number of temporal samples for the window, H is the number of overlapping windowed segments, and $\hat{X}_h$ is the Fourier transform in the frequency and spatial domains, described by Eq. 2.38.

Proper Orthogonal Decomposition

Proper orthogonal decomposition (POD) is used to identify coherent structures in a dataset [124]. POD separates the coherent structures in a dataset, e.g., a pressure field, into a linear combination of orthogonal modes. For example, if a pressure field consists of a linear combination of acoustic duct modes, as discussed in sub−section 2.1.2, decomposing the pressure field with POD will identify these separate modes. The analyzed dataset can be numerical or experimental in origin and consists of data sampled at discrete spatial locations and over time.

The dataset is structured as shown in Eq. 2.40, where $\mathbf{D} \in \mathbb{R}^{N_s \times N}$ is the dataset containing the sampled temporal data at discrete Cartesian locations. N_s is the number of spatial points and N is total number of temporal samples. The spatial data can be either 2D or 3D and the spatial data matrix is flattened into a row vector with index n_s and length N_s. The temporal data are contained in the column vectors.

$$\mathbf{D} = \begin{bmatrix} \hat{x}_1[1] & \dots & \hat{x}_{n_s}[1] & \dots & \hat{x}_{N_s}[1] \\ \vdots & \vdots & \vdots & \vdots & \vdots \\ \hat{x}_1[N] & \dots & \hat{x}_{n_s}[N] & \dots & \hat{x}_{N_s}[N] \end{bmatrix} \tag{2.40}$$

The dataset can be reconstructed summing each mode; the modes are expressed as the inner product of the mode amplitude (σ_r), spatial structure (ϕ_r), and the transpose of the temporal base (ψ_r), where r is the mode number, as shown in Eq. 2.41.

$$\mathbf{D}[n_s, n] = \sum_{r=1}^{\text{rk}(\mathbf{D})} \sigma_r \phi_r[n_s] \psi_r^{\top}[n] \tag{2.41}$$

In this equation, r is the mode number, $\text{rk}(\mathbf{D})$ is the rank of the data matrix, and n is the temporal index [124].

To calculate these vectors, first a singular value decomposition (svd) is performed on the temporal correlation matrix, $\mathbf{K}$ [124, 125]. $\mathbf{K}$ is defined as:

$$\mathbf{K} = \mathbf{D}^{\dagger}\mathbf{D} \tag{2.42}$$

where † is the Hermetian transpose operator, also known as the conjugate transpose. Equation 2.43 shows the application of singular value decomposition to obtain the matrices $\mathbf{\Psi}$ and $\mathbf{\Lambda}$,

$$[\mathbf{\Psi}, \mathbf{\Lambda}] = \text{svd}(\mathbf{K}) \tag{2.43}$$

where $\mathbf{\Psi}$ is the correlation matrix and $\mathbf{\Lambda}$ is the diagonal matrix of the modal energy. The temporal base vectors, $\psi_{\mathbf{r}}$, are the eigenvectors of $\mathbf{\Psi}$.

The amplitudes of each mode, σ_r, are the diagonals of the matrix $\mathbf{\Sigma}$, which is calculated using Eq. 2.44:

$$\mathbf{\Lambda} = \mathbf{\Sigma}\mathbf{\Phi}^{\top}\mathbf{\Phi}\mathbf{\Sigma} = \mathbf{\Sigma}^2 \tag{2.44}$$

where $\mathbf{\Phi}$ is the spatial structure matrix and $\mathbf{\Phi}^{\top}$ is its transpose. Since $\mathbf{\Phi}^{\top}\mathbf{\Phi}$ is equal to the identity matrix $\mathbf{I}$, $\mathbf{\Sigma} = \sqrt{\mathbf{\Lambda}}$. The energy of each mode, σ_r is normalized by $\sqrt{N_s N}$.

The spatial component of the modes, ϕ_r are the column vectors of the matrix $\mathbf{\Phi}$ which is calculated using Eq. 2.45.

$$\mathbf{\Phi} = \mathbf{D}\mathbf{\Psi}\mathbf{\Sigma}^{-1} \tag{2.45}$$

3

Physical Model of the Propagation of TBL Pressure Fluctuations

A physical model is presented that models the propagation of turbulent boundary layer (TBL) pressure fluctuations toward the bottom of a cavity. The pressure field at the top of the cavity is modeled using Corcos' model for the TBL cross–spectra. This pressure field is subsequently decomposed into acoustic circular duct modes. Whether or not these modes propagate into the cavity depends on whether they are cut–on or cut–off as cut–off modes decay exponentially into the cavity. A mode being cut–on or cut–off depends on the cavity aperture size, depth, wall material, as well as frequency. This model predicts that larger diameter cavities attenuate the TBL more than smaller ones, which agrees with experimental data. This increase in attenuation is explained by the modal decomposition of the TBL pressure field, for larger cavities, resulting in a higher proportion of energy being contained in higher–order modes in contrast to smaller cavities where the energy is concentrated in the first planar mode. Since the higher–order modes decay, the larger cavities increase the amount of TBL attenuation. Furthermore, the model confirms that cavities with sound–absorbing walls attenuate the TBL noise more than hard–walled cavities.

3.1 Introduction

Microphone arrays measurements in wind tunnels are used to record acoustic data that can be used to localize and quantify aeroacoustic noise sources through the application of beamforming [127]. These arrays are either installed along the wall of a closed test section wind tunnel or outside the jet of an open–jet wind tunnel. Closed test section wind tunnels are preferable for aerodynamic measurements due to the reduction in jet deflection, blockage, and non-zero circulation effects. However, the acoustic signal is contaminated by the turbulent boundary layer (TBL) surface pressure fluctuations [48], which convect across the microphone array. These undesirable sources of noise subsequently reduce the signal-to-noise ratio (SNR) of the acoustic measurements. One solution to reduce the influence of

This chapter is based upon work originally presented at the 25th AIAA/CEAS Aeroacoustics Conference, Delft The Netherlands 2019 [126].

the TBL is to recess the microphones in a cavity [61]. These cavities are typically covered with a finely woven stainless steel cloth [61] or Kevlar [16] to reduce recirculation within the cavities, a source of hydrodynamic noise. This leaves the pressure perturbations from the TBL above the covering as the primary source of TBL noise. In order to better understand the relationship between the attenuation of the TBL pressure field and the cavity geometry, this chapter introduces a physical acoustic model. This model quantifies the influence of cavity aperture size, depth, and wall material on the boundary layer pressure fluctuations at the bottom of the cavity.

This physical model applies analytical solutions to the wave equation for acoustic waves within a circular duct to model the propagation of pressure fluctuations into a circular cavity. This approach has been used for many applications [66], e.g., to model the propagation of acoustic waves within turbofan engines [128, 129] and also to model the excitation of acoustic modes due to a TBL in rectangular and circular cavities [63]. The model presented in this chapter provides insights into the underlying physics and acoustic propagation mechanisms into a circular cavity. The drawback of this approach is that modeling non-axisymmetric shapes and varying cross–sections is challenging as the boundary conditions for solving the wave equation need to be carefully considered and implemented and analytical solutions may not exist [69].

This chapter evaluates three cavity aperture radii (0.005–0.0225 m), three depths (0.01–0.05 m), and whether the cavity wall is hard or made of sound–absorbing melamine foam. Only cylindrical cavities are considered, i.e., with a constant cross–sectional area. The model trends agree with the trends seen in experimental measurements, presented in this chapter.

3.2 The Acoustic Model

The propagation of acoustic waves into a circular duct can be solved using the wave equation [130] and applying the relevant boundary conditions. The same approach is used to model the propagation of pressure fluctuations from the TBL into a cavity. The cavity is modeled with an acoustically transparent covering, e.g., Kevlar or a fine stainless steel cloth, which are used in practice to improve the TBL attenuation by reducing recirculation within the cavities. Covering the cavity is necessary to enable the assumption that the TBL pressure fluctuations propagate as acoustic waves within the cavity. This model considers three-dimensional acoustic wave propagation within a cylindrical cavity and neglects thermoviscous losses.

Figure 3.1 illustrates the geometric parameters. In this figure, the cavity depth is D, and the radius is defined as a. The shaded region in the diagram represents the location of the covering. The side and bottom walls are modeled as either 100% reflective hard walls or soft walls with a frequency-dependent impedance. The pressure field from the TBL at the top of the cavity is modeled using Corcos' model [80] for turbulent boundary layer wall pressure cross-spectra.

Corcos' cross-spectral model [131] was used to model the streamwise and spanwise variation in the TBL pressure field at different frequencies. The spectrum of this field was modeled using the Goody model [72]. Note that the model presented in this chapter assumes that only acoustic waves are propagating within the cavity and not the hydrodynamic component of the boundary layer.

3.2.1 Cavity Boundary Conditions

The boundary conditions define the acoustic pressure and velocity at the cavity boundaries [132]. Figure 3.1 illustrates these boundary conditions for an axisymmetric cavity. The cavity is defined using cylindrical coordinates, r, θ, and z. In order to simplify calculations, the fluid properties and geometric variables are normalized so that $\tilde{p} = p/\rho_0 c_0^2$, $\tilde{\rho} = \rho/\rho_0$, $\tilde{v} = v/c_0$, $\tilde{\omega} = \omega a/c_0$, $\tilde{r} = r/a$, $\tilde{t} = tc_0/a$, and $\tilde{z} = z/a$ represents the normalized values for pressure, density, acoustic particle velocity, angular frequency, radius, time, and propagation distance.
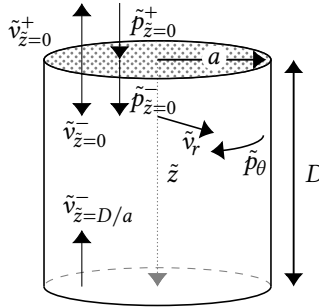

Figure 3.1: Model geometry and boundary conditions, the shaded area represents the acoustically transparent covering.

The first boundary condition considered is that for the acoustic particle velocity in the radial direction. The radial acoustic particle velocity boundary condition at the cavity center line, $\tilde{r} = 0$, must have a finite value [63]. This boundary condition is expressed by Eq. 3.1, where $\tilde{v}_{\tilde{r}}$ is the radial acoustic particle velocity.

$$\tilde{v}_r|_{\tilde{r}=0} = \text{finite} \tag{3.1}$$

The velocity boundary condition at the wall, $\tilde{r} = 1$, depends on whether the cavity has hard or soft walls. For hard walls, Eq. 3.2 states that the radial velocity must be equal to zero at the wall in the wall–normal direction.

$$\tilde{v}_r|_{\tilde{r}=1} = 0 \tag{3.2}$$

The relationship between the acoustic pressure and acoustic particle velocity is shown in Eq. 3.3 [69].

$$\tilde{v}_{\tilde{r}} = -\frac{1}{\tilde{\rho}} \int \frac{\partial \tilde{p}}{\partial \tilde{r}} dt \tag{3.3}$$

For soft walls, e.g., walls made of melamine foam, the partial derivative of pressure with respect to the radial direction is inversely proportional to the impedance of the wall material, as shown in Eq. 3.4.

$$\left. \frac{\partial \tilde{p}}{\partial \tilde{r}} \right|_{\tilde{r}=1} = -\frac{i\tilde{\omega}\tilde{p}}{Z} \tag{3.4}$$

In this equation, Z is the dimensionless wall acoustic impedance, $\tilde{p}$ is the normalized pressure, and $\tilde{\omega}$ is the normalized angular frequency. Acoustic impedance is defined as

the acoustic pressure divided by its acoustic velocity [69]. For the case of hard walls, $Z = \infty$, which results in the right hand side in Eq. 3.4 being equal to zero. For soft walls, this expression states that the acoustic velocity at the wall is inversely proportional to the impedance of the wall [133].

In the z direction, the boundary conditions are defined at the bottom of the cavity and the top. Equation 3.5 states that the velocity, $\tilde{v}_{\tilde{z}}$, is zero at the bottom of the cavity for the case of a hard wall.

$$\tilde{v}_z|_{\tilde{z}=\tilde{L}} = 0 \tag{3.5}$$

For the soft wall case, a reflection coefficient, R_{refl} for the ratio between the incident and reflected pressure waves at $\tilde{z} = \tilde{D}$ must be defined [69]. This expression is given in Eq. 3.6,

$$R_{\text{refl}} = \frac{Z-1}{Z+1} \tag{3.6}$$

where Z is the normalized acoustic impedance, the impedance of the material for a 90° angle of incidence, at the bottom of the cavity.

The cavity cover is modeled by imposing boundary conditions for the acoustic velocity through the cover and the pressure jump across it. The acoustic velocity in the z-direction is assumed to be equal on either side of the material, as represented by Eq. 3.7:

$$\tilde{v}_z^+|_{\tilde{z}=0} = \tilde{v}_z^-|_{\tilde{z}=0} \tag{3.7}$$

where $\tilde{v}_z$ is the normalized acoustic velocity in the vertical direction. The change in pressure across the mesh is derived from the impedance across the covering material. For this model, the impedance is assumed to be equal to the characteristic specific acoustic impedance ($\rho_0 c_0$) multiplied by a dimensionless acoustic resistance term, R, as shown in Eq. 3.8.

$$\frac{\tilde{p}^-|_{\tilde{z}=0} - \tilde{p}^+|_{\tilde{z}=0}}{\tilde{v}_z|_{\tilde{z}=0}} = R \tag{3.8}$$

The final boundary condition considers the pressure in the azimuthal direction [69]. Equation 3.9 shows that the pressure at $\theta = 0$ must not have a discontinuity at $\theta = 2\pi$.

$$\tilde{p}(\tilde{r}, \theta, \tilde{z}) = \tilde{p}(\tilde{r}, \theta + 2\pi, \tilde{z}) \tag{3.9}$$

3.2.2 Solving the Wave Equation
The wave equation is defined as follows,

$$\frac{\partial^2 p}{\partial^2 t} - c_0^2 \nabla^2 p = 0 \tag{3.10}$$

where p is the pressure, t is time, and c_0 is the speed of sound in air. Solving this partial differential equation for a cavity requires the imposition of boundary conditions, which define the constraints on the acoustic velocity and pressure due to the cavity walls, covering, and cross-sectional shape. With the previously defined boundary conditions, the wave equation, Eq. 3.10, can be solved by using the separation of variables method [69, 132]. The pressure field solutions will be in the form of the generic equation, Eq. 3.11, where

$F_{\text{sol}}(\tilde{r})$, $G_{\text{sol}}(\theta)$, and $H_{\text{sol}}(\tilde{z})$ are solutions to the radial, azimuthal, and axial ordinary differential equations.

$$\tilde{p}(\tilde{r}, \theta, \tilde{z}, \tilde{t}) = e^{i\tilde{\omega}\tilde{t}} F_{\text{sol}}(\tilde{r}) G_{\text{sol}}(\theta) H_{\text{sol}}(\tilde{z}) \tag{3.11}$$

Equation 3.11 is substituted into the wave equation resulting in the three dimensional partial differential equation, shown in Eq. 3.12.

$$-k^2 - \frac{G_{\text{sol}}^{''}(\theta)}{\tilde{r}^2 G_{\text{sol}}(\theta)} - \frac{H_{\text{sol}}^{''}(\tilde{z})}{H_{\text{sol}}(\tilde{z})} - \frac{F_{\text{sol}}^{''}(\tilde{r})}{F_{\text{sol}}(\tilde{r})} - \frac{F_{\text{sol}}^{'}(\tilde{r})}{\tilde{r} F_{\text{sol}}(\tilde{r})} = 0 \tag{3.12}$$

This substitution results in three independent ordinary differential equations that are each equal to a constant [132]. This substitution is shown in Eqs. 3.13, 3.14, and 3.15,

$$\frac{F_{\text{sol}}^{''}(\tilde{r})}{F_{\text{sol}}(\tilde{r})} + \frac{F_{\text{sol}}^{'}(\tilde{r})}{\tilde{r} F_{\text{sol}}(\tilde{r})} = \frac{m^2}{\tilde{r}^2} - \alpha^2 \tag{3.13}$$

$$\frac{G_{\text{sol}}^{''}(\theta)}{G_{\text{sol}}(\theta)} = m^2 \tag{3.14}$$

$$\frac{H_{\text{sol}}^{''}(\tilde{z})}{H_{\text{sol}}(\tilde{z})} = \alpha^2 - k^2 \tag{3.15}$$

where the constants are defined as follows: α is the radial wave number, m is the azimuthal mode number, and k is the axial wavenumber [69].

The solution to Eq. 3.13 has the form of a generic Bessel function, seen in Eq. 3.16,

$$F_{\text{sol}}(\tilde{r}) = A J_m(\xi\tilde{r}) + C Y_m(\xi\tilde{r}) \tag{3.16}$$

where $J_m(\xi\tilde{r})$ is a Bessel function of order m of the first kind with amplitude A, $Y_m(\xi\tilde{r})$ is a Bessel function of order m of the second kind with amplitude C. When the radial boundary conditions, Eqs. 3.1 and 3.2 are applied to Eq. 3.16, C is set equal to zero. This is because the solution of Eq. 3.16 must exist and $Y_m(\xi\tilde{r})$ is infinite at $\tilde{r} = 0$, therefore C must equal zero to satisfy Eq. 3.1. For the hard wall case, velocity is zero at the wall, $\tilde{v}_r|_{\tilde{r}=1} = 0$, thus $J_m^{'}(\xi\tilde{r}) = 0$. The eigenvalue of this equation is the radial wavenumber, $\alpha_{m\mu}$, which is equal to $\xi\tilde{r}$. Each eigenvalue of $J_m^{'}(\alpha_{m\mu}) = 0$ is indexed by the radial mode number μ and azimuthal mode number, m.

For the soft wall case, the boundary condition Eq. 3.4 is applied, which results in Eq. 3.17.

$$\frac{J_m(\alpha_{m\mu})}{\alpha_{m\mu} J_m^{'}(\alpha_{m\mu})} = \frac{iZ}{\omega} \tag{3.17}$$

For soft wall cavities, the eigenvalue $\alpha_{m\mu}$ is complex valued.

The solution for F_{sol} is normalized by $N_{m\mu}$, which is defined in Eq. 3.18,

$$N_{m\mu} = \begin{cases} \sqrt{2}, & \text{for } m = 0 \ \& \ \mu = 1 \\[2mm] \dfrac{\sqrt{2}}{J_m(\alpha_{m\mu}) \sqrt{\left(1 - \dfrac{m^2}{\alpha_{m\mu}^2}\right)}}, & \text{all other values} \end{cases} \tag{3.18}$$

where $N_{m\mu}$ is the scaling factor, which scales with the energy content of the corresponding mode [69]. The final form of the solution to F_{sol} is defined in Eq. 3.19.

$$F_{\text{sol}} = F_{m\mu}(\tilde{r}) = N_{m\mu}J_m(\alpha_{m\mu}\tilde{r}) \tag{3.19}$$

The solution for the azimuthal equation, $G_{\text{sol}}(\theta)$, is shown in Eq. 3.14. This equation is periodic per the boundary condition shown in Eq. 3.9. This boundary condition requires the solutions at $\theta = 0$ and $\theta = 2\pi$ to be equal. Equation 3.20 is the resulting solution, where $m = 0, \pm 1, \pm 2, \dots, \infty$.

$$G_{\text{sol}} = G_m(\theta) = e^{-im\theta} \tag{3.20}$$

Equations 3.19 and 3.20 define the shape of the mode in the radial and azimuthal directions. The acoustic mode shapes for circular apertures are thus defined in Eq. 3.21.

$$\phi_{m\mu}(\tilde{r}, \theta) = F_{m\mu}(\tilde{r})G_m(\theta) = N_{m\mu}J_m(\alpha_{m\mu}\tilde{r})e^{-im\theta} \tag{3.21}$$

Figure 3.2 shows the mode shapes for the first three azimuthal mode numbers and the first two radial mode numbers.
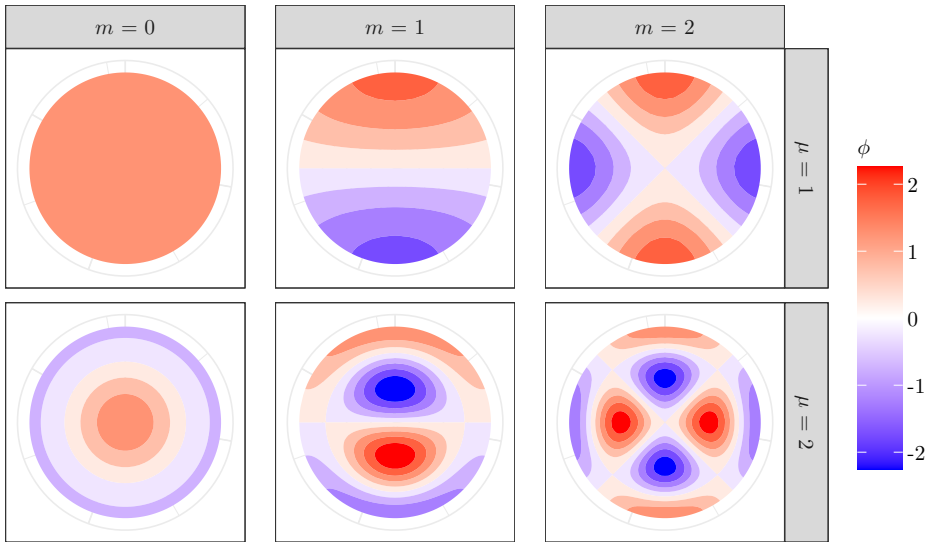

Figure 3.2: Mode shapes, $\phi_{m\mu}$, for a circular duct with hard walls. Calculated using Eq. 3.21. The planar mode has the following azimuthal and radial mode numbers $m = 0$ and $\mu = 1$.

The solution to the differential equation in the axial direction, $H_{\text{sol}}(\tilde{z})$, Eq. 3.15, for the wave propagation in the axial direction is shown in Eq. 3.22. $A_{m\mu}$ and $B_{m\mu}$ are the modal amplitudes, where $k_{m\mu}$ is the axial wavenumber. $A_{m\mu}$ is the amplitude of the inward propagating mode and $B_{m\mu}$ is the amplitude of the outward propagating mode.

$$\begin{cases} H_{m\mu}(\tilde{z}) = A_{m\mu}^+ e^{ik_{m\mu}\tilde{z}} + B_{m\mu}^+ e^{-ik_{m\mu}\tilde{z}}, & \tilde{z} < 0 \\ H_{m\mu}(\tilde{z}) = A_{m\mu}^- e^{ik_{m\mu}\tilde{z}} + B_{m\mu}^- e^{-ik_{m\mu}\left(\tilde{z}-\frac{D}{a}\right)}, & \tilde{z} > 0 \end{cases} \tag{3.22}$$

The amplitudes of the modes on either side of the cavity cover are not equal. This discontinuity requires the solution to be split into a solution above the cavity and below. The amplitudes of the modes above the cover are denoted by the $+$ superscript and the ones below are denoted by the $-$ superscript. Figure 3.3 illustrates the location and direction of the propagation of these modes.
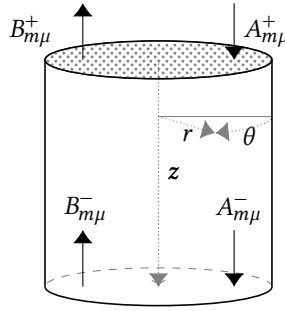

Figure 3.3: Definition of modal amplitude coefficients.

The amount of energy that propagates into the cavity is determined by the axial wavenumber of each mode. The axial wavenumber, $k_{m\mu}$, is defined in Eq. 3.23 [69].

$$k_{m\mu} = -\text{sgn}\left(\mathfrak{I}\left(\sqrt{\tilde{\omega}^2 - \alpha_{m\mu}^2}\right)\right)\sqrt{\tilde{\omega}^2 - \alpha_{m\mu}^2} \tag{3.23}$$

where sgn is the sign function with extracts the sign of a real number and $\mathfrak{Im}$ is the imaginary component. The axial wavenumber, at a given angular frequency, determines whether a mode is cut-on or cut-off. A mode is cut$-$on if $k_{m\mu}$ is real. The acoustic energy of a cut$-$on mode propagates toward the bottom of the cavity [130]. Cut-off modes have imaginary axial wavenumbers, which results in the energy decaying exponentially, per Eq. 3.22.

Using the previous expressions for the boundary conditions and the solutions to the ordinary differential equations, a system of equations for three of the four modal amplitude coefficients can be defined. This system of equations is calculated by applying the boundary conditions, Eqs. 3.5, 3.7, and 3.8 to the expressions for the pressure, Eq. 3.11, and velocity, Eq. 3.24. The latter is calculated using Eq. 3.24.

$$\tilde{v}_z\left(\tilde{r}, \theta, \tilde{z}, \tilde{t}\right) = -\int \frac{\partial \tilde{p}}{\partial \tilde{z}} \partial \tilde{t} = -\frac{k_{m\mu}}{i\tilde{\omega}} e^{i\tilde{\omega}t} F_{\text{sol}}(\tilde{r}) G_{\text{sol}}(\theta) H'_{\text{sol}}(\tilde{z}) \tag{3.24}$$

The solutions for the pressure and velocity are determined by substituting the solutions to the differential equations, Eqs. 3.19 - 3.22 into the general equations for pressure and velocity. Equation 3.25 is the result of applying the boundary conditions, Eqs. 3.2, 3.4, 3.5, 3.7, and 3.8 to the previously described expressions.

$$R_{\text{refl}} A_{m\mu}^- e^{-ik_{m\mu}\tilde{D}} - B_{m\mu}^- = 0$$
$$A_{m\mu}^+ - B_{m\mu}^+ = A_{m\mu}^- - B_{m\mu}^- e^{-ik_{m\mu}\tilde{D}} \tag{3.25}$$
$$A_{m\mu}^- + B_{m\mu}^- e^{-ik_{m\mu}\tilde{D}} - A_{m\mu}^+ - B_{m\mu}^+ = -R\frac{k_{m\mu}}{\tilde{\omega}}\left[A_{m\mu}^+ - B_{m\mu}^+\right]$$

The coefficients $A_{m\mu}^+$, $A_{m\mu}^-$, $B_{m\mu}^+$, and $B_{m\mu}^-$ vary with frequency, $\tilde{\omega}$, because of the frequency dependence of $k_{m\mu}$ and the variation of TBL pressure at the top of the cavity with frequency.

The coefficient, $A_{m\mu}^+$, is calculated by decomposing the pressure field above the cavity into circular duct modes using Eq. 3.26 [69].

$$A_{m\mu}^+ = \frac{1}{2\pi} \int_0^{2\pi} \int_0^1 \tilde{p}(\tilde{r},\theta,\omega)\phi_{m\mu}(\tilde{r},\theta)\tilde{r}d\tilde{r}d\theta \tag{3.26}$$

Where $\tilde{p}(\tilde{r},\theta,\omega)$ is the normalized pressure due to the TBL. The modal amplitude, $A_{m\mu}^+$, is the energy for each mode shapes $\phi_{m\mu}$, which represents a portion of the total energy in the pressure field at the top of the cavity. The original pressure field can be reconstructed by the summation of the $A_{m\mu}^+\phi_{m\mu}$ for all mode numbers.

The spectral energy at the top and bottom of the cavities is calculated through the summation of the modal amplitudes, $A_{m\mu}^+$ and $B_{m\mu}^-$. The calculation of the spectral energy at the top, at a given frequency, is shown in Eq. 3.27.

$$P_{\text{top}} = \left|A_{01}^+\right|^2 + \frac{1}{2} \sum_{m=-\infty}^{\infty} \sum_{\mu=1}^{\infty} \left|A_{m\mu}^+\right|^2 \tag{3.27}$$

At the bottom of the cavity for $\tilde{z} = D/a$, $H_{m\mu}(D) = 2B_{m\mu}^-$. The spectrum at the bottom of the cavity is calculated using Eq. 3.28.

$$P_{\text{bot}} = 4\left|B_{01}^-\right|^2 + 2 \sum_{m=-\infty}^{\infty} \sum_{\mu=1}^{\infty} \left|B_{m\mu}^-\right|^2 \tag{3.28}$$

3.2.3 Modeling the TBL Pressure Spectral Energy

The pressure field at the top of the cavity ($\tilde{z} = 0$) is modeled using Corcos' semi–empirical model with Efimtsov's modification [80, 81]. Corcos' model describes how the TBL wall pressure cross–spectra vary with increasing distance in the streamwise and spanwise directions from a given point. Equation 3.29 describes this model.

$$\Phi_p\left(r_x,r_y,\omega\right) = \Phi_{xx}(\omega)e^{\frac{-\alpha_y|\omega r_y|}{U_c}} e^{\frac{-\alpha_x|\omega r_x|}{U_c}} e^{\frac{i\omega r_x}{U_c}} \tag{3.29}$$

In this model, $\Phi_{xx}(\omega)$ is the spectral energy at a given angular frequency (ω) at the wall. $\Phi_{xx}(\omega)$ can be calculated from an experimental or simulated dataset. It can also be estimated using a TBL wall pressure spectra model. The distance from a given point is defined by r_x in the streamwise direction and r_y in the spanwise direction. The constants, α_y and α_x are calculated using Efimtsov's model and define the TBL pressure coherence length in the streamwise and spanwise directions. These constants are calculated using Efimtsov's definition for coherence lengths, Λ_x and Λ_z, which are shown in Eqs. 3.30 and 3.31,

$$\frac{\Lambda_x}{\delta_{99}} = \left[\left(\frac{a_1\omega\delta_{99}/u^\star}{U_c/u^\star}\right)^2 + \frac{a_2^2}{(\omega\delta_{99}/u^\star)^2 + (a_2/a_3)^2}\right]^{-1/2} \tag{3.30}$$

$$\frac{\Lambda_z}{\delta_{99}} = \left[\left(\frac{a_4 \omega \delta_{99}/u^\star}{U_c/u^\star}\right)^2 + \frac{a_5^2}{(\omega \delta_{99}/u^\star)^2 + (a_5/a_6)^2}\right]^{-1/2} \tag{3.31}$$

where U_c is the TBL convection velocity, δ_{99} is the boundary layer thickness, $u^\star$ is the TBL friction velocity and the empirical constants are as follows: $a_1 = 0.1$, $a_2 = 72.8$, $a_3 = 1.54$, $a_4 = 0.77$, $a_5 = 548$, $a_6 = 13.5$. The Efimtsov modification was used because the resulting cross–spectra agree better with experimental data for flows with $M < 0.75$, where M is the Mach number [81]. The resulting modeled cross–spectra using Eq. 3.29 is the pressure at $\tilde{z} = 0$, the interface of the cavity with the boundary layer.

The Goody model for TBL wall pressure spectra was used as input to Eq. 3.29. The characteristics of this model are discussed in detail in Chapter 2. This boundary layer wall pressure model assumes that the pressure fluctuations are a result of the TBL present on a hard wall [49]. However, this model features a permeable covering above the cavity. Therefore, the physical model assumes that the cover does not affect the TBL wall spectra.

The pressure field used for the modal decomposition in Eq. 3.26 is defined as follows in Eq. 3.32,

$$\tilde{p}(\tilde{r}, \theta, \omega) = \frac{\sqrt{\Phi_p(\tilde{r}, \theta, \omega)\Delta\omega}}{\rho_0 c_0^2} \tag{3.32}$$

where $\Phi_p(\tilde{r}, \theta, \omega)$ is determined using the polar transform of the Corcos model in Eq. 3.29.

3.2.4 Model Implementation

The system of equations listed in Eq. 3.25 is solved using an iterative approach until the solution converges. The first step calculates $A_{m\mu}^+$ using the modal decomposition in Eq. 3.26. As part of this step, $B_{m\mu}^-$ is assumed to be equal to zero in order to solve Eq. 3.25. Thus, the second equation is rearranged in terms of $A_{m\mu}^-$ and substituted into the third, in order to solve for $B_{m\mu}^+$. This gives the initial guess for the amplitudes of the modes. For the subsequent iterations, the value of equation $A_{m\mu}^-$ used in Eq. 3.25 is reused from the previous step. The remaining coefficients are then calculated. The solver iterates until the error term is less than 1×10^{-16}. Error is defined as follows: $\left|\sum |B_{m\mu}^{(n)-}| - \sum |B_{m\mu}^{(n-1)-}|\right|$, which is the difference between the absolute value of the sum of all values of $B_{m\mu}$ at the current iterative step and the previous one. This process is repeated at each frequency of interest.

Figure 3.4 illustrates the model steps as implemented. The model inputs are the TBL parameters used for the Corcos and Goody models, the frequency of interest, and the cavity geometry. Additional model parameters include the error term at which to stop iterating and the number of modes to include in the solution.

3.2.5 Modeled Cavity Geometries

The modeled cavity geometries are listed in Table 3.1. The TBL parameters used for the Corcos and Goody models are: $U_\infty = 32\,\mathrm{m\,s^{-1}}$, $U_c = 0.66 U_\infty$, $u^\star = 1.13\,\mathrm{m\,s^{-1}}$, $\tau_w = 1.52\,\mathrm{Pa}$, and $\delta_{99} = 0.0365\,\mathrm{m}$. The TBL pressure field was decomposed into 36 modes using Eq. 3.26. These modes have the following azimuthal and radial mode numbers: $m = 0$ to 5 and $\mu = 1$ to 6. Increasing the number of modes, increases accuracy at the expense of computational
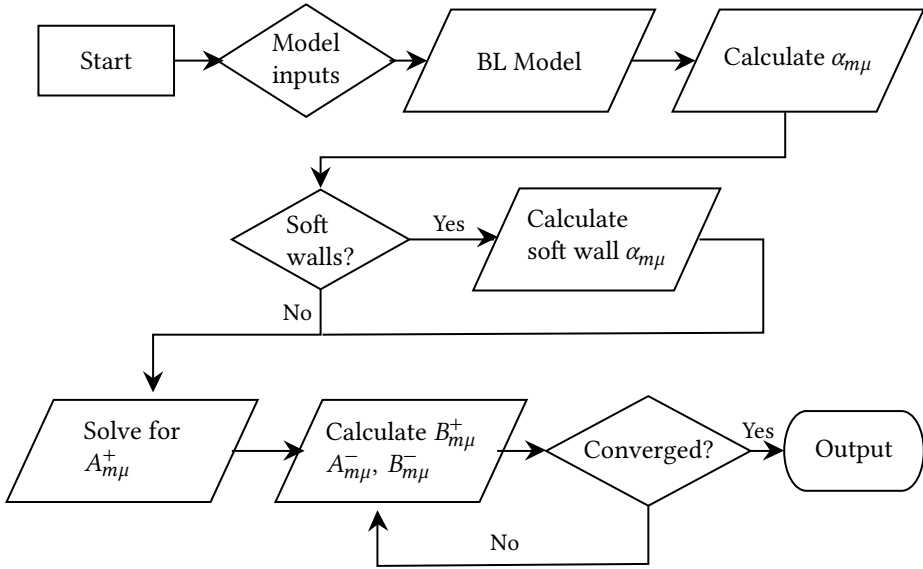
Figure 3.4: Model implementation flow diagram

time. Thirty–six modes was found to be sufficient to model the propagation of the TBL pressure fluctuations into the cavity. Finally, the spectra were modeled for frequencies between 0.2 kHz and 10 kHz.

Table 3.1: Modeled cavity geometric parameters.

Radius (a), m	Depth (D), m	Wall Boundary Condition
0.005, 0.008, 0.0225	0.01, 0.03, 0.05	Hard, Soft

3.3 Experimental Details

The model predictions were compared against experimentally measured data, which were also used for the analysis in Chapter 7. These data were measured in the TU Delft A–Tunnel, which is a vertical open jet wind tunnel located within an anechoic chamber. The pressure fluctuations at the bottom of three covered cavities were measured and the corresponding spectra were calculated using Welch's method, which is described in Chapter 2. These three cavities include a cylinder with a radius, a, of 0.005 m and a depth, D, of 0.01 m, a cylindrical cavity with a countersink with a radius of 0.008 m (1.6a) and a depth of 0.01 m, and a conical cavity with a radius of 0.0225 m (4.5a) and a depth of 0.012 m. The cavities were mounted on a plate flush with the tunnel exit nozzle. The poly-carbonate plate with dimensions of 1.1 m × 0.4 m was covered with a 200 threads per cm^2 (#500) stainless steel mesh cloth. A flush-mounted microphone was placed in the center of the

array to measure the TBL pressure fluctuations for the case without a cavity. This base-line measurement was used to quantify the amount of attenuation of the TBL spectra for each cavity. The cavities were placed 0.76 m downstream of the tunnel nozzle exit and the tunnel flow speed was 32 m s^{-1} at the cavity's location.

Sonion 8010T omnidirectional MEMS microphones were used for these measurements. Each microphone has an outer diameter of 2.5 mm and a transducer diameter of 0.05 mm. The microphones were center–mounted on a 7 mm diameter holder to fit securely within the cavities. All the microphones were calibrated individually using a *G.R.A.S. 42AG* pis-tonphone following the guidelines of Mueller [35]. The transducers have a flat frequency response within ±1 dB from 100 Hz to 10 kHz. The data acquisition system consists of a *National Instruments* (NI) *NI9215* analog input module mounted in the NI *cDAQ-9178 Com-pactDAQ* with 16–bit resolution. The sampling frequency of the recordings was 51.2 kHz and the signal was recorded for a duration of 45 s. The spectra are calculated using the Welch's method with 1024 samples with a 50% overlap using Hanning windowing for a frequency resolution of 50 Hz.
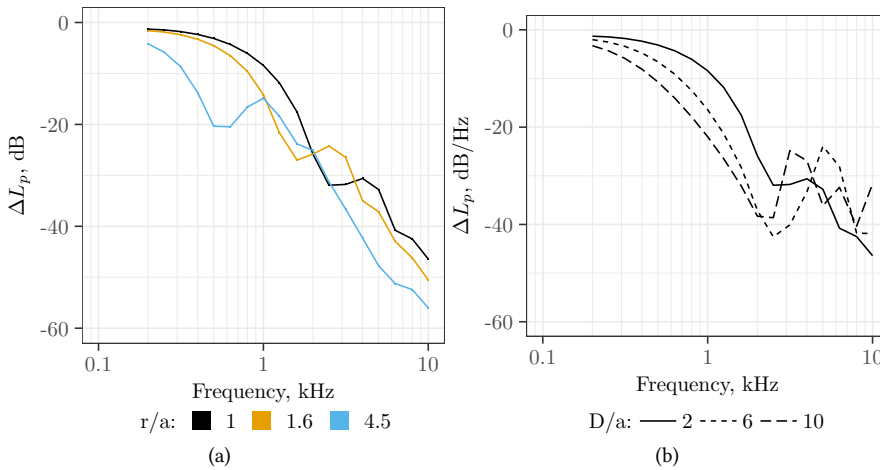
3.4 Model Results

3.4.1 Hard Wall Results

Figure 3.5: Change in the TBL pressure spectra (ΔL_p) between the top and bottom of the cavity. a) Increasing TBL spectra attenuation with increasing cavity aperture radius. b) Increasing TBL spectra attenuation with increasing cavity depth for the *a* = 0.005 m cavity.

Figure 3.5 compares cavities with different aperture radii and depths. This figure shows the amount of attenuation, ΔL_p for the modeled spectra at the bottom of the cavities with respect to the flush spectra. The flush spectrum was modeled using the Goody model as discussed previously. The change in spectrum levels, ΔL_p is defined in Eq. 3.33,

$$\Delta L_p = L_{p,\text{bottom}} - L_{p,\text{Goody}} \tag{3.33}$$

where L_p is the sound power level, $L_{p,\text{bottom}} = 10\log_{10}(P_{\text{bot}})$, and $L_{p,\text{Goody}} = 10\log_{10}(\Phi_{xx})$. The hard–walled cavity results, presented in Fig. 3.5a, show that increasing the cavity aperture increases the amount of TBL attenuation, especially at lower frequencies. This trend is explained by comparing the size of the cavity diameter to the modeled TBL pressure field, which can be seen in Fig. 3.6. In this figure the TBL pressure field is plotted at two frequencies (300 Hz and 5000 Hz) using Eq. 3.29 with two cavity sizes, $r = a$ and $r = 4.5a$ plotted for reference with respect to the pressure field. The smaller cavity, $r = a$, for the 300 Hz case, has a diameter close to the coherence length in the streamwise and spanwise directions. Therefore, it encompasses an almost uniform pressure field. In contrast, the larger cavity, $r = 4.5a$ is larger than the modeled coherence length and thus the pressure field is not uniform. For the higher frequency case, $f = 5000$ Hz both cavities are larger than the modeled coherence length.
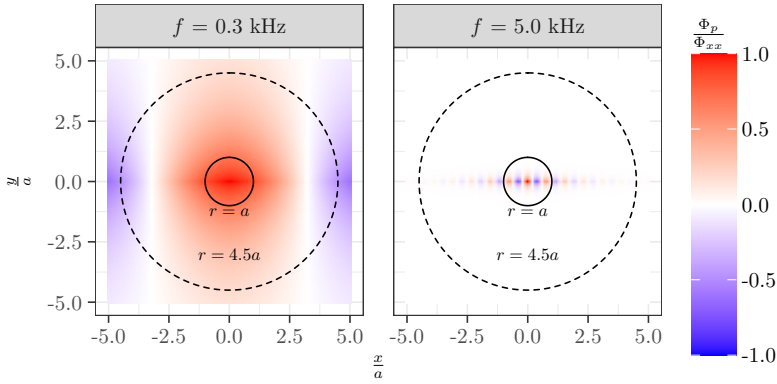

Figure 3.6: Plot of pressure spectra at two frequencies using the Corcos model, Eq. 3.29, with the pressure field, Φ_p normalized by Φ_{xx}. Two cavity aperture sizes are plotted for reference. The nominal radius is defined as $a = 0.005$ m.

The effect of the cavity size on the modal decomposition of the pressure field and distribution of the TBL energy across these modes is shown in Fig. 3.7. This figure shows the resulting normalized coefficients $A_{m\mu}^+$ for the modeled modes. For the smallest cavity at $f = 300$ Hz, the majority of energy is located in the planar mode, $m = 0$, $\mu = 1$. This result is expected because the smaller cavity in Fig 3.6 encompasses a pressure field that varies less than the pressure field covered by the larger cavity, $r = 4.5a$. The energy in the modes for the larger cavity is more spread out across higher-order modes, as shown in Fig. 3.7. More energy is contained in the first azimuthal mode ($m = 1$, $\mu = 1$) than the planar mode. This result occurs because the mode shape for the first azimuthal mode, seen in Fig. 3.2, is more representative of the pressure field across the top of the cavity. Therefore, the modal decomposition results in this mode containing more energy. For the $f = 5000$ Hz case, the TBL energy in the higher–order modes is greater than for the $f = 300$ Hz case to match the imposed pressure field. For this case, the smaller cavity's planar mode has more energy than that of the larger cavity. Given that only this mode is cut–on, as indicated by the blue outline in Fig. 3.7, the smaller cavity has more energy at the bottom of the cavity than the larger one.

Figure 3.8 shows the combined effect of cavity aperture size and frequency on whether the axial wavenumbers are cut–on or cut–off. This is shown for two cases, a cavity with $a = 0.005$ m at a frequency of 300 Hz, and a cavity with a larger radius, $a = 0.0225$ m and at a higher frequency, $f = 10.0$ kHz. Cut-off modes have an imaginary axial wavenumber, $k_{m\mu}$. For the first case, all modes but the plane wave mode ($m = 0$, $\mu = 1$) are cut-off which means that the acoustic energy decays exponentially with distance, per Eq. 3.22. This figure shows that for a larger cavity, more modes at higher frequencies are cut-on, which means less attenuation. This explains why Fig. 3.5a shows less reduction in acoustic energy at higher frequencies for increasing cavity radii.
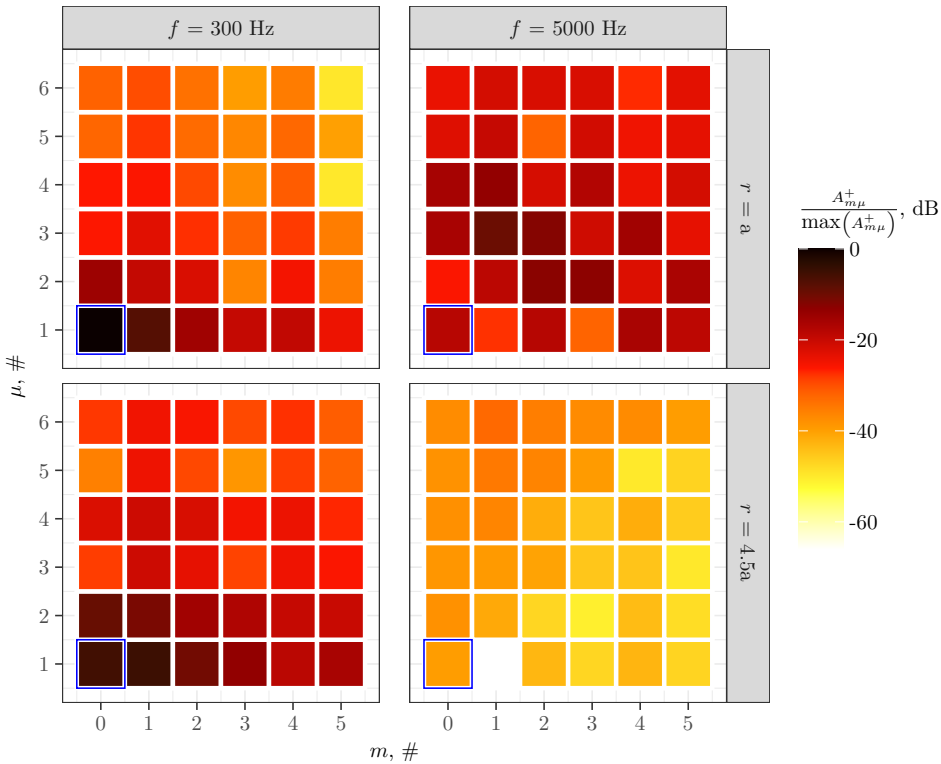
Figure 3.7: Normalized coefficients $A_{m\mu}^+$ for 36 acoustic modes, where m is the azimuthal mode number and μ is the radial mode number. Equation 3.26 was used to decompose the pressure field in Fig. 3.6 at 300 Hz and 5000 Hz for cavities with radii of a and $4.5a$, where $a = 0.005$ m. The blue boxes indicate that the mode is cut-on.

The effect of depth on the smallest cavity, $a = 0.005$ m is shown in Fig. 3.5b. The amount of attenuation increases with increasing cavity depth. This is due to all but the planar modes being cut-off and thus decaying exponentially with increasing distance.

3.4.2 Soft Wall Results

For the soft wall cavities, the walls were modeled as melamine foam. The MLULb2016 semi–empirical model was used to calculate the impedance of the melamine foam [134].
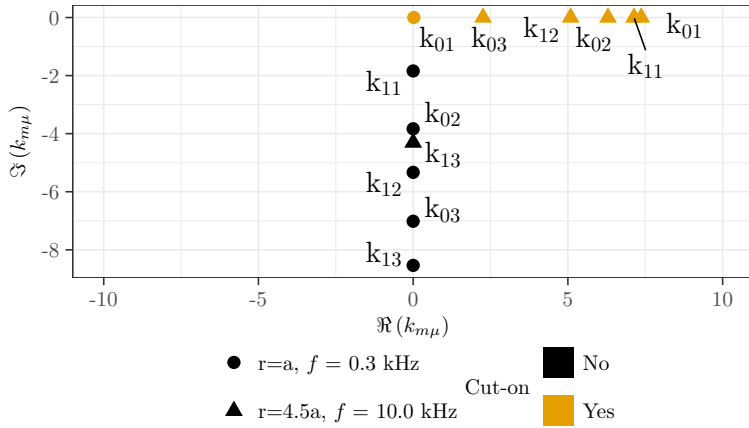
3

Figure 3.8: Comparison of axial wavenumbers, $k_{m\mu}$, with cut-on and cut-off values for a cavity with $a = 0.005$ m, $f = 0.3$ kHz and a cavity with $r = 4.5a$, $f = 10.0$ kHz.
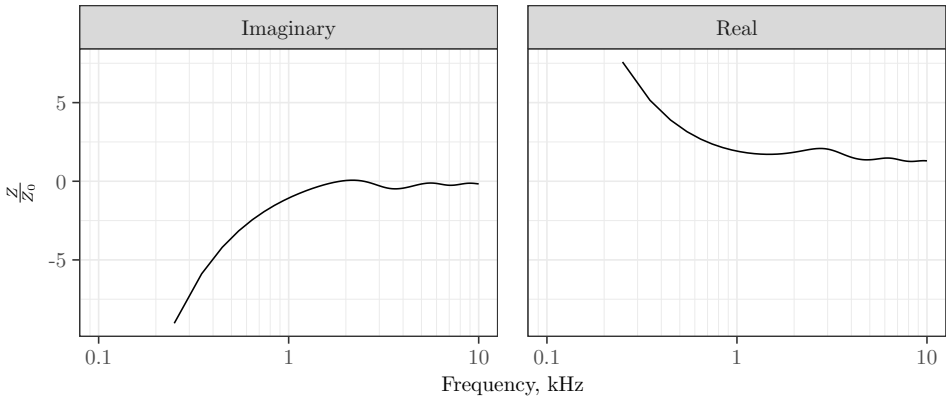

Figure 3.9: Modeled impedance of melamine foam.

Figure 3.9 shows the resulting impedance values with respect to frequency. The impedance of the foam is used to calculate the radial wavenumbers, $\alpha_{m\mu}$ and the reflection coefficient, R_{refl}, at the bottom of the cavity, Eq. 3.6. The radial wavenumbers for the soft wall case were calculated with Eq. 3.17. The resulting radial wavenumbers are complex and close to their respective hard wall values. The comparison between the soft–wall radial wavenumbers and the hard–wall values is shown in Table 3.2.

The model results for the soft–wall cavities are compared with the hard wall results in Fig. 3.10. This figure shows that the melamine walls reduce the acoustic energy by 5 — 10 dB compared to the hard wall case with the same aperture radius. This reduction is due to the sound absorbing material at the bottom of the cavity reducing the amplitude of the reflected wave. The soft sidewalls attenuate the TBL pressure fluctuations by a negligible amount. This was verified by modeling the bottom of the cavity as a hard surface, which showed that the soft sidewalls reduce the acoustic energy by 0.3 dB.

Table 3.2: Radial wavenumber comparison for hard and soft walls for $\mu = 1$, $\tilde{\omega} = 0.0684$, $a = 0.005\,\text{m}$.

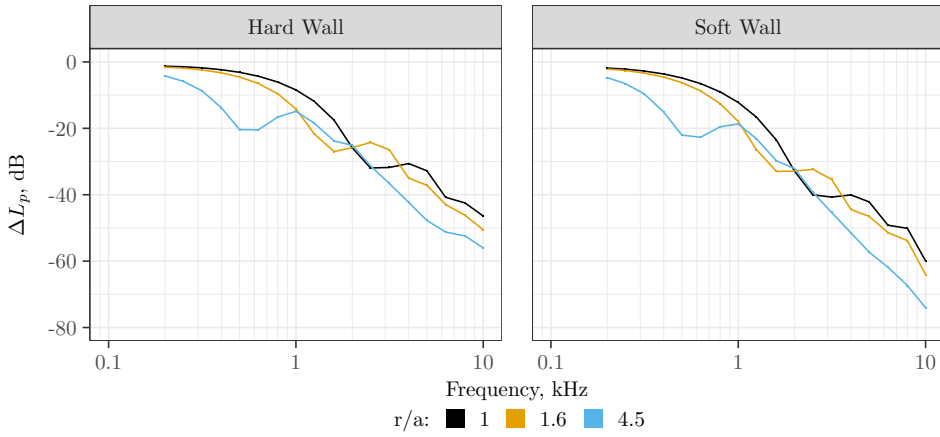| m	$\alpha_{m\mu}$ Hard	$\alpha_{m\mu}$ Soft
2	3.8317	3.8291+0.0016i
3	7.0156	7.0141+0.0009i
4	10.1735	10.1725+0.0006i
5	13.3237	13.3230+0.0004i

Figure 3.10: Soft–wall model with melamine foam compared to the hard–walled case. The cavity depths are constant with $D = 0.01\,\text{m}$.
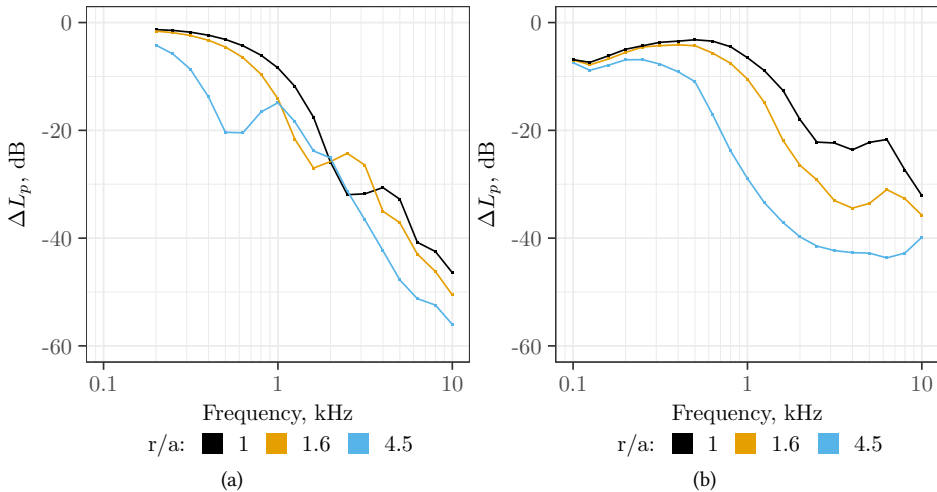

Figure 3.11: Comparison to experimental data: a) model predictions; b) experimental measurements.

3.4.3 Comparison to Experimental Data

The model trends, that show decreasing pressure spectra at the bottom of the cavity with increasing aperture size, agree with those of the experimental measurements. This agreement is seen in Fig. 3.11. For the experimental spectra, ΔL_p is the difference between the spectra calculated from the flush–mounted microphone measurements and the experimental spectra at the bottom of the cavity. The model shows the same trend seen in experimental measurements, where increasing the cavity aperture diameter results in more TBL attenuation. In both results, the larger cavity, $r = 4.5a$, features more attenuation compared to the smallest cavity. The peaks in the experimental data, especially for the $r = a$ and $r = 1.6a$ cavities, are due to acoustic depth modes. Similar peaks are also present in the modeled results, but only the $r = a$ cases are directly comparable as they are both cylindrical without angled walls.

The model over predicts the TBL attenuation compared to the experimental data, especially for frequencies above 4.0 kHz. This over prediction is most likely due to the TBL pressure model not being sufficiently representative of the pressure field at higher frequencies. For higher frequencies, the TBL model, as shown in Fig 3.6, models the TBL wall spectra as a series of closely spaced peaks. The resulting decomposition of this pressure field using Eq. 3.26 increases the energy represented by the higher-order modes. Therefore, the amount of attenuation is sensitive to the amount of energy in the plane wave mode relative to the energy in the higher–order cut–off modes. The model results are therefore sensitive to the spatial composition of the pressure field. The amount of energy in the higher–order modes, relative to the plane wave mode, is hypothesized to be over predicted. This explains the higher attenuation compared to the experiments.

3.5 Conclusions

This chapter describes the development of a physical model to predict the attenuation of turbulent boundary layer pressure fluctuations as they propagate toward the bottom of a cylindrical cavity. This model applies the methods for solving the wave equation within a duct to axisymmetric cavities. The effect of hard walls versus soft walls, consisting of melamine foam, was evaluated. The cavities are modeled with a covering, hence, the pressure fluctuations within the cavity are assumed to be acoustic. The TBL pressure field above the cavity is modeled using the wall pressure spectral predictions from the Goody and Corcos' models.

Larger diameter cavities, compared to the TBL coherence length, have more energy in the higher-order modes, while the smaller cavities have more energy in or near the planar mode. The higher-order modes are cut–off, which decay exponentially into the cavity. Thus, larger cavities have increased TBL attenuation. These results agree with the trends seen in experimental data for cavities of the same aperture radii. This suggests that the acoustic propagation assumption is valid for estimating the relationship between TBL attenuation and cavity geometry.

This chapter's model is sensitive to the TBL pressure field model at the top of the cavity. The spatial composition of this pressure field is determined by using the Corcos model. When comparing the model predictions with data, it is found that the model over predicts the attenuation of the cavities. It is hypothesized that an improved representation of the TBL pressure field would improve the accuracy of the predictions. Despite

this limitation, this model provides a useful framework, using the concept of cut-on and cut-off acoustic modes, to understand the relationship between cavity geometry and the amount of attenuation. Another drawback of this model is that it is limited to simple cavity geometries. Therefore, using a finite element method based simulation to analyze the propagation of TBL pressure fluctuations into a cavity will allow for the study of arbitrary geometries. This approach was used in Chapter 5 to investigate the acoustic response of the cavities. This type of simulation would also support a more realistic representation of the TBL pressure field.

3

4

Empirically Modeling the TBL Attenuation and Change in SNR

This study investigates how embedding microphones in different cavity geometries, along the wall of a wind tunnel, reduces the measured turbulent boundary layer pressure (TBL) fluctuations. The effect of these cavities on the measured signal-to-noise ratio (SNR) of an acoustic source with flow present was also quantified. Twelve cavity geometries defined by their depths, diameters, countersink, opening percentage, and presence of a cover were tested. The cavity geometries were selected using a design of experiments (DoE) methodology. The application of DoE enabled a statistically sound and efficient test campaign. This was done by applying a D-optimal selection criterion to all possible cavity geometries in order to select 12 cavities to allow for the individual effect of the geometric parameters such as depth and diameter to be quantified with statistical confidence. The resulting wind tunnel test data were fit to a generalized additive statistical model (GAM). This approach quantified the relative effect of these parameters on the TBL pressure spectral energy and SNR while accounting for non-linear frequency dependence. This experimental investigation quantified how much increasing depth reduces the TBL spectral energy and increases SNR. It also showed that a covering reduces the boundary layer noise by 8 dB. It also quantified how much reducing the cavity area from the opening of the cavity to the base of the microphone reduces the measured boundary layer spectral energy. Additionally, the model quantified the interactions between the cover and cavity area as well as the change in area.

4.1 Introduction

Acoustic arrays are frequently used with beamforming algorithms in wind tunnels to localize and quantify acoustic noise within a region of interest. These techniques are successfully used for aeroacoustic measurements [35] of conventional airfoils whose trailing edge noise is approximately $60\,\mathrm{dB\,m^{-1}}$ depending on the flow conditions [136]. However, as the sound generation characteristics of airfoils are modified such that the radiated noise

levels become lower by incorporating features such as trailing edge serrations [137], it is important to optimize acoustic measurement techniques for these lower levels. These measurements in closed test section wind tunnels can be hindered by turbulent boundary layer (TBL) noise generated by the wind tunnel wall along with other acoustic noise sources [35]. These fluctuations create a lower bound, below which acoustic measurements are not feasible. This is due to the acoustic pressure waves generated by the test article being overwhelmed by the higher background noise [16]. Therefore, this noise needs to be mitigated to enable effective aeroacoustic measurements of low intensity sources.

Signal processing and recessing cavities are two approaches to reducing TBL noise and thus increasing the signal–to–noise ratio (SNR). Turbulent boundary layer noise is primarily generated from the incoherent pressure fluctuations in the viscous and logarithmic regions of the boundary layer [49], which signal processing techniques can remove from the acoustic signal. For example, one method to achieve this is by removing the diagonal of the beamforming covariance matrix [106, 119, 127] which can reduce the measured background noise by approximately 25 dB at 5 kHz for a tunnel Mach number of 0.22 [16]. However, it is advantageous to couple these signal processing techniques with actual reductions in the TBL hydrodynamic fluctuations to improve the SNR of acoustic beamforming arrays. Recessing microphones in cavities and covering these cavities with a metallic cloth or Kevlar [16, 50, 61] is a common approach for reducing TBL wall noise. These methods, coupled with signal processing, can reduce the measured background noise approximately by an additional 10 to 20 dB for an array [16], which improves the SNR of the acoustic measurements. The focus of this study is to evaluate how cavity geometries attenuate the impingement of boundary layer hydrodynamic pressure fluctuations on a microphone and the resulting improvement to SNR.

An experiment was designed to study the influence of cavity geometry on two response variables: the amount of the spectral energy due to the TBL pressure fluctuations and the SNR with respect to a broadband acoustic source. This experiment used a design of experiments (DoE) methodology to select the number of cavities and their geometry. DoE is a statistical tool for test planning, that ensures randomization while covering a broad range of the design space of interest. The primary advantage of DoE over the more traditional one-factor-at-a-time (OFAT) approach to testing is that it reduces required test resources by making more efficient use of the potential experimental design space while providing insight into how different factors interact with each other [138]. The resulting test matrix ensures a sufficient number of runs to quantify the influence of different factors with statistical confidence. The resulting data are used to develop a stochastic model to determine which parameters have the most influence on the response variables. In this experiment the following geometric parameters were systematically varied: depth, opening area, cover, and change in area with depth. The wind tunnel speed was varied to determine how different designs perform at different wind speeds. The presence of a broadband noise source was used to calculate the SNR of the cavities when measuring an acoustic source. Two generalized additive models (GAM) with mixed effects were developed to quantify the relationship between different geometries and the TBL energy and SNR response variables.

This chapter has two goals. The first goal is to demonstrate the application of the DoE methodology to efficiently maximize the potential experimental space. The second

goal is to describe the application of generalized additive models to identify and quantify the influence of geometric parameters and their mutual interactions on the response variables of interest: the propagation of TBL spectral energy within a cavity and SNR. The long term application of this experimental data and resulting insights is to support future deterministic model development with the goal of optimizing cavity designs.

In the section *Theoretical Background* the background on how the cavity depth and the cover affect the TBL attenuation is introduced. In the section *Experimental Set-up*, the details of the experiments are provided. The *Experimental Results* section summarizes the boundary layer hot-wire and pressure fluctuations measurements. The section *Establishing an Empirical Model* discusses the approach to developing the statistical models. The section *Experimental Results* presents the results and analysis of the measured response variables. From this we established an empirical model in the section *Model Predictions*. The last section summarizes the conclusions of this work.

4.2 Theoretical Background

Cavity depth, area, change in area, and the presence of a covering affect the measured boundary layer pressure spectra [16, 61]. Increasing the cavity depth reduces the wall pressure fluctuations measured by the microphones. This reduction is explained by the physical model presented in Chapter 3 which describes how the TBL pressure field can be decomposed into acoustic modes. These modes are characterized as being either cut−on or cut−off. The area of the cavity along with the wavenumber of the propagating wave determines whether or not a wave is cut-on [68]. Cut−on modes propagate into the cavity while the cut−off modes decay exponentially with depth [35]. Thus the portion of energy contained in the cut−off modes does not propagate towards the microphone, resulting in a reduction in the pressure fluctuations. Furthermore, changing the area along the direction of propagation results in transmission losses due to partial reflection of incoming waves [68]. The cover further attenuates the hydrodynamic fluctuations while eliminating vortex shedding from the upstream edge of the cavity which can cause resonance within the cavity [16] as discussed in greater detail in Chapter 2. The model discussed in this work is empirical and is intended to be used to validate future cavity designs. Further discussion of developing a deterministic model applying this theory to cavity geometries is discussed in Chapter 3.

4.3 Experimental Set-up

The experimental campaign was designed to quantify the effect of the interaction between cavity geometries and boundary layer pressure fluctuations on two response variables. These response variables are the amplitude of the boundary layer hydrodynamic spectral energy measured at the base of the cavity and the resulting SNR of the acoustic source with respect to this TBL spectra. These data were collected with LinearX M51 and M53 microphones installed at the base of each cavity. Twelve cavity geometries were tested in the TU Delft Low Turbulence Tunnel (LTT) by mounting them flush on the tunnel floor. TBL spectral measurements were taken in an empty wind tunnel test section to minimize unwanted sources of noise. SNR measurements used an omnidirectional speaker mounted in the tunnel center line, 0.53 m above the cavities. In addition to the microphone

measurements, the boundary layer along the tunnel wall was measured with hot-wire anemometry (HWA). HWA data were used to calculate boundary layer thickness (δ_{99}, Θ), the shape factor (H), and to estimate the friction velocity ($u^\star$). These properties are used to normalize the pressure spectra of the boundary layer [49, 72]. The boundary layer was not tripped and therefore it was varied by changing the tunnel speed. Measurements were taken at flow speeds of $30\,\mathrm{m\,s^{-1}}$, $50\,\mathrm{m\,s^{-1}}$, and $70\,\mathrm{m\,s^{-1}}$.

Table 4.1: 12 Cavity Geometries, Flush A and Flush B are the flush–mounted microphones for each plate.

Designation	Diameter, mm	Cover	Depth, mm	Gap, %	Countersink, mm
1A	10.0	Yes	5.0	100	4.0
2A	10.0	Yes	10.0	100	0.0
3A	5.0	No	5.0	100	4.0
4A	5.0	No	5.0	50	0.0
5A	10.0	Yes	10.0	50	4.0
6A	10.0	No	5.0	100	0.0
Flush A	6.0	No	0.1	100	0.0
7B	5.0	No	10.0	50	0.0
8B	5.0	Yes	10.0	100	0.0
9B	10.0	No	10.0	50	0.0
10B	5.0	Yes	5.0	100	4.0
11B	10.0	Yes	10.0	50	4.0
12B	5.0	No	5.0	50	4.0
Flush B	2.7	No	1.0	100	0.0

The twelve cavities were analyzed in terms of the following geometric parameters: depth, opening area, cover, and change in area with depth. For the manufacturing of the cavity, they were defined in terms of depth, diameter, cover, opening percentage, and the 45° countersink depth. For the subsequent analysis the geometric parameters were defined in terms of opening area, depth, change in area, and presence of a cover. The opening area is calculated from the diameter, opening percentage, and the countersink. The change in area is defined as the ratio between the area of the opening of the cavity and the bottom, which is therefore calculated from the countersink, diameter, and opening percentage. The geometries, as machined, are defined in Table 4.1. Figure 4.1 illustrates the definition of these parameters. The diameter and depth of the cavities was chosen to avoid acoustic resonance within the frequency range of interest, 250 Hz to 7 kHz. The lowest estimated acoustic eigenfrequency for all cavities was 12 kHz for cavity *5A* which was modeled as a Helmholtz resonator. The stainless steel cloth was placed over the top of six cavities and was installed with epoxy. The cloth cover has a density of 200 threads per cm with a wire diameter of 0.025 mm. The twelve cavities, were machined into two aluminum plates, each consisting of 6 cavities and one flush–mounted microphone. This was done to allow for multiple cavities to be tested simultaneously. Cross sections of both plates can be seen in Fig. 4.2. The plates are 1 m wide and each cavity was spaced at least 120 mm apart to avoid spanwise coherence [121, 139].
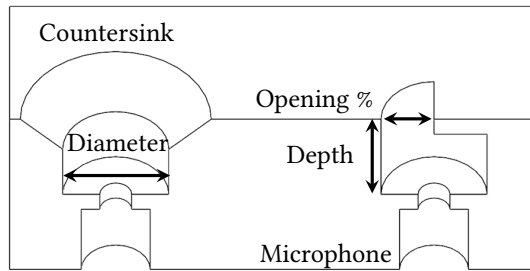
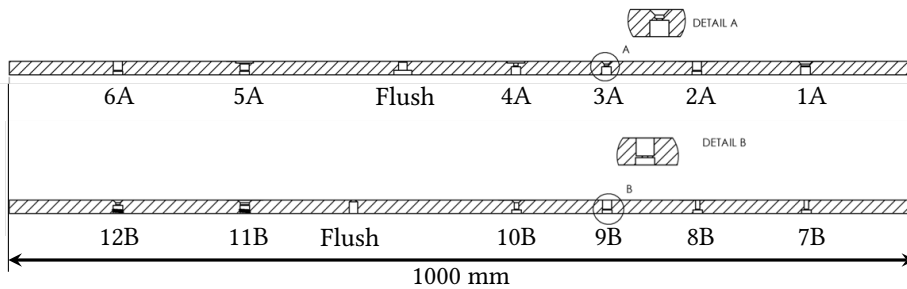Figure 4.1: Cut away illustration of the cavity geometric parameters, cloth covering not pictured.

Figure 4.2: Cross–section of the plates containing the cavities under test.

4.3.1 Wind Tunnel Measurements

The experiment was conducted at the TU Delft LTT wind tunnel. The LTT is an atmospheric closed test section wind tunnel capable of air speeds up to $120\,\mathrm{m\,s^{-1}}$. The test section is $1.8\,\mathrm{m}$ wide by $1.25\,\mathrm{m}$ tall. Free-stream turbulence is 0.015% with smooth walls. The tunnel has a contraction ratio of 17.8. The cavity plates were flush–mounted with the bottom of the test section. The design of the cavities will be discussed in the *Design of Experiments* subsection.

Measurements were taken over 24 wind tunnel runs. Twelve of these runs were with the acoustic source mounted and 12 were with only the plate mounted cavities. The entire speaker support was removed from the tunnel to minimize noise sources for the tunnel only runs. The cavity plates, presence of the acoustic source, and wind tunnel velocity were randomized between each run. Data were collected for all 7 microphones simultaneously.

Acoustic Source

A calibrated acoustic speaker, by Qsources BVBA, was used to produce an omnidirectional broadband noise source at a sound power level (PWL) of 45 dB. This is the maximum sustained output of the source. This source was chosen as it is designed for use in a wind tunnel and produces a constant sound intensity level between $0.3\,\mathrm{kHz}$ and $7\,\mathrm{kHz}$. The speaker produced a white noise signal. This was selected in order to replicate broadband
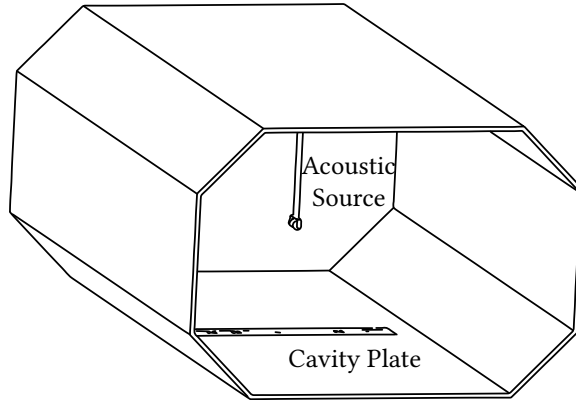
Figure 4.3: LTT test section with acoustic source and cavity plate installed.

airfoil trailing edge noise. A NACA 0018 profile support with a chord of 8 cm held the source 0.53 m above the cavities.

Data Acquisition
Microphone measurements were made with a combination of LinearX M51 and M53 $\frac{1}{2}$" condenser microphones. These microphones have a dynamic range of 122 ($\pm$1) dB up to 20 kHz. The microphone baffles were removed and the microphones were directly mounted at the base of each cavity. A National Instruments data acquisition system (DAQ), model NI9215, acquired the pressure fluctuations measurements at 51.2 kHz. For every run, data for each cavity in the installed plate were captured simultaneously. Forty-seconds of data were taken. Between each cavity configuration change, the microphone positions were redistributed randomly to reduce the likelihood of biased data due to microphone offset. The microphones were calibrated with a calibrated GRAS 42AA piston phone immediately after completing the measurement campaign.

Hot-Wire Measurements
A calibrated Dantec 1-channel hot-wire probe measured the velocity profile at 9 different spanwise locations. The sample rate was 50 kHz with a 10 kHz low-pass filter with a 3% measurement uncertainty. Each spanwise measurement point corresponds to a cavity location. The probe was located 25 mm in front of each cavity. The boundary layer was measured at 30 m s^{-1} and 70 m s^{-1}.

4.3.2 Design of Experiments
Cavity depth, diameter, cover, countersink, opening percentage, and the boundary layer characteristics affect the spectral energy at the base of a cavity [16, 50, 61] and the SNR of the microphone measurements. These parameters are the independent experimental variables that were varied during the experiment. This experiment was designed to quantify the relationship between these independent variables and the response variables (the spectral energy and SNR). Table 4.2 shows the variables, their type, and the maximum and

minimum levels considered. These bound the potential design space and the resulting cavities are a combination of these geometric variables. To establish a model describing the relationship between these variables, each variable needs to be varied and the resulting response compared. One approach is to vary one variable or factor at a time while holding the others constant. This is known as the one-factor-at-a-time (OFAT) approach. For this experiment, OFAT would require 1458 different combinations of cavity geometric parameters [138]. As this is not feasible, a subset of this design space needs to be selected for the test.

Table 4.2: Experimentally varied variables, type, and respective levels. All variables have an estimated power greater than 0.99.

Experimental Variables	Type	Levels
Tunnel Velocity, $\mathrm{m\,s^{-1}}$	Continuous	30, 70
Diameter, mm	Continuous	5, 10
Cover	Categorical	Yes, No
Depth, mm	Continuous	0, 5, 10
Opening, %	Continuous	50, 100
Chamfer, mm	Continuous	0, 4

Design of experiments (DoE) [140] is a methodology used to optimize the selection of test variables, number of runs, and run order to support statistically sound analysis of the resulting measurements. Specifically, it enforces randomization, statistical replication, and orthogonality in the experimental design. This is done by applying an optimization criterion to all the possible permutations of experimental variables to determine which subset of the experimental design space provides the most meaningful data. This resulting design allows for the development of an empirical model that evaluates the effect of experimental variables and the effect of their interactions on the response variables of interest. This methodology is widely used in many research fields as well as industrial applications [140, 141] to design experiments that yield meaningful results while minimizing the number of experimental runs. For this experiment, DoE was used to select the combination of geometrical parameters that define each of the 12 cavities discussed previously and the run order. DoE enables an efficient use of test resources to characterize the effects different cavity geometries have on the TBL spectral energy and SNR with statistical confidence.

For this experiment, a D-optimal [140] design criterion was used to optimize the choice of the values of each experimental variable seen in Table 4.2, to fully evaluate their effect on the spectral energy and SNR. The selected combinations form the experimental design. This design is expressed as an $n \times m$ design matrix, $\boldsymbol{X}$, where m is the number of experimental variables and n is the number of experimental measurements, selected a priori [140]. Within the matrix, $\boldsymbol{X}$, each value of the experimental variable is normalized so that the lowest value is -1 and the largest value is 1. The D-optimal algorithm selects the combination of variables that maximize the determinant of $\boldsymbol{X}^T \boldsymbol{X}$. This criterion also minimizes the correlation among experimental factors by maximizing the difference between the values

of each variable for each run which is ideal for exploring a new design space [140].
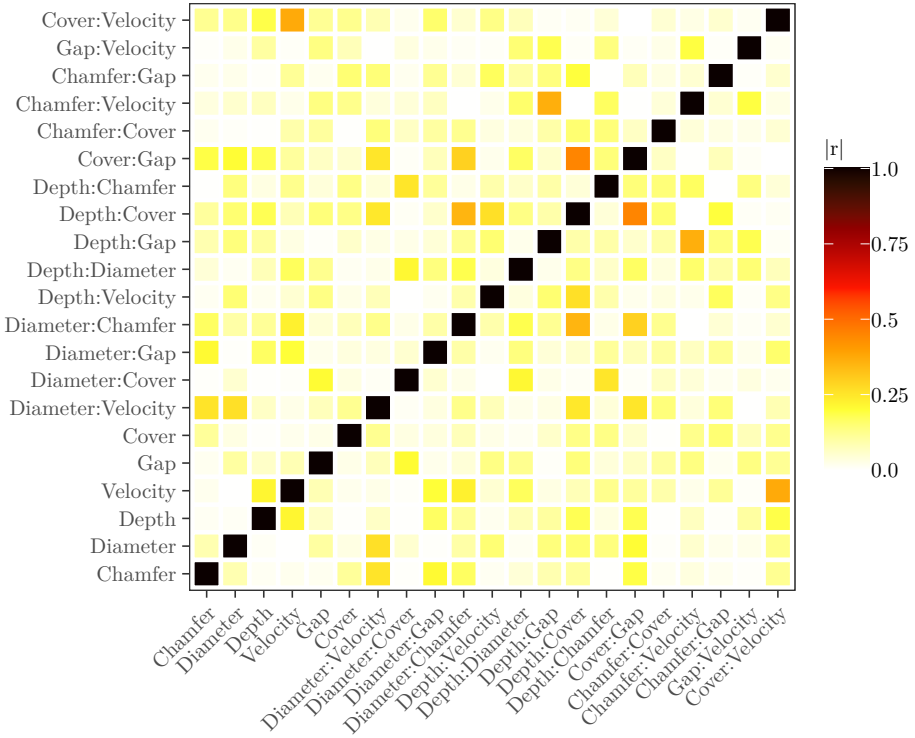

Figure 4.4: Correlation matrix of interaction between experimental variables

The results of this optimization are shown in Table 4.1. This DoE was performed using the *R* software package, *skpr* [142]. In addition to selecting the 12 cavities, the resulting experimental design also determined how many runs were required to measure sufficient data to develop a statistically sound empirical model. The resulting experimental design includes testing the cavities at two velocities, with and without an acoustic source, and with three replications which results in 144 total measurements. This compares favorably to the OFAT approach of 1458 different measurements, which would not include any statistically beneficial replications.

Experimental designs are evaluated by the resulting statistical power and the correlation between experimental variables. Statistical power is the probability that the experiment will result in statistically significant outcomes for each factor [140]. This design predicts that each experimental variable has a statistical power of greater than 0.95. Therefore the significance level, α, is 0.05. Figure 4.4 presents the predicted correlation matrix between all of the variables. The correlation coefficient is calculated by dividing the covariance of the variables by the standard deviations of the same variables. This correlation defines the linear relationship between the two variables. The correlation between variables should be low, which suggests there is a sufficient number of runs to fully evaluate

the design space without conflating the effect of two or more factors [140]. This is the case for all of the experimental variables, however some of the interaction terms have higher correlations with some of the variables. This means that should these terms appear to be statistically significant during the analysis then is important to study them closely before including them in the empirical model.

4.4 Experimental Results

4.4.1 Boundary Layer Measurements

HWA measured the boundary layer properties at 9 positions over the wind tunnel span and at two free-stream velocities. The boundary layer profiles were measured 1.5 m downstream of the tunnel nozzle exit. Temperature variations in the free-stream flow are the primary source of measurement error due to the variation in tunnel temperature over the time spent characterizing the boundary layer at each spanwise location. The recorded temperature range during each measurement campaign was used to correct the HWA measurements per Ref. 143 using the following equation:

$$E_{w,r} = E_w \sqrt{\frac{T_w - T_r}{T_w - T_a}} \tag{4.1}$$

Where $E_{w,r}$ is the temperature corrected hot-wire voltage, E_w is the measured hot-wire voltage, T_r is the hot-wire reference temperature, T_w is the hot-wire temperature, and T_a is the tunnel ambient temperature. The resulting profiles are shown in figure 4.5a. The boundary layer properties were calculated from the mean of HWA measurements. These properties are listed in Table 4.3. From the shape factor, H, it is evident that the boundary layer for both velocities is fully turbulent.
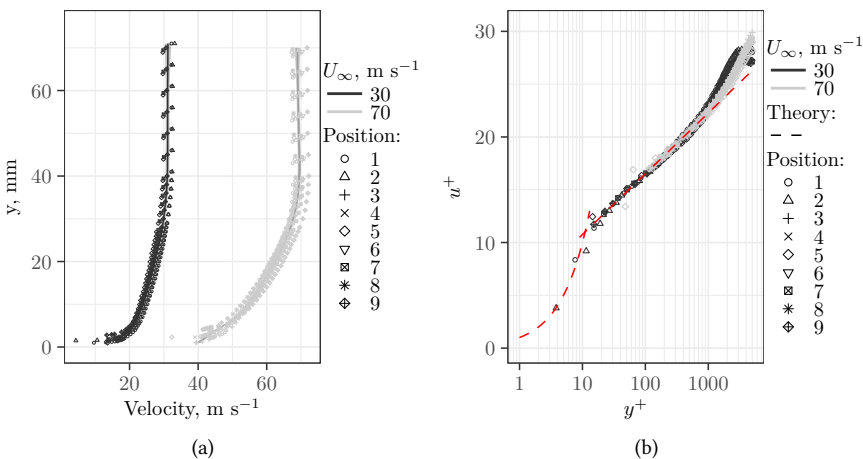

Figure 4.5: Boundary layer measurements. a) Boundary layer velocity profiles measurements at spanwise positions. b) Boundary layer data logarithmic profile fit.

Table 4.3: Boundary layer properties, where Re_Θ is the Reynolds number, δ_{99} is the boundary layer thickness, Θ is the boundary layer momentum thickness, H is the boundary layer shape factor, $u^\star$ is the friction velocity, and τ_w is the wall shear stress.

| BL | Tunnel Velocity, $\mathrm{m\,s^{-1}}$ | |
Properties	30.0	70.0
Re_Θ	8627 ±1330	17050 ±1103
δ_{99}, mm	50.7 ±16.0	46.5 ±9.47
Θ, mm	4.35 ±0.69	3.70 ±0.24
H	1.33 ±0.01	1.40 ±0.04
$u^\star$, $\mathrm{m\,s^{-1}}$	1.10 ±0.02	2.40 ±0.02
τ_w, Pa	1.45 ±0.04	6.96 ±0.13

4

The measurements showed no variation in boundary layer properties with spanwise position. From these measurements the boundary layer thickness (δ_{99}), momentum thickness (Θ), shape factor (H), friction velocity ($u^\star$), and wall shear stress (τ_w) were calculated. Their mean values and 95% confidence intervals are shown in Table 4.3. The friction velocity was calculated [71] from τ_w. The shear stress was calculated from Θ using the Karman-Schoenherr (K-S) relation [144]. These boundary layer properties were then used to normalize the boundary layer profile in terms of $u^+ = \frac{u}{u^\star}$ and $y^+ = \frac{yu^\star}{\nu}$, where the value of $u^\star$ is listed in Table 4.3. For this fit it was assumed that the wind tunnel surface was smooth. For the $30\,\mathrm{m\,s^{-1}}$ measurements, the HWA probe could be placed within 0.5 mm of the wall and within 2.5 mm for the $70\,\mathrm{m\,s^{-1}}$ case due to the flow induced vibrations in the support sting.
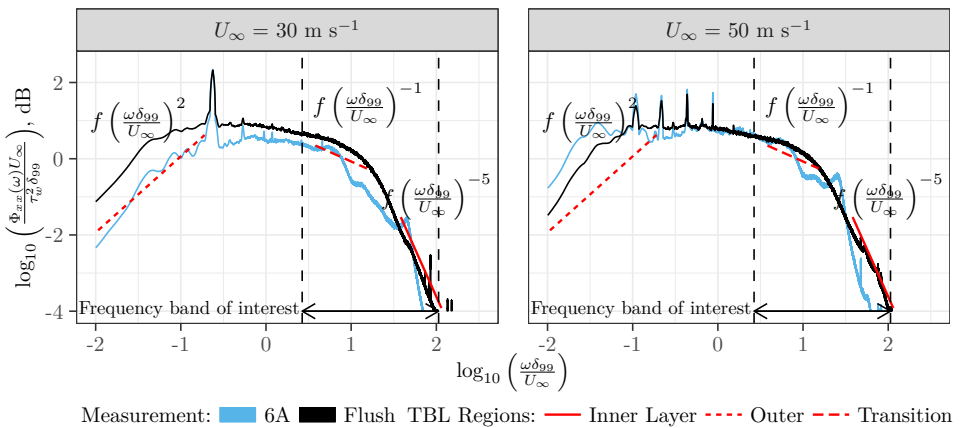

Figure 4.6: Cavity 6A, no cover and no change in area, pressure spectra normalized with the boundary layer properties. Vertical dashed lines demarcate the frequency band of interest.
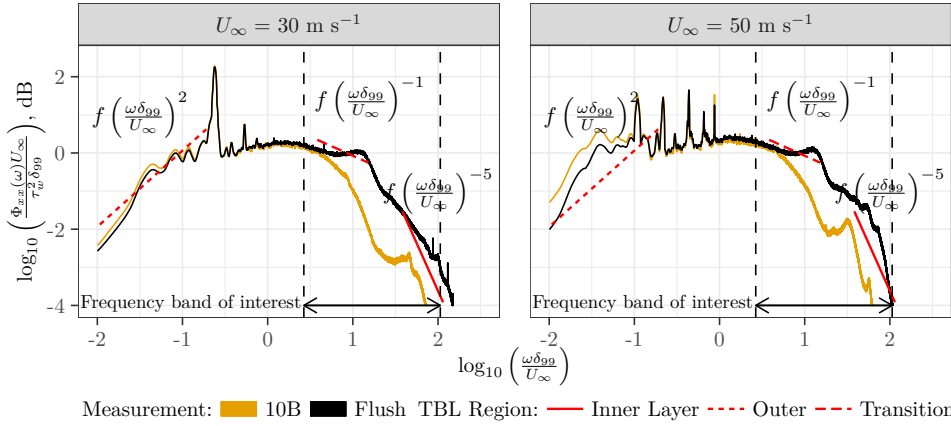
Figure 4.7: Cavity 10B, covered with change in area, pressure spectra normalized with the boundary layer properties. Vertical dashed lines demarcate the frequency band of interest.

4.4.2 Microphone Measurements

The spectral energy level and SNR at the base of the cavities were evaluated between 250 Hz and 7 kHz, the frequencies typically of interest for aeroacoustic measurements of wind turbine blades. The analysis was performed for the 30 m s^{-1} and 50 m s^{-1} runs due to some microphones being saturated for the 70 m s^{-1} measurements. These runs correspond with Reynolds numbers of 2.1×10^4 and 3.5×10^4 based on a 1 cm diameter cavity. Figures 4.6 and 4.7 illustrate the influence of cavity design on the measured TBL spectral energy, Φ_{pp} compared to a flush–mounted microphone for cavities 6A and 10B. The spectral energy is normalized by free stream velocity U_∞, wall shear stress τ_w, and the boundary layer thickness, δ_{99}. The angular frequency, ω is normalized by the ratio between δ_{99} and U_∞. The vertical dashed lines delineate the frequency region of interest. For cavity 6A, whose spectra are shown in Fig. 4.6, the cavity is not covered with a stainless steel cloth and the cavity area is constant with depth. At the horizontal axis value of 1, the spectral energy is slightly less than the baseline flush case. In contrast, cavity 10B, whose spectra are shown in Fig. 4.7, has a cover and due to the added countersink, the area decreases with depth. This cavity shows much less TBL spectral energy with respect to frequency as cavity 6A. This shows a clear effect due to covering the cavity with a cover and having a change in the cavity area. The variation in spectral energy with frequencies matches the expected empirical variation in spectral energy for each region of the boundary layer [49]. Spectral energy is higher in the outer and transition region while it decreases towards the wall where the higher frequency fluctuations are generated. For all of the cavities, reductions in the energy spectra were generally seen at frequencies above 1.5 kHz or at normalized values of 0.75 in figs. 4.6 and 4.7. While comparing the spectral energy at the base of each cavity provides insight into the effect of cavity geometry, fitting an empirical model allows for the effect of specific cavity geometric parameters to be evaluated independently. This allows us to quantify and interpret why one cavity is more performant than another.

4.5 Modeling the Change in TBL Attenuation and SNR

Two empirical models were developed to identify the relationship between the response variables, spectral energy and SNR, and the cavity geometric parameters for different tunnel velocities. These were calculated from the power spectral density (PSD) of the microphone data. The inputs to the model include cavity depth, area of the cavity opening, change in area with depth, i.e., if there is a countersink or partial covering over the cavity, and whether or not the cavity is covered. Additional terms include the wind tunnel free stream velocity and the microphone used for measurements. Since both response variables are frequency dependent, frequency was included as a model term. Initially a generalized linear mixed model (GLMM) was fit to the data. This provided insight into the relationship between the model terms and the response variables but due to the non-linear dependence on frequency, a generalized additive model (GAM) was implemented.

Data Preparation

The response variables, spectral energy and SNR, were calculated over the frequency range of interest, 250 Hz - 7500 Hz. Figures 4.6 and 4.7, show the relationship between frequency and the spectral energy response variable and thus the importance of including this dependency in the analysis. A bandwidth of 50 Hz was selected in order to accurately capture the relationship between the response variables and frequency while maintaining a reasonable computational time.

Table 4.4: 12 Cavity Geometries, Flush A and Flush B are the flush–mounted microphones for each plate.

Designation	Depth, mm	Cover	Area, mm	Change in Area, x100%
1A	5.0	Yes	254.5	-2.2
2A	10.0	Yes	78.5	0.0
3A	5.0	No	132.7	-5.8
4A	5.0	No	9.8	0.5
5A	10.0	Yes	127.2	-0.6
6A	5.0	No	78.5	0.0
7B	10.0	No	9.8	0.5
8B	10.0	Yes	19.6	0.0
9B	10.0	No	39.3	0.5
10B	10.0	Yes	132.7	-5.8
11B	5.0	Yes	127.2	-0.6
12B	5.0	No	66.4	-2.4
FlushA	0.1	No	28.5	0.0
FlushB	1.0	No	5.7	0.0

Initial Linear Modeling

Generalized linear mixed effect models are widely used for interpreting experimental results. The advantage of this model over standard linear regression is that both fixed and

random effects can be included in the model [145]. Equation 4.2 represents a generalized linear mixed effects model.

$$y = X\beta + Zb + \epsilon \tag{4.2}$$

Here y is an n-vector of the response variable (spectral energy or SNR) at each cavity geometry, frequency band, and velocity. The vector length n is then the number of experimental observations which is calculated by $n_{cavity} \cdot n_{bands} \cdot n_{velocity} \cdot n_{replications}$, where the terms are the number of cavities, number of frequency bands, number of velocities, and number of experimental replications. For this experiment there were 11508 observations. X is an $n \times m$ design matrix where m is the number of model terms. Each column contains the continuous variable values such as the geometric parameters, e.g., the cavity area, depth, and change in area with depth, frequency, and tunnel velocity. The microphone used for the measurement as well as the presence of a cover are modeled as categorical variables which result in a column for each variable with a value of either 1 or 0 within the respective column. Additionally, the interactions between these terms are included as additional columns. β is an m-vector containing the unknown coefficients of the linear model corresponding to the columns of the design matrix. Z is the design matrix of random observations or known sources of error. It has dimensions $n \times p$, where p is the number of random variables, whose values are fixed at the p-vector b. ϵ is the model error or residuals, an n-vector.

A mixed effects model was chosen because it allows for known sources of error to be accounted for as random effects. For this experiment, tunnel velocity and the microphones are specified as random effects. Velocity is accounted for as a random effect to separate it from X. This approach improves the estimate of the effect size of each geometric parameter because all of data points are used to create one estimate with the differences due to velocity being accounted for a separate variable. This is in contrast to grouping the data into separate groups for each velocity and calculating the effect size within each group. By using more data points, the fit of the model is improved. Modeling the microphones as random effects enabled any bias in the measurements due to a specific microphone to be accounted for separately from the geometric parameters of interest.

The results obtained from the linear mixed model showed that parameters such as depth, cover, and change in area are statistically significant and that their effect is congruent with previous experimental data and physical intuition. For example, an 8 dB reduction in spectral energy can be attributed to the presence of the cover. However, this linear model does not capture the non-linear dependence of the spectral energy with frequency. This is shown by plotting the residuals of the model in Fig. 4.8a, which shows the heteroskedasticity of the linear model residuals as described by Eq. 4.2. Heteroskedasticity is when the variance of residuals are not randomly distributed about 0. This suggests that a linear model may not be suitable to fully evaluate how the effect of different experimental factors changes with frequency. For this reason an extended model that allows for using splines to model non-linear terms was investigated.

Generalized Additive Model
Following the GLMM model development, a generalized additive model (GAM) was developed to model the data set. GAMs are extensions of linear models and the primary difference between them is that instead of only linear terms, GAMs allow for the experi-
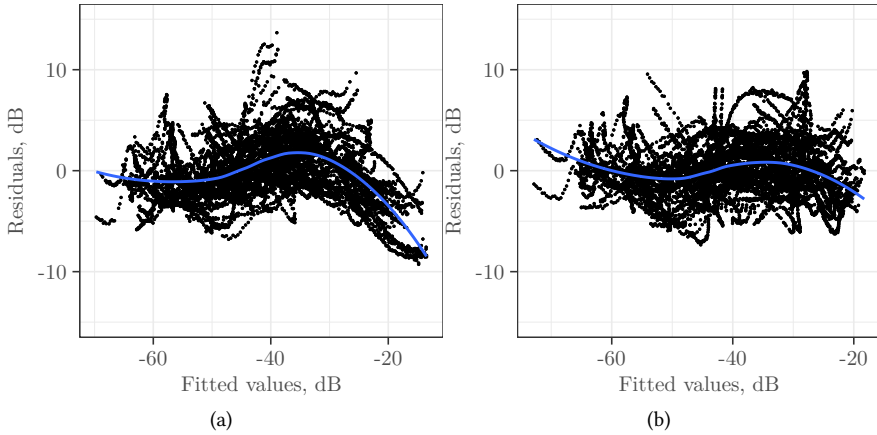
Figure 4.8: Comparison of the effect of model selection on residual distribution. a) The residual distribution for the linear model shows heteroskedasticity. b) The residual distribution for the GAM shows improved homoscedasticity.

mental factors x_i, from the matrix $\boldsymbol{X}$, to be modeled with smooth splines [146]. Notionally, the coefficients in a linear model are replaced by smooth splines as shown in equation 4.3, where $f_m(x_{im})$ are splines that replace the coefficients in $\boldsymbol{\beta}$, and β_0 is the model intercept. The i$^{\text{th}}$ entry of y is then represented as the equation 4.3.

$$y_i = \beta_0 + f_1(x_{i1}) + f_2(x_{i2}) + \ldots + f_m(x_{im}) + \epsilon_i \quad i = 1 \ldots n \qquad (4.3)$$

Each spline term is the estimate of the contribution of each experimental factor to the overall response variable. These terms are additive and when combined result in the estimate of the response variable. These splines can represent individual factors or combinations of factors, known as interaction terms. GAMs can also be applied to mixed effect modeling as discussed previously. Figure 4.8b shows the improvement over a linear model. The curve of the mean residual distribution is now much closer to the ideal zero mean line which is known as homoskedasticity. Additionally, the magnitude of residuals is also smaller, implying a better fit of the data. GAMs were fit to both the SNR and the spectral energy response variables data-sets using the *lme4 R* package [145]. When goodness of fit is compared between the GAM and the GLMM, the GAM results in a better model. Goodness of fit can be evaluated in terms of the Akaike information criterion (AIC) which is a metric describing the percent of deviance explained by the model, and the residuals. The AIC is a standard metric which combines an expression for the goodness of fit with the number of parameters used to fit the model [140]. A lower AIC is better but this can only be used to compare models based on the same data set, which is the case here. The AIC for the GLMM is 63350 and for the GAM it is 58162.

Turbulent Boundary Layer Spectra
A generalized additive model was developed to examine the relationship between the wall pressure spectral energy and the experimental factors. Given that the spectral energy re-

sponse variable decays with frequency [72] with a non-linear dependence, as shown in Fig. 4.7, it is important to model the spectral energy as a non-linear function of frequency. Applying a GAM allowed this term to be modeled with a spline, which resulted in a substantial model improvement compared to the GLMM.

Table 4.5: Cavity spectral energy statistical models comparison.

	Linear Mixed Model	Random Effects Only	Final Model
AIC	63350.39	74592.22	58162.02
Log Likelihood	-31665.19	-37277.37	-29038.42
Num. obs.	11508	11508	11508
Dispersion (Variance)	13.3	38.17	9.14
R^2	0.90	0.73	0.93
Num. smooth terms	0	3	7

Table 4.6: Cavity spectral energy model parameters.

Linear Parameters	Coefficients, dB (Standard Error)
(Intercept)	-61.48 (0.325)***
Area	-0.02 (0.002)***
log(Depth)	-0.64 (0.029)***
Change in Area	1.67 (0.042)***
Cover Yes	-6.56 (0.153)***
Change in Area×Cover Yes	-1.56 (0.053)***
Area×Cover Yes	-0.02 (0.002)***
Spline Parameters	Est. Degrees of Freedom (Standard Error)
s(Frequency)	6.99 (7.94)***
s(Microphone)	7.89 (8.00)***
s(Tunnel Velocity)	1.00 (1.00)***
s(Frequency)×Cover Yes	7.90 (8.59)***
s(Frequency)×Resonance Yes	8.69 (8.95)***

*** $p < 0.001$, ** $p < 0.01$, * $p < 0.05$

Fitting the spectral energy GAM to the experimental data requires careful consideration of potential model parameters. Parameter selection is a balancing act between explaining as much variance in the data as possible while avoiding over fitting the model by including all possible model terms. Model parameters were added and removed progressively, beginning with a random effects only model that contained tunnel velocity and the microphones. As model parameters were included and removed, subsequent model iterations were compared against this random effects only model. In generalized additive modeling, parameters can be added as linear parameters or as spline basis functions
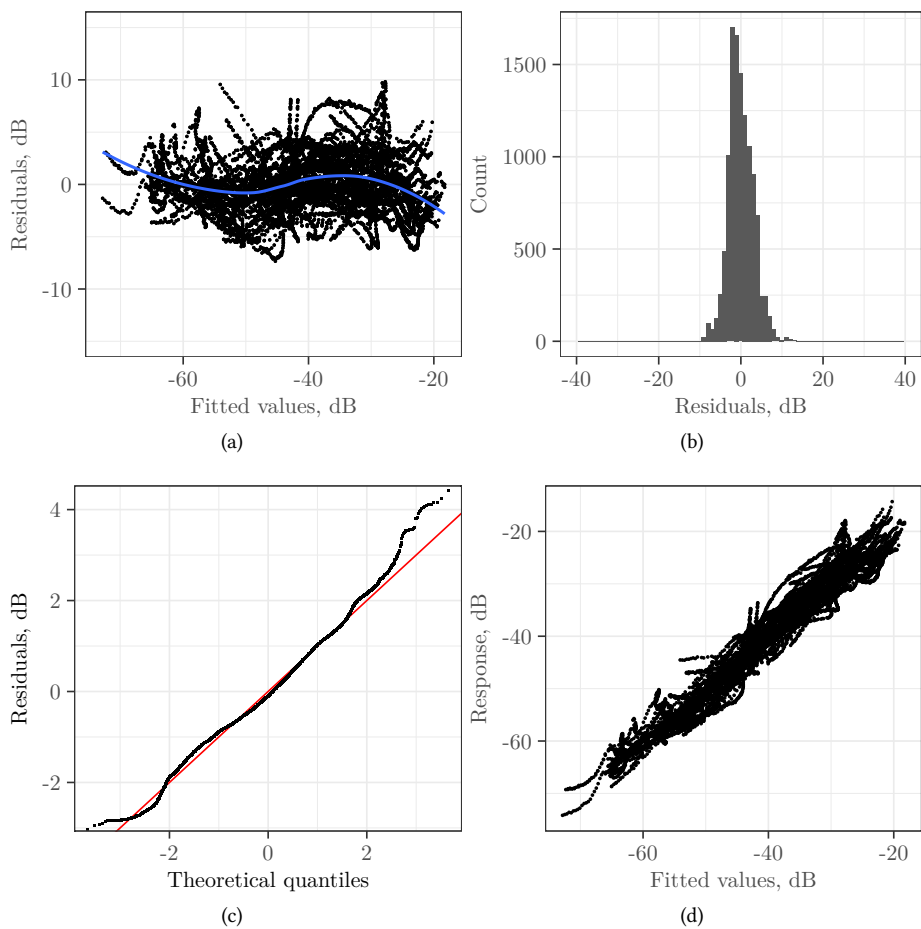
Figure 4.9: Boundary layer spectral energy GAM model residual diagnostic plots: a) Homoscedasticity of residuals. b) Histogram of residuals. c) Quantile - Quantile plot. d) Model response vs. measured values.

(applied to the response variables with a frequency dependence) which estimate the non-linear relationship between the response variable and the experimental parameters.

Each geometric parameter was added as a model parameter and after each one was incorporated, the updated model was compared against the initial random effects only model, using the AIC selection criterion. In addition to using the AIC to optimize the model, the distribution of residuals was also considered. Ideally, residuals should be normally distributed and as close to zero as possible [146]. The size of the residuals and their shape when plotted can indicate if the model is missing a key parameter. Large residuals suggest that the model is missing a term that potentially explains the source of variance. The heteroskedasticity of the residuals also implies that there is a non-linearity that the model does not account for. Finally, the physical interpretation of model parameters is an important consideration. In practice this means that instead of fitting all model terms and removing those that have p-values > 0.05, the model terms need to have a physical explanation. For example, both the cavity depth and presence of a cloth covering have physical interpretations. It is assumed that a cover can be modeled by imposing an impedance across a cavity opening. As discussed previously, Eq. 3.22 suggests that cavity depth can be explained by cut-off modes decaying exponentially with distance [68]. This exponential relationship for depth was linearized by taking the natural log in order to better model the relationship between depth and spectral energy. In contrast, if a model parameter had a small coefficient and did not have a physical significance, it was removed even if it was statistically significant. Once evaluating the inclusion of cavity depth, change in area, area, and cover, including the interactions between these terms was evaluated using the same approach. Being able to evaluate interactions is an important benefit of using DoE methods [138, 141]. This model selection approach avoids over fitting the model to the data. The risk of an over-fitted model is that by tuning a model to explain as much of the variance in the data as possible, it is possible to get a model that is less accurate when applied to other data sets. By avoiding over-fitting, this GAM supports future comparison to analytical models, computational fluid dynamics (CFD) simulations, and experiments.

Table 4.5 compares the random effects only GAM with the final GAM as well as the GLMM. The final GAM has a reduced AIC and dispersion. The R^2 value increased from 73% to 92% compared to the random effects only model. Figure 4.9 shows the residual diagnostic plots using the final GAM. The histogram in Fig. 4.9b shows that the residuals are close to zero and indicates that they are normally distributed. This is further supported by the quantile-quantile plot, Fig. 4.9c, which plots the probability distribution of the model residuals against a normal distribution. Since the residuals are close to the line, this supports the assumption that the residuals are normally distributed [146]. Figure 4.9a shows that the model residuals are homoscedastic as they are closely distributed around zero, indicating that there are no non-linear effects remaining unincorporated into the model. Figure 4.9d compares the experimental data with the model prediction. As shown, these points are closely distributed around a slope of one, indicating that the model adequately represents the data.

The estimated individual contributions to the spectral energy for each of the model parameters are listed in Table 4.6. Depth, area, change in area, and presence of a cover are shown to be statistically significant (p-values < 0.05) linear model parameters. Two significant interactions between model parameters are the cover and the cavity area and
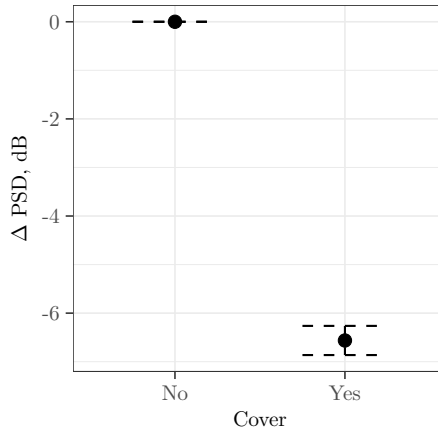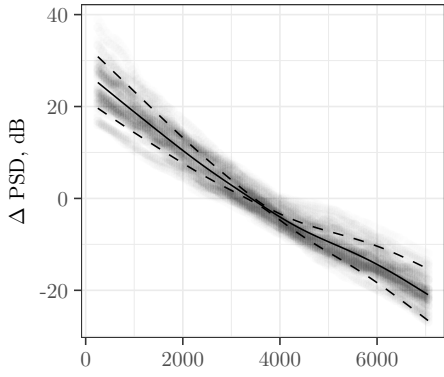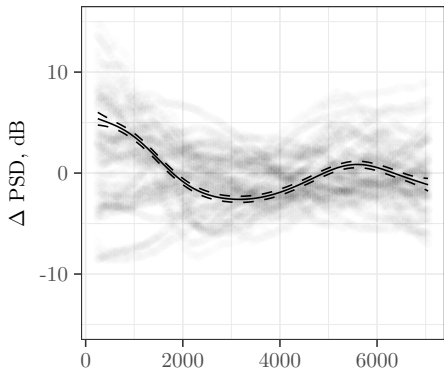
Figure 4.10: Effect size of cover linear term.

the cover and change in area percentage. The interpretation of these interaction terms is that when the cavities are covered, increasing the cavity area or the amount of area reduction reduces the pressure spectra at the cavity bottom. These parameter coefficients are also commonly referred to as the parameter effect size for the linear coefficients. These values are interpreted by multiplying this coefficient by the value of the model term. For example, for a cavity that has a depth of 10 mm, the overall change due to depth is $\ln(10) \cdot (-0.64) = -1.5$ dB. It is important to note that despite the area term having a small coefficient, its net contribution to the model is still substantial. This is because the area is on the order of 100 mm^2 and when multiplied by -0.02 results in a reduction around 2 dB. The cover is estimated to reduce the spectral energy by 6.5 dB, Fig. 4.10, which is in agreement with previous experimental work [50, 61]. The interaction terms are interpreted by multiplying all terms in the interaction by the coefficient, e.g., the value of the area multiplied by the coded value for the cover, 1, by -0.02. This shows that there is a greater reduction in the spectral energy with increasing area if there is a cover present. For the other interaction term, the change in area only reduces the spectral energy when there is no cover. Otherwise, changing the area has minimal effect. To predict the amount of spectral energy for a given geometry, these linear terms, the model intercept, and the spline terms are summed together.
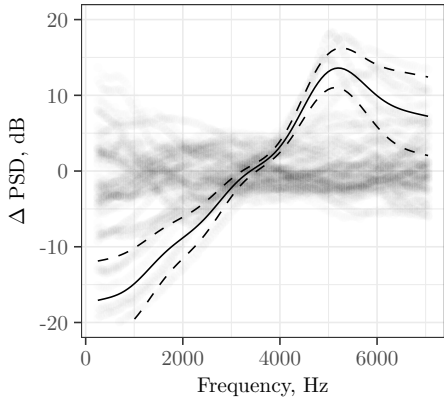
Spline basis functions for frequency, presence of a cover with frequency, and resonance with frequency were included in the GAM. Given that spatial averaging of turbulent structures is dependent on the transducer area as described by Corcos [131], a spline term for the variation in spectral energy due to area with respect to frequency was considered. However, the predicted reduction in spectral energy for the frequencies and cavity areas considered was relatively small at approximately 2 dB and the resulting spline term showed an even smaller reduction in spectral energy with frequency due to cavity area. Therefore this term was neglected in favor of simplifying the model. The resonance term was added to account for a peak in spectral energy between 5000 Hz and 6000 Hz present for some cavities due to an acoustic depth mode, in order to avoid attributing this peak to other model terms. As with the previously discussed spectral energy model, tunnel veloc-

Figure 4.11: Change in spectral energy with frequency GAM splines. The dashed lines are 95% confidence intervals. Grey points are the observed data. a) Estimated change in spectral energy with frequency. b) Estimated change in spectral energy due to the cover with respect to frequency. c) Estimated change in spectral energy due to resonant modes with respect to frequency.

ity and the microphone were modeled as random effects. Table 4.6 lists the final model parameters and their estimated degrees of freedom. The estimated degrees of freedom are lower than the number of degrees of freedom for each variable to avoid over fitting the spline. This table shows that the following splines are statistically significant: spectral energy with respect to frequency, spectral energy and the cover with respect to frequency, and the presence of a resonant mode with respect to frequency.

Figure 4.11 shows the three splines for the change in PSD with frequency, the change in PSD due to the cover with frequency, and the change in PSD due to the acoustic mode. Figure 4.11a shows the decay in spectral energy with increasing frequency. Figure 4.11b shows how the influence of the cover is frequency dependent. When this plot is combined with the linear component of the cover as shown in Fig. 4.10, -6.5 dB, a net reduction of 10 dB is estimated at 3000 Hz. Given that for most materials impedance often is frequency dependent, this dependence is expected. However, additional experiments are required to determine how the geometry of the cover, e.g., thread diameter and density, influence this relationship. Figure 4.11c shows the resonant mode peaking at 5000 Hz. When these spline terms are combined with the linear terms in Table 4.6 the resulting combination estimates the total spectral energy for an arbitrary cavity geometry.

Through the use of a mixed effects model, the presence of microphone bias was confirmed. Figure 4.12 shows that several microphones have a measurement offset that is statistically significant compared to the other microphones. The microphones should be statistically indistinguishable from each other and centered around 0 dB, however as an example, microphone 7 is shown to have the largest offset, with a 1.5 dB bias compared to the other microphones. By accounting for this in a mixed model, the measurement error in the response variables due to the microphones is accounted for and does not influence the results by biasing the data towards measurements made with a specific microphone. This bias was only detectable due to randomizing runs and randomizing which microphones were used with which cavity for each run.
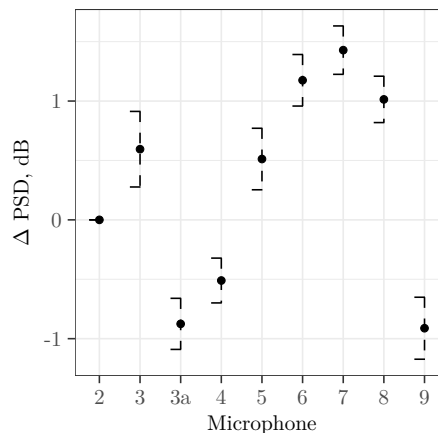

Figure 4.12: Effect of microphone measurement bias with 95% confidence intervals.
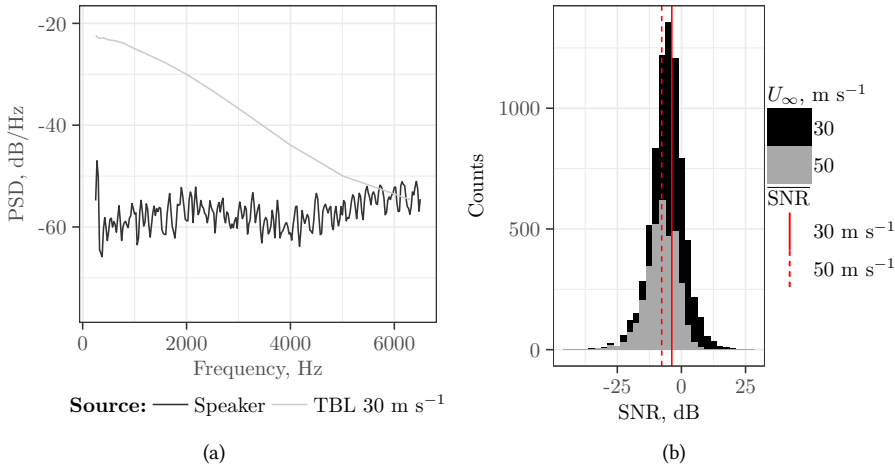
Figure 4.13: Signal spectral energy level compared to boundary layer pressure spectra levels. a) Spectral energy comparison for flush–mounted microphone. b) Effect of velocity on SNR.

Signal–to–Noise Ratio
Using cavities to reduce the boundary layer energy at the microphone is only useful for aeroacoustic testing if the acoustic signal of interest is not reduced proportionally with the reduction in TBL noise. The ratio between the signal of interest and background noise due to the boundary layer is the SNR. For this experiment, the runs to measure the pressure fluctuations of the boundary layer were repeated with an acoustic source in the center line of the wind tunnel. The intent of this set-up was to be able to compare the spectral energy of the source with that of the boundary layer. However, for most cavities, the acoustic energy was lower than the boundary layer energy, at frequencies below 6 kHz as shown in Fig. 4.13a. This figure compares the spectral energy of the boundary layer measured by a flush–mounted microphone with the acoustic source without flow. The omnidirectional source had a maximum PWL of 45 dB which was not sufficient to adequately characterize the SNR. Both the boundary layer pressure fluctuations and the acoustic source are broad-band sources. Extracting the signal level from the noise level is non-trivial. The SNR was estimated using equation 4.4 where $\mathrm{PSD_{signal\ +\ TBL}}$ is the spectral energy with the acoustic source and $\overline{\mathrm{PSD}}_{\mathrm{TBL}}$ is the average spectral energy per cavity with no source with respect to tunnel velocity and frequency.

$$\mathrm{SNR} = 10\log_{10}\left(\frac{\mathrm{PSD_{signal\ +\ TBL}} - \overline{\mathrm{PSD}}_{\mathrm{TBL}}}{\overline{\mathrm{PSD}}_{\mathrm{TBL}}}\right) \tag{4.4}$$

The average boundary layer spectral energy, $\overline{\mathrm{PSD}}_{\mathrm{TBL}}$, for each cavity was calculated with respect to frequency and velocity resulting in an average spectrum for each cavity at both $30\,\mathrm{m\,s^{-1}}$ and $50\,\mathrm{m\,s^{-1}}$. The resulting average ensemble was subtracted [16] from each run with the acoustic source at matching velocities. This was done over the frequency range of 250 Hz to 7 kHz. The resulting distribution of the SNR shows that most are below

Table 4.7: Cavity SNR statistical model diagnostics.

	Random Effects Only	Final Model
AIC	48724.67	46147.91
Log Likelihood	-24351.47	-23043.40
Dispersion	37.41	26.51
R^2	0.14	0.39
Num. obs.	7541	7541
Num. smooth terms	2	4

4

0 dB as shown in Fig. 4.13b. This process introduces uncertainty because variation in the signal level between runs was approximately ± 2 dB. If the difference between $\overline{\text{PSD}}_{\text{TBL}}$ and $\text{PSD}_{\text{signal + TBL}}$ is within this variation, it is difficult to determine if the signal is above the noise level. Given that 70% of SNR values are within ± 2 dB, this is a significant source of error.

A GAM was developed to fit the SNR response variable to the experimental parameters. The objective was to identify the influence of the cavity geometry on SNR. Due to the errors introduced by calculating SNR for the comparatively weak acoustic source with respect to the TBL pressure fluctuations, the resulting statistical model does not fully explain the sources of variance. As with the spectral energy model, an initial random effects only model was developed as a starting point. Velocity and microphones were modeled as random terms. SNR decreases with increasing velocity, as shown by Fig. 4.13b. An iterative process of adding and removing model parameters was followed using the same criterion as performed in the development of the spectral energy model. Frequency was the initial parameter included as a spline due to SNR increasing non-linearly with frequency, as inferred from Fig. 4.13a which shows the energy level of the acoustic source and boundary layer converging with increasing frequency. This increase is due to the decay in boundary layer energy with frequency. The linear and non-linear terms for the geometric factors and their interactions were iteratively added and removed as before. The resulting model shows that the cover, depth, change in area, as well as the following interaction terms: depth and change in area and cover and change in area; are statistically significant terms. This is consistent with the GAM developed for TBL spectral energy.

The final model explains more of the SNR variance in the data than the random effects only model as detailed in Table 4.7. The AIC and dispersion are lower, and the percentage of variance as expressed by R^2 is higher. These three diagnostic terms show that the final model is a better fit of the data. The final SNR model is only marginally better at explaining the variance in the data as quantified by the R^2. This is due to the uncertainty in the data stemming from the SNR calculation, this model only explains 39% of the variance. The final model was also compared against the random effects model with a χ^2 statistical test and is significant with a $p \ll 0.001$. The resulting diagnostic plots for the final model in Fig. 4.14 show that assuming the residuals to be normally distributed is reasonable. Figure 4.14a shows that the sources of non-linearity have been reduced due to the GAM. However, the dispersion of the residuals is large compared to that of the spectral energy, 26.5 dB (Table
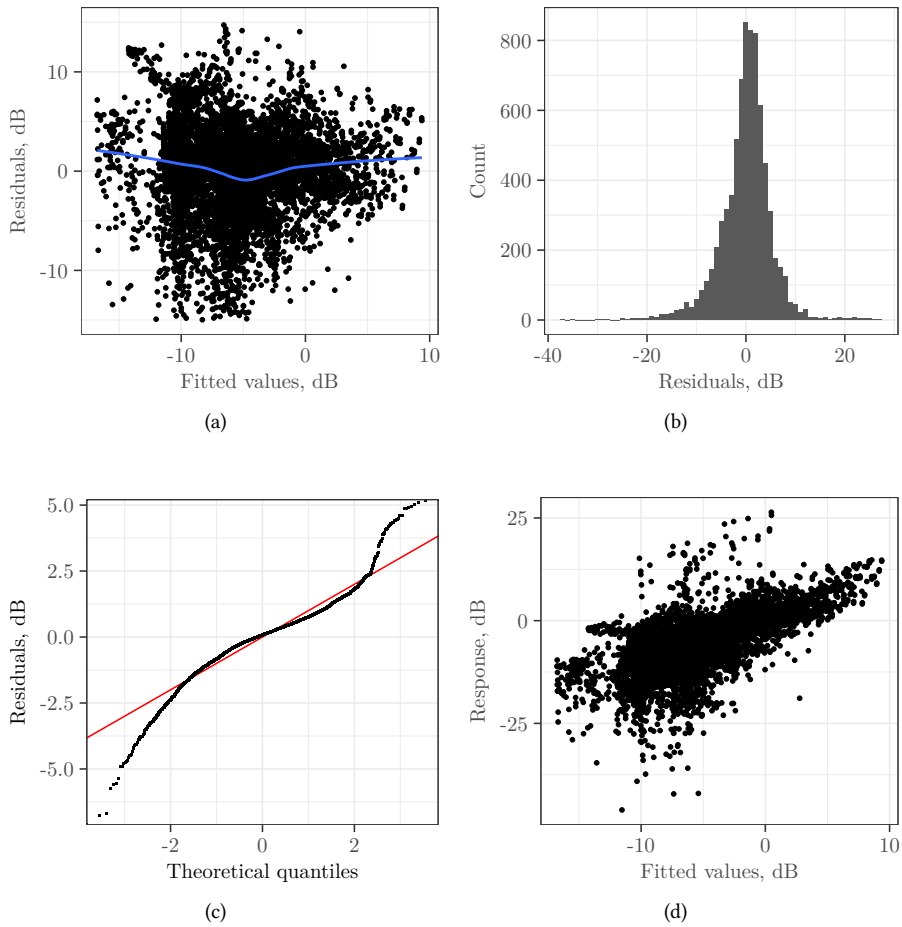
(a)

(b)

(c)

(d)

Figure 4.14: SNR GAM model residual diagnostic plots: a) Homoscedasticity of residuals. b) Histogram of residuals. c) Quantile - Quantile plot. d) Model response vs. measured values.

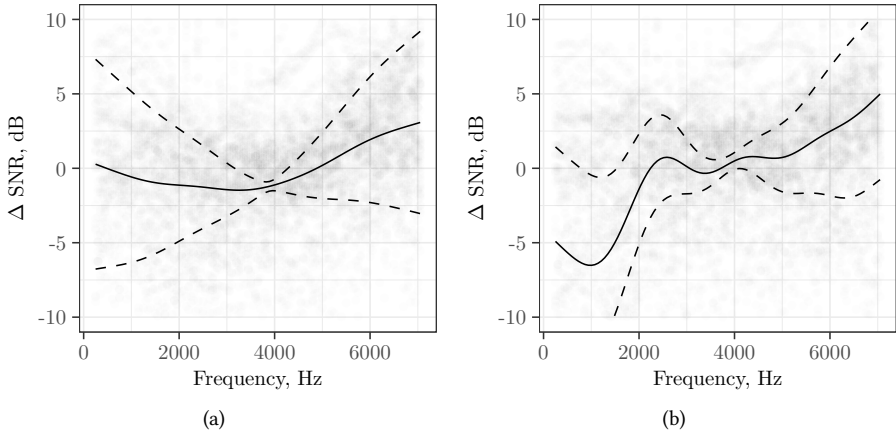(a)   (b)

Figure 4.15: SNR GAM spline models. a) Change in SNR with frequency. b) Change in SNR due to the cover with frequency.

4.7) and 9.1 dB (Table 4.5) respectively. The source of this dispersion is attributed to the uncertainty introduced through the calculation of SNR.

Table 4.8 lists the linear and non-linear terms for the SNR model. All of the terms in the model are significant with p-values $\ll 0.001$. The cover improves the overall SNR by 2 dB and has a non-linear dependence on frequency, as shown in Fig. 4.16. When the linear and non-linear terms are combined (Fig. 4.16 and Fig. 4.15b, the cover increases the SNR by 5 dB at 6 kHz. The influence of the cover is intuitively given since it reduces the energy of the boundary layer hydrodynamic fluctuations impinging on the microphone. The positive value for the depth linear coefficient suggests that SNR decreases with increasing depth. As the microphone is moved further from the acoustic source, the acoustic energy received at the microphone is lower. Because the acoustic waves from the speaker are assumed to be plane waves, the energy decays with the inverse square of the distance due to geometrical spreading. Therefore cavity depth should not have a substantial effect on the acoustic signal because the depths of the cavities are at most 1 cm in comparison to the 0.75 m distance between the speaker and the cavity. Plane waves do not decay at the same rate as the boundary layer pressure waves because the plane waves are cut-on while the other waves have modes that are cut-off within the cavity. Therefore it is suspected that the increasing depth reduces the SNR. Further study is required to determine if this measured effect is real or due to the uncertainty in the SNR estimation. Changing the cavity area has a significant effect on increasing the SNR which is logical given that this parameter reduces the boundary layer spectral energy. The interactions terms involve the change in depth and the presence of the cover interacting with the change in area. The cover combined with the change in area increases the SNR. However, the increase due to the change in area is not substantial without the cover present. The final interaction term between depth and the change in the area suggests that there is a minimal change in SNR with depth if there is no change in area. This shows that changing the cavity area is more

Table 4.8: Cavity SNR model parameters, standard error is listed parenthetically.

Linear Parameters	Coefficients, dB (Standard Error)
(Intercept)	0.37 (0.47)
Cover Yes	1.96 (0.22)***
log(Depth)	-0.27 (0.07)***
Change in Area	-3.87 (0.29)***
Cover Yes×Change in Area	-1.67 (0.14)***
log(Depth)×Change in Area	2.24 (0.18)***
Spline Parameters	Est. Degrees of Freedom (Standard Error)
s(Frequency)	4.93 (5.99)***
s(Microphone)	7.60 (8.00)***
s(Frequency)×Cover Yes	7.27 (7.80)***
s(Tunnel Velocity)	1.00 (1.00)***

*** $p < 0.001$, ** $p < 0.01$, * $p < 0.05$

important to improving the SNR than the depth term. Given the uncertainty present in the dataset due to the calculated SNR, it is difficult to state unequivocally which geometrical parameters have an important effect on the SNR. Future experiments should incorporate an acoustic source with higher power levels to achieve a SNR that is significantly higher than those seen in this experiment. This would reduce the uncertainty and result in a better GAM for SNR.
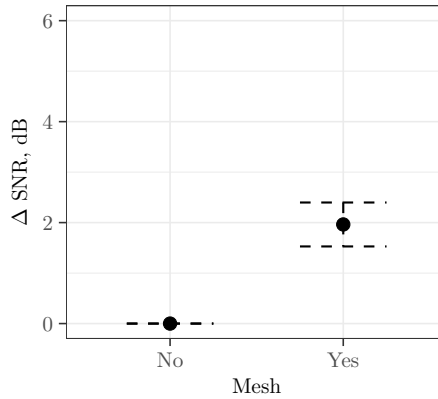
Figure 4.16: Change in SNR due to the cover

4.6 Model Predictions

The spectral energy and SNR model predictions are useful in the evaluation of how the cavity geometric parameters affect the response variables of interest. The predicted values were calculated by using the the cavity geometries (Table 4.4) as the input to the model. The resulting data were used to evaluate the net effect different combinations of cavity geometries have on spectral energy and SNR.

Spectral Energy Predictions
The GAM spectral energy predictions provide a basis for interpreting how the cavity depth, area, change in area, and presence of a cover influence the spectral energy. Figures 4.17 - 4.19 depict the total change in spectral energy as a function of different parameters. Figure 4.17 shows the reduction in spectral energy with depth. Increasing depth has an exponential relationship with the overall reduction in spectral energy as described in Eq. 3.22. It is predicted that the deeper the cavity is, the less effective depth is at reducing the spectral energy. This is logical as the cut-off modes decay exponentially with distance and at a certain depth only the cut-on modes will continue to propagate. This figure also depicts the cover reducing the spectral energy. The attenuation due to the cover is frequency dependent and can be modeled using the impedance of the cloth. There is no interaction between the cover and depth factors as shown by the fact that the change in energy with depth is constant between the two plots. Figure 4.18 shows that increasing the cavity area reduces the spectral energy measured by the microphone. This figure also shows the interaction between the cover and the area term in the model. When a cover is present, the cavities with a larger area show a much larger reduction in spectral energy. The underlying physical explanation for this interaction necessitates further investigation but a possible explanation is that the cover reduces the energy in the hydrodynamic modes resulting in weaker cut-on modes for larger diameters. Reducing the area of the cavity from the aperture to the base of the cavity reduces the spectral energy as shown in figure 4.19. However, the reduction due to this area change is only significant when there is no
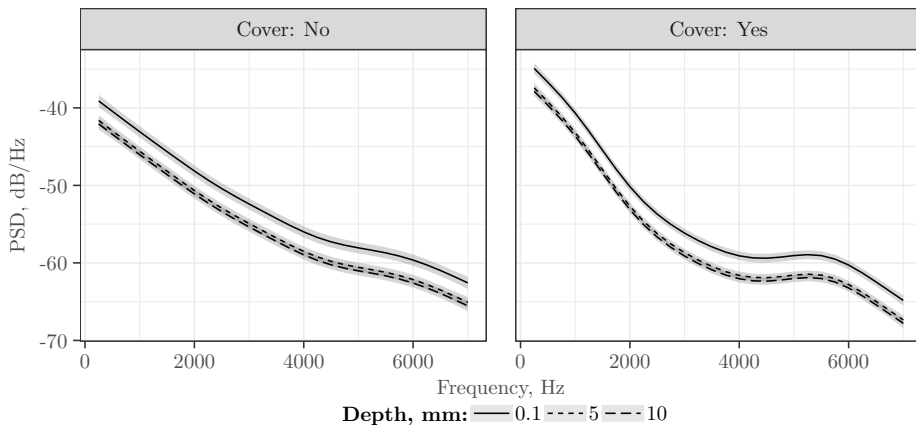
Figure 4.17: Effect of increasing depth on boundary layer spectra.
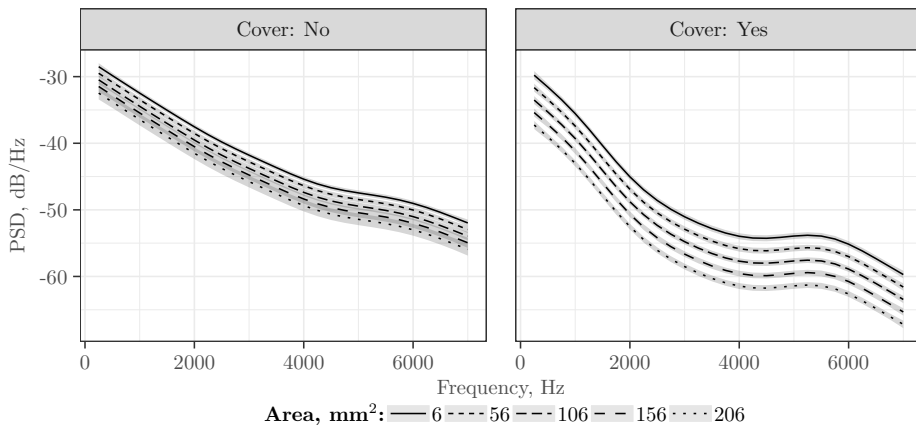

Figure 4.18: Effect of interaction between cavity opening area and cover on boundary layer spectra.
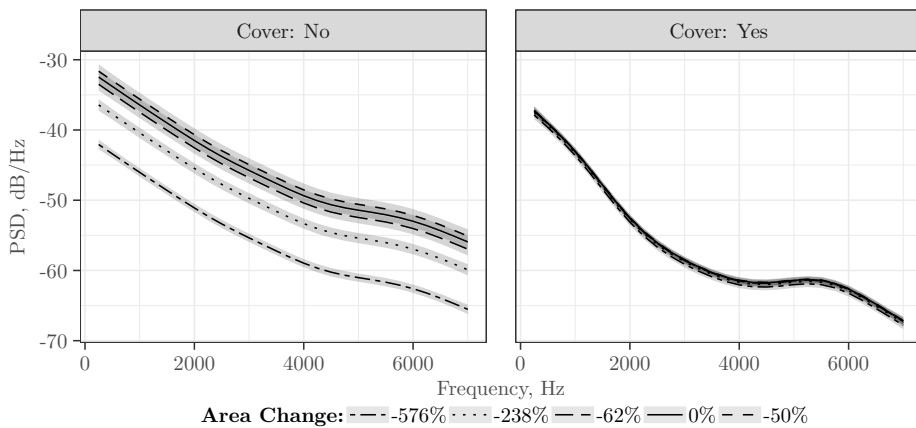

Figure 4.19: Effect of changing cavity area with the cover on boundary layer spectra.
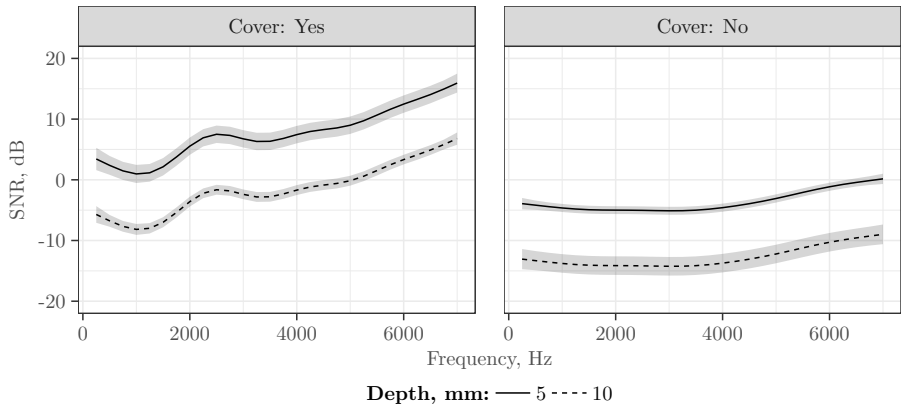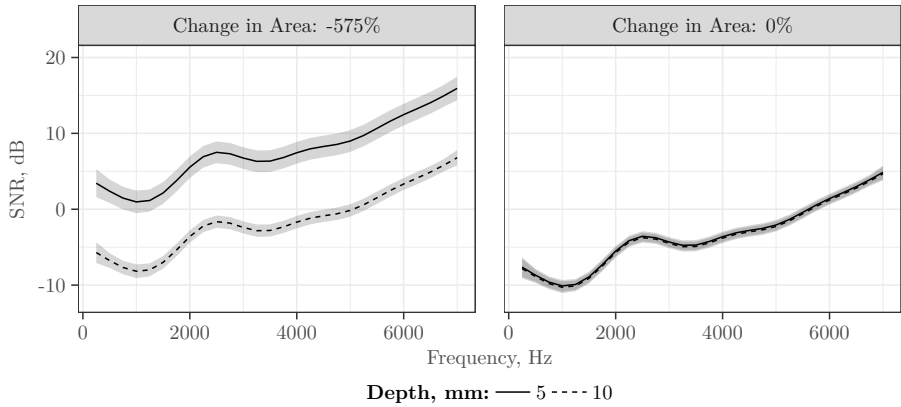
Figure 4.20: Change in SNR with increasing depth.

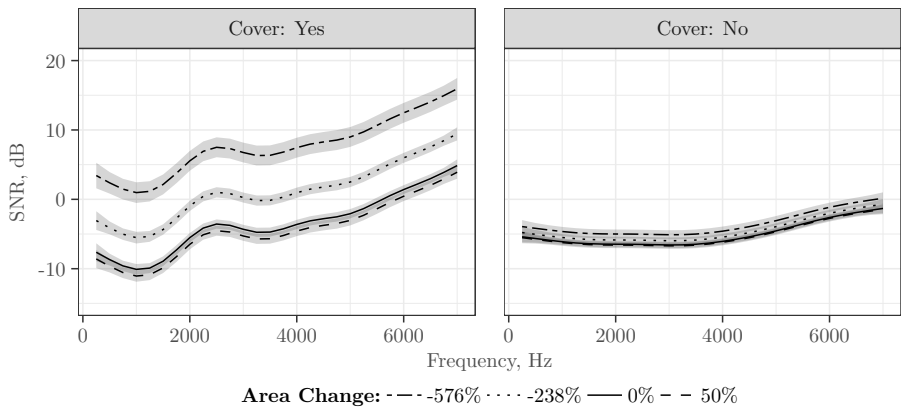Figure 4.21: Change in SNR due to the interaction between change in area with depth.

Figure 4.22: Change in SNR due to change in area with and without a cover.

cover. It is known from duct acoustics that changing the cross sectional area causes reflections that reduce the transmitted energy [68]. A possible explanation is that the cover reduces the energy in the transmitted pressure fluctuations to the point that when the area is reduced, the effect on the transmitted energy is insignificant.

Signal-to-Noise Ratio Predictions

The SNR GAM predictions aggregate the model parameters into a predicted value for the SNR. This model output delineates how the cavity geometric parameters and their interactions influence the SNR. Figure 4.20 shows that shallower cavities have improved SNR performance. However there is no interaction between cavity depth and the presence of a cover. Therefore the cover increases the SNR independently of the depth. The model predictions show a 7 dB improvement in SNR with decreasing depth. This prediction is questionable because the GAM for the TBL spectral energy shows a significant reduction, which should correspond to an increase or minimal change to the SNR. Unlike the spectral energy model, there is an interaction between the change in area and the cavity depth. Figure 4.21 shows that when the area of the cavity is reduced by 575% with respect to the aperture of the cavity, a shallower cavity has a higher SNR. Cavities with a constant area, show an insignificant change in SNR with increasing depth. SNR increases with reduction in the cavity area. This is shown in figure 4.22. This implies that the hydrodynamic fluctuation component of the signal is more affected by the changing area than the acoustic component. This improvement is amplified by the presence of the cover. For that case, a 10 dB improvement in SNR can be seen when reducing the cavity area by 575% compared to the cavity with no change in area. This is logical as the pressure spectra at the microphone decreases with decreasing area as seen in Fig. 4.19.

4.7 Summary

This study used design of experiments (DoE) methodology to systematically evaluate the effect of cavity geometry on the pressure spectra calculated from measurements made with a microphone mounted at the bottom of a cavity. The DoE approach supported the development of empirical models that quantify the effect individual geometric factors including depth, area, cover, and change in area have on the reduction in turbulent boundary layer spectral energy and increasing the signal-to-noise ratio (SNR) of an acoustic source. This approach provides a statistically rigorous framework for the experiment plan and follow on analysis while making efficient use of test resources.

A generalized additive model (GAM) quantified the effect of individual cavity geometric parameters and some of their mutual interactions have with respect to the two response variables. GAMs provide insight into the non-linear relationship between cavity geometries and the response variables over the frequency range of interest. This modeling approach is well suited for the boundary layer spectra and shows that the cover reduces the spectral energy by 10 dB when the linear and non-linear terms are combined. It also shows that energy decreases exponentially with increasing depth. Finally it quantified the relationship between the amount of reduction in cavity area and the presence of a cover. The GAM fit of the SNR data was complicated by the fact that error was introduced by estimating the response variable by subtracting the empty tunnel spectra. Despite this,

the model shows that a cover improves the SNR by up to 5 dB and that having a cavity area that reduces with depth, increases the SNR as well.

The experimental results and the explanatory stochastic model are initial steps in developing a framework for designing microphone cavities to enable improved aeroacoustic measurements. These data will be used to validate deterministic models that implement solutions to the wave equation within a cavity by imposing the constraints of the cavity geometry. Additionally these data will support the development of models that use finite element methods and a lattice Boltzmann computational fluid dynamics simulations to analyze future cavity designs that further reduce TBL noise while improving the SNR of acoustic measurements.

4

5

Simulating the Acoustic Response of Cavities

Cavities placed along wind tunnel walls can attenuate the turbulent boundary layer (TBL) fluctuations as they propagate into the cavity. Placing microphones within the cavities can thus improve the signal-to-noise ratio of acoustic data. However, standing waves form within these cavities, distorting the acoustic measurements. This work uses a finite element (FE) solver to evaluate how cavity geometry (depth, diameter, wall angle) and wall material (hard-walled and melamine foam) affect the amplitude and eigenfrequency of standing waves when excited by an incident acoustic plane wave. Good agreement between predicted and measured acoustic transfer functions is shown. Compared to cylindrical cavities, countersunk and conical cavities improve the overall response, i.e., reducing the quality factor, which quantifies the resonance and damping characteristics. Stainless steel coverings also reduce the quality factor. A finding of this chapter is that the shape of the external foam holder rather than the cavity shape drives the standing wave characteristics for the melamine foam cavities. The optimization problem of minimizing the acoustic response while also attenuating the TBL is thus decoupled by using the melamine foam. Consequently, these considerations can be addressed independently by optimizing the outer cavity shape for acoustics and the melamine foam insert for TBL attenuation.

5.1 Introduction

Acoustic array measurements on the wall of closed test section wind tunnels are affected by turbulent boundary layer (TBL) hydrodynamic pressure fluctuations. When their levels are higher than those of the signal of interest, the resulting low signal–to–noise ratio (SNR) hinders source identification and quantification. There are two complementary approaches to improve the SNR. The first is to use beamforming with an array of microphones [113]. The array intrinsically reduces the influence of incoherent TBL pressure fluctuations by using the microphones, integral to the array, to perform beamforming

which identifies coherent (over the microphones) acoustic sources. This reduces but does not eliminate the effect of the incoherent TBL pressure fluctuations. Applying beamforming post-processing techniques such as removing the diagonal of the cross-spectral matrix (CSM), using other imaging methods such as CLEAN-SC [148], or performing principal component analysis on the CSM [120] further reduces the TBL noise contribution. However, these techniques cannot detect sources more than 20 dB below that of the TBL noise level, depending on the microphone array configuration [56]. The second technique is to place the microphones within cavities embedded in wind tunnel walls. Cavities improve the SNR by attenuating the TBL hydrodynamic fluctuations at the microphone location [16, 57, 61]. The attenuation of TBL pressure fluctuations is dependent on several geometrical parameters. Specifically, the cavity depth [59, 61], diameter as discussed in Chapters 3 and 4, and presence of a countersink [59, 61] have been shown to influence the measured TBL spectra. Furthermore, covering the cavities with an acoustically transparent material such as Kevlar [16, 43] or a finely woven stainless steel cloth [59] has been shown to reduce the TBL spectra levels further by approximately 10 dB compared to the same cavity without a covering. Although there are a significant amount of studies focusing on the noise radiated from cavities [149–151], there are limited studies on the impact of cavity geometry on acoustic measurements made with microphones placed within the cavities. The cavity shape determines the frequencies at which standing waves occur and the amplitude of the resulting spectral peaks. In addition to amplifying the acoustic signal, cavities can distort the signal by attenuating it. This chapter describes a simulation framework for improving cavity designs for wind tunnel acoustic measurements.

The standing waves, also referred to as quarter–wavelength modes, and the resulting amplification occur when the incident acoustic wave and the wave reflecting off the cavity bottom constructively coincide, at a frequency near the cavity's quarter-wavelength mode harmonic frequency. The cavity geometry (depth, diameter, wall angle), boundary materials, and fluid properties determine these harmonic frequencies. Ideally, the cavities should have a negligible effect on the acoustic wave with thus minimal distortion of the acoustic measurements.

Figure 5.1 illustrates typical acoustic and hydrodynamic responses for a given cavity geometry. The change in sound pressure level (ΔL_p) between measurements taken at the bottom of the cavity and flush with the wall is used to derive this response. A typical covered cavity attenuates the TBL noise, illustrated by the dashed line, with increasing frequency, thus improving the overall SNR as described later in Chapter 7. However, the same cavity distorts the acoustic signal by introducing a standing wave centered at a specific frequency, as shown by the solid line. This standing wave amplifies the measured sound level, introducing errors into the acoustic measurements, and must be accounted for when processing data.

The focus of this chapter is on how the geometry of the cavity affects its acoustic response. Acoustic plane waves emanating from a far-field acoustic source and propagating into different cavity shapes were simulated using the multiphysics simulation software package COMSOL. The acoustic propagation is simulated without background flow and assumes linear acoustics with no thermoviscous acoustics effects present. The cavity radiation acoustics dominate the thermoviscous acoustics for larger aspect ratio cavities, such as those examined in this study. The latter thus do not contribute significantly to the over-
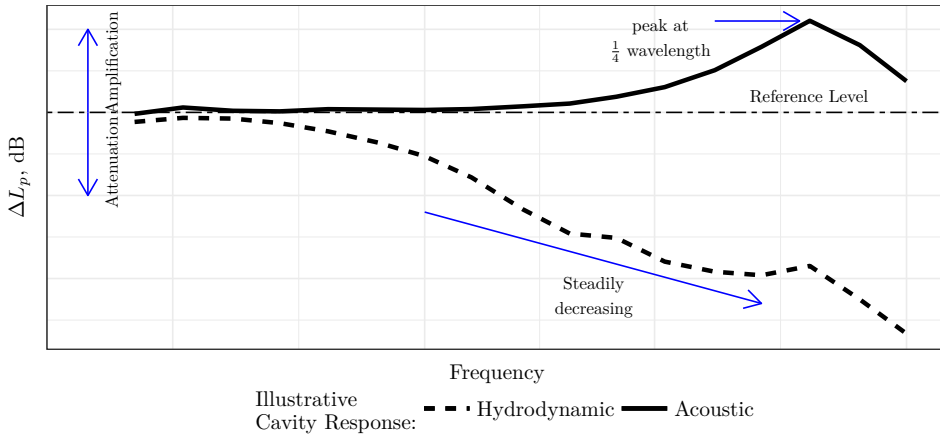
Figure 5.1: Example illustrating the effect a cavity has on the incident acoustic wave and the TBL pressure fluctuations.

all response. Since the effect of the cavity on the plane wave measurements should have minimum attenuation or amplification on the far-field signal of interest, it is important to identify how the acoustic transfer function between the incident plane wave and the acoustic response at the cavity bottom is affected by the cavity geometry. Three families of cavity shapes are studied to understand the effect of geometry on the response. First, this study investigates cylindrical cavities of different depths and diameters. The overall acoustic response of cylindrical cavities is, for example, also investigated in Ref. 152. Secondly, this work investigates the effect of different countersink angles on a cylinder of constant depth. Lastly, a conical cavity with varied wall angles is investigated. For all cavities, the aperture is simulated with and without a stainless steel cloth covering. The cavity walls were simulated as either perfectly reflecting or sound-absorbing using a porous model for melamine foam. A finding of this study is a suggested method of cavity design, where optimizing the balance between the acoustic and hydrodynamic response is no longer necessary. These responses can be addressed independently through the use of sound-absorbing melamine.

This chapter is structured as follows: Section 5.2, *Numerical Set-up*, describes the simulation assumptions, defines the geometric parameters, and evaluates the simulation convergence. Section 5.3, *Model Validation*, compares the simulated cavity results with experimental data as well discusses how the acoustic cavity response can be treated as independent of the TBL flow. Section 5.4, *Analysis of Results*, quantifies the effect of cavity depth, diameter, stainless steel cloth covering, wall angle, sound absorbing melamine material, and plane wave incident angle on the acoustic response. Section 5.5, *Conclusions*, summarizes the major findings of this chapter.

5.2 Numerical Set–up

The COMSOL multiphysics simulation software package is used to simulate the incident plane wave, its propagation into a cavity, and its subsequent reflection. The *Pressure Acous-*

tics Frequency Domain interface, which is part of the *Acoustics Module*, uses a finite element (FE) solver to solve the Helmholtz equation. In this work thermoviscous effects are neglected because the cavity diameters and acoustic wavelengths of interest are significantly larger than the thermal and viscous boundary layer thicknesses [153]. As a result, radiation acoustics are dominant for these large aspect ratio cavities.

Figure 5.2 defines the geometric parameters for the three families of cavities considered in this chapter. These shapes are representative of the cavities used in practice. Figure 5.2a is the straight-walled cylindrical cavity with depth D, and aperture radius a being equal to the bottom radius b. The radius, b, is 0.005 m based on the experimental work presented in Chapters 4 and 7 which used cavities of this size to study their effect on TBL attenuation. The ideal cavity diameter for TBL attenuation is application specific. The countersunk family of cavities is shown in 5.2b. For this cavity, b is the radius of the cavity bottom, and a is the aperture radius. Figure 5.2c shows the conical cavity, where b is the radius of the conical frustum, a is the aperture radius, x_0 is the distance from the frustum to the imaginary vertex. The conical cavities are truncated at the location of the microphone. The cavity depth, for all cavities, is defined by D, nominally 0.01 m. For the countersunk and conical cavities, the wall angle is defined by ψ with $\psi = 90°$ being the straight-walled cylinder case. The countersunk cavity features a straight wall from the bottom of the cavity to $z = 2L/3$.
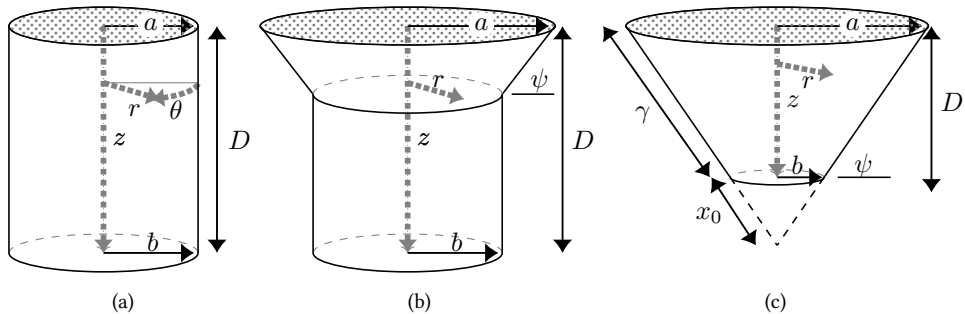

Figure 5.2: Generic cavity shapes considered in the experiment and FE studies: a) straight-walled cylindrical cavity; b) cylindrical cavity with countersink; c) conical cavity. Parameters r, z, and θ are the cylindrical coordinates; a is the aperture radius, b is the bottom radius, D is the cavity depth, ψ is the wall angle, and x_0 is the distance from the conical vertex to the frustum.

Cases Modeled

The cavity depth (D), bottom radius (b), covering, wall angle (ψ), and wall material were varied to study the relationship between cavity geometry and the quarter–wavelength mode characteristics. Table 5.1 lists the geometrical parameters that were studied. The radii and cavity depths for the countersunk and conical cavities were chosen to match the cavities used in the experiments discussed in Chapters 4 and 7. Additionally, the incident plane wave angle ϕ was varied between 0° and 90° for the cylindrical and conical cavities.

Table 5.1: Simulated cavity geometric parameters.

Cavity	Depth (D), mm	Radius (b), mm	Angle (ψ), °	Covered	Wall Material
Cylindrical	5, 10, 15 20, 30	5, 10	90	Yes, No	Hard Melamine
Countersunk	10	5	80, 70, 60, 45 30, 20, 10	Yes, No	Hard Melamine
Conical	10	5	80, 70, 60, 45 30, 20, 10	Yes, No	Hard Melamine

5.2.1 Model Set–up

Figure 5.3 illustrates the three-dimensional computational domain. A symmetric boundary condition divides the domain in half to reduce computational time. This plane is perpendicular to the acoustic wave front. A cylindrical perfectly matched layer (PML) simulates an open boundary by absorbing all outgoing wave energy. It imposes a complex-valued coordinate transformation in the domain so that the energy of the waves that enter the PML region decays rapidly [153]. The quarter-arc cylinder shape eliminates discontinuities at the boundary between the PML and the pressure acoustics domain. This shape ensures that the PML mesh elements remain isotropic to avoid spurious reflections. Periodic boundary conditions, defined using the Floquet periodicity condition, are placed on the left and right sides of the domain. This allows for non-normal ($\phi > 0$°) incident pressure waves to enter and leave the domain with no spurious reflections.

The incident plane wave is modeled as a background pressure field within the quarter cylinder region. The plane wave is defined by Eq. 5.1 where p_0 is the wave amplitude, $\mathbf{x}$ is the wave position vector, k the wavenumber, and $\mathbf{e_k}$ is the wave direction unit vector. For this simulation, the plane wave amplitude was held constant with respect to frequency at 1.0 Pa and the frequency was varied between 0.25 kHz and 10 kHz.

$$p = p_0 \exp\left[-ik\left(\frac{\mathbf{x} \cdot \mathbf{e_k}}{|\mathbf{e_k}|}\right)\right] \tag{5.1}$$

The top of the cavity is either open or defined by an interior impedance boundary condition. The latter accounts for the stainless steel covering. The measured normalized acoustic impedance, Z, of the stainless steel cloth is 0.15. The normalization is with respect to the characteristic acoustic impedance of air, z_0 which is defined as ρc^2. The cloth has 200 threads per cm^2 and is 0.05 mm thick. The Netherlands Aerospace Centre (NLR) measured the cloth impedance in their impedance tube for this research. The plane surrounding the cavity represents the wind tunnel wall and is a hard wall boundary condition.

The cavities are either modeled as shown in Fig. 5.2 or out of melamine as shown in Fig. 5.3. For the cases without melamine, the cavity walls are defined as perfectly reflecting hard walls. For the melamine foam cavities, the foam is a poroacoustics region with a radius of 2.25 cm and a depth of 4.5 cm with the cavity formed at the top. The Johnson-Champoux-Allard (JCA) semi-empirical poroacoustic model is used. Table 5.2 lists the porous matrix properties for Basotec TG melamine [154] used in this chapter.
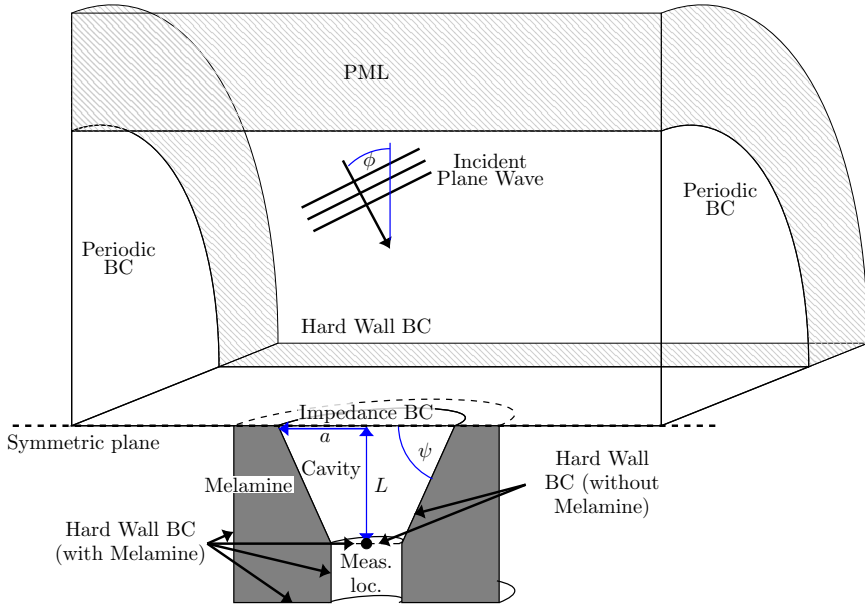
Figure 5.3: COMSOL computational domain set–up where ϕ is the countersunk and the conical cavity wall angle, D is the cavity depth, and r is the radius of the cavity with a value a at the top and b at the bottom. The light shaded region is the perfectly matched layer (PML).

The properties are as follows: ϵ_p is the material porosity, R_f is the flow resistivity, the viscous characteristic length is L_v, the thermal characteristic length is L_{th}, and τ_∞ is the tortuosity factor.

Table 5.2: Melamine porous matrix properties for the Johnson-Champoux-Allard semi-empirical model.

ϵ_p	R_f, $\mathrm{Pa\,s\,m^{-2}}$	L_v, m	L_{th}, m	τ_∞
0.993	9297.6	2.12×10^{-4}	4.35×10^{-4}	1.0133

Domain Mesh Convergence

The computational domain is meshed using a combination of tetrahedral elements and swept elements. The tetrahedral elements are used everywhere except for the PML. The PML uses isotropic swept elements to minimize spurious reflections. The simulation discretization used a quadratic lagrange basis function. The maximum mesh element size is $\lambda/8$ where λ is the wavelength of the highest frequency studied, 10 kHz. The resulting element size upper limit is 4.3×10^{-3} m. Figure 5.4a shows the acoustic response at the bottom of a cylindrical cavity for five different mesh sizes. As this figure shows, once the maximum mesh size approaches $\lambda/8$, the solution converges. Figure 5.4b shows the root mean square deviation (RMSD) of the cavity acoustic response. The RMSD is the difference between the solution for the finest mesh and the solution for the coarser meshes.

The vertical line is the RMSD for the $\lambda/8$ case (10 kHz acoustic wave). These figures show that choosing a maximum element size of $\lambda/8$ is sufficient for an accurate solution. A comparison between the coarse mesh and the mesh is shown in Fig. 5.5.
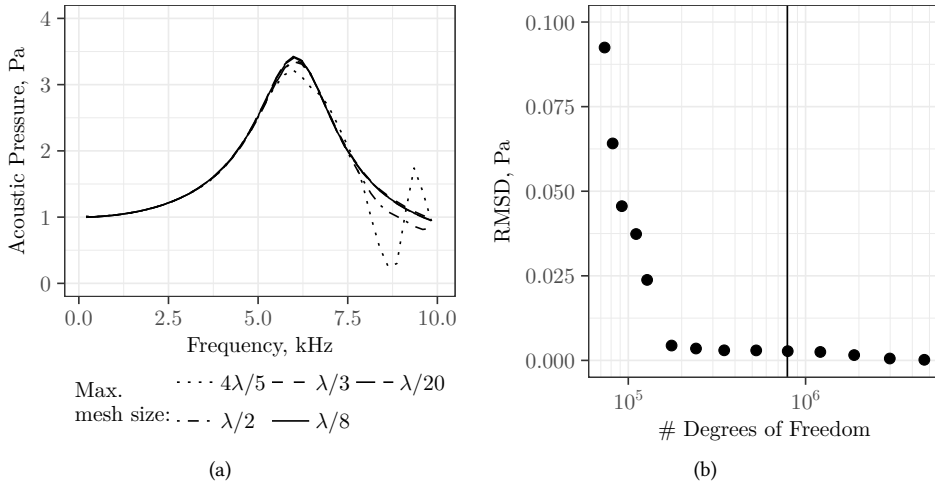

Figure 5.4: Mesh convergence on the: a) Acoustic pressure at the bottom of a cylindrical cavity with respect to the mesh element size upper limit, defined by the fractional size of the acoustic wavelength at 10 kHz. $\lambda/8$ (4.3×10^{-3} m) is the mesh size upper limit used in this chapter. b) Root mean square deviation (RMSD) between the pressure of different meshes and the solution for the finest mesh ($\frac{\lambda}{20}$). Plotted with respect to the number of degrees of freedom (DoF) in the simulation for a given mesh size. The vertical line is the $\lambda/8$ case.
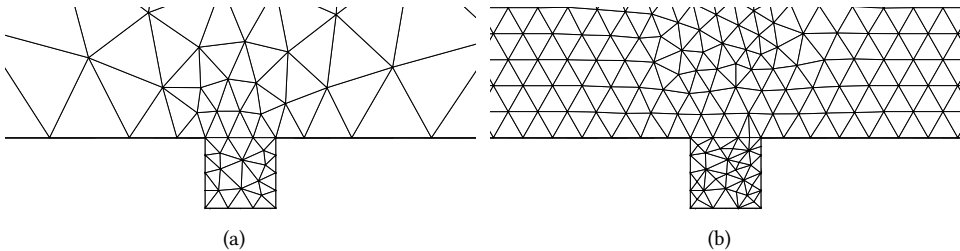

Figure 5.5: Computational domain meshes for two maximum mesh element sizes, zoomed into the cavity: a) Coarse mesh ($\frac{4\lambda}{5}$); b) fine mesh ($\frac{\lambda}{8}$).

5.3 Model Validation

5.3.1 Description of the Measurements

The experimental data used to validate this work originated from the experimental campaign described later in Chapter 7, which studied the effect of cavity geometry on beam-forming measurements. In that campaign, 16 cavities were installed in a 1.1 m $\times$ 0.4 m poly-carbonate plate covered with the 200 threads per cm^2 (#500) stainless steel cloth as described previously. The 16 cavities are interchangeable and installed in 5 cm diameter

holes. A flush-mounted microphone is placed in the center of the array. The three cavity shapes of Fig. 5.2 were tested with the stainless steel cloth covering. The cylindrical and countersunk cavities have poly-carbonate walls and the conical cavity is cut out of a melamine foam cylindrical insert.

Only measurement data from one cavity position is used to validate the work of this chapter, since the acoustic response was found to be independent of cavity location. The acoustic signal was generated by a Visaton K 50 SQ speaker, mounted at a distance 0.8 m normal to the flat plate containing the cavities. The speaker has a baffle diameter of 4.5 cm. The speaker emitted white noise with an overall sound pressure level ($L_{\mathrm{p,overall}}$), measured at the plate location without flow, of 64 dB.

G.R.A.S. 40PH analog free-field microphones were used. This microphone features an integrated constant current power (CCP) amplifier and a 135 dB dynamic range. Each microphone has a diameter of 7 mm and a length of 59.1 mm. All the microphones were calibrated individually using a G.R.A.S. 42AA pistonphone following the guidelines of Ref. 35. The transducers have a flat frequency response within ± 1 dB from 50 Hz to 5 kHz and within ± 2 dB from 5 kHz to 20 kHz. The data acquisition system consists of a *National Instruments* (NI) PXIe-4499 sound and vibration module with 24–bit resolution. The board is controlled by a NI RMC-8354 computer via a NI PXIe-8370 board. The sampling frequency of the recordings was 51.2 kHz. The signal was sampled for a duration of 45 s. The spectra are calculated using Welch's method with 1024 samples with a 50% overlap using Hanning windowing with a resulting frequency resolution of 50 Hz.
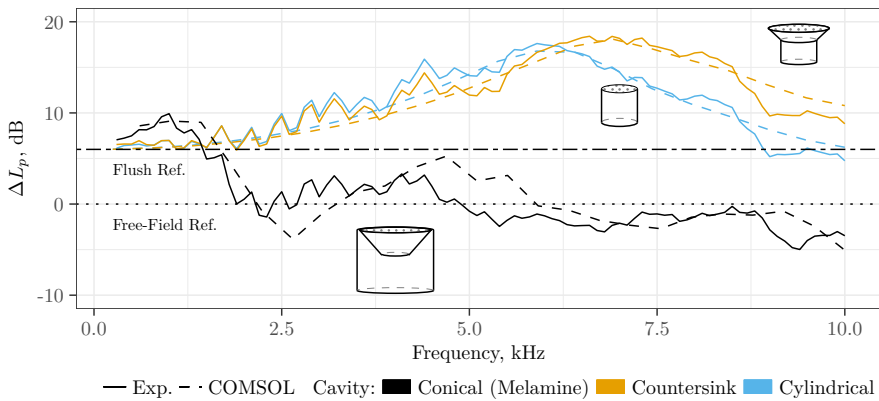
5

Figure 5.6: The simulated and experimental acoustic transfer functions between the cavity bottom and flush measurements are shown for three cavities. The cavities are two hard-walled cavities (countersunk and cylindrical) and a conical cavity made of melamine foam. ΔL_p is the deviation from the free-field, $\Delta L_p = 0$ corresponds to the expected free-field spectra level.

5.3.2 Comparing Acoustic Simulations and Measurements

The acoustic transfer function is defined as the difference between the decibel scale spectra of the flush and cavity bottom microphone measurements. This is equivalent to dividing the cavity spectra by the flush spectra at each frequency before converting to a decibel

scale. The spectral responses are calculated using Welch's method. 6 dB is added to the transfer functions to account for the difference between the free-field and flush measurements since flush measurements feature a doubling of the pressure due to the reflection off of the flat plate. Two hard-walled cavities (cylindrical and countersunk) and one conical cavity formed out of melamine foam were simulated and compared with experimental data. Figure 5.6 shows the SPL deviation, ΔL_p, from the expected free-field measurement for these cavities. The simulations (dashed lines) agree closely with the experimental data (solid lines). The hard-walled cylindrical and countersunk cavities match the predicted standing wave amplitude as well as the frequency of their respective peaks: 6.3 kHz for the straight-walled case and 7.0 kHz for the countersunk case. The fluctuations in the experimental data below 5.0 kHz are hypothesized to be due to the flush reference microphone being offset slightly from the cavity in the experimental measurements as well as reflections from the wind tunnel exit nozzle. Figure 5.6 also shows that the JCA porous prediction is close to the measured response of the melamine cavity. The melamine conical cavity simulation data matches the trends in the experimental data with at most a 4 dB difference in predicted amplitude near 5 kHz due to a frequency shift between the model and experiment. This difference could be reduced with the application of a different porous model. These results give confidence that the simulation results, analysis, and conclusions presented in this chapter are accurate.

5.3.3 Independence of Acoustic and Hydrodynamic Response

This work assumes that the acoustic response of the cavities is not influenced by the presence of a TBL. This assumption of independence is based on insight discussed in Chapter 7, in which an acoustic source was measured with a turbulent boundary layer present over the microphone array. Figure 5.7a shows the spectra of the measurements for either the acoustic source or the TBL being present. Figure 5.7b shows the summation of these spectra (dotted line), and also the measurements obtained with the two sources (TBL and acoustic) being present simultaneously (long-short dashed line). A close agreement per cavity geometry between the lines in Fig. 5.7b is observed. A maximum deviation of 3 dB is seen between 1 and 3 kHz in Fig. 5.7b. This close agreement between the two suggests that the acoustic signal at the microphone can be considered to be independent of the flow over the cavities for the frequency range of interest (0.25 kHz to 10.0 kHz). This assumption is key to applying this acoustic analysis to cavities used in a closed test section wind tunnel with flow present.
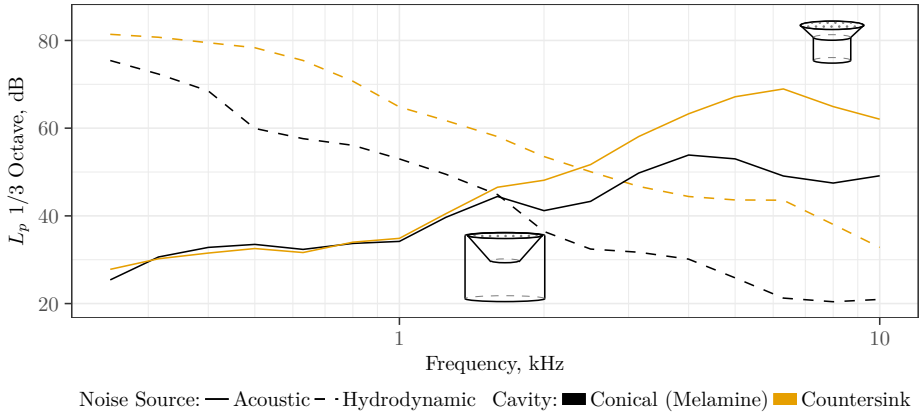
(a)
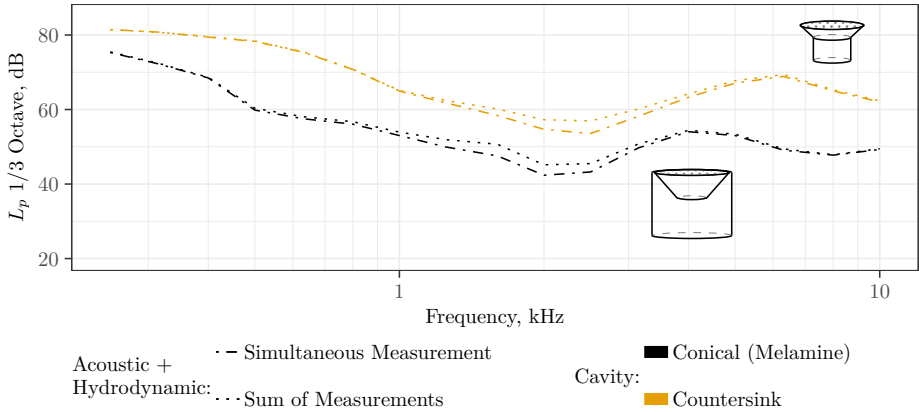
(b)

Figure 5.7: a) Independent cavity microphone measurements with only an acoustic source and with only the TBL ($U_\infty = 20\,\mathrm{m\,s^{-1}}$) present over two cavities. b) Comparison of the measurement of the acoustic source with the TBL present and the sum of the independent measurements.

5.4 Analysis of Results

The goal of this study is to quantify how cavity shape, the presence of a stainless steel cloth, and wall material affect acoustic measurements at the cavity bottom. The geometric characteristics and the boundary conditions, e.g., fluid properties, determine the amplitude and frequency of the quarter–wavelength cavity modes. The cavity depth, diameter, covering, countersink angle, conical wall angle, and wall material were varied to find the relationship between geometry and the quarter-wavelength mode frequencies, f_n, and amplification, quantified by the quality factor Q, which is defined in Section 2.1. Q was calculated by performing an eigenfrequency analysis for each simulation. The fluid properties and other boundary conditions are held constant for this analysis.

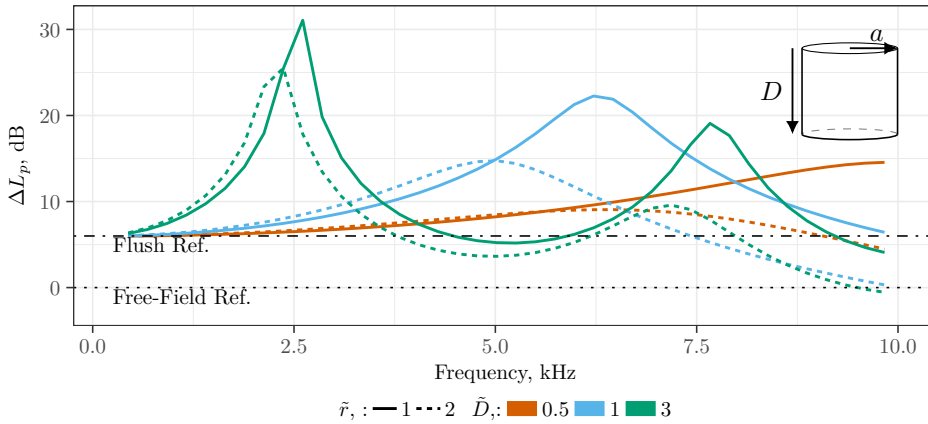## 5.4.1 Effect of Cavity Depth and Diameter

Figure 5.8: Simulated ΔL_p values with respect to the free-field for different normalized cylindrical cavity depths ($\tilde{D} = D/0.01$ m) and radii ($\tilde{r} = a/0.005$ m). The solid lines represent the responses for $a = 0.005$ m. The dashed lines represent the responses for $a = 0.01$ m. The horizontal dash-dotted and dotted lines represent the flush and free-field responses, respectively. The cavities feature hard walls with no stainless steel cloth covering.

The response of cylindrical cavities to an incident plane wave was simulated for several cavity depths and diameters. Figures 5.8 and 5.9a show the resulting acoustic response (ΔL_p) with respect to the free-field levels and the simulated flush microphone reference levels. The latter measurements are approximately 6 dB higher than the free-field due to the doubling of the incident pressure wave amplitude at the wall.

The cylindrical cavity depths range from 0.005 m to 0.03 m and their radii vary from 0.005 m and 0.01 m. The incident plane wave frequencies are between 0.25 kHz and 10 kHz. ΔL_p is plotted with respect to both frequency in Fig. 5.8 and the non-dimensional Helmholtz number (He) in Fig. 5.9a. Figure 5.8 shows how with decreasing cavity depth, D, the peak frequency increases. Also with decreasing diameter for the same depth, the peak frequency increases. Figure 5.9a shows that when normalizing by He, the peaks collapse to the same value of He. The Helmholtz number is defined as follows: He $= \frac{D_{\text{eff}}\omega}{c}$ where ω is the angular frequency, and c the speed of sound. D_{eff} is the cavity depth plus a correction term for the cavity diameter which is discussed later in this section.

The peaks in Fig. 5.9a are from an acoustic mode within the cavity. While longitudinal, radial, and azimuthal [130] modes can be present, it is the longitudinal mode that appears in Fig. 5.9a. The longitudinal mode is also referred to as a depth mode, and is the quarter–wavelength mode [130] as mentioned in the previous sections. These modes form standing waves in the longitudinal direction of the cavity. Standing waves occur when an acoustic wave reflects at a change in impedance, e.g., a duct opening or cavity bottom, and the resulting reflection constructively interferes with another incident wave. This results in peaks [155] at odd-numbered harmonics.

To understand why these peaks are only due to the longitudinal modes, it is useful to evaluate the cavity in terms of the pressure field for a circular duct. Applying the principles
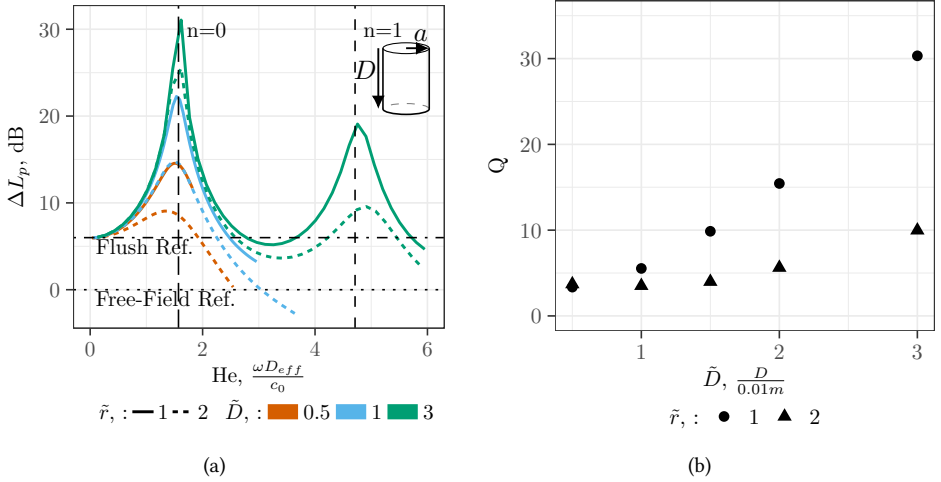
Figure 5.9:   a) Simulated ΔL_{p} values with respect to the free-field for different normalized cylindrical cavity depths ($\tilde{D}$) and radii ($\tilde{r}$). The dimensions are normalized with respect to $D = 0.01$ m and r =0.005 m. The cavities feature hard walls with no stainless steel cloth covering. The horizontal dash-dotted and dotted lines represent the flush and free-field responses, respectively. b) The effect of cavity depth and diameter on the quality factor (Q).

of duct acoustics [63] shows this to be the case, as discussed in Chapter 3. At the cavity aperture, the incidence pressure wave must match the pressure field at the aperture of the cavity. This pressure field at the cavity aperture can be decomposed into radial and azimuthal mode shapes. These modes propagate in the longitudinal direction into the cavity. However, for the cavity diameters (≈ 0.01 m) and frequencies (≤ 10 kHz) in this study, the higher-order radial and azimuthal modes, referred to by their mode numbers $m > 0$ and $\mu > 1$ do not propagate as they are cut-off. Equation 5.2, where a is the cavity aperture radius and $\alpha_{m\mu}$ is the radial wavenumber, defines this cut-off condition.

$$\frac{\omega a}{c} > \alpha_{m\mu} \tag{5.2}$$

As an example, assuming a cavity diameter of 0.01 m and using the first Bessel derivative root whose value is $\alpha_{m=1,\mu=1} = 1.8412$, Eq. 5.2 states that the first non-planar mode will only propagate for frequencies above 20.1 kHz. Further details can be found in the description of a previously developed analytical model introduced in Chapter 3. The resulting planar mode propagates in the longitudinal direction. The reflection of this wave off of the cavity bottom interferes constructively with the incident wave at the harmonic frequency, resulting in a peak. Since the quarter–wavelength mode is the dominant mode, this analysis will focus on how the cavity geometry affects this mode's harmonic frequency and amplification.

   For straight-walled cavities, Eq. 5.3 predicts the harmonic frequency, f_n, where n is the mode number and D_{eff} is the effective cavity depth. The effective depth, D_{eff}, is the depth of the cavity, D, with a depth correction term, δ, applied. This correction term accounts

for the radiation impedance of the open end [64]. The radiation impedance is dependent on the cavity diameter, covering, frequency, and whether or not it is flanged or unflanged.

$$f_n = \frac{(2n+1)c}{4D_{\text{eff}}} \tag{5.3}$$

For a cavity in a wall, the wall is treated as an infinite flange. The depth correction, δ, for an infinitely flanged opening is defined in Eq. 5.4 [64]. Where k is the wavenumber and a is the cavity aperture radius, see Fig. 5.2a. For the cavities of interest, δ ranges between $0.597a$ and $0.707a$.

$$\delta = 0.8216a \left[1 + \frac{(0.77ka)^2}{1+0.77ka} \right]^{-1} \tag{5.4}$$

Figure 5.8 shows that increasing the cavity diameter, while holding depth constant, reduces the harmonic frequency. This shift increases for larger aspect ratio (a/D) cavities because δ increases D_{eff}. According to Eq. 5.3 and Eq. 5.4 the standing wave peak locations collapse to $He = \pi/2$ for the fundamental mode (see Fig. 5.9a). The vertical dashed lines in Fig. 5.9a are the fundamental mode ($n = 0$) and the first harmonic ($n = 1$) predictions made with Eq. 5.3. Applying this equation shows that the cavities with highest values of f_n are the shallowest with the smallest diameter, e.g., $\tilde{D} = \frac{D}{0.01m} = 0.5$ and $\tilde{r} = \frac{a}{0.005m} = 1$, as shown in Fig. 5.8. The deeper the cavity, the lower values of f_n, e.g., $\tilde{D} = 3$. The amplitudes also depend on cavity depth and diameter. The deeper the cavity, the higher the amplitude of the standing wave while the larger the aspect ratio, the lower the amplification.

The effect of cavity geometry on the amplification is quantified by the quality factor, Q, shown in Fig. 5.9b. Q is defined as the ratio between the real and imaginary components of the eigenfrequency, ζ, of the standing wave; $Q = \text{Re}(\zeta)/\text{Im}(\zeta)$. The quality factor is also calculated by $Q = f_n/(f_u - f_l)$ where f_u and f_l are the upper and lower frequencies at the 1/2 power location, defined as 3 dB below the peak harmonic, see Fig. 2.1. Thus, Q describes the amplitude and width of the standing wave spectral peak. The higher the value of Q, the greater the amplification, which is undesirable. Figure 5.9b shows that Q increases both with increasing cavity depth and with decreasing diameter. This effect is more pronounced when the depth is significantly larger than the diameter. For example, the $\tilde{D} = 3$ case Q drops from 30 to 10 when the diameter is doubled while at $\tilde{D} = 1$ the reduction drops by approximately 2, from 5 to 3. This trend does not hold for shallow cavities. Cavities with the same aspect ratio have similar harmonic amplification. This is seen for the cavities where $\tilde{D} = 1$, $\tilde{r} = 2$ and $\tilde{D} = 0.5$, $\tilde{r} = 1$ in Fig. 5.9a. Figure 5.9b also shows that Q is close for these two cavities as well as for the cavities with $\tilde{D} = 2$, $\tilde{r} = 2$ and $\tilde{D} = 1$, $\tilde{r} = 1$.

These results show that a deep cylindrical cavity is undesirable for acoustic measurements due to the high Q and due to the presence of multiple harmonics. Shorter and wider cavities are more desirable as the standing wave amplitudes are minimized and shifted to higher frequencies. Ideally, the harmonic frequencies of the standing waves would be higher than the upper range of the frequency of interest (10 kHz), however, this is not feasible for the cavity geometries that attenuate the TBL noise contribution. For example, applying Eq. 5.3, a 1.0 cm diameter cavity, would have to have a depth of 0.52 cm, which would limit its effectiveness in reducing the TBL noise contribution compared to a deeper

cavity. The optimal cavity depth for improving acoustic measurements by reducing the TBL noise at the microphone is application dependent.

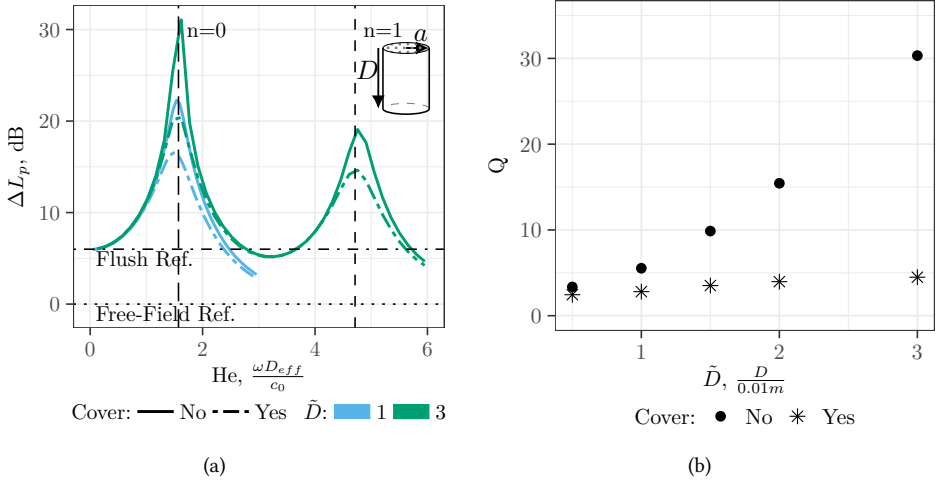## 5.4.2 Effect of Stainless Steel Cloth Covering

Figure 5.10: a) Simulated effect of stainless steel cloth on ΔL_p values with respect to the free-field for selected normalized cylindrical cavity depths $\tilde{D} = D/0.01$ m and $\tilde{r} = a/0.005$ m = 1. The cavities are cylindrical with hard walls. The horizontal dash-dotted and dotted lines represent the flush and free-field responses, respectively. b) The effect of the stainless steel cloth on the quality factor, Q, for cylindrical cavities of different depths.

Placing a stainless steel or Kevlar cloth on top of the cavity reduces the TBL fluctuations at the microphone [16, 43], however one area of concern is its effect on the acoustic signal. Simulations were run for the straight-walled cavities with an impedance boundary condition at the top of the cavity, as discussed previously in the *Model Set-up* subsection. Figure 5.10a shows the effect of this impedance on the peak locations and amplitudes for the same cavities. The cloth reduces the location of the peak from a He of 1.55 to 1.50 for $\tilde{D} = 1$ and from 1.57 to 1.55 for $\tilde{D} = 3$ ($\Delta f = 0.2$ kHz). The effect of the cloth on the location of the peak is small due to its normalized acoustic impedance of 0.15 being smaller than the radiation impedance of an infinitely flanged cylindrical cavity. The radiation impedance of the cavity opening can be estimated using the reflection coefficient R_{refl}, Eq. 5.5, in the expression for normalized radiation impedance Z_r Eq. 5.6 [156], where $Z_c = 1/\pi a^2$ is the impedance of the cavity.

$$R(\omega) = -\frac{1 - 0.182ika}{1 - 1.825ika + 0.649(ika)^2} \tag{5.5}$$

$$Z_r = Z_c \frac{1 + R_{\text{refl}}}{1 - R_{\text{refl}}} \tag{5.6}$$

For the case of the cylindrical cavity where $\tilde{D} = 1$ and $\tilde{r} = 1$, the estimated normalized radiation impedance (Z_r) is 1948.

The stainless steel cloth's effect on Q is greater than its effect on the frequency of f_n. Figure 5.10b shows that the stainless steel cloth reduces Q for the same cavities. The deeper the cavity, the larger the reduction in Q, for example for the $\tilde{D} = 3$ case, Q drops from 30.3 to 4.5. while for the $\tilde{D} = 1$ case, the effect is less dramatic with Q decreasing from 5.5 to 2.8. The transmission loss through the cloth is calculated to be approximately 1 dB. From these simulations, it is apparent that a low impedance covering, such as the fine stainless steel mesh, improves the acoustic response of the cavity by reducing the amplitude of the quarter–wavelength modes with minimal transmission loss.

Section 5.4.1 showed that larger aspect ratio cavities (larger diameters and shorter depths) are more desirable, i.e., they have lower values of Q than low aspect ratio cavities. However, a stainless steel cloth covering allows for the cavity depth to be increased, reducing the TBL noise, while minimizing the amplification due to the quarter–wavelength mode.
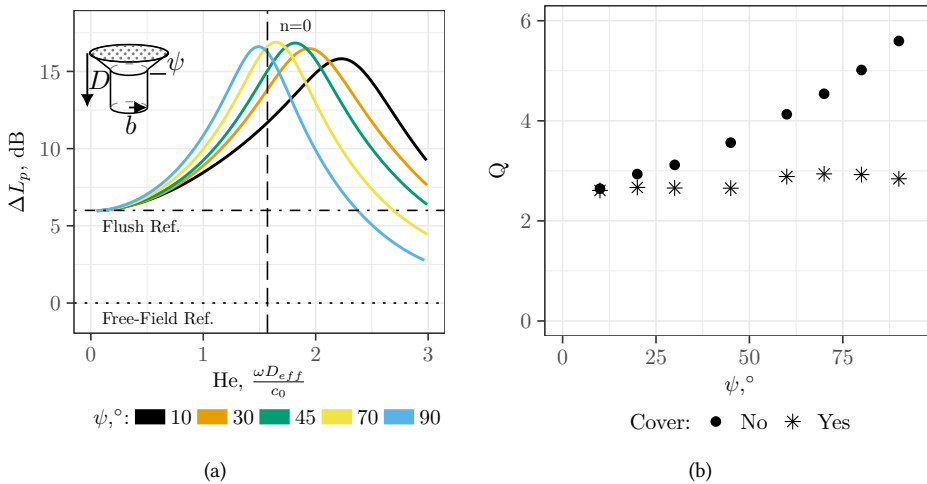
5.4.3 Effect of Wall Angle

Figure 5.11: a) Simulated ΔL_{p} for different countersink angles (ψ) with respect to the free-field and flush cases. Cavities have a normalized depth $\tilde{D} = D/0.01$ m $= 1$ and $\tilde{r} = b/0.005$ m $= 1$, the countersink depth is $\tilde{D}/3$. All cavities have a stainless steel cloth covering. b) Quality factor for different countersink angles (ψ) with and without a stainless steel cloth.

Figure 5.11a shows the effect of different countersink wall angles on the acoustic response of a cavity covered with a stainless steel cloth. The angle, ψ, was varied from a shallow angle, $\psi = 10°$ to the straight-walled case, $\psi = 90°$, in $10°$ increments. Additionally, a $45°$ countersunk cavity was simulated to match experimental data. The depth of the cavities, D, was held constant and is the same as the $\tilde{D} = 1$ cases simulated previously. The response for different values of ψ is plotted versus the Helmholtz number. δ is calculated using the aperture radius a shown in Fig. 5.2b and Eq. 5.4. For the steeper angles, $\psi \geq 70°$, the harmonic frequency agrees with the predictions using Eq. 5.3, shown by the vertical

dashed line. As the angle decreases, the values of f_n increase compared to the straight–walled cavity. The effect of ψ on the harmonic peak, quantified by Q is shown in Fig. 5.11b. As ψ decreases, Q decreases. This dependence is more significant for the cases without a stainless steel cloth. Without this covering, Q decreases from 5.6 for the straight–walled case to 2.6 for $\psi = 10°$. With the cloth, the amplitude of the standing wave is damped and Q decreases from 2.9 to 2.6 with decreasing ψ.
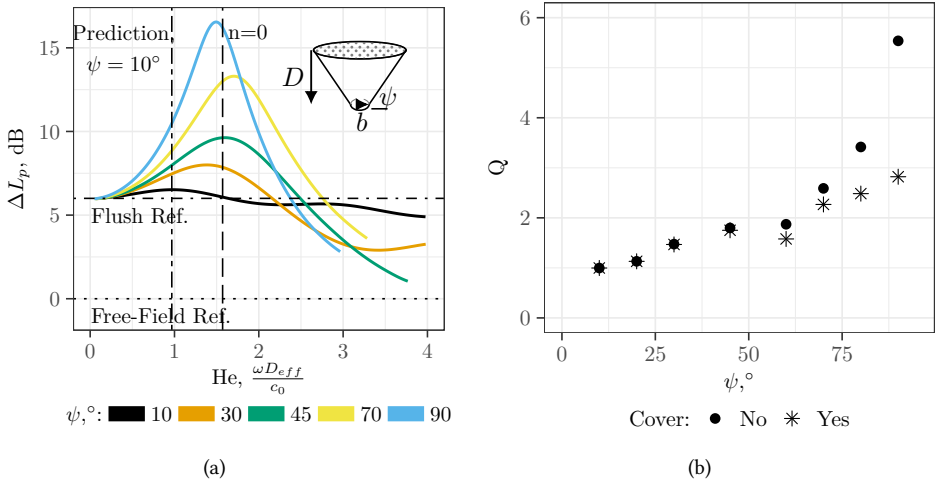
5

Figure 5.12: a) Simulated ΔL_p for different conical angles with a stainless steel cloth covering (ψ) with respect to the free-field and flush cases. Cavities have a normalized depth $\tilde{D} = D/0.01\ \mathrm{m} = 1$ and $\tilde{r} = b/0.005\ \mathrm{m} = 1$. Also shown is the analytical prediction for the harmonic frequency for $\psi = 10°$. b) Quality factor for different conical angles (ψ) with and without a stainless steel cloth.

The acoustic responses of conical cavities with the stainless steel cloth covering, are shown in Fig. 5.12a. These cavities were simulated at the same wall angles, depth, and radius at the frustum (b) as the countersunk cavities. The Helmholtz number was calculated using $D_\mathrm{eff} = D + \delta$ with δ being calculated in the same manner as the countersunk cases. Decreasing ψ decreases the harmonic amplitude, even with the stainless steel cloth covering in contrast to the countersunk cases. The harmonic frequency increases slightly with respect to the straight-walled case for $\psi \geq 70°$. For shallower angles, f_n can be estimated by solving the transcendental equation, Eq. 5.7. Here k is the wavenumber, x_0 is the distance between the bottom frustum and the conical vertex, and γ is the length of the cavity sidewall, i.e., the distance between the vertex and the aperture [65], see Fig. 5.2c. The resulting harmonic frequencies do not occur at integer values of the fundamental frequency but are spaced at slightly monotonically increasing intervals, depending on x_0.

$$\tan(k\gamma) = -kx_0 \tag{5.7}$$

The predictions made with Eq. 5.7 agree with the simulation for $\psi < 45°$. As an example, the prediction for $\psi = 10°$ is shown in Fig. 5.12a. For steeper angles, f_n is over predicted.

This is presumably due to the lack of a correction term for the infinite flange at the opening for conical waveguides [65].

Figure 5.12b shows that decreasing ψ has a greater effect on Q than for the countersunk cavities. From $\psi = 90°$ to $\psi = 10°$, Q drops from 5.5 to 1.0 for the case without the cloth covering. With the covering, Q drops from 2.8 to 1.0. Below $\psi = 50°$, the stainless steel cloth has minimal effect on the harmonic response of the cavity.

The ideal cavity should have the fundamental standing wave harmonic frequency higher than the highest frequency of interest. Barring that, its response should be as flat as possible. From these simulations, it is clear that cavities with angled sides perform better by having a lower harmonic amplitude than the equivalent straight-walled cylindrical cavity. Conical cavities feature a flatter response than countersunk cavities. For conical cavities with shallow angles, $\psi \leq 10°$, the cavity response approaches that of the flush wall. However, at these angles, the cavity is less effective at attenuating the TBL because the TBL will stay attached to the cavity walls and the response will be similar to that of the flush case. However, the limiting value of ψ depends on the TBL properties and will be application-dependent. Having a low wall angle limits the depth of the cavity because the beamforming array limits the cavity aperture size. This limit is due to the microphone spacing requirements. Therefore conical cavities should have wall angles between $10°$ and $45°$.

5.4.4 Effect of Melamine Walls

Cavities formed out of melamine foam attenuate TBL noise more than hard–walled cavities, as was observed in the work described in Chapter 7. Therefore, this study evaluates the effect of this sound absorbing material on the standing wave amplitudes and harmonic frequencies within cavities. The JCA porous acoustic model was used to simulate the melamine foam. The model parameters are listed in Table 5.2. All cavities considered in this section share the same outer construction with only the inner cavity (made out of melamine) shape changing. An example of this can be seen in Fig. 5.3 where the exterior of the cavities is a cylinder and the interior a cone. The normalized depth of this cylinder is $\tilde{D} = 4.3$ and its normalized radius is $\tilde{r} = 4.5$. The outer surface is modeled as a hard–walled boundary condition. The top of the cavity is simulated with the stainless steel cloth covering. Three inner melamine cavities were studied: two cylindrical cavities and a conical cavity. The cylindrical ones have normalized depths of $\tilde{D} = 1$ and $\tilde{D} = 3$ with a normalized radius of $\tilde{r} = 1$. The conical one has a wall angle $\psi = 30°$ and a depth of $\tilde{D} = 1.2$. As a baseline comparison, a solid block of foam was also considered, in other words, without any interior cavities present.

Figure 5.13a shows the acoustic responses measured at the bottom of the two cylindrical cavities and the conical cavity. As a comparison, the measurement from the top of the solid cylindrical foam block is included. Compared to the hard wall cavities, Figs. 5.9a - 5.12a, the melamine reduces the amplitude of the standing waves harmonic amplitudes and no strong peaks are present. When comparing the conical cavity and the cylindrical cavity, which have similar depths ($\tilde{D} = 1.2$ and $\tilde{D} = 1$), it is apparent that the cavity shape has minimal influence on the acoustic spectral response. In order to determine if the acoustic response is primarily influenced by the measurement location along the z-axis and not the cavity shape, the response measured at different locations along the z-axis within the
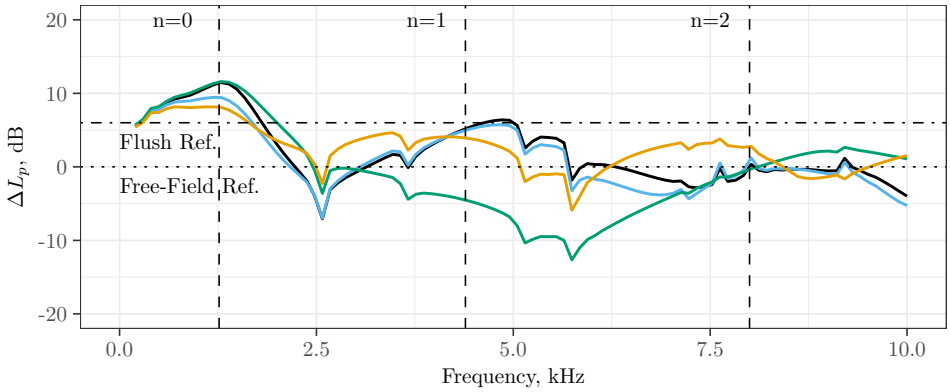
(a)
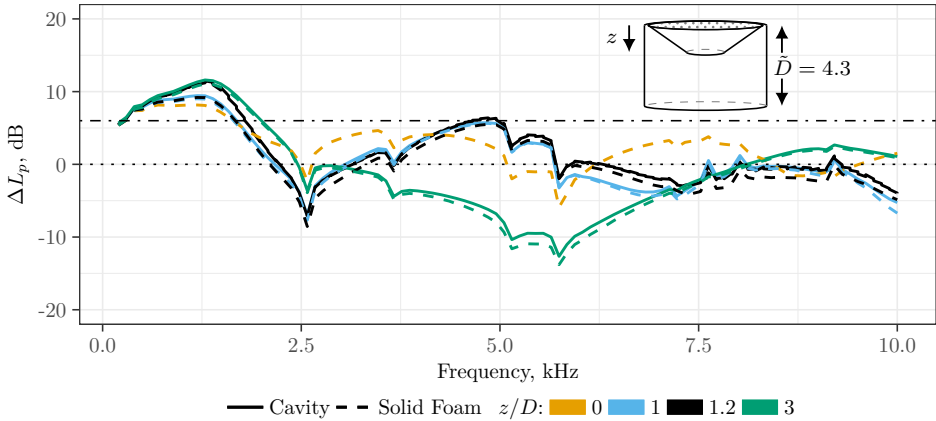
(b)

Figure 5.13: a) Simulated acoustic response (ΔL_p) of cavities made of melamine foam: Conical ($\psi = 30°$, $\tilde{D} = 1.2$); Cylindrical ($\tilde{D} = 1$ and $\tilde{D} = 3$, $\tilde{r} = 1$); Cylindrical foam insert ($\tilde{D} = 4.3$ and $\tilde{r} = 4.5$) b) ΔL_p at different depths (z) within the foam insert, represented by the dashed lines compared to cavities of equivalent depth, represented by the solid lines.

solid foam block is shown with dashed lines in 5.13b. The locations chosen correspond to the depths of the three cavities ($z = \tilde{D}$), which are shown with solid lines. It is clear that the responses, ΔL_p, are similar which suggests that the interior cavity shape has minimal influence on the acoustic response. Instead, the measurement location within the cylindrical foam block drives the response. In other words, the acoustic response within the foam is driven by the shape of the outer cylindrical cavity, $\tilde{D} = 4.3$, $\tilde{r} = 4.5$, formed by the hard backing walls surrounding the foam insert and not the cavity cut out of the foam. Applying Eq. 5.3 to the outer shape of the melamine foam and substituting the speed of sound in the porous medium for the speed of sound in air, gives reasonable agreement
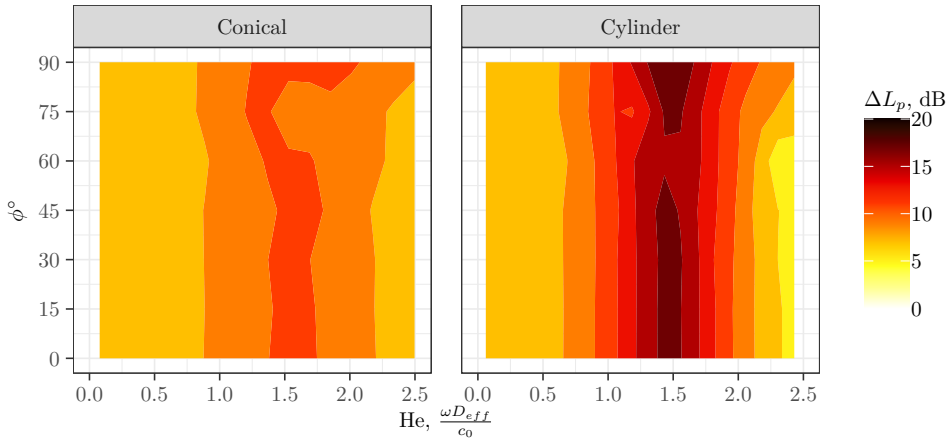
Figure 5.14: Simulated acoustic response for conical cavity with $\psi = 45°$ and the straight walled cavity for incidence angles (ϕ) from 0° to 90°. The cavities feature hard walls with no stainless steel cloth covering.

5

with the simulation results, shown by the vertical dashed lines in Fig. 5.13a. The speed of sound in the melamine JCA porous model is calculated as follows: $c = \sqrt{\kappa(\omega)/\rho_{\text{rig}}(\omega)}$ [133], where κ is the equivalent bulk modulus and ρ_{rig} is the equivalent rigid density which are determined from the material properties in Table 5.2.

The shape and material of the foam insert can be optimized to minimize the standing wave amplifications using the guidelines for depth and wall angle previously discussed. The cavity shape cut into the foam can thus be optimized independently to minimize the turbulent boundary layer pressure fluctuations at the microphone. Figure 5.7a, as an example, shows that a conical shape in the melamine reduces the hydrodynamic TBL noise significantly while Fig. 5.6 shows the impact on the acoustic signal is minimal. Therefore the problems of optimizing the cavities for minimizing the distortion of acoustic measurements and optimizing the cavities to maximize the attenuation of the TBL noise can potentially be decoupled.

5.4.5 Effect of Incidence Angle

The microphone arrays used for beamforming can be several meters in diameter. Therefore the incidence angle, ϕ, of the acoustic waves varies across the array. Only the cavities aligned with the acoustic source of interest have an incident wave angle close to 90°. To evaluate the dependence of the cavity acoustic response on the incident angle, the incidence angle was varied from 0° to 90°. A conical cavity ($\psi = 45°$) and a straight-walled cylindrical cavity, both with depths of $\tilde{D} = 1$ were simulated. The resulting acoustic response (ΔL_p) is shown in Fig. 5.14. As this figure shows, the straight-walled cavity has a minimal change in its response for the range of ϕ. The conical cavity shows a small amount of variation of approximately 3 dB at ϕ around 75°. The standing waves excitation can thus be treated as independent of the incident far-field wave angle.

5.5 Summary

This chapter quantifies the effect of different cavity shapes and materials on the acoustic response at the bottom of a cavity. Furthermore, the work presented here shows that conical cavities with wall angles less than 45° reduce the amplitude of the acoustic standing waves and that forming the cavities out of melamine foam allows for the cavity acoustic response to be decoupled from the hydrodynamic response. The COMSOL multiphysics software package was used to simulate the acoustic response of cylindrical, countersunk, and conical cavities. Cavity depth, diameter, and wall angles were systematically varied. This chapter also quantifies the influence of a stainless steel cloth covering. The cavities were simulated as both hard-walled and with melamine foam walls. The results of the simulation matched the experimental measurements for the hard-walled cavities. The JCA poroacoustic model, used to model the melamine foam, agreed with the experimental trends but additional studies are necessary to rectify the frequency shift observed.

The longitudinal quarter–wavelength modes are the dominant acoustic phenomena present in the cavity. To minimize distortion of the acoustic signals, the frequency of the quarter–wavelength modes should be as high as possible with the amplitude as low as possible. For cylindrical cavities this frequency decreases with increasing cavity depth. Increasing the cavity diameter reduces the amplitude of these standing waves while slightly decreasing their harmonic frequency. Cavities with the same depth to diameter ratio have similar quality factors, Q, which quantifies the amount of amplification. Adding a stainless steel cloth covering reduces the harmonic frequency by approximately $2 - 5\%$ while reducing the amplification significantly. For the conical and countersunk cavities, changing the countersink angle and wall angle further reduced the standing wave amplitude. The response was found to be independent of the incident plane wave angle. Forming the cavities out of a melamine foam insert showed that the acoustic response of the cavity is driven by the shape of its hard-walled outer construction, with the interior cavity shape having minimal influence. This finding is important because instead of designing one cavity to attenuate the turbulent boundary layer (TBL) pressure fluctuations while also minimizing the strength of the standing waves, these constraints can be optimized separately.

Specifically, a conical outer shape with a low acoustic impedance covering can minimize the influence of standing waves. The conical shape reduces the amplitude of standing waves compared to an equivalent cylindrical cavity, while the covering further reduces the strength of these waves. The inner foam cavity can thus be designed to maximize the attenuation of the TBL. The work presented here supports optimizing cavity shapes for wind tunnel acoustic measurements as well as understanding the acoustic performance of existing ones.

6

Simulating Turbulent Flow Over Cavities with the Lattice Boltzmann Method

Microphone measurements in a closed test section wind tunnel are affected by turbulent boundary layer (TBL) pressure fluctuations. These fluctuations are mitigated by placing the microphones at the bottom of cavities, usually covered with a thin, acoustically transparent material. Prior experiments showed that the cavity geometry affects the propagation of TBL pressure fluctuations toward the bottom. However, the relationship between the cavity geometry and the flowfield within the cavity is not well understood. Therefore a very large–eddy simulation was performed using the Lattice–Boltzmann method. A cylindrical, a countersunk and a conical cavity are simulated with and without a fine wire-cloth cover, which is modeled as a porous medium governed by Darcy's law. Adding a countersink to an uncovered cylindrical cavity is found to mitigate the transport of turbulent structures across the bottom by shifting the recirculation pattern away from the cavity bottom. Covering the cavities nearly eliminates this source of hydrodynamic pressure fluctuations. The eddies within the boundary layer, which convect over the cover, generate a primarily acoustic pressure field inside the cavities and thus suggesting that the pressure fluctuations within covered cavities can be modeled acoustically. As the cavity diameter increases compared to the eddies' integral length scale, the amount of energy in the cut–off modes increases with respect to the cut–on modes. Since cut–off modes decay as they propagate into the cavity, more attenuation is seen. The results are in agreement with experimental evidence.

6.1 Introduction

The signal–to–noise ratio (SNR) of flush-mounted microphone array measurements in closed test section wind tunnels is reduced by the presence of a turbulent boundary layer

---

(TBL) over the tunnel walls. The amount of SNR reduction by the TBL pressure fluctuations can be minimized, relative to a microphone mounted flush to the tunnel wall, by placing microphones within cavities. Research on flow over cavities has focused primarily on radiated noise from the interaction of the shear layer over rectangular cavities. The research presented in this article focuses on how the pressure fluctuations at the bottom of axisymmetric cavities, resulting from turbulent flow, are affected by cavity geometry.

Pressure fluctuations within cavities are produced by several mechanisms, which include the Rossiter feedback loop, turbulence within the shear layer, and the transport and production of turbulence due to recirculation within the cavity. The Rossiter feedback loop [82, 85, 87] is a self–sustaining noise generation mechanism produced by Kelvin–Helmholtz type vortices [157] shed from the cavity upstream edge. When the vortices impinge on the downstream wall, pressure waves are produced [83, 158] that perturb the shear layer, which further produces vortex shedding. The feedback loop is characteristic of cavities exposed to a boundary layer with relatively large momentum thickness, with respect to the cavity aperture [159]. For rectangular cavities, these vortices extend along the spanwise length of the cavity [160] and their impingement produces tonal peaks in the far-field noise spectra. Axisymmetric cavities exhibit similar behavior [98], however the vortices shed by cylindrical cavities are affected by the curved cavity edge [161]. Specifically, the vortex spanwise length is smaller than the cavity diameter and they are shed from multiple spanwise locations along the upstream edge [162]. This results in a weaker and broader spectral peak compared to rectangular cavities [87].

In addition to the shed vortices, the shear layer contains randomly fluctuating turbulence, which produces pressure fluctuations that propagate into the cavity, referred to as turbulent rumble [163]. The strength of these fluctuations increases from the leading edge towards the downstream edge as shown by PIV measurements [162]. The shape of the upstream edge influences the stability of the shear layer because non–sharp edges can cause the location of the separation point to vary in time [139], which affects the amplitude of the turbulent rumble [164].

Recirculation of the fluid due to the flow entering the cavities results in the presence of turbulent pressure fluctuations at the cavity bottom [97]. For deep cylindrical cavities, the recirculating flow is symmetric with respect to the cavity center line [101]. The recirculation patterns within these deep cavities are stable, in contrast to shallower cavities, which feature unsteady and asymmetric recirculation patterns [103, 165]. The recirculating flow causes strong wall shear, which generates fluctuations as high as $\approx 35\%$ of the local velocity [97]. These velocity fluctuations are highest between the downstream bottom corner and the cavity center, along the cavity center line [98, 165]. This region of increased turbulence corresponds to a region of higher static pressure [165].

These phenomena can excite acoustic cavity modes that radiate acoustic noise into the far-field. For example, the Rossiter mode produces strong acoustic tones if they are locked on with an acoustic cavity mode [63, 86, 95]. Acoustic depth modes are also excited by the turbulent rumble as well as the acoustic energy produced by the shed vortices [158]. For the deep cavities, defined as $L/D \leq 1$, acoustic depth modes are the most significant [92, 93].

A previous study [61] characterized how axisymmetric cavities with different diameters, depths, countersink depths, coverings, and wall angles affect the pressure fluctua-

tions, produced by the TBL, at a microphone placed at the bottom. Cavities with angled walls, e.g., cavities with a countersink, reduce the TBL noise more than cylindrical cavities [61]. Additionally, covering the cavity with Kevlar [16] or finely woven stainless steel cloth [61] reduces the amplitude of pressure fluctuations at the microphone location by 10 - 20 dB [16]. This reduction is assumed to be caused by the cover preventing flow into the cavity, reducing the hydrodynamic source of pressure fluctuations. Previous experiments, conducted as part of this project [135, 166], have measured the effect that cylindrical cavities, with and without a countersink, and conical cavities, as illustrated in Fig. 6.1, have on the attenuation of pressure fluctuations due to the TBL. When these three cavities are uncovered, the countersunk cavity attenuates the TBL pressure fluctuations the most, followed by the cylindrical one. The conical cavity performs the worst as the pressure spectra at the bottom are higher than the spectra measured by a flush-mounted microphone. Covering the cavities alters this trend: the conical cavity attenuates the pressure spectra at the bottom more than the countersunk and cylindrical cavities. However, better insight into the relationship between the mechanisms that produce pressure fluctuations and cavity geometry is needed to further optimize the geometry. Currently, there is a lack of literature describing the physical mechanisms that affect the amplitude of pressure fluctuations at the bottom of axisymmetric microphone cavities, especially for covered cavities.

The objective of this work is to understand the effect of aperture size, different countersink depth ratios, i.e., the ratio between the cavity depth and the countersink depth, wall angles, and the presence of a covering have on the recirculation within the cavities, vortex shedding, and turbulence generation, which contribute to the pressure fluctuations at the cavity bottoms. Given the size and geometry of the cavities, non–intrusive velocity–field measurements to identify and study the flow phenomena within the cavity are challenging. Hence, a very–large eddy simulation (VLES) was performed using a Lattice–Boltzmann method (LBM) solver, SIMULIA PowerFLOW. This article is organized as follows: Section 6.2 describes the cavity geometries and the PowerFLOW simulation parameters, the validation measurements, and the post-processing used in this analysis. Section 6.3 discusses the simulation verification and validation. Section 6.4 analyzes the flowfield and pressure field in the time–averaged, instantaneous, and wavenumber domains. Section 6.5 evaluates the porous covering's effect on the flowfield in the time–averaged, frequency, and wavenumber domains. Additionally, the effect of geometry on the propagation of the pressure fluctuations is analyzed. Finally Section 6.6 summarizes the major findings of this article.

6.2 Methodology

6.2.1 Computational Set-up

Geometry

The following axisymmetric cavity geometries are studied: a cylindrical cavity with and without a countersink, and a conical cavity. These three cavities and their geometric parameters are shown in Fig. 6.1. These cavity geometries were chosen because they are representative of the cavities commonly used in wind tunnel experiments [135, 166]. Each cavity is investigated with and without a stainless steel cloth cover. The following cavity geometric parameters are defined in Table 6.1: aperture size (L), depth (D), countersink

depth ratio (d_c/D), ratio of aperture size to BL momentum thickness (L/Θ), and wall angle (ψ). For the cylindrical cavity, the aperture diameter is $L = 2.5\Theta$, where Θ is the momentum thickness of the incoming boundary layer (described in Sec. 6.3.2). The relatively small L/Θ is expected to avoid the cavity wake mode described in Ref. 159. For an array of microphone cavities, the cavity wake mode would likely cause the downstream cavities to experience a highly turbulent incoming flow.

Table 6.1: Cavity geometric parameters.

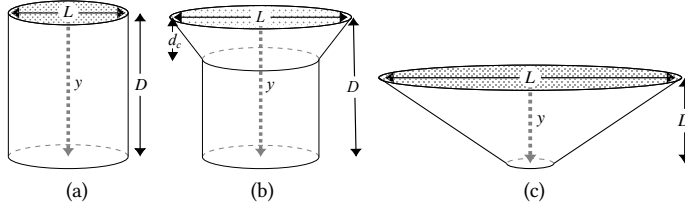| Cavity	L, cm	D, cm	d_c/D	L/Θ	ψ
Cylindrical	1.0	1.0	0.0	2.5	90°
Countersunk	1.6	1.0	0.3	4.1	45°
Conical	4.5	1.23	1.0	11.4	30°

Figure 6.1: Simulated cavity geometries: a) Cylindrical, b) Countersunk, and c) Conical

Solver Set–up

The simulations are performed with the commercial software SIMULIA PowerFLOW 6-2019, which is based on the Lattice–Boltzmann method, coupled with a VLES approach. The LBM is based on kinetic models which take into account mesoscopic processes in order to obtain reliable continuum flow quantities, in agreement with the macroscopic dynamics of a fluid. PowerFLOW solves the LBM equation on a lattice, i.e., a Cartesian grid. The lattice consists of cubic cells, referred to as voxels, with 19 degrees of freedom. The LBM-VLES solver considers a discrete form of the lattice-Boltzmann equation, which can be written as [167]:

$$F_i\left(\boldsymbol{x} + V_i \Delta t, t + \Delta t\right) - F_i(\boldsymbol{x},t) = C_i(\boldsymbol{x},t) \tag{6.1}$$

where $\boldsymbol{x}$ and t are the space and time coordinates. F_i is the particle distribution function along the ith lattice direction, and V_i is the discrete particle velocity in the same direction. The collision operator, C_i, is based on the Bhatnagar–-Gross-–Krook kinetic model [168], and is defined as:

$$C_i = -\frac{\Delta t}{\tau}\left[F_i(\boldsymbol{x},t) - F_i^{eq}(\boldsymbol{x},t)\right], \tag{6.2}$$

where $F_i^{eq}(\boldsymbol{x},t)$ is the equilibrium distribution function, estimated from statistical physics considerations [169]. τ is the viscosity–dependent, collision relaxation time [169].

In a LBM-VLES approach, the small scales of turbulence are accounted for by correcting the relaxation time used in the calculation of the collision term. The correction applied to the relaxation time is based on the $k - \epsilon$ turbulence model [167]. The solver can realistically represent boundary layer profiles at large Reynolds number without resolving the flow in the viscous sub-layer of the boundary layer by using a pressure gradient dependent wall model [169].

Porous Model

The covered cavities are covered with a finely woven stainless steel cloth, which has a wire diameter of 2.6×10^{-3} cm and a density of 200 wires per cm^2. This cloth was used in prior cavity experiments described in Chapter 7 and in this work is modeled as a porous medium, as proposed in Ref. 170. This model uses the experimentally measured viscous and inertial resistivities, R_v and R_i, of the cloth, as described in Section 6.2.2, to impose Darcy's law in the porous medium. Literature [167] suggests this simulation approach is capable of predicting the influence of a porous region on a grazing turbulent boundary layer. This provides confidence that the porous model can be used to simulate the current unsteady problem. Darcy's law relates the pressure drop across the porous medium, Δp, to the Darcy's velocity, ν_d, according to [167]:

$$\frac{\Delta p}{t} = R_v \nu_d + \rho R_i \nu_d^2, \tag{6.3}$$

where t is the thickness of the porous medium and ρ is the density of air. In order to have sufficient cells inside the porous region, so that the solver can simulate the relationship between flow velocity and pressure gradient, the thickness of the porous medium in the simulation is approximately three times larger than the thickness of the physical stainless steel cloth (exact dimensions in Table A.1). To account for this, the resistivity values R_v and R_i were multiplied by the ratio between the thickness of the measured sample and the thickness of the porous medium in the simulation. A permeability tube simulation (with the numerical setup described in Ref. 171) to confirm that the porous medium with increased thickness, and corrected R_v and R_i, matches the experimental $\Delta p / t$.

Domain and Operating Conditions

The computational domain for the circular and countersunk cavities is shown in Fig. 6.2. The bottom of the domain is a flat plate with a no-slip condition at the wall. The cavity, which also contains no-slip walls, is placed at the origin of the domain, i.e., at the center with respect to the length of the streamwise and spanwise domain lengths. This center is located 150 cm (150 $L_{\text{Cylindrical}}$) downstream of the inlet. At the inlet, a turbulent boundary layer mean velocity profile, based on experimental measurements from Chapter 7, is imposed ($\delta_{99} = 1.4$ cm at the inlet). A zigzag trip is placed downstream of the inlet, introducing coherent vortices in the boundary layer. The (no-slip) zigzag trip is 0.16 cm high and has 0.427 cm length, 0.427 cm pitch and 90° of top angle (dimensions as defined in Ref. 172). The boundary layer downstream of the zigzag trip is turbulent. The free-stream velocity, U_∞, is set at 32 m s^{-1}, which is within the U_∞ range of interest for closed wind tunnel wind turbine airfoil aeroacoustic testing [173]. As shown in Fig. 6.2, the sides of the domain have a periodic boundary condition (BC). The span of the domain was
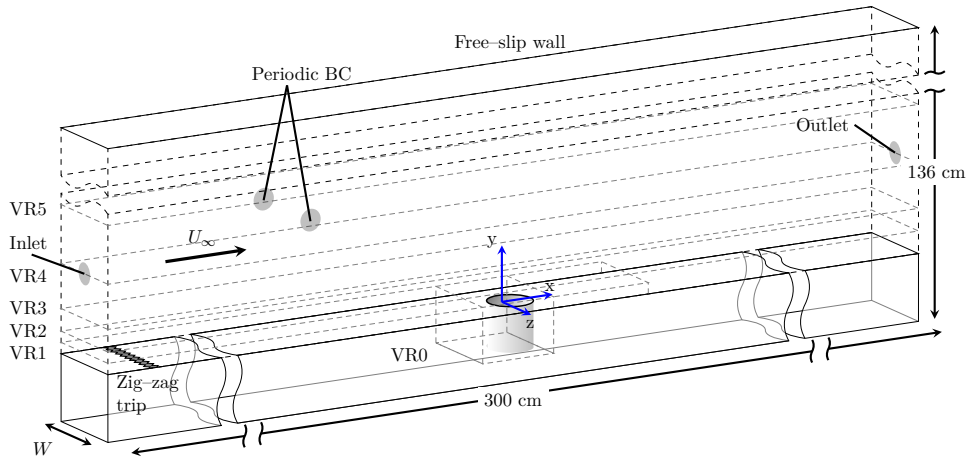
Figure 6.2: Representation of the computational domain

chosen to minimize the influence of the boundaries on the cavity flowfield. For the cylindrical and countersunk cavities, a value of $3.2L_{\mathrm{Countersunk}}$ was selected. The distance from the cavity to the boundaries is larger than the spanwise coherence length of the pressure fluctuations in the boundary layer, which is typically on the order of the boundary layer displacement thickness [80]. The span of the domain for the conical cavity simulations is increased to $2.6L_{\mathrm{Conical}}$ because of the larger cavity aperture diameter. The top of the domain is bounded by a free-slip wall and is located 136 cm above the bottom wall (flat-plate). The outlet of the domain imposes an ambient static pressure (sea level pressure). Figure 6.2 shows a representation of the variable resolution (VR) regions in the computational domain. The VR regions specify the amount of lattice refinement, where VR0 is the finest and VR5 the coarsest, for the uncovered cavities. The VR regions are similar for the covered cavity simulations, which have an additional finer resolution region around the location of the cloth cover.

6.2.2 Experimental Set-up

Cavity Pressure Measurements

The experimental data used for validation were measured in the TU Delft A–Tunnel using the same procedure as described in Chapter 7. This tunnel is a vertical open jet wind tunnel located within an anechoic chamber [174]. The cavities in Fig. 6.1 were made of poly–carbonate and mounted on a plate flush with the exit nozzle. The cavities were placed 76 cm downstream of the tunnel nozzle exit. Two plates with dimensions of 110 cm × 40 cm were used. One was uncovered and the other was covered with a 200 threads per cm^2 (#500) stainless steel cloth. A flush-mounted microphone was placed 3.2 cm downstream with a spanwise offset of 4.5 cm. The three cavities were tested in each plate. The tunnel flow speed was $32\,\mathrm{m\,s^{-1}}$ at the cavity's location.

Sonion 8010T omni-directional MEMS microphones were used to measure the pressure fluctuations. This microphone has an outer diameter of 2.5 mm and a transducer diameter

Table 6.2: Experimentally measured stainless steel cloth permeability characteristics with 95% confidence intervals.

K, m^{-2}	C, m^{-1}	R_v, s^{-1}
$3.0 \times 10^{-11} \pm 1.0 \times 10^{-14}$	$3.1 \times 10^4 \pm 1.6 \times 10^5$	$5.0 \times 10^5 \pm 1.7 \times 10^2$

of 0.05 mm. The microphones were center mounted on a 7 mm diameter holder in order to fit securely within the cavities. All the microphones were calibrated individually using a *G.R.A.S. 42AG* pistonphone following the guidelines of Mueller [35]. The microphones have a flat frequency response within ± 1 dB from 100 Hz to 10 kHz. The data acquisition system consists of a *National Instruments* (NI) *NI9215* analog input module mounted in the NI *cDAQ-9178 CompactDAQ* with 16–bit resolution. The sampling frequency of the measurements was 51.2 kHz and the data were recorded for 45 s.

Stainless Steel Cloth Permeability Measurements
A 7.5×10^{-3} cm thick stainless steel cloth sample were installed in a permeability tube to determine the viscous and inertial resistance of the cloth. The pressure drop, Δp, across the sample as well as the volumetric flow, $\dot{V}$, through the sample were measured. The Darcy velocity, v_d, is calculated as follows: $v_d = \dot{V}/A$, where A is the cross–sectional area of the tube. The measured Δp and v_d are fit to the Hazen-Dupuit-Darcy equation,

$$\frac{\Delta p}{t_c} = \frac{\mu}{K} v_d + \rho C v_d{}^2, \tag{6.4}$$

using a least squares fit method [31, 32] to determine the permeability, $K = \frac{\mu}{R_v}$, and the form drag coefficient, $C = R_i$. t_c is the thickness of the cloth sample, μ is the viscosity of air. Further details on the permeability tube can be found in [31] and [32]

The cloth sample was mounted between two 9.0 cm × 9.0 cm polycarbonate plates each with 5.1 cm diameter holes at the center. Epoxy was applied to one polycarbonate plate and the cloth was then stretched across the plate so that the material was tensioned across the opening. Pressure taps within the tube are located 5 cm upstream and downstream of the sample [31]. The static pressure was measured with a Mensor 2101 differential pressure sensor, which has a range of 1.2–15 kPa and an accuracy of 2 Pa. The volumetric flow rate was controlled using an Aventics pressure regulator and measured by a TSI4040 volumetric flowmeter. The Darcy's velocity flow range in the tube is between 0 and 2.5 m s^{-1}, and the permeability tube has a cross–sectional area of 2.04×10^{-3} m^2. The flowmeter has an accuracy of 2% [31, 32]. The pressure drop was measured at 22 discrete velocities ranging from 0 to 2.2 m s^{-1}. The resulting permeability K, the form drag coefficient C, inertial resistance, and viscous resistance are provided in Table 6.2.

6.2.3 Post-Processing Methods
Spectral Analysis
The power spectral density (PSD) of the pressure field at a given point within the cavity, P_{xx}, was calculated using the Welch's method, as described in Chapter 2. A Hanning window was used with 50% overlap when computing the spectra. For all cavities, with

Table 6.3: Wavenumber—Frequency spectrum calculation parameters for each cavity, normalized by $L_{cyl} = 1.0$ cm.

	Cylinder	Countersunk	Conical
		Uncovered	
Sample Rate, kHz	15.32	15.32	367.6
# Time steps	4307	4307	14705
N_{fft}	512	512	2048
Δf, Hz	29.9	29.9	179.4
Δx, cm	1.5×10^{-2}	1.5×10^{-2}	1.5×10^{-2}
Top Sampling Location, y/D	0.0	0.0	0.0
Top Sample Length, cm	1.0	1.6	4.5
Bot. Sampling Location, y/D	-1.0	-1.0	-1.0
Bot. Sampling Length, cm	1.0	1.0	0.7
		Covered	
Sample Rate, kHz	183.8	183.8	367.6
# Time steps	7353	7353	14705
N_{fft}	2048	2048	2048
Δf, Hz	89.7	89.7	179.4
Δx, cm	1.5×10^{-2}	1.5×10^{-2}	1.5×10^{-2}
Top Sampling Location, y/D	-1.5×10^{-2}	-1.5×10^{-2}	-2.4×10^{-2}
Top Sample Length, cm	1.0	1.6	4.5
Bot. Sampling Location, y/D	-1.0	-1.0	-1.0
Bot. Sampling Length, cm	1.0	1.0	0.7

6

and without a covering, a window size of 512 samples was used. The PSD was converted to a decibel scale with a reference pressure of 2×10^{-5} Pa.

Wavenumber Analysis

A wavenumber-frequency spectral analysis was performed to decouple the acoustic and hydrodynamic contribution to pressure fluctuations within the cavity. The acoustic region contains the pressure fluctuations that propagate at the speed of sound. The acoustic wavenumbers, k_0, associated with this region are between $-f/c_0$ and f/c_0. The hydrodynamic region is defined by wavenumbers outside of the acoustic region. However, at low frequencies, the hydrodynamic wavenumbers are difficult to decouple from the acoustic wavenumber. Therefore, a limiting frequency is defined, below which the distinction between acoustic and hydrodynamic spectra is uncertain. This frequency is defined as [123] $f \leq U_\infty/\Delta k$, where Δk is the wavenumber resolution.

The wavenumber spectra were calculated using a 2-D Fourier transform applied to the pressure fluctuations sampled along the cavity center line, aligned with the freestream direction. A Hanning window with 50% overlap was applied in the time domain using the approach described in Ref. 123 and in Chapter 2. The data were sampled with a spacing of $\Delta x = 1.5 \times 10^{-2}$ cm at the top and bottom of each cavity in the streamwise direction. For the covered cavities, the pressure was sampled just below the interface between the porous region and the cavity volume. The sampling rates, number of time steps, Hanning window size (N_{fft}), and sampling locations are defined in Table 6.3.

Proper Orthogonal Decomposition

Proper orthogonal decomposition (POD) was used to decompose the pressure fluctuations into a linear combination of orthogonal modes to identify coherent structures [124, 175]. The POD method is described in greater detail in Chapter 2. The resulting modes are defined in terms of their spatial structures, ϕ, and temporal bases, ψ, [124]. Subsequently, the original data can be reconstructed with the summation of these inner products.

The tool *MODULO* [176] was used to perform this decomposition. The pressure fluctuations were sampled from the PowerFLOW simulation output with an equal spacing of Δx = Δz = 2.5×10^{-2} cm. *MODULO* requires a Cartesian grid of equally sampled points, thus a square grid was used. As the cavity cross-sections are circular, the data for the region outside of the cavities are padded with zeros. The sample rate and sampling location with respect to cavity depth (y) are the same as described in Table 6.3. The resulting modes are defined in terms of their spatial structures, ϕ, and temporal bases, ψ, [124]. The estimated energy, i.e., the amplitude, of each mode, σ_r is weighted by $\sqrt{N_s N}$, where N_s are the number of sampled spatial points and N are number of time samples [124].

6.3 Grid Convergence and Data Validation

6.3.1 Grid and Data Validation

The effect of grid resolution on the flat plate's boundary layer profile and the pressure spectrum inside the cylindrical cavity (covered and uncovered) were evaluated using five grid refinement levels. For the uncovered simulations, these levels are specified in Table 6.4. The smallest voxels are located inside the uncovered cavities. The minimum size of the voxels above the flat plate, upstream of the cavity, is twice the minimum voxel size inside the cavity. Table 6.4 lists as well the non-dimensional wall distance, y^+, from the center of the smallest voxels to the flat plate wall. The non-dimensional wall distance is defined as:

$$y^+ = \frac{y u^\star}{\nu},\tag{6.5}$$

where y is the vertical coordinate, $u^\star$ is the friction velocity, and ν is the kinematic viscosity. The value of $u^\star$ is measured $3L_{\text{Cylindrical}}$ upstream of the cavity center. Table 6.4 shows the relative cell size between grids, h_i/h_1, where h_1 is the smallest voxel size of the finest grid tested, and h_i is the smallest voxel size of grid i. The timestep in the LBM simulation is set to maintain a Courant-Friedrichs-Lewy (CFL) number of 1, considering the sound speed, and is therefore dependent on voxel size. For the different grids, the timestep at VR0 is shown in Table 6.4.

The convergence of the boundary layer velocity profile, 3.0 cm upstream of the cavities, is analyzed with respect to the displacement thickness, $\delta^\star$, and the boundary layer momentum thickness, Θ. The grid dependence of $\delta^\star$ and Θ is shown in Fig. 6.3a. Figure 6.3b shows the convergence of the pressure fluctuations at the bottom center of the cylindrical cavity (covered and uncovered), for the one–third-octave band centered at 6.3 kHz since this band contains the acoustic depth mode for the cylindrical cavity. Furthermore, this band is associated with smaller eddies (at higher frequencies), which are therefore expected to be more sensitive to the cell size.

Table 6.4: Grid sizes used in the convergence study (uncovered cylindrical cavity).

Grid i	Min. voxel size, m excl. cavity	Min. y^+ excl. cavity	h_i/h_1	Timestep, μs at VR0
Very Coarse	4.00×10^{-4}	15	3	0.34
Coarse	2.67×10^{-4}	10	2	0.23
Medium	2.00×10^{-4}	8	1.5	0.17
Fine	1.60×10^{-4}	6	1.2	0.14
Very Fine	1.33×10^{-4}	5	1	0.11

The fits shown in Fig. 6.3 are defined by:

$$f(h_i) = \phi_0 + \alpha h_i^o, \tag{6.6}$$

where α is a constant, o is the order of convergence, ϕ_i is the parameter, e.g., $\delta^\star$, obtained from the simulation with grid i, and ϕ_0 is the estimated exact solution, i.e., the solution for a grid with infinite resolution. The order of convergence is 3 [167]. ϕ_0 and α are calculated with the least squares regression described in Ref. 177. Figure 6.3a indicates that the grids with a medium, fine, and very fine resolution (see Table 6.4) result in approximately equal values of $\delta^\star$ and Θ. Figure 6.3b also shows that the medium grid ($h_i/h_1 = 1.5$) results in a Φ_{pp}, at the bottom of the cavity, close to the estimated exact solution, i.e., the value at $h_i/h_1 = 0$ for the 6.3 kHz one–third-octave band.

Based on the previous results, the fine resolution is chosen for the cylindrical and countersunk cavities (covered and uncovered). The conical cavity simulations use the medium grid resolution, because it has a larger outer diameter, which increases the computational costs, particularly for the simulation with the cloth cover.

6.3.2 Comparison with Experiments

Figure 6.4 shows the experimental and simulated streamwise velocity, u, and turbulence intensity (TI) profiles of the boundary layer, measured upstream of the cavity location. The profiles from the simulation are measured 3 cm upstream of the cylindrical cavity center and the profiles for the experimentally measured profiles were sampled 10 cm upstream of the cylindrical cavity. The turbulence intensity is defined as:

$$TI = u'/U_\infty, \tag{6.7}$$

where u' is the root mean square (RMS) of the streamwise velocity fluctuations in the boundary layer. The profiles are normalized with the free–stream velocity, U_∞. Figure 6.4a indicates that the simulated TBL has a slightly higher velocity deficit than the experimental TBL. The boundary layer thickness is 3.3 cm in the simulation and 3.7 cm in the experiment. This leads to a negligible difference in momentum thickness between the experiment and the simulation (below 3%). The ratio Θ/L has been identified as a dominant driving parameter for cavity flow [159, 178], and the simulation and experiment have equivalent ratios. The momentum thickness–based Reynolds number is therefore also identical in the experiment and the simulation: $Re_\Theta = 8.6 \times 10^3$. The shape factor of $\delta^\star/\Theta = 1.3$ is indicative of a fully developed simulated turbulent boundary layer [179].
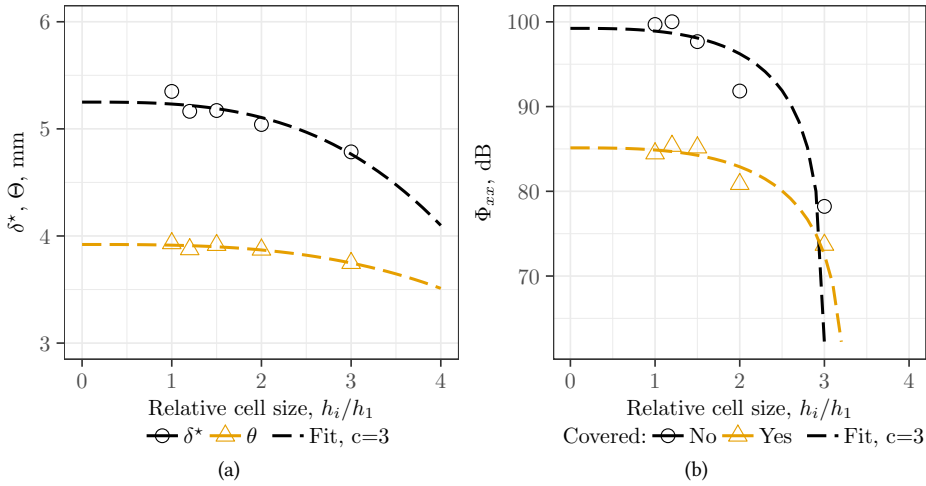
Figure 6.3: Grid convergence study comparing the following variables: a) BL displacement and momentum thicknesses, $\delta^\star$ and Θ, and b) pressure fluctuations (in the 6.3 kHz one–third–octave–band) at the bottom of the cylindrical cavity.

Figure 6.4b shows that, for $y^+ > 100$, the boundary layer TI levels in the simulation are close to those from the experiment. $y^+ \approx 50$ was the smallest wall distance at which experimental hot-wire measurements were made, due to limitations of the hot–wire measurement system. Marusic's empirical model was used to estimate the boundary layer TI profile close to the wall [180], using experimental data as input. Marusic's empirical model estimates a boundary layer TI profile from the inputs: δ_{99}, U_∞ and u_τ. The experimental u_τ is obtained from Re_Θ, using the Kármán–Schoenherr (KS) formula [181]. Figure 6.4b shows a reasonable agreement between the simulated and empirical TI profiles, with the model's estimate of TI having a lower peak. This result indicates that the highest TI levels in the simulation may be slightly higher than in the experiment. The result is associated with the (approximately 10%) higher wall shear in the simulation, in comparison with the experiment. The study focuses on the relative difference between the turbulent fluctuations upstream of the cavities and at the cavity bottoms. Therefore, small differences in turbulence levels over the flat plate, between experiment and simulation, are assumed to have minimal effect on the analysis.

Figure 6.5 compares the wall pressure spectra at the bottom of each cavity from the experiment with those of the simulations. ΔPSD is defined as the difference between the wall pressure spectrum at the bottom of the cavity and the wall pressure spectrum upstream of the cavity, i.e., the flush microphone measurement:

$$\Delta\text{PSD} = \text{PSD}_{\text{cavity}} - \text{PSD}_{\text{flush}}, \tag{6.8}$$

Figure 6.5 shows a good agreement between the numerical and experimental ΔPSD for each uncovered cavity. This indicates that the flow features that lead to pressure fluctuations at the cavity bottoms are realistically represented in the simulations. Only for
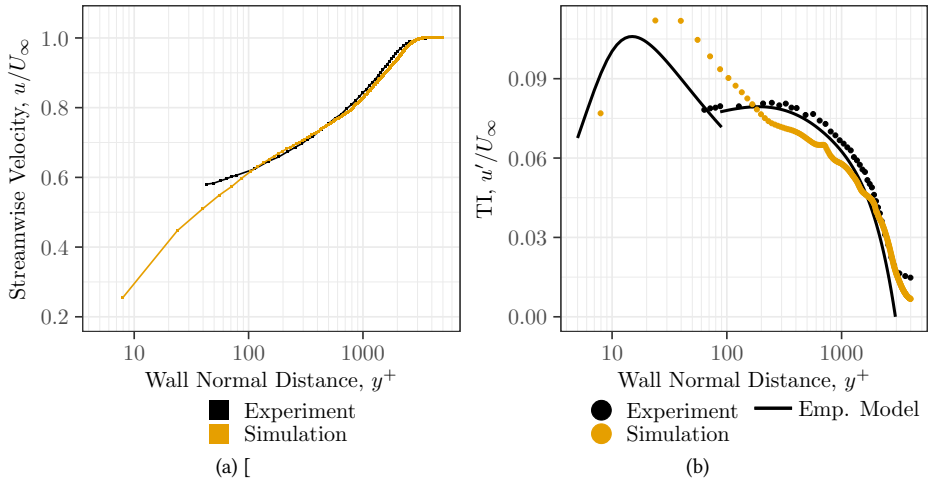
Figure 6.4: Simulated and experimental boundary layer profiles: a) Velocity profile and b) turbulence intensity profile. Empirical turbulence intensity profiles were obtained with Marusic's model [180].

frequencies above 4 kHz, do the simulations over–predict the pressure fluctuations at the bottoms. Figure 6.5 shows that the simulations for the covered cavities show a reduction of the TBL pressure spectra at the bottom of the cavities with respect to the flush spectrum. These trends agree with the experiment but under–predict the amount of attenuation. This result suggests that the attenuation, caused by the stainless steel cloth cover, is higher in the experiment than in the simulation, especially towards higher frequencies. The results suggest that, when the eddy size becomes small in comparison with the cavity aperture diameter (see discussion of Fig. 6.6), the validity of the equivalent fluid approach for simulating covered cavities is reduced. The discrepancy in the amount of attenuation is independent of the cavity geometry, and is therefore considered to not affect the conclusions of this investigation.

Figure 6.6 shows the coherence length of the TBL pressure fluctuations calculated from a flat plate simulation without a cavity present. The sampling location of the data was centered at $x = 0$, i.e., at the cavities' streamwise location. Figure 6.6a shows that the streamwise coherence length, which is indicative of eddy size, is comparable to the cylindrical and countersunk cavity aperture diameters at low frequencies (at 1000 Hz). The spanwise coherence length of the pressure fluctuations, is considerably smaller than the cylindrical cavity's diameter, for frequencies higher than 350 Hz). As seen in previous experimental studies, e.g., Refs. 182 and 183, the coherence length agrees with Efimtsov empirical model calculated using Eq. 2.19, (see dashed line) at high frequencies.
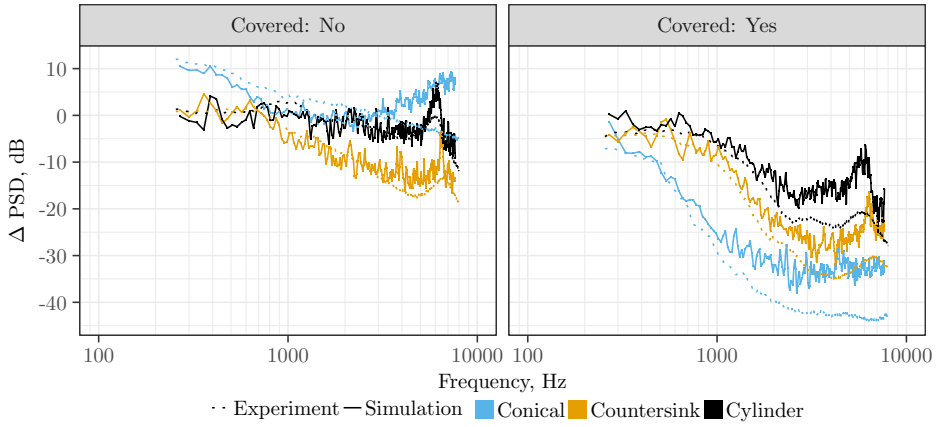
Figure 6.5: Simulated and experimental pressure spectra: difference between the spectra at the bottom of the cavities, and the spectra over the flat plate for both uncovered cavities and covered cavities.
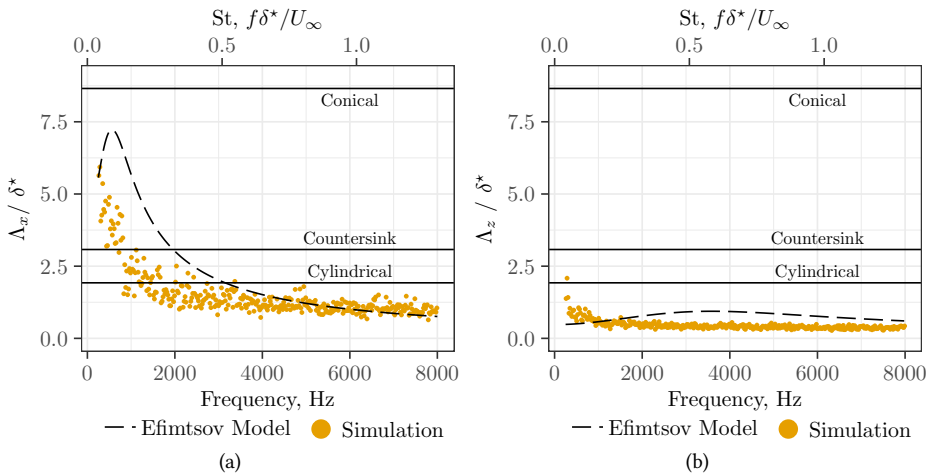
6

Figure 6.6: Coherence length of the pressure fluctuations at $y = 0$ for the flat plate simulation, in comparison with Efimtsov empirical models: a) Streamwise coherence length and b) Spanwise coherence length. The cavity diameters are shown for reference as horizontal lines. Data extracted from a flat plate simulation (without cavity), at $x = 0$.

6.4 Uncovered Cavities

6.4.1 Effect of Geometry on the Time–Averaged Flowfield

Figure 6.7 presents the average streamwise velocity, u, and static pressure coefficient:

$$C_p = (p_s - p_\infty)/q_\infty, \tag{6.9}$$

inside the uncovered cavities. p_s is the static pressure, p_∞ is the free-stream static pressure and q_∞ is the free-stream dynamic pressure. Figure 6.7 shows u/U_∞ and C_p in a plane aligned with the cavity center–line, $z = 0$. The streamtraces in Fig. 6.7 are defined as lines which follow the local in–plane velocity vector.

The comparison of Figs. 6.7a and 6.7b indicates that decreasing the wall angle ψ from 90° to 45° and increasing d_c/D to 3, for the case of the countersunk cavity, shift the center of recirculation away from the bottom, resulting in a lower velocity along the bottom when compared to the cylindrical cavity. Figure 6.7c indicates that further increasing d_c/D to 1.0 (see Fig. 6.1) and increasing the cavity aperture, increases the recirculation velocities at the bottom, in contrast with the countersunk cavity. Furthermore, the streamtraces in Fig. 6.7c indicate that, due to the upstream wall angle, the stagnation point on the downstream cavity wall moves toward the bottom, changing the recirculation pattern. Shifting the recirculation towards the bottom of the cavity increases pressure fluctuations at the bottom, as it leads to the convection of eddies from the boundary layer towards the bottom. Additionally, higher velocities inside the cavity are associated with higher shear forces, which generate turbulence. The wall friction due to increasing cavity wetted area has minimal effect on recirculation because the reduction in velocity at the bottom does not increase substantially with the increasing wetted area.

A comparison of Figs. 6.7d and 6.7e shows that the downstream angled wall of the countersunk cavity leads to regions of higher positive and negative C_p, with a corresponding larger pressure gradient. The downstream edge of the conical cavity also leads to a high C_p region at the stagnation point inside the cavity (Figs. 6.7c and 6.7f). Pressure gradients can accelerate or decelerate the flow inside the cavity, further increasing the shear forces acting on the fluid.

Figure 6.8 shows average spanwise velocity, w, contours in the $x = -0.25L$ plane. The angled walls of the countersink and conical cavities increase the spanwise velocity at the top, compared to the cylinder, as shown in Figs. 6.8b and 6.8c. This result and the previous one indicate that the upstream angled wall of the countersunk and conical cavities cause stronger velocity fields within the cavities that contribute towards increased pressure fluctuations, i.e., turbulence, at the top of the cavity.

6.4.2 Influence of Wall Angle and Countersink Depth

Figure 6.9 shows the contours of the root mean square of the pressure fluctuations, p'_{rms}, for the uncovered cavities. This figure shows that p'_{rms} is higher in the shear layer at the top of the cavities due to the local turbulence generation and vortex shedding. Beneath the shear layer, the differences between the cavities are associated with the cavities' respective recirculation patterns, as discussed previously. p'_{rms} increases near the downstream walls and the bottoms of the cavities compared to the upstream wall where the local velocity is lower. Decreasing the recirculation velocity at the bottom results in lower values of p'_{rms}
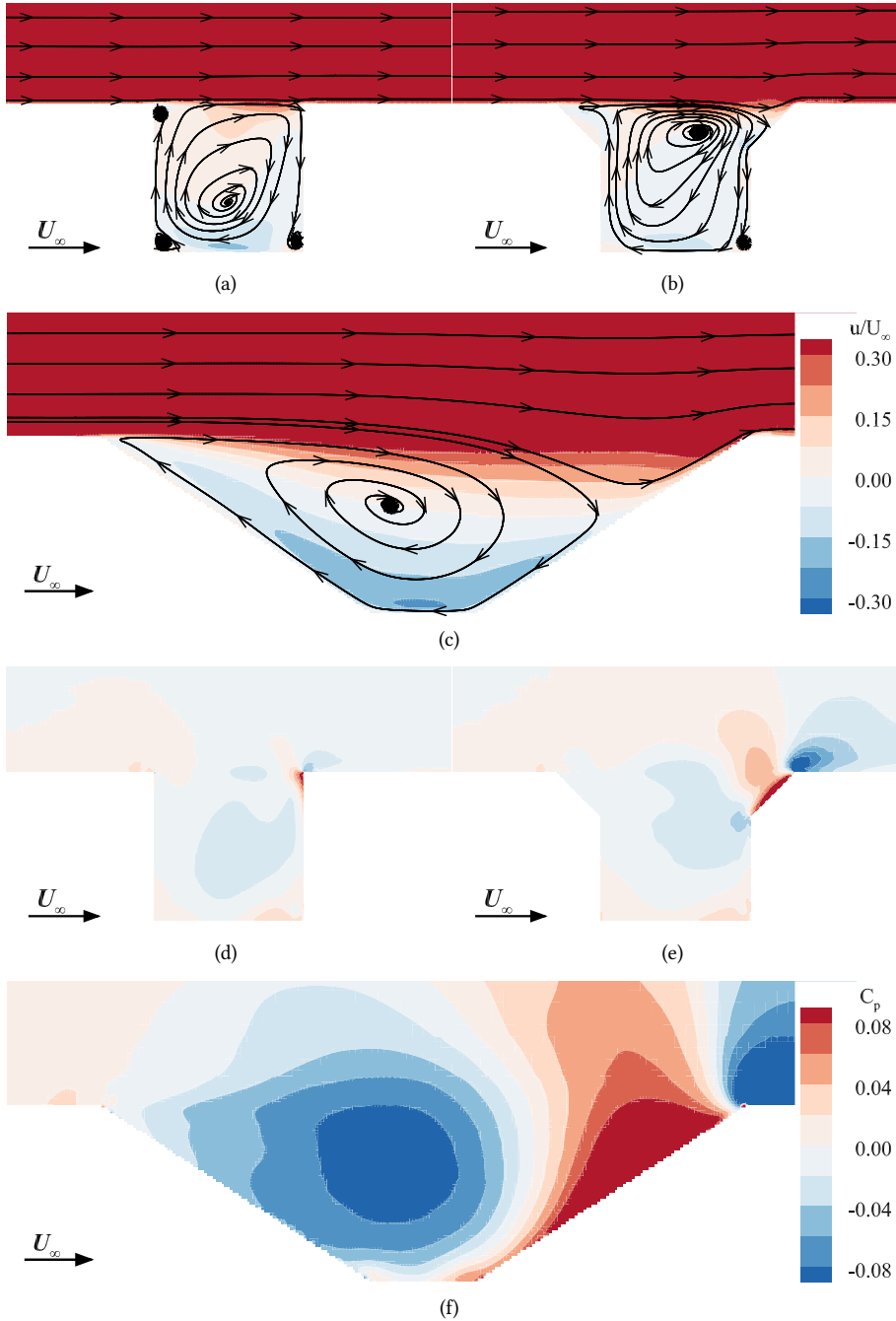
Figure 6.7: Uncovered cavities average flowfield, located at the $z = 0$ plane (center of the cavities). Streamwise velocity contours and in–plane streamtraces: a) cylindrical, b) countersunk, and c) conical. Pressure coefficient contours: d) cylindrical, e) countersunk, and f) conical.
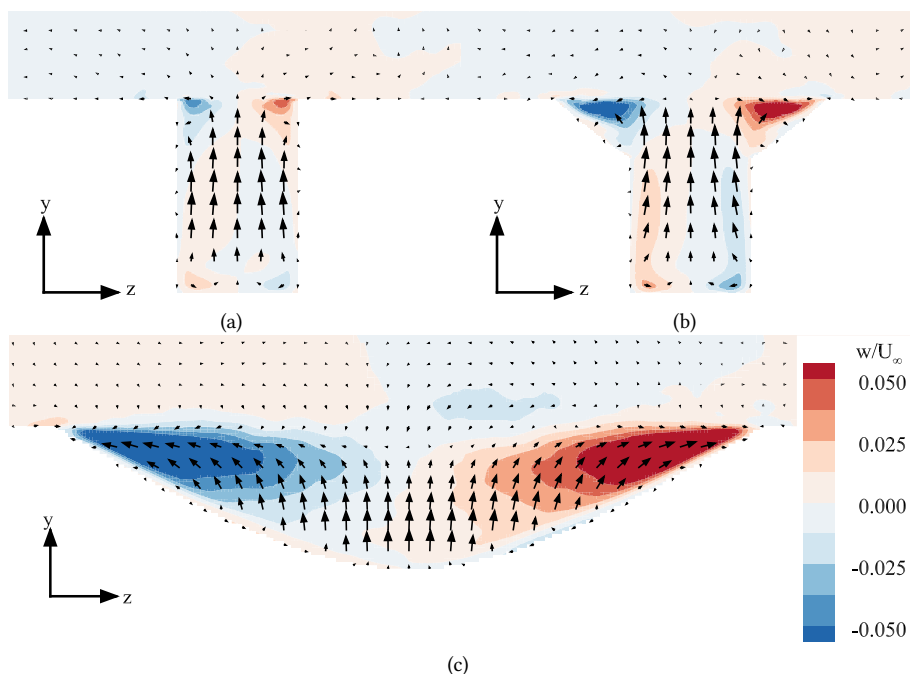
(a)

(b)

(c)

Figure 6.8:   Average spanwise velocity, w, contours and in-plane vectors ($x = -0.25L$ plane) for the following uncovered cavities: a) cylindrical, b) countersunk, and c) conical.
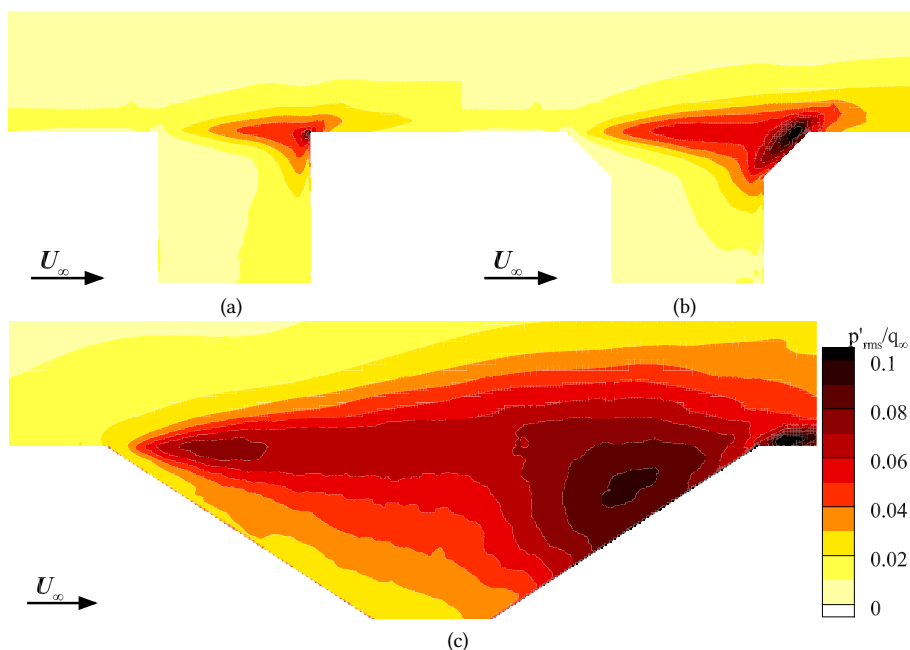

(a)

(b)

(c)

Figure 6.9:   Contours of the root mean square of the pressure fluctuations, for the uncovered cavities: a) cylindrical, b) countersunk, and c) conical.
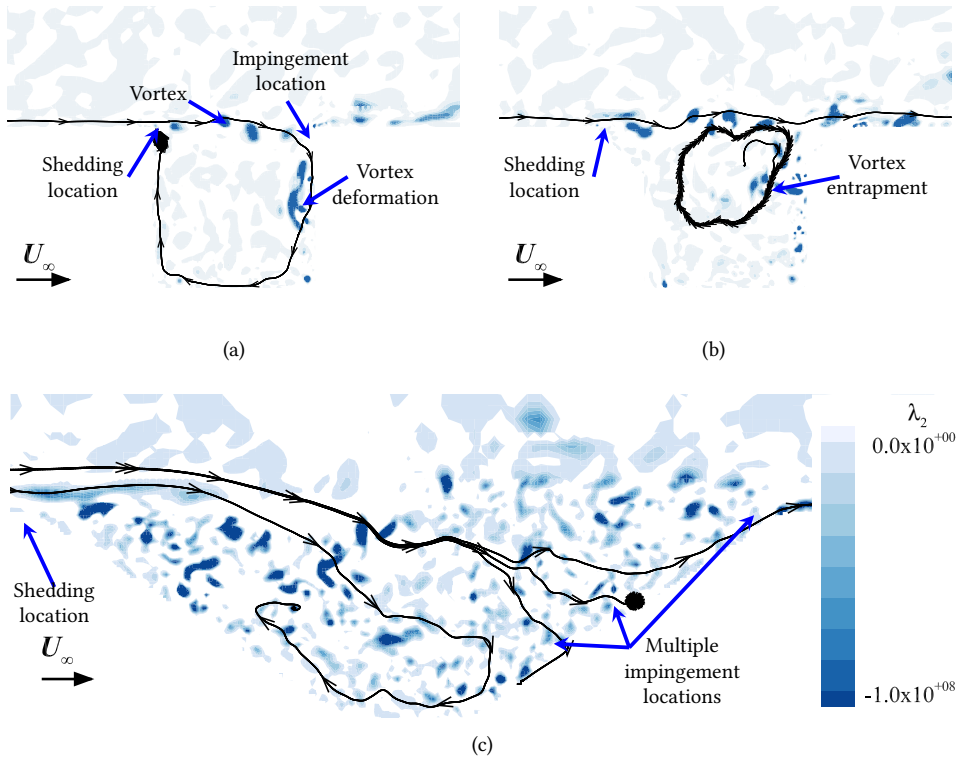
Figure 6.10: Instantaneous vortex visualization using the λ_2 criterion with streamtraces, $\lambda_2 < 0$ indicates the location of a vortex for the following cavities: a) cylindrical, b) countersunk, and c) conical.

as seen when comparing the countersunk cavity in Fig. 6.9b to the cylindrical (Fig. 6.9a) and conical cavities (Fig. 6.9c).

Decreasing the downstream wall angle from 90° (Fig. 6.9a) to 45° (Fig. 6.9b) or from 45° to 30° (Fig. 6.9c), increases the levels of p'_{rms} in the vicinity of the stagnation point. This location is where vortex impingement and subsequent deformation occurs, due to strong pressure gradients in the region. However, the effect of decreasing downstream wall angle on p'_{rms} at the bottom is minimized when the cavity has a countersink depth ratio of 0.3, as indicated by the comparison between cylindrical and countersunk cavities (Figs. 6.9a and 6.9b). Decreasing the upstream wall angle from 90° to 30° increases p'_{rms} within the shear layer. This is in line with the inclined angle backward facing step flow results presented in Ref. 164.

Figure 6.10 shows the Kelvin–Helmholtz type vortices [83] at an instantaneous stream-wise slice at $z = 0$. The λ_2 criterion is used to identify vortices, where $\lambda_2 < 0$ indicates vortex structures [184]. The streamlines show instantaneous convection paths for vortices within the cavities.

The vortices shed near the spanwise center ($z = 0$) of the upstream edge of the cylinder in Fig. 6.10a are of approximately constant size and extend in the spanwise direction (not

shown), more so than the other cavities. Decreasing the wall angle results in the shear layer altering the convection path of the vortices, which follow the previously described recirculation patterns. This is shown in Figs. 6.10b and 6.10c. For the countersunk cavity, the vortex impingement and recirculation create a region of increased turbulence along the angled wall, as shown by the higher levels of p'_{rms} in Fig. 6.9b. Additionally, these vortices tend to be transported away from the cavity bottom instead of toward it as for the cylindrical case. For the conical cavity, the large region of increased pressure fluctuations shown in Fig. 6.9c, is explained by the vortices not following a clearly defined streamtrace, and thus impinging at random locations along the downstream wall. Furthermore, the flowfield induced by the conical cavity's upstream angled wall increases the deformation of the vortices, which contributes to the increase in pressure fluctuations.
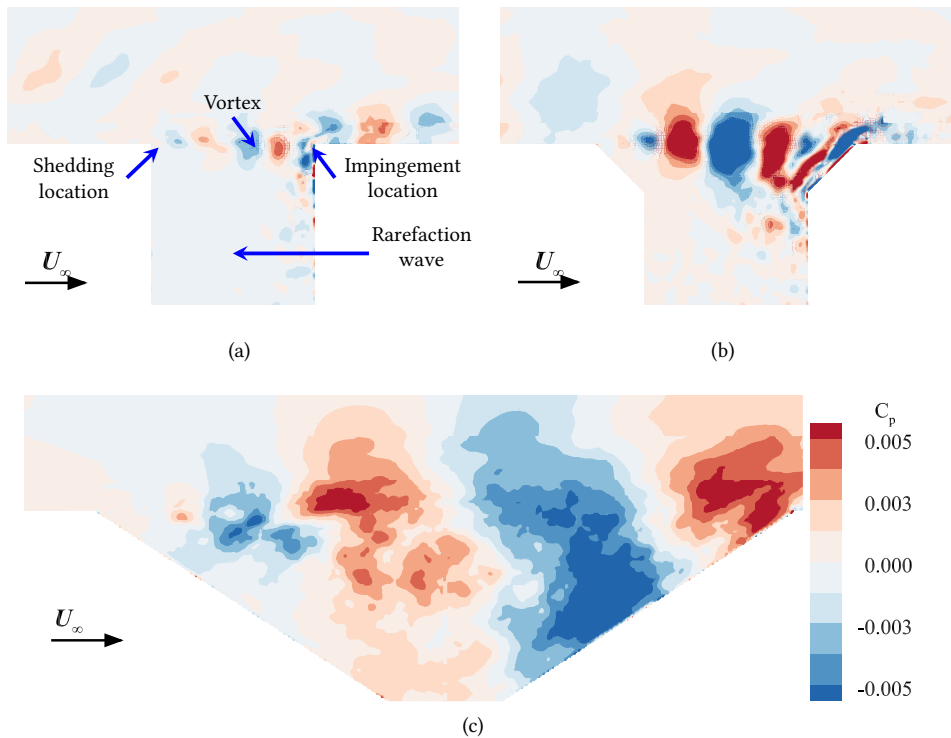
Figure 6.11: Band–pass filtering of p' at the one third–octave–band containing the peak vortex shedding frequency. The streamwise slice is located at z = 0.0 for the following cavities and one–third–octave bands: a) cylindrical, f_{band} = 2.5 kHz (St = 0.69), b) countersunk, f_{band} = 1.6 kHz (St = 0.66), and c) conical, f_{band} = 0.4 kHz (St = 0.56).

The instantaneous pressure field within the uncovered cavities is shown by Fig. 6.11. This figure shows the band-pass filtered pressure field at the one–third–octave band containing the peak vortex shedding frequency for each cavity. The shedding frequency is

analyzed in terms of Strouhal number, which is defined as:

$$St = \frac{f L_{\text{eff}}}{U_\infty},\tag{6.10}$$

where L_{eff} is the effective cavity diameter, defined as $L_{\text{eff}} = L\sqrt{2}/2$ [185]. The peak shedding frequency, where the pressure spectra is highest, Strouhal numbers for each cavity are: 0.69 (2.5 kHz), 0.66 (1.6 kHz), and 0.56 (0.4 kHz) for the cylindrical, countersunk, and conical cavities.

The regions of negative C_p, shown in blue in Figs. 6.11a and 6.11b, correspond to vortex cores [83], that are shown in Fig. 6.10. When these vortices impinge on the downstream wall, a rarefaction acoustic wave is produced and propagates from the impingement location [83]. The resulting negative pressure from this wave can be seen within the cylindrical cavity in Fig. 6.11a. Acoustic compression waves are generated in between the impingement of these vortices, as described by Ref. [83]. Unlike the cylindrical and countersunk cavity, the pressure waves produced by the vortex impingement do not substantially contribute to the conical cavity's internal pressure fluctuations.

Hydrodynamic and Acoustic Components of the Pressure Spectra

The wavenumber–frequency spectra at the bottom of the uncovered cavities are shown in Fig. 6.12. In this figure, the contributions to the spectrum by both the hydrodynamic and acoustic phenomena are seen. The spectra within the hydrodynamic regions are concentrated near the wavenumbers, $k = \frac{f}{U_c}$, associated with the recirculation velocity, i.e., U_c along the bottom of the cavity. This velocity is $-4.9\,\text{m s}^{-1}$, $-3.0\,\text{m s}^{-1}$, and $-7.6\,\text{m s}^{-1}$ for the cylindrical, countersunk, and conical cavities. The spectrum levels within the hydrodynamic region decrease with decreasing recirculation velocity due to the reduced transport of turbulence across the bottom. The spectra in and near the acoustic regions, seen for the cylindrical and countersunk cavities, are due to the pressure waves from the vortices impinging on the downstream wall. Peaks at 6.0 kHz and 6.3 kHz are the cylindrical and countersunk cavity acoustic depth modes. However, the conical cavity does not have a well–defined acoustic region. This suggests that the scattered energy due to the vortex impingement seen in Fig. 6.10c does not result in strong pressure waves from the downstream wall. At the top of all cavities (not shown), the spectrum levels are highest near the TBL convective wavenumber, k_c, which is defined as $k_c = \frac{f}{U_c}$. The flow at the top of the cavities has a convective velocity, $U_c = 18\,\text{m s}^{-1}$, which is 52% of the free stream velocity, U_∞.

Figure 6.13 shows the pressure spectra for the acoustic and hydrodynamic components of the pressure field. The acoustic component is calculated by integrating the spectrum within the acoustic wavenumber domain, while the hydrodynamic component is represented by the integrated spectrum outside this acoustic region. In these simulations the cavity diameters are smaller than the acoustic wavelength, i.e., for frequencies below 34 kHz for the cylindrical cavity. Therefore the wavenumber resolution, Δk_x, is larger than the acoustic wavenumber, $k_0 = f/c_0$, below this frequency. $\Delta k_x = 1/L$ is $100\,\text{m}^{-1}$ for the cylinder and countersunk cavities, and is $142\,\text{m}^{-1}$ for the conical cavity. As a result, the spectral energy of the acoustic region is concentrated in the $k_x = 0$ region. The shaded
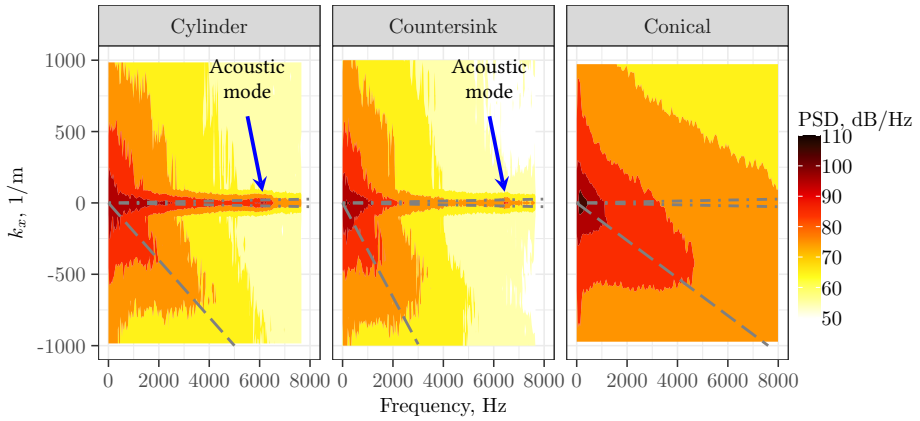
Figure 6.12: Wavenumber - frequency spectra across the bottom of the uncovered cavities (- -) lines represent the hydrodynamic peak due to recirculation, (– •) represents the acoustic region. $p_{\text{ref}} = 2 \times 10^{-5}$ Pa.

area in the figures highlights the frequency bands where differentiating between acoustic and hydrodynamic is difficult.

The hydrodynamic components of the spectra in Fig. 6.13 are dominant relative to the acoustic component for all three cavities. The cylindrical cavity's acoustic depth mode at 6.0 kHz is identifiable in the spectrum of the acoustic component and has an amplification of 8.5 dB with respect to the broadband spectrum level. The frequency of this depth mode agrees with predictions, using the expression $f = \frac{(2n+1)c_0}{4D+\delta}$, where n is the mode number beginning at 0, c_0 is the speed of sound, and δ is the correction term for the cavity diameter, as discussed in Chapter 5. The acoustic component is higher for the cylindrical cavity than those of the other cavities due to the stronger pressure waves generated by the impinging vortices. The countersunk cavity's hydrodynamic component is lower than that of the cylindrical cavity due to the lower recirculation velocity. The countersunk cavity's depth mode at 6.3 kHz is also identifiable within the acoustic component of the spectrum. The countersunk cavity's acoustic mode is amplified by 7.5 dB, which is less than the cylindrical case due to the higher countersunk ratio of 0.3 resulting in a shallower straight walled portion. The conical cavity's hydrodynamic component is higher than its acoustic component because the vortex impingement produces lower amplitude pressure waves compared to the other cavities. Additionally, the flow along the downstream wall transports turbulence across the bottom resulting in higher pressure fluctuations. This explains the higher hydrodynamic spectral levels for the conical cavity compared to the other two cavities. The depth mode for a conical cavity is estimated to be at $f = 5.0$ kHz using the method described in Scavone [65]. This mode is not identifiable, presumably because conical cavities have much weaker depth modes than straight walled cavities due to their lower quality factor (refer to Chapter 5).
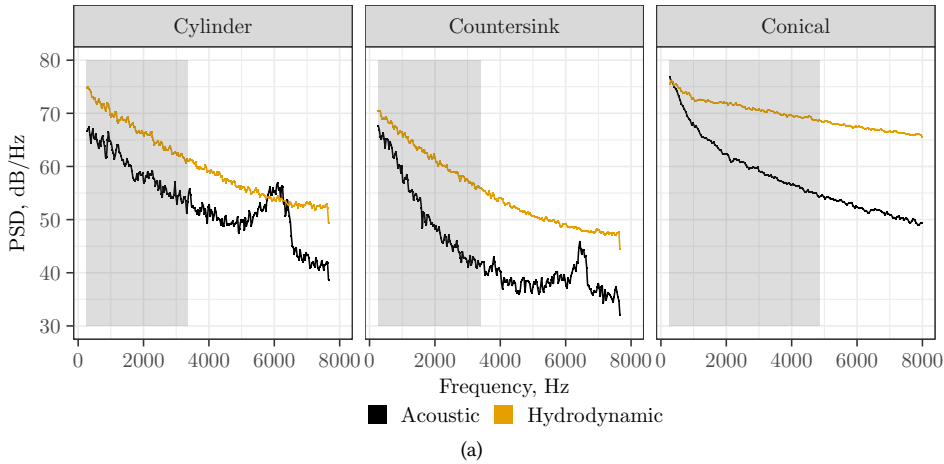
Figure 6.13: Wavenumber spectra decomposed into acoustic and hydrodynamic components for all three uncovered cavities. Shaded area is the region of uncertainty, defined as $f \leq \frac{U_\infty}{\Delta k}$.

6.5 Covered Cavities

In contrast to the uncovered cavities, the streamwise velocity magnitudes of the covered cylindrical, countersunk, and conical cavities are below $0.002U_\infty$, as shown in Fig. 6.14. Therefore, the flow beneath the cover is nearly stagnant. Covering the cavities eliminates the dominant propagation mechanism of the pressure fluctuations. As expected, eliminating recirculation partially explains why the covered cavity spectra in Fig. 6.5 are lower than the uncovered cavities.

6.5.1 Pressure Fluctuations Due to the Convection of TBL Eddies

Figure 6.15 shows the band–pass filtered pressure at the 1 kHz one–third–octave band for each cavity. This frequency band was chosen because the integral length scale of the eddies, as shown in Fig. 6.6a, is of the order of the diameter of the cylindrical cavity. The TBL eddies convect across the top of the covering at the boundary layer convective velocity, U_c [49]. Immediately above the covering, $y = 0.0$ cm, the pressure fluctuations due to the eddies are visible. The distance between these eddies is indicative of the TBL streamwise coherence length, which approximates the size of the eddies. The eddies immediately above the cover create a pressure field inside the cavity. This pressure field decays as it expands within the cavity volume. This pressure field is the dominant source of noise (p') at the bottom of the covered cavities and can be considered a near field acoustic perturbation.

The cylindrical cavity band–passed pressure field is shown in Fig. 6.15a. The pressure field within the cavity is almost spatially uniform (coherent) due to the eddies at the top of the cavity being close in size to the cavity aperture size. As a result the pressure field within the cavity is highly coherent with respect to the microphone location (center of the cavity bottom). The countersunk cavity in Fig. 6.15b exhibits similar behavior as the cylindrical cavity with the pressure field becoming increasingly uniform towards the cavity bottom. At the top, the eddies are smaller than the aperture size. This results in a
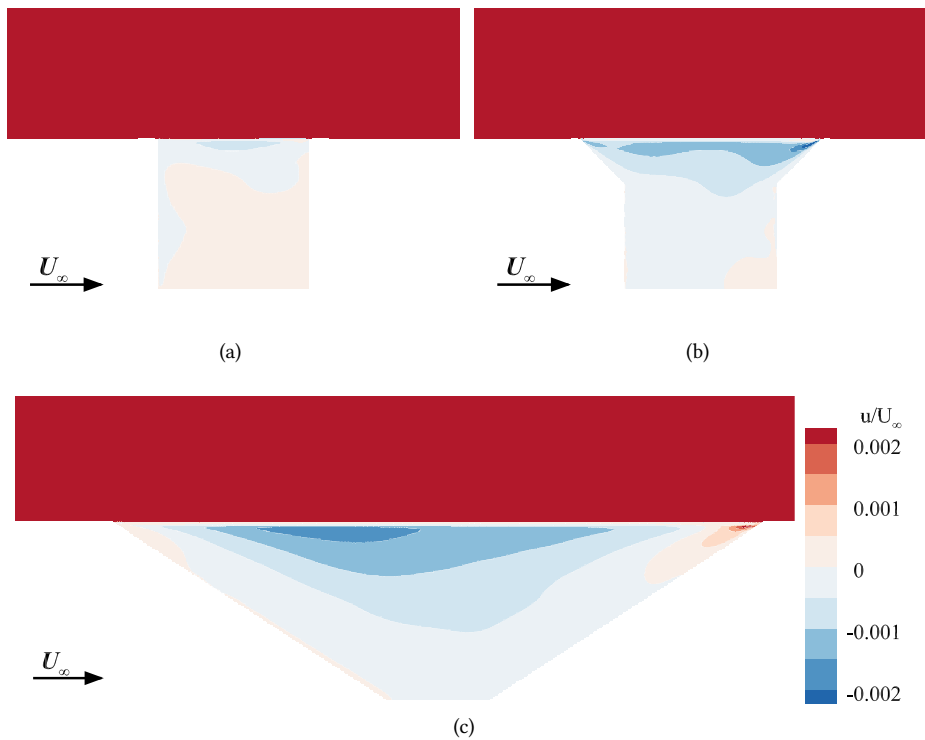
Figure 6.14: Average streamwise velocity field for the following covered cavities: a) cylindrical, b) countersunk, and c) conical.
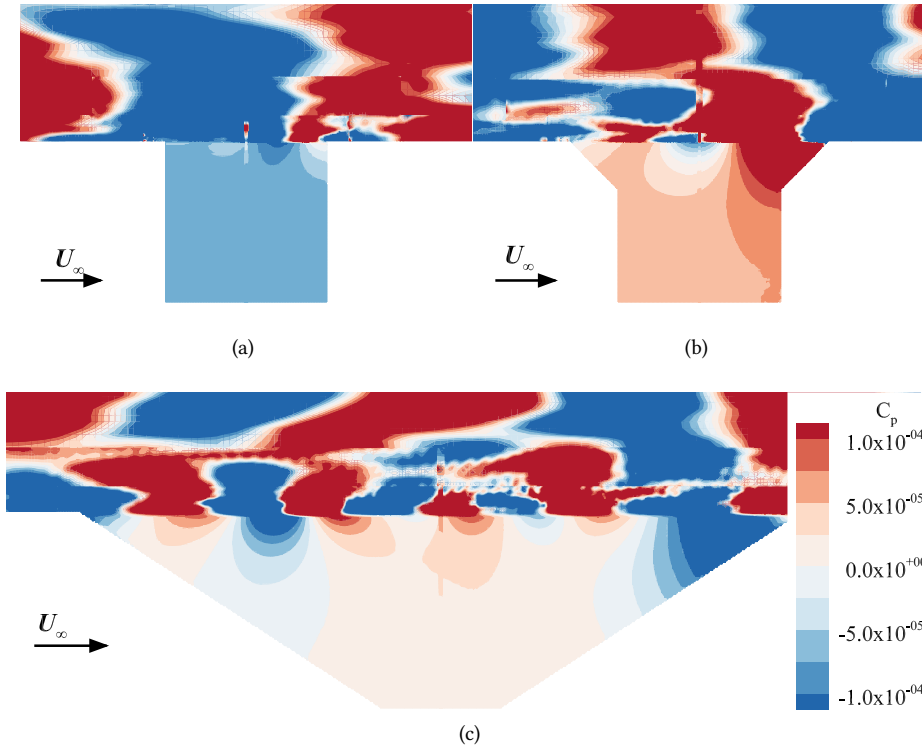
Figure 6.15: Band–pass filtered pressure fluctuations at the 1.0 kHz one–third–octave frequency band. The streamwise slice is centered at z = 0.0 cm for the following covered cavities: a) cylindrical, b) countersunk, and c) conical.

more complex pressure field at the top of the cavity, especially near the angled walls. The pressure field within the conical cavity, shown in Fig. 6.15c, is much less uniform than the other cavities. This is due to the aperture being approximately a factor of 4.5 larger than the eddies, as indicated by Fig. 6.6a. The resulting pressure field within the conical cavity is the summation of the rarefactions and compressions at the top. The eddies immediately above the conical cavity center contribute to p' at the microphone location. This is shown by Fig. 6.15c.

Hydrodynamic and Acoustic Components of the Pressure Fluctuations

The wavenumber–frequency spectra for the cylindrical cavity are shown in Fig. 6.16. Figure 6.16 shows the spectrum just beneath the covering, $y = −1.5 \times 10^{−3}$ cm. The covering reduces the amplitude of the spectrum at the top of the cavities compared to the uncovered case in Fig. 6.12 by approximately 20 dB. The spectral energy is more concentrated near the convective wavenumber, k_c, as shown by a similar wavenumber analysis in Ref. 91. This convective ridge is due to the convecting eddies within the TBL being the primary source of pressure fluctuations. At the bottom of the cylindrical cavity, shown in Fig. 6.16, the spectrum is highest at or near the acoustic wavenumber, k_0, i.e., at the bot-
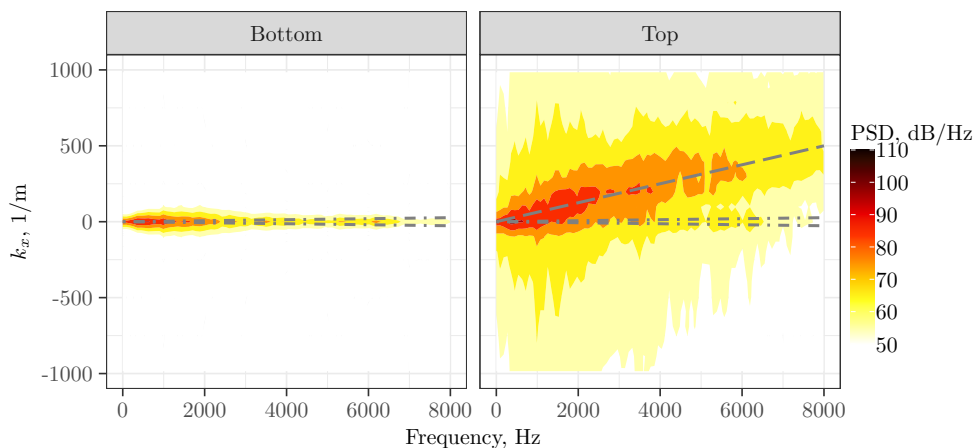
Figure 6.16: Wavenumber - frequency spectra across the top and bottom of the covered cylindrical cavity (- -) lines represent the hydrodynamic peak, (– •) represents the acoustic region. $p_{\mathrm{ref}} = 2 \times 10^{-5}$ Pa.
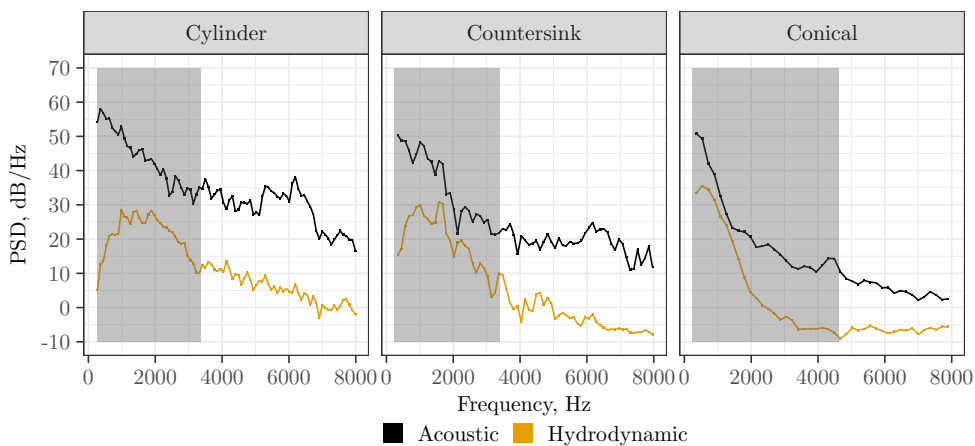

Figure 6.17: Decomposition of the wavenumber spectra into acoustic and hydrodynamic components for all three covered cavities. Shaded area is the region of uncertainty.

tom of the cavity the pressure fluctuations propagate primarily at the speed of sound. The countersunk and conical cavities exhibit similar wavenumber-frequency spectra.

Figure 6.17 compares the hydrodynamic and acoustic components of the spectra at the bottom of all three covered cavities. The acoustic component is dominant at the bottom of all covered cavities. For the covered cylindrical cavity, the acoustic contribution is approximately 20 dB higher than the hydrodynamic contribution at the bottom. The depth mode is visible near 6.0 kHz with a reduced amplitude compared to the uncovered cavity in Fig. 6.13. The porous cover changes the acoustic impedance at the top of the cavity and consequently reduces the quality factor of the cavity [147]. The countersunk cavity's spectrum levels are 5–10 dB lower than the cylindrical cavity. The depth mode is also visible at 6.3 kHz. The covered conical cavity reduces the acoustic spectrum by an additional 10 dB for frequencies greater than 4.0 kHz compared to the countersunk cavity. A small peak near the conical cavity's predicted depth mode can be seen near 4.5 kHz. The acoustic component of the TBL spectra levels at the bottom decrease with increasing cavity aperture size.

Modal Decomposition of p'

Proper orthogonal decomposition was performed on the pressure fluctuations in the 2–D plane at the top (under the covering) and bottom of the covered cavities. Figure 6.18 shows the first three mode shapes, $\boldsymbol{\phi}_r$, sorted by the energy content of each mode, σ_r, at the top of a covered cylindrical cavity. The energy of each mode, as a percentage of the sum of the energy of all the modes, is illustrated by the vertical gray bar. The first mode contains about 61% of the total energy and resembles an acoustic plane wave mode ($m = 0$, $\mu = 1$), where m is the azimuthal mode number, and μ is the radial mode number [68]. This mode is dominant because the cavity diameter is close to the eddy size for frequencies below 2.0 kHz, shown in Fig. 6.6. Modes 2 and 3 have the same shape as the acoustic modes in a circular duct [68]. Specifically, they are the $m = 1$, $\mu = 1$ acoustic mode. Thus, Fig. 6.18 suggests that acoustic modes are dominant when the eddy size is larger than the cavity aperture.
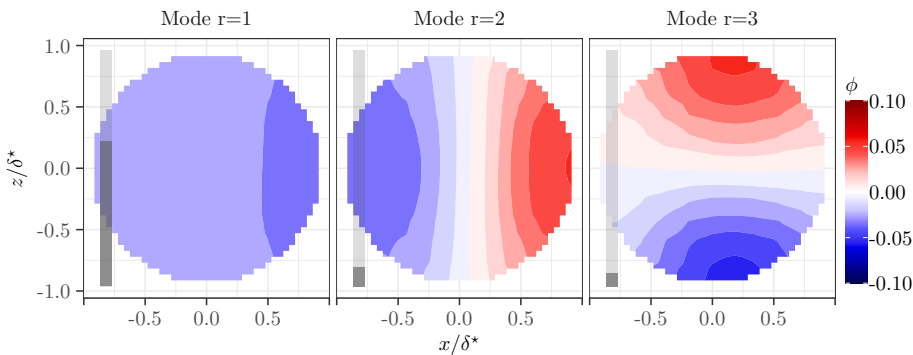

Figure 6.18: First three mode shapes, ϕ, at the top of the covered cylindrical cavity, y = -1.5×10^{-2} cm. The modes are sorted by energy content, with the gray bars indicating the percentage of total energy, $\sum \boldsymbol{\sigma}$, each mode contains.
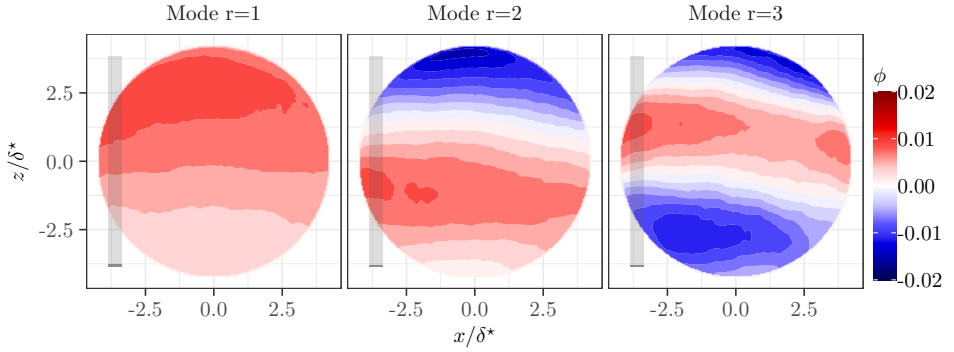
Figure 6.19: First three mode shapes, ϕ, at the top of the conical cavity, y $= -1.5 \times 10^{-2}$ cm. The gray bars indicate the percentage of total energy, $\sum \sigma$, each mode contains.

The first three POD modes at the top of the covered conical cavity are shown in Fig. 6.19. Unlike the cylindrical cavity, whose first mode represents the majority of the energy in the pressure field, the energy at the top of the conical cavity is spread out across more modes, with the first mode having only 1.3% of the total energy. This is due to the conical aperture diameter being larger than the TBL streamwise coherence length, as shown in Fig. 6.6. The mode shapes do not correspond to acoustic mode shapes as the pressure fluctuations are not coherent with a single eddy due to the conical cavity diameter being a factor of 4.5 larger than the cylindrical diameter. These mode shapes are indicative of different sized eddies present at the top of the conical cavity. Mode #1 features a larger structure and has the highest energy content while modes 2 and 3 are indicative of smaller structures within the TBL.

At the bottom of the covered cavities, the mode shapes correspond to the acoustic mode shapes of a circular duct. This is shown in Fig. 6.20 for the conical cavity. POD mode 1 is similar to the acoustic plane wave mode, ($m = 0$, $\mu = 1$), mode 2 corresponds to the acoustic mode ($m = 1$, $\mu = 1$), mode 4 is similar to the acoustic mode ($m = 2$, $\mu = 1$), mode 6 matches the ($m = 0$, $\mu = 2$) mode, mode 8 is the ($m = 3$, $\mu = 1$) acoustic mode, and mode 10 is the ($m = 1$, $\mu = 2$) mode. The first POD mode contains the largest percentage of the total estimated energy, 83%. This is in contrast to the same mode at the top in Fig. 6.19. The explanation is that the higher order modes are cut off in the cavity and thus exponentially decay as they propagate towards the bottom of the cavity as described in Chapters 2 and 3. The first mode and its associated energy propagates to the cavity bottom resulting in it containing the majority of the energy at the cavity bottom. The cut-off condition is defined by the following expression,

$$\frac{\omega a}{c_0} > \alpha_{m\mu} \tag{6.11}$$

where a is the cavity aperture radius and $\alpha_{m\mu}$ is the radial wave number. The radial wavenumber is the Bessel (of the first kind) derivative root [68]. For example, for mode $n = 2$ in Fig. 6.20 ($m = 1$, $\mu = 1$) the root of the Bessel function of the first kind derivative is $\alpha_{11} = 1.8412$. Eq. 6.11 states that for the cylindrical cavity with a diameter of 1.0 cm the first non-planar acoustic mode will propagate for frequencies above 20.1 kHz. Therefore,
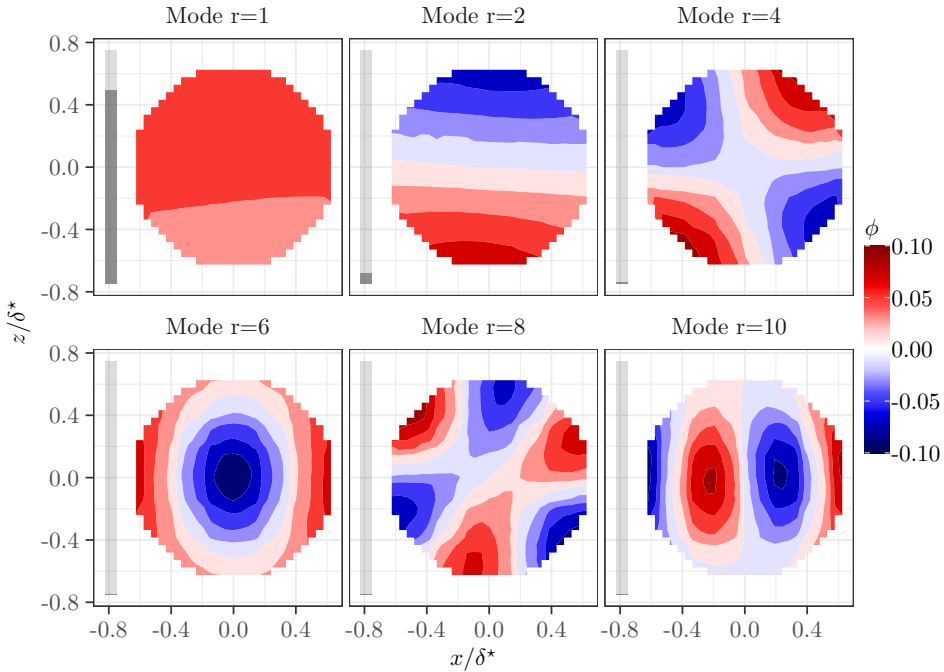
Figure 6.20: First six unique modes, ϕ, at the bottom of the covered conical cavity. The gray bars indicate the percentage of total energy, $\sum \sigma$, each mode contains.
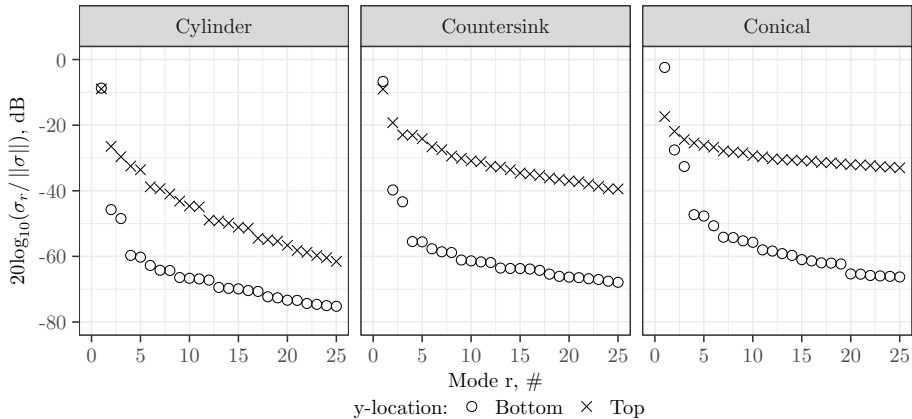

Figure 6.21: Normalized energy per mode, $\sigma_r / \|\boldsymbol{\sigma}\|$, at the top and bottom of the cavities with a stainless steel cloth covering.

only mode 1, the planar mode, is cut–on for the frequencies of interest and propagates without decaying.

The effect of cavity aperture size on the attenuation of the TBL spectra is shown in Fig. 6.21. This figure shows the normalized energy content of each mode, $\sigma_r/\|\boldsymbol{\sigma}\|$, where $\|\boldsymbol{\sigma}\| = \sqrt{\sigma_1^2 + \sigma_2^2 + \cdots + \sigma_r^2}$, at the cavity top and bottom for all three covered cavities. At the top of the cylindrical cavity, the normalized amplitude of the first mode is 18 dB higher than the next highest mode. As the cavity aperture diameter increases for the countersunk and conical cavities, the difference between the first two modes at the cavity tops decreases to 10 dB and 5 dB. Thus, the energy of the TBL pressure field is increasingly spread across the higher order POD modes for larger cavities. This is due to the cavity aperture size increasing with respect to the coherence length of the TBL and therefore the number of pressure rarefactions and compressions present at the top of the larger cavities, due to the TBL eddies, increases. In contrast, the pressure fluctuations at the top of the smaller cavities can be represented primarily by the planar mode as it contains significantly more energy because the TBL eddies convecting over the cavity are larger than the cavity, as shown in Fig. 6.6a.

At the bottom of all cavities, the first mode has a 30–40 dB higher amplitude that the next highest mode. This is explained by this mode being planar and thus cut on. The higher–order modes are cut off, thus their energy decays exponentially as they propagate from the top to the cavity bottom. Furthermore, as the cavity aperture size increases, the energy at the bottom of the cavity is increasingly concentrated in the first mode, as shown by the conical cavity having a normalized amplitude 6 dB higher than the cylindrical cavity. This is attributed to the TBL energy being spread out over higher–order modes. Therefore, larger diameter covered cavities will attenuate the TBL pressure fluctuations more than smaller ones. This explains why the covered conical cavity attenuates the TBL pressure fluctuations the most, as plotted in Fig. 6.5.

An important result of the wavenumber and POD analysis is that the pressure field beneath a covered cavity exhibits behavior similar to an acoustic wave propagating in a duct. The wavenumber analysis in Fig. 6.17 shows that at the bottom of the cavity the pressure spectral energy is primarily contained within the acoustic wavenumber domain. The POD analysis shows that the pressure fluctuations at the bottom are decomposed into mode shapes that correspond to acoustic circular duct modes. This suggests that modeling the propagation of the TBL pressure field into a covered cavity can be simplified with an acoustic model, thus decoupling the acoustic from the hydrodynamic contributions to the pressure spectra at the bottom of the cavities.

6.6 Summary

The present study used the Lattice–Boltzmann based commercial software package PowerFLOW to simulate turbulent flow with a freestream velocity of $32 \, \mathrm{m \, s^{-1}}$ over axisymmetric cavities placed in a flat plate. The following geometries were simulated: a cylindrical cavity, a countersunk cavity, and a conical cavity. In addition to simulating these open cavities, the effect of a finely woven stainless steel cloth covering is evaluated by using an equivalent fluid approach, modeled by imposing Darcy's law, at the top of each cavity. The simulated pressure spectrum at the bottom of the cavities is validated with experimen-

tal measurements. Both show that the uncovered countersunk cavity has the lowest TBL spectrum, followed by the uncovered cylindrical and uncovered conical cavities. The simulated trend in covered cavity performance is also in agreement with the measurements. The covered conical cavity attenuates the pressure fluctuations at the microphone location (cavity bottom) the most and therefore performs the best. The covered countersunk cavity performs better than the covered cylindrical cavity. The porous medium model is found to be capable of modeling the effect of covering the cavities. This analysis identifies the behavior of the hydrodynamic and acoustic components of the pressure fluctuations within these axisymmetric cavities.

Based on a wavenumber analysis, it is found that the pressure fluctuations at the bottom of uncovered cavities are dominated by hydrodynamic phenomena. These phenomena include recirculation and turbulence generation inside the cavities. Adding a countersink at the top of the cylindrical cavity is found to reduce recirculation towards the cavity bottom by shifting the center of recirculation away from the cavity bottom. However, extending the countersink to the bottom (conical cavity) increases the recirculation velocity and turbulence generation at the bottom. It is reasoned that the upstream angled wall deflects the flow downwards and thus moves the downstream shear layer reattachment point towards the bottom, increasing the recirculation velocity. This is most noticeable in the conical cavity. Furthermore, the angled downstream walls also cause strong pressure gradients inside the cavities, which are associated with turbulence generation in the region of vortex impingement. Based on these observations, an optimal uncovered cavity should feature a perpendicular upstream wall to reduce turbulence generation and inflow, an angled downstream wall to reduce the effect of vortex impingement, and a countersink that does not extend to the bottom of the cavity to reduce the recirculation at the bottom.

Covering the cavity opening with the cloth reduces the flow across the covering, mitigating the entrance of turbulent structures into the cavity. The flow is mostly stagnant inside the covered cavities, and turbulent structures are not produced inside. The pressure field within the cavities is due to the pressure fluctuations generated by the eddies convecting across the top. The pressure field created by the TBL eddies propagates towards the bottom of the cavities at the speed of sound, as shown by the wavenumber analysis. The pressure field within the cavities is dependent on the cavity size relative to the eddy size. When the cavity diameter is nearly the same size as the eddy, the pressure field within the cavity is coherent with the pressure fluctuations corresponding to the convecting eddy. When the cavity is larger than the eddies, the pressure field from individual eddies is evanescent resulting in attenuation of the pressure field at the cavity bottom.

The proper orthogonal decomposition (POD) analysis shows that the energy distribution of the resulting orthogonal modes at the top of each cavity is dependent on cavity aperture size. For smaller apertures, the energy is concentrated in the first mode due to the cavity size being close to that of the eddy size. For larger cavities, e.g., the conical cavity, a larger ratio of the energy is decomposed into higher order modes with less energy, relative to the smaller cavities, in the first mode. The spectra at the bottom of the cavities is attributed to the first POD mode as this mode is cut on. By shifting more energy into cut-off modes, the larger cavities have lower spectra levels at the cavity bottom. At the bottom of all cavities, the POD modes correspond to acoustic duct mode shapes. This is an important finding as it suggests that the propagation of TBL pressure fluctuations

for covered cavities can be accurately modeled with an acoustic approach. The acoustic modeling could be performed using the same approach as Chapter 5. With this approach, a pressure field representative of the TBL at the top of the cavity could be simulated as propagating acoustically into the cavity.

Covered cavities reduce the TBL spectral levels at the bottom of the cavity more than uncovered cavities. Therefore, future optimization of the cavity geometry should start with a covered cavity. The present work suggests that the propagation of the pressure fluctuations into a covered cavity can be simplified by solving only the wave equation. This may enable optimization of cavity shape and wall material, with affordable computational costs. However, the very-large eddy simulation using the Lattice–Boltzmann method is capable of simulating the propagation of the TBL pressure fluctuations into a cavity and therefore is suitable for evaluating future cavity designs, to improve the attenuation of the turbulent boundary layer pressure fluctuations. The computational method used in this study may also apply to cavity design studies at higher Mach numbers when compressible effects become dominant. Which would apply to improving the design of microphone cavities for direct noise measurements on aircraft skins.

6

7

The Cumulative Effect of Cavities and Beamforming on the SNR

Aeroacoustic measurements performed by flush-mounted microphone arrays on the walls of closed test section wind tunnels are contaminated by the hydrodynamic pressure fluctuations of the wall's boundary layer. This study evaluates three different microphone cavity geometries that mitigate this issue. The improvement to the signal-to-noise ratio (SNR) due to these arrays and the accuracy of their acoustic imaging results are compared to a flush-mounted microphone array. The four geometries include: (1) an array of flush-mounted microphones as the baseline, (2) a cylindrical hard-plastic cavity with a countersink, (3) a conical cavity made of melamine acoustic absorbing foam, and (4) a conical cavity with star-shaped protrusions, also made of melamine. The three arrays with cavities were covered with a finely woven stainless steel cloth to reduce the boundary layer fluctuations at the microphone while the baseline array was uncovered. Two sound sources were tested in an aeroacoustic wind tunnel for assessing the performance of the different cavities: a speaker placed outside the flow and a distributed sound source generated by a flat plate inside of the flow. When using conventional frequency domain beamforming, both cavities made of melamine offer up to a 30 dB increase in SNR with respect to the flush-mounted case, followed by the hard-walled cavity with up to a 20 dB increase. This is a 20 dB improvement when compared to the single microphone cases. The melamine cavities also provide cleaner acoustic source maps and accurate spectral estimations for a wider frequency range. The effect of cavity placement and geometry on the coherence, which affects the beamforming analysis of the acoustic signal was negligible for all cases. Distributed sound source measurements using the three arrays agreed with predictions using the Brooks, Pope, and Marcolini (BPM) model, showing that the cavities could detect vortex shedding that was undetectable by the flush array.

7.1 Introduction

Aeroacoustic experiments in wind tunnels are often performed in open-jet facilities as they allow for placing the microphones outside of the flow [186]. However, the aerodynamic

conditions in open-jet wind tunnels [117] are less well-controlled than in closed test section wind tunnels and require corrections to account for the acoustic signal refracting as it passes through the shear layer. Acoustic measurements in closed test section wind tunnels, on the other hand, are affected by several sources of noise inherent to wind tunnels [35], including the ones from the turbulent boundary layer (TBL) along the tunnel's walls, the tunnel's machinery, and reflections that propagate within the tunnel's closed test section. For this application, microphones are typically mounted flush and, consequently, the measurements are contaminated with TBL noise. The present chapter focuses on the effect cavities, which minimize the influence of the TBL hydrodynamic noise (pressure fluctuations), have on single microphone acoustic measurements and acoustic imaging measurements using a microphone array.

The signal-to-noise ratio (SNR) of the microphone array when measuring the far-field emissions of an acoustic source can be increased by attenuating the level of TBL noise at the microphone. This can be achieved in two ways. First, employing acoustic beamforming and applying techniques that average out the incoherent noise, which includes TBL noise [187], such as removing the main diagonal of the cross-spectral matrix (CSM) or advanced imaging methods, such as CLEAN-SC [148] and others [188, 189]. Second, recessing the microphones behind an acoustically transparent covering [16] and within cavities [61] further reduces the measured TBL noise as shown in Chapter 4. The latter approach normally uses a finely woven stainless steel cloth or a Kevlar sheet [16, 43, 190], which reduces the intensity of the boundary layer's hydrodynamic pressure fluctuations that enter the cavity but allows for the propagation of acoustic waves. The geometry of the cavity itself also has a significant effect on the amount of attenuation. Previous literature focused on studying the influence that different cavity geometric parameters, such as depth [57] and countersink [61], had on the reduction of TBL noise for a single microphone. However, there is a lack of research in quantifying the effects that different cavities have on microphone array measurements, in terms of TBL noise attenuation and accuracy of the acoustic imaging results. This chapter aims to quantify the impact different cavities have on aeroacoustic measurements by comparing three microphone arrays equipped with different cavity geometries with respect to a flush-mounted baseline array, all of which using the same microphone distribution. Both SNR (microphone level) and acoustic imaging performance are assessed.

The cavity shape and wall material have a significant influence on its performance with respect to TBL noise attenuation [61] as discussed in Chapters 3, 4, and 5. The relevant geometric parameters include: cavity depth, cavity aperture area, aperture area reduction with respect to depth, wall material (acoustic absorbing or not), and the presence of an acoustically transparent material (in this case a stainless steel cloth) over the top of the cavity. In general, increasing the depth, smaller aperture areas, and reducing the aperture area with cavity depth, i.e., conical shape, all attenuate the measured TBL noise [61].

In general, for flow over a cavity, the wave numbers associated with TBL noise are much higher than the typical acoustic wave numbers of interest. This is due to the speed of sound being considerably greater than the TBL convective velocity. Therefore, considering the excitation of acoustic modes by the TBL, the dispersion relation for acoustic waves only permits imaginary wave numbers in the direction perpendicular to the wall, i.e., into the cavity, which means an exponential decay. For cavities with circular aper-

tures, the TBL excitation is decomposed in duct modes. If the hydrodynamic wavelength is short compared to the aperture area, modes with imaginary axial wave numbers (cut-off modes) prevail. Specifically, the acoustic wave number is imaginary (cut-off) when a mode's radial wavenumber is larger than the Helmholtz number, $He = \omega a/c_0$, where ω is the angular frequency, c_0 is the speed of sound, and a is the cavity radius [68]. For Helmholtz numbers less that 1.84, all modes are cut-off, except for the plane duct mode. If the wavelength is long with respect to the aperture radius (low frequency, small aperture, high convection speed) then mainly the plane duct mode is excited. In that case, there is not much TBL noise attenuation. For the cavities considered in this chapter, the radii are on the order of 10 mm, and the frequency range of interest is in between 250 Hz and 10 kHz, therefore, only the plane wave is cut-on. Other acoustic modes decay exponentially with increasing cavity depth. When the radius of the cavity is no longer constant with depth, such as for a countersink, further attenuation occurs. This is due to the fact that the change in area results in a transmission loss for the propagating wave, as shown in Chapter 4, due to the change in acoustic impedance.

Cavity walls made of sound absorbing materials, such as melamine, reduce the intensity of reflections and standing wave amplitudes within the cavity. This results in a further reduction in the TBL noise at the microphone compared to hard–walled cavities. Finally, covering the cavity with an acoustically transparent material, such as a finely woven stainless steel cloth or a Kevlar sheet [16, 43], reduces the transmission of the TBL's hydrodynamic fluctuations into the cavity. The latter results in as much as a 10 dB additional reduction in TBL noise at the microphones. The cavities in this study have both hard and soft walls, a stainless steel cloth covering, and different depths and aperture areas.

In addition to the spectra measured by the individual microphones, conventional frequency domain beamforming (CFDBF) [55] is employed to locate and quantify the sound pressure level (L_p) of the sound sources. Since TBL noise is generally incoherent from microphone to microphone [127], beamforming itself also improves the SNR of the measurements by reducing the effects of this noise source. It should be noted that, whereas the use of some advanced acoustic imaging algorithms [148, 188, 189, 191] can further reduce the effect of TBL and background noise, most of them rely on the results of CFDBF. Thus, this chapter only considers CFDBF results, since improving these is consequently expected to also improve the results of other advanced methods. Additionally, the effect of applying coherence weighting [192] to the microphone signals was briefly investigated.

The measurements were performed in the anechoic open-jet wind tunnel of Delft University of Technology (A-Tunnel) [39] where a microphone array was used to measure a speaker emitting white noise located outside of the airflow and the trailing edge noise of a flat plate.

The objective of this chapter is to quantify the SNR improvement due to different cavity geometries for different flow speeds. The acoustic measurements are evaluated in terms of the integrated L_p and SNR when applying CFDBF with diagonal removal. Additionally, the coherence levels between cavities are evaluated for the speaker measurements to quantify the effect different cavity designs, especially due to the presence of a stainless steel cloth, have on the coherence of the acoustic signal.

This chapter is organized in the following manner: *Experimental set-up* which discusses the test facility, array design, and measurements; *Experimental results* which dis-

cusses the boundary layer measurements, the acoustic measurements of the speaker, the influence of the TBL on the acoustic measurements for single microphones and the array, the results of the distributed sound source measurements, and the resulting effect of cavity geometry on signal coherence; and finally the *Conclusions*.

7.2 Experimental Set-up

7.2.1 Wind Tunnel Facility

The test section of the A-Tunnel is located within an anechoic chamber that measures 6.4 m (length) × 6.4 m (width) × 3.2 m (height). The chamber is covered with acoustic absorbing foam wedges, which provides free-field sound propagation properties for frequencies higher than 200 Hz [39, 106], thus reducing unwanted reflections from walls, floor, and ceiling. An open-jet geometry configuration was employed for this study, with one of the (rectangular) nozzle edges extended with a plate in which the microphones were mounted. With this geometry the sound perceived by the microphones is dominated by the TBL noise over the array, as would be the case in a closed test section wind tunnel. This set-up also allows for a speaker to be placed outside of the flow, avoiding the interaction of the flow with the speaker and its support hardware. The rectangular nozzle employed has an exit area of 0.7 m × 0.4 m, see Fig. 7.1a, and provides a maximum flow velocity, U_∞, of 34 m s^{-1}. For this experiment flow velocities of 20 and 34 m s^{-1} are considered.

7.2.2 Microphone Array

The acoustic array consists of 16 microphones with two additional flush-mounted reference microphones. These 16 microphones are placed in a sunflower pattern [107] with an array diameter of approximately 0.35 m as seen in Fig. 7.1b. The layout was optimized [112] to minimize sidelobes and, thus, maximize the dynamic range between the frequencies of 2 kHz and 4 kHz. This design was predicted to have a maximum dynamic range of 9.6 dB based on a simulated monopole source [112]. Having only 16 microphones with this array diameter, limits the dynamic range and beamwidth compared to typical acoustic arrays that feature more microphones spread out over a larger area. The usable frequency range of this array is 1075 Hz to 9187 Hz. Usability for the lower frequency limit is defined as the main lobe width (3 dB below its peak value) for a point sound source placed in the direction normal to the array's center fitting within a 45° wide beam with respect to the same direction. The usability of the upper frequency limit is defined as the sidelobes being 8 dB below the peak L_p of the main lobe. This array configuration was chosen to limit the complexity and allow for the experiment to be carried out for different cavity geometries.

G.R.A.S. 40PH analog free-field microphones [193] were used in the array which feature an integrated constant current power amplifier and a 135 dB dynamic range. Each microphone has a diameter of 7 mm and a length of 59.1 mm. All the microphones were calibrated individually using a *G.R.A.S. 42AA* pistonphone [194] following the guidelines of Mueller [35]. The transducers have a flat frequency response within ±1 dB from 50 Hz to 5 kHz and within ±2 dB from 5 kHz to 20 kHz. The data acquisition system consisted of 4 *National Instruments* (*NI*) *PXIe-4499* sound and vibration modules with 24 bits resolution. The boards are controlled by a *NI RMC-8354* computer via a *NI PXIe-8370* board.

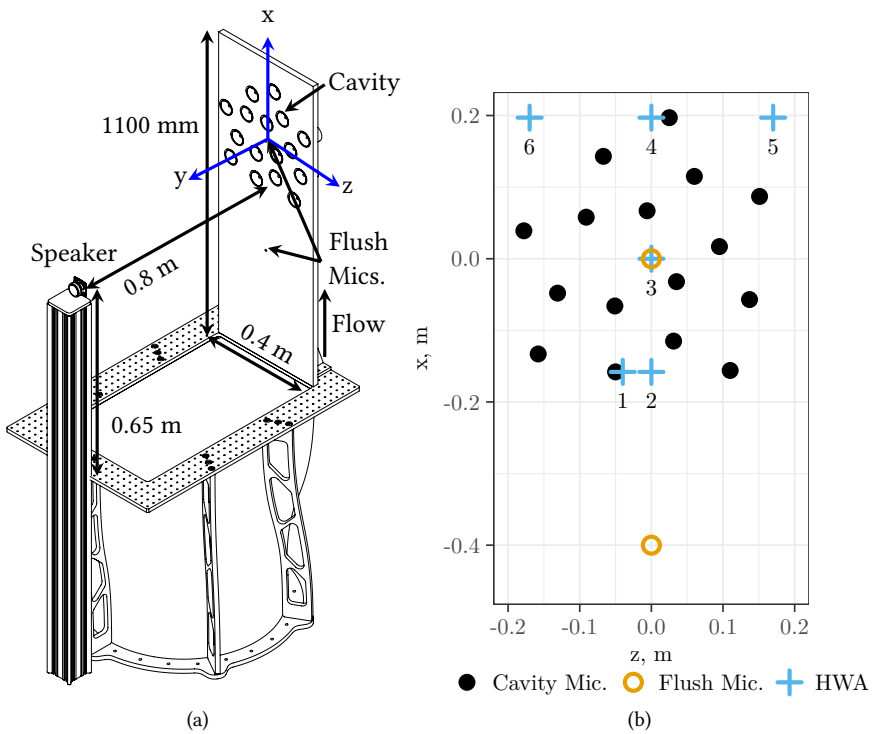The array cavities were installed in a 1.1 m × 0.4 m poly-carbonate plate, see Fig. 7.1a.

Figure 7.1: Experimental set-up at the A-Tunnel. a) array mounted on nozzle. b) array microphone distribution with hot-wire anemometry (HWA) measurement locations as seen from in front.
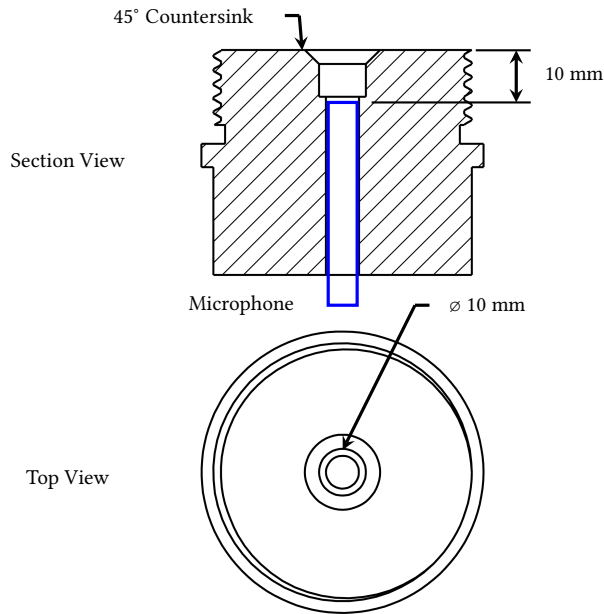
Figure 7.2: Example shape and dimensions of the hard–walled countersunk cavity used in array 2 for this experiment. All three cavity types were mounted in similar holders, indicated by the cross–hatched area.

Two different plates were manufactured: one with 7 mm diameter holes for the flush-mounted microphones (array 1) and a second one (arrays 2–4) that is covered with a 500 thread per square inch (#500) stainless steel cloth with a thread diameter of 0.025 mm. Arrays 2–4 are the arrays for each cavity type, as defined in the *Cavity design* section. The second plate features 16 threaded holes of 50 mm diameter at the microphone positions, which allowed for different cavity inserts to be installed for each array. The center of the microphone distribution ($x = y = z = 0$ m) is located 0.8 m downstream of the nozzle exit plane in order to allow for the boundary layer along the plate to become fully turbulent. The flush-mounted reference microphones were mounted along the array center line ($z = 0$ m) with one at $x = 0$ m and the other was located upstream at $x = -0.4$ m , as seen in Fig. 7.1b.

7.2.3 Cavity Design

Three cavity geometries were designed to compare against the baseline flush-mounted microphone array, array 1. These cavities are subsequently referred to as arrays 2, 3, and 4. The cavities in array 2 are made of a poly-carbonate material and, therefore, feature hard walls. It features a 45° countersink at the top and has a diameter of 10 mm and a depth of 10 mm. The schematic of this cavity can be seen in Fig. 7.2. This geometry was chosen based on it being the most effective shape for attenuating TBL noise in the experiments discussed in Chapter 4. The cavity for array 3 features soft walls made of melamine foam. It has a conical shape and features 10 evenly distributed ridges. The

ridges were included to study whether this cavity's performance would be different than a perfectly conical cavity. These ridges were thought to better attenuate azimuthal modes [130]. Array 4 features cavities made of melamine foam with the same conical geometry as cavity 3 but without the ridges. The cavities of arrays 3 and 4 were installed in a threaded poly-carbonate insert with the same outer mold line as those from array 2. The cavities for arrays 3 and 4 are derived from a confidential design. The cavities of arrays 2, 3, and 4 were covered with the aforementioned stainless steel cloth.

7.2.4 Hot-wire Anemometry

Hot-Wire Anemometry (HWA) data were measured at 6 locations and for flow speeds of 20 and $34\,\mathrm{m\,s^{-1}}$. This was done to verify that the untripped boundary layer was turbulent and attached, especially near the upper edges of the plate. These 6 locations include three points along the top of the plate, two points along the center line, and one point just over a cavity, see Fig. 7.1b. The coordinates of these points are contained in Table 7.1 using the coordinate system defined in Fig. 7.1a. A calibrated *Dantec* 1-channel hot-wire probe was used. The sampling frequency was 50 kHz and each point was measured for 10 s. These measurements were performed for both the baseline flush-mounted array which was made of smooth poly-carbonate and for the other arrays which were covered by a stainless steel cloth to determine whether this cloth affected the boundary layer.

7.2.5 Acoustic Measurements

A single Visaton K 50 SQ speaker [195] was mounted at a distance 0.8 m normal to the array. This position is outside of the flow to avoid additional noise sources due to shear layer impingement. It was located 0.65 m downstream from the nozzle outlet (at $x = -0.15\,\mathrm{m}$), and aligned with the axis of the jet, as seen in Fig. 7.1a. The speaker has a baffle diameter of 45 mm and an effective piston area of $1250\,\mathrm{mm^2}$. The frequency response ranges between 250 Hz and 10 kHz and a maximum power of 3 W. The speaker was used to emit white noise with an overall sound pressure level ($L_{\mathrm{p,overall}}$), measured at the array center (without flow), of 64 dB.

The sampling frequency of the acoustic recordings was 51.2 kHz. The signal was sampled for a duration of 45 s. CFDBF, as described in Chapter 2, was applied to the acoustic data with diagonal removal. The CSM is calculated using 4096 samples with a 50% overlap using Hanning windowing. The scan grid is located 0.8 m away from the array in the z direction, at the speaker plane, and centered at the origin of the coordinate reference system shown in Fig. 7.1a. The scan grid is 1 m × 1 m with a spacing between scan points of $\Delta x = \Delta z = 0.01\,\mathrm{m}$. The frequency spectra were obtained per microphone and by integrating the source maps using the Sound Power Integration (SPI) technique within a region of integration (ROI) [127, 189, 196, 197] covering the speaker's position. The acoustic spectra, shown in subsequent sections, are presented for the frequencies between 250 Hz and 10 kHz because the beamforming array was optimized for a maximum frequency of 10 kHz and due to the maximum frequency response of the speaker.

7.2.6 Distributed Acoustic Source

A distributed line source was generated at the trailing edge of a flat plate mounted at $z = 0.35\,\mathrm{m}$ from the microphone array plane. The flat plate was mounted along the jet axis
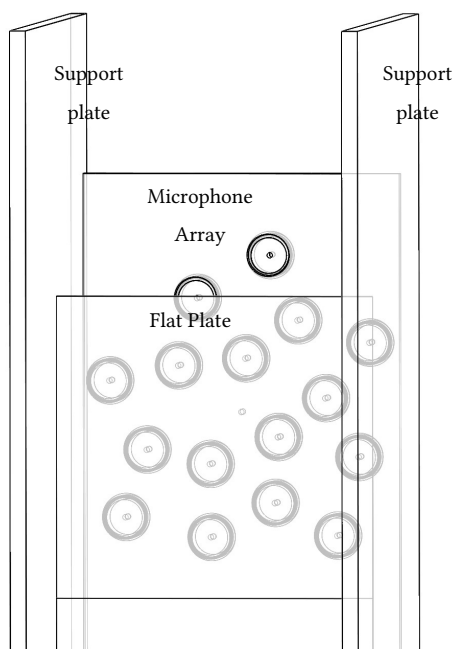
Figure 7.3: Flat plate mounted used for distributed acoustic source with array 4 pictured.

and held by two support plates, as shown in Fig. 7.3. The plate was 0.4 m wide and 1.0 m long and was mounted with a 0° angle of attack. The trailing edge had a thickness of 1 mm and was located at $x = 0.16$ m downstream of the array center point. The flat plate was tripped at 5% of the chord from the leading edge and the estimated boundary layer displacement thickness at the trailing edge, $\delta^\star$ is 0.0028 m, from the expression, $\delta^\star = \frac{0.048x}{\mathrm{Re}^{1/5}}$, where x is the streamwise position and Re is the chord-based Reynolds number [198]. This plate was chosen to provide a more representative test case [199] for aeroacoustic applications. However, the details with respect to the noise generating mechanisms by this trailing edge are beyond the scope of this chapter.

7.3 Experimental Results

7.3.1 Boundary Layer Measurements

The boundary layer properties calculated from the HWA measurements show that the boundary layer characteristics are consistent at the several spanwise and streamwise positions on the array. Table 7.1 lists the measurement locations as well as the boundary layer thicknesses δ_{99}, displacement thicknesses $\delta^\star$, momentum thicknesses Θ, and the shape factors H. The data shown were measured for a free stream flow velocity of $U_\infty = 20\,\mathrm{m\,s^{-1}}$ for the array covered with the stainless steel cloth. Measurements were also taken for the $U_\infty = 34\,\mathrm{m\,s^{-1}}$ case in order to verify consistency in the boundary layer characteristics at different velocities. Additionally, measurements were taken for array 1 which has a smooth surface to quantify the difference due to the surface roughness. For the $20\,\mathrm{m\,s^{-1}}$ case with

stainless steel cloth covering, the boundary layer was turbulent as defined by the shape factor, H, being between 1.2 and 1.4 for all cases indicating a turbulent flow regime. The regions near the spanwise edges of the plate (points 4 and 6) show no significant changes from the flow near the plate center line. The HWA measurements taken for $34\,\mathrm{m\,s^{-1}}$ are similarly turbulent and consistent across the array. The values for the smooth array 1 are not significantly different from those of the array covered with the stainless steel cloth. For the stainless steel covered array for the $34\,\mathrm{m\,s^{-1}}$ case, the TBL has a shape factor of $H = 1.29$ and boundary layer thickness of $\delta_{99} = 32.4$ mm as measured at point 4. For the smooth baseline array 1, the characteristics are: $H = 1.31$ and $\delta_{99} = 36.4$ mm. H has an estimated 95% confidence interval of ± 0.1 and δ_{99} has an estimated confidence interval of ± 3.9 mm. This consistency between the different cases, reduces the likelihood of any differences between arrays being attributable to differences in the TBL that forms over the stainless steel cloth covered arrays and the baseline case.

Table 7.1: Hot-Wire Anemometry measurement locations with boundary layer statistics for the $U_\infty = 20\,\mathrm{m\,s^{-1}}$ and $34\,\mathrm{m\,s^{-1}}$ cases for the stainless steel cloth covered array used for arrays 2, 3, and 4.

	Point 1		Point 2		Point 3		Point 4		Point 5		Point 6	
x, m	-0.158		-0.158		0.0		0.197		0.197		0.197	
z, m	0.040		0.0		0.0		0.0		-0.170		0.170	
U_∞, $\mathrm{m\,s^{-1}}$	20	34	20	34	20	34	20	34	20	34	20	34
δ_{99}, mm	29.4	33.4	27.7	33.5	33.0	35.4	31.8	32.4	44.5	41.3	39.2	34.9
$\delta^\star$, mm	4.21	4.25	3.74	4.34	4.94	5.19	4.49	4.60	3.59	4.08	4.42	3.78
Θ, mm	3.23	3.28	2.95	3.41	3.75	3.97	3.45	3.56	2.96	3.34	3.58	3.11
H	1.30	1.29	1.27	1.27	1.32	1.31	1.30	1.29	1.21	1.22	1.23	1.22

7

7.3.2 Turbulent Boundary Layer Noise Attenuation

The baseline flush-mounted microphone array (array 1) presents the highest TBL noise levels. This is expected behavior as the TBL pressure fluctuations were impinging directly on the microphones. All three cavity geometries considered in this chapter have a significant effect on the measured TBL noise. Figure 7.4a shows the one-third-octave band TBL spectra for the flush-mounted microphone and each cavity for both flow velocities considered. Figure 7.4b depicts the relative reduction in TBL level with respect to the values measured by array 1, i.e, $\Delta L_p = L_{p_{\mathrm{cavity}}} - L_{p_{\mathrm{array\,1}}}$, in one-third-octave bands for arrays 2, 3, and 4. These results represent the average spectra measured by the 16 microphones in each array (without applying beamforming) and were obtained without an acoustic source being present, i.e., simply with the wind tunnel operating at the velocities specified. For the case of $20\,\mathrm{m\,s^{-1}}$, array 2 provides a maximum reduction in TBL noise of 25 dB between 3 kHz and 4 kHz, whereas arrays 3 and 4 show an even better performance, demonstrating a reduction of 40 dB between 2.5 kHz and 6 kHz. The TBL attenuation increases with frequency due to the increasing effectiveness of the cavity. For the higher flow velocity case
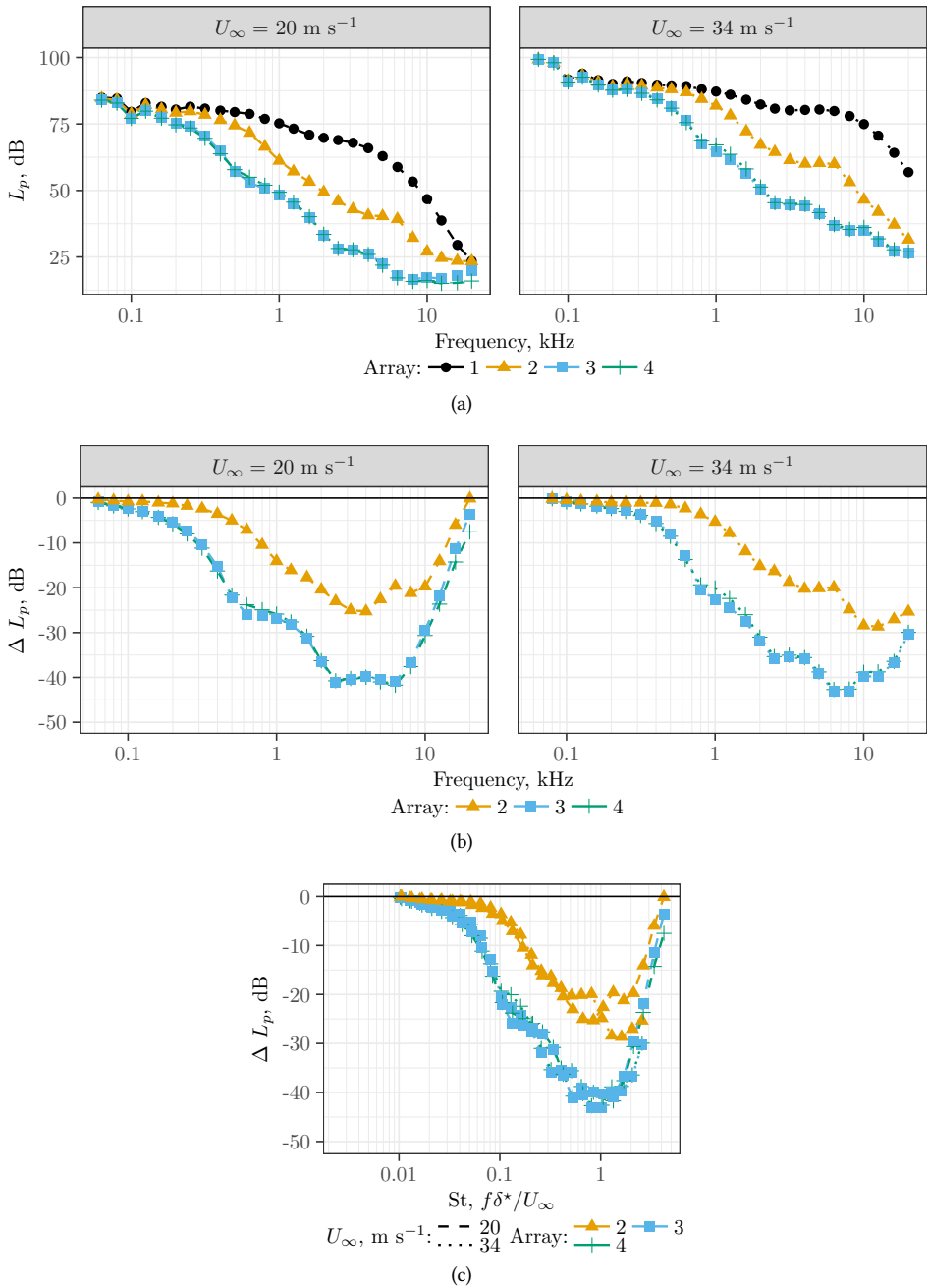
Figure 7.4: Relative increase in the attenuation of TBL spectral energy of the averages over 16 microphones for arrays 1, 2, 3 and 4 for $U_\infty = 20\,\mathrm{m\,s^{-1}}$ and $34\,\mathrm{m\,s^{-1}}$. a) Measured TBL spectra, absolute frequencies, b) Change in spectra with respect to array 1, absolute frequencies, c) Change in spectra with respect to array 1, non-dimensional frequencies (St).
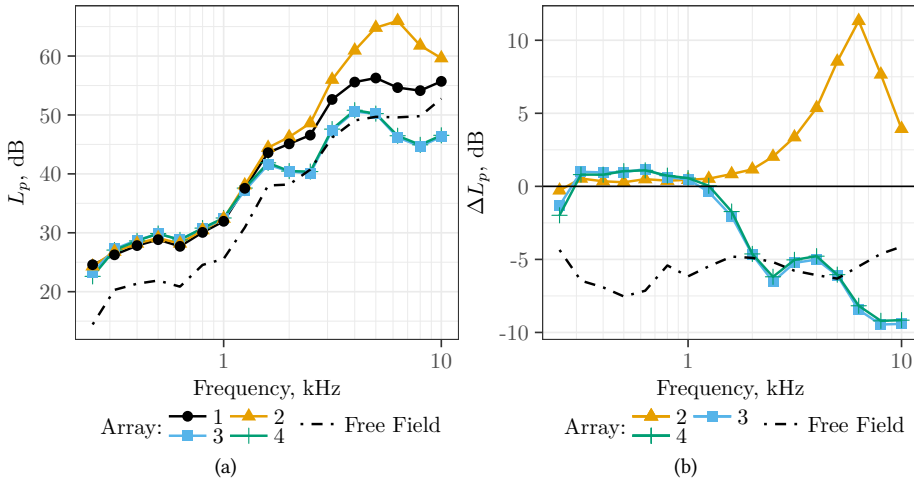
Figure 7.5: a) Comparison of the SPI one-third-octave band spectra emitted by the speaker by the four arrays with no flow ($U_\infty = 0$ m s^{-1}) and the measurements taken by a free–field microphone. b) Relative ΔL_p values with respect to array 1 for arrays 2–4 and with respect to a single flush microphone for the free-field case.

of 34 m s^{-1}, all the curves shift to higher frequencies and provide slightly higher maximum reductions in TBL noise. Figure 7.4c contains the same values as Fig. 7.4b but with the frequency axis expressed in terms of the Strouhal number, St $= f \delta^\star / U_\infty$, based on the free stream velocity and a reference distance of the boundary layer displacement thickness, $\delta^\star$ as measured at the array center, point 4 as seen in Fig. 7.1b. A very good agreement is observed for the two sets of curves at different flow velocities, as expected, except for array 2 for St ≥ 0.4 indicating that the behavior in this region may be dominated by acoustic behavior given its similarity to the acoustic transmission function seen in Fig. 7.5b. This Strouhal number corresponds to a frequency of 6 kHz, which will be discussed in the next section.

In order to increase the SNR of the acoustic measurements, the cavities' effect on the acoustic measurements with respect to the free-field must be smaller than that of TBL. This relationship will be discussed in the next subsection.

7.3.3 Acoustic Measurements with the Speaker without Flow

Figure 7.5a shows the one-third-octave band spectra obtained by each array for the case with the speaker emitting white noise with no flow. A microphone placed in the free-field was used to characterize the signal. The free-field measurements were made by placing a free-field microphone on a tripod at the same location as where the cavity closest to the array center would be. The spectra for the array measurements shown here were obtained from beamforming. However, similar results are obtained from averaging the spectra from the array microphones, since the source is almost in the center of the array and no flow is present. For frequencies higher than 2 kHz, array 2 presents higher L_p values than the baseline array 1 (flush-mounted microphones), whereas arrays 3 and 4 measure consis-
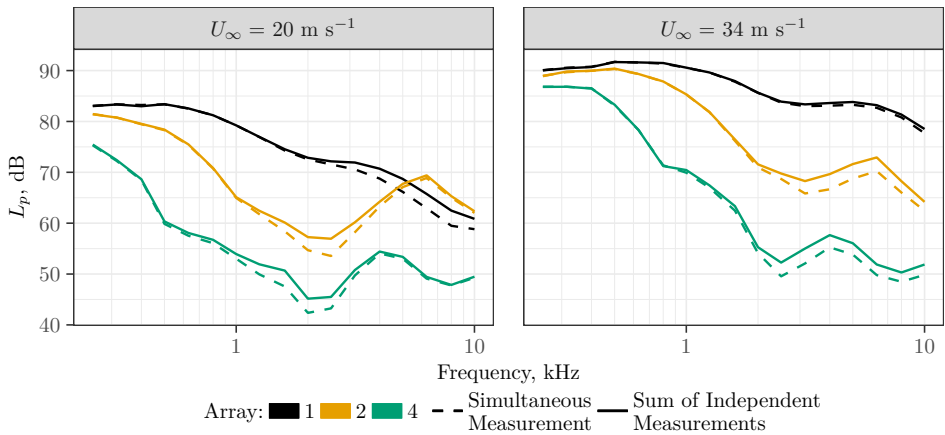
Figure 7.6: Comparison between the single microphone measurement for the case where the TBL was present simultaneously with the acoustic source and the summation of the independently measured TBL only and acoustic source only measurements. The summation of independent measurements was calculated by adding the acoustic powers, i.e., before transforming to the decibel scale. Array 3 is not shown to improve readability.

tently lower L_p values. Figure 7.5b shows the relative values of $\Delta L_p = L_p - L_{p,\text{Array 1}}$ of arrays 2–4 with respect to array 1 as well as the free–field microphone. The results for the free-field microphone indicate the expected 6 dB increase for the baseline array due to the doubling of the pressure at the interface due to the reflection. As a general trend, the differences in L_p for the arrays seem to increase for higher frequencies, achieving maximum ΔL_p values of 11.2 dB for array 2 at 6.3 kHz and a minimum of -9.3 dB for arrays 3 and 4 at 8 kHz. The sound amplification observed from array 2, is most likely due to standing waves amplified by the hard walls in the cavity. This acoustic excitation was also observed in a modal analysis performed using the COMSOL finite element package (not shown here). The sound reduction for the case of arrays 3 and 4 is due to the sound absorbing material reducing these standing waves and the cavity shape attenuating the acoustic signal.

It is evident that the cavities influence the measurement of the signal of interest. To account for this, the measured ΔL_p can be used to correct acoustic array measurements. This was performed for the speaker with flow and distributed noise sound measurements discussed later in sections 3.4 and 3.5. Given that the previous section shows that the cavities reduce the TBL by 25 to 40 dB which is more than their effect on the acoustic signal, the SNR is increased with all cavities.

7.3.4 Acoustic Measurements with the Speaker and Flow

Individual Microphone

The combined effect of the cavities on the TBL noise and acoustic measurements is discussed in this section. Since the TBL is attenuated more than the acoustic signal by the cavities, an improvement of the SNR is expected. Figure 7.6 shows the independence of the acoustic signal from the hydrodynamic TBL noise. This is evident from the close agreement of the measurements for the simultaneous presence of the TBL with the acoustic
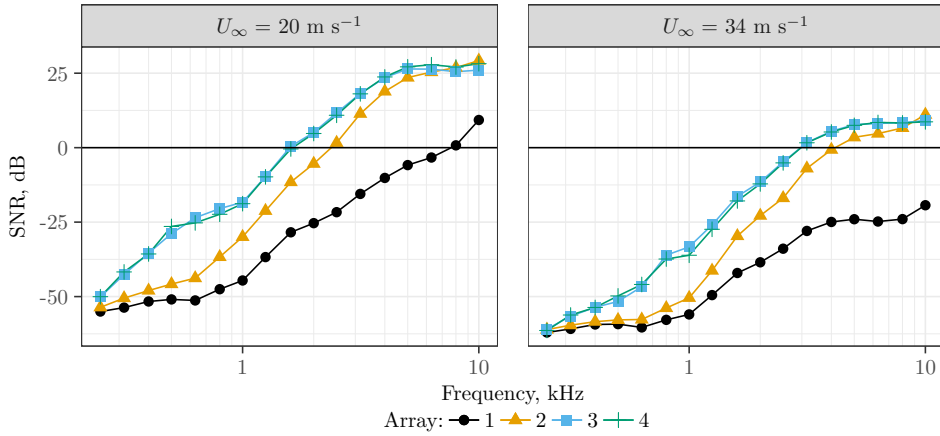
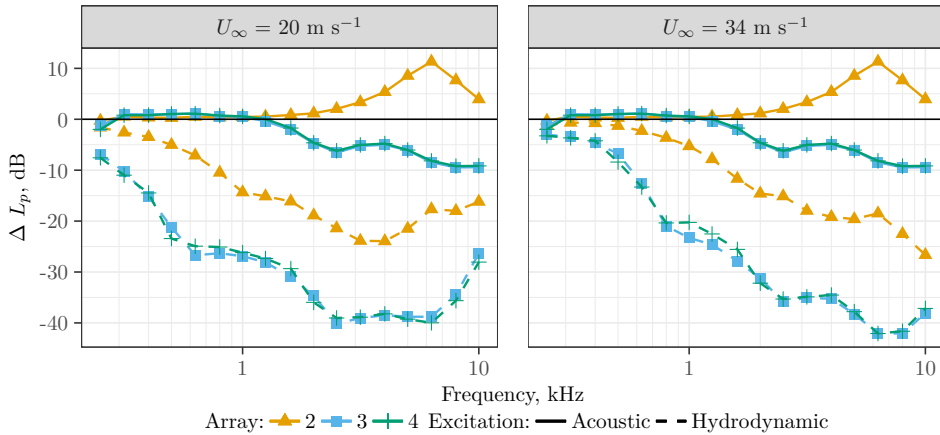Figure 7.7: SNR for a single microphone for each array for the $20\,\mathrm{m\,s^{-1}}$ and $34\,\mathrm{m\,s^{-1}}$ cases.

Figure 7.8: Acoustic and hydrodynamic transfer functions for the individual cavities for the $20\,\mathrm{m\,s^{-1}}$ and $34\,\mathrm{m\,s^{-1}}$ cases.

source and the summation of the independently measured TBL only and source only cases. The summation is calculated as the sum of acoustic powers, i.e., before transforming to the decibel scale,. With this assumption, we can calculate the SNR as SNR = $L_{p,\text{signal}} - L_{p,\text{TBL}}$ with $L_{p,\text{signal}}$ being the level of the acoustic signal measured without flow (Fig. 7.5a) and $L_{p,\text{TBL}}$ being the TBL noise measured without the speaker (Fig. 7.4a). The results are shown in Fig. 7.7. From this figure we see a significant improvement in SNR due to the cavities with a dependence on flow speed. The maximum SNR for the $20\,\text{m s}^{-1}$ case is $25\,\text{dB}$ and for the $34\,\text{m s}^{-1}$ case is a much lower $8\,\text{dB}$, which is expected since TBL noise scales with velocity. Also shown in this figure is the gain in frequency range at which the acoustic signal is measurable due to the cavities. Although SNR is an important metric it is dependent on the signal level (and also the background noise level). It is more important to look at the transfer function for the acoustic and hydrodynamic cases.

This is depicted in Fig. 7.8, where it is shown that the cavities attenuate the hydrodynamic noise from the TBL more significantly than their effect on the acoustic signal. Also in the low frequency range the TBL fluctuations are found to be attenuated while there is minimal effect on the acoustic signal. The transfer function for the acoustic signal shows a different shape compared to that of the TBL pressure fluctuations. This highlights the fact that the acoustic and hydrodynamic induced fluctuations measured by the microphone within the cavity have different mechanisms. For frequencies below $3\,\text{kHz}$, the hydrodynamic component of the TBL noise is dominant as evident by its different behavior when compared to the acoustic wave case. However, above $3\,\text{kHz}$, the TBL measurements show a slightly similar behavior as for the acoustic only case suggesting that the acoustic component of the TBL noise may be dominant at the microphone position. This is especially noticeable for the peak at $6\,\text{kHz}$ for array 2. A similar conclusion can be drawn from Fig. 7.4c where a collapsing curve with respect to the Strouhal number indicates hydrodynamic behavior and deviations suggest acoustic phenomena are present.

Microphone Array

The increase in SNR due to the cavities is further improved by the application of CFDBF to the entire microphone array. Figure 7.9 illustrates the source map plot of each array for the case with $U_\infty = 34\,\text{m s}^{-1}$ for the $2\,\text{kHz}$ one-third-octave band. In this case the speaker is emitting sound and flow is present over the array. The integrated frequency spectra over a ROI, defined as square $0.2\,\text{m} \times 0.2\,\text{m}$ box centered at the speaker location, are obtained with the SPI method [127, 196, 197]. The acoustic array data were also processed by using EHR-CLEAN-SC [148, 200] and functional projection beamforming [174, 201], but no major differences were found in comparison with CFDBF. The beamwidth and dynamic range were shown to be independent of cavity geometry and correspond with predictions made during the array design process [202].

For arrays 1 and 2 (Fig. 7.9a and 7.9b), the source localization fails due to the poor SNR at this frequency band. The L_p values of array 1 are also considerably higher than for the other arrays due to the dominance of TBL noise. Arrays 3 and 4 (Fig. 7.9c and 7.9d) provide similar source maps with the speaker clearly identified at its correct location. Array 3 provides a slightly cleaner source map, with fewer and lower sidelobes.

Figure 7.10 depicts the source maps for the case with $U_\infty = 34\,\text{m s}^{-1}$ but now for the $4\,\text{kHz}$ one-third-octave band. Once again, array 1 (Fig. 7.10a) is not able to properly localize the speaker due to the poor SNR. The L_p values are again considerably higher than
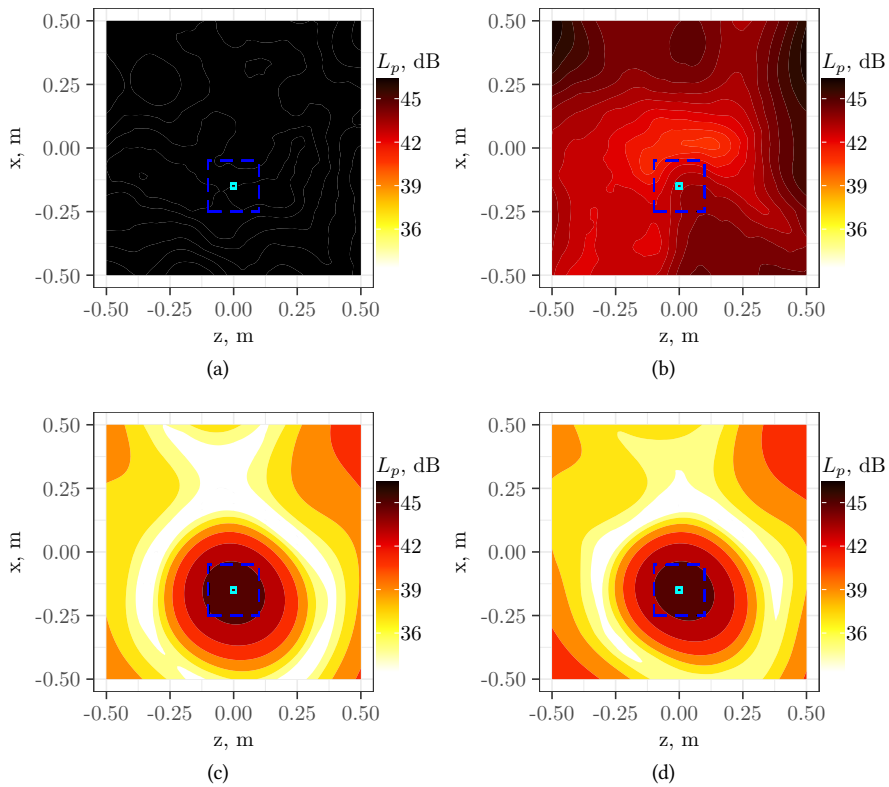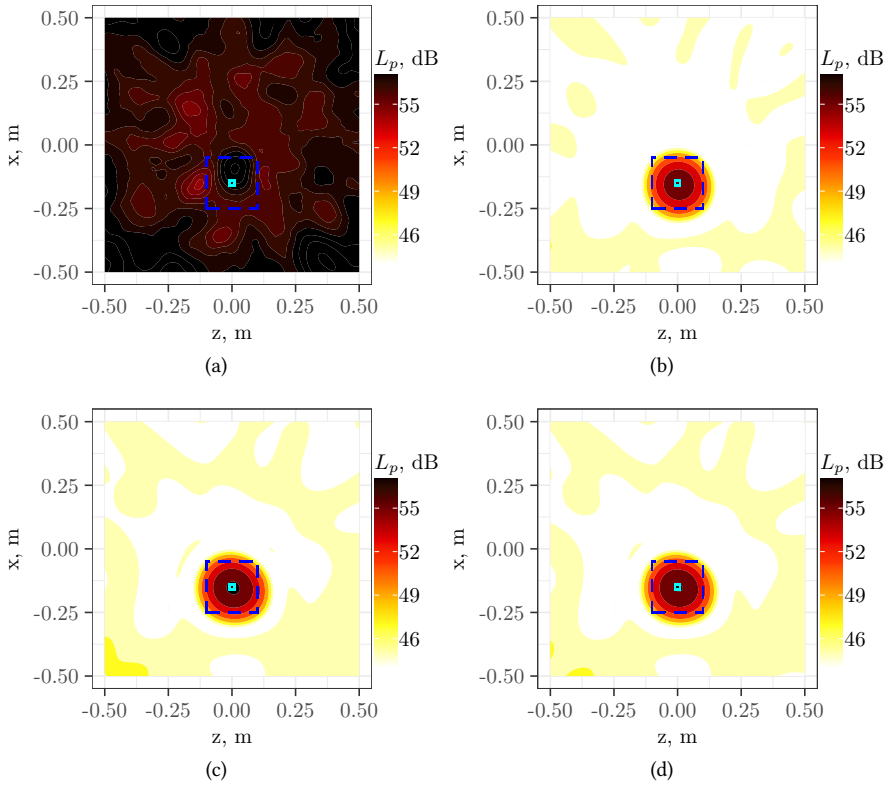
Figure 7.9: CFDBF source maps for the case with the speaker for the 2 kHz one-third-octave band and $U_\infty = 34\,\mathrm{m\,s^{-1}}$ for a) array 1, b) array 2, c) array 3, and d) array 4. The ROI is depicted as a dashed blue square. ΔL_p correction applied.

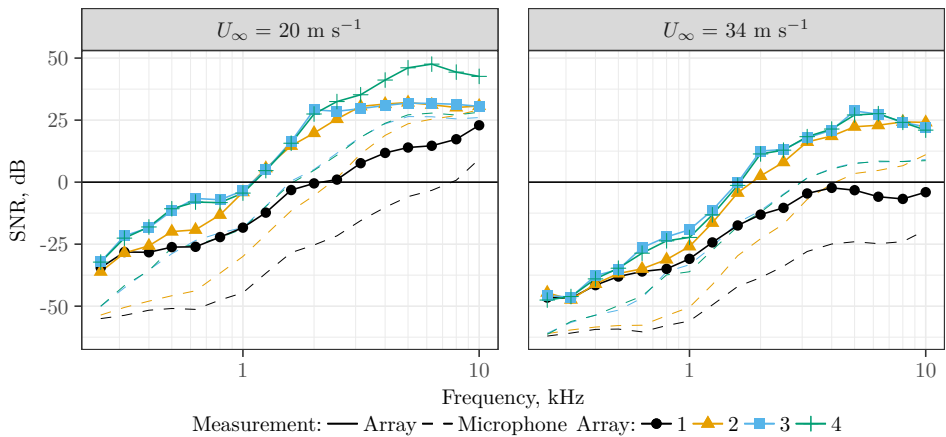Figure 7.10: CFDBF source maps for the case with the speaker for the 4 kHz one-third-octave band and $U_\infty = 34\,\mathrm{m\,s^{-1}}$ for a) array 1, b) array 2, c) array 3, and d) array 4. The ROI is depicted as a dashed blue square. ΔL_p correction applied.

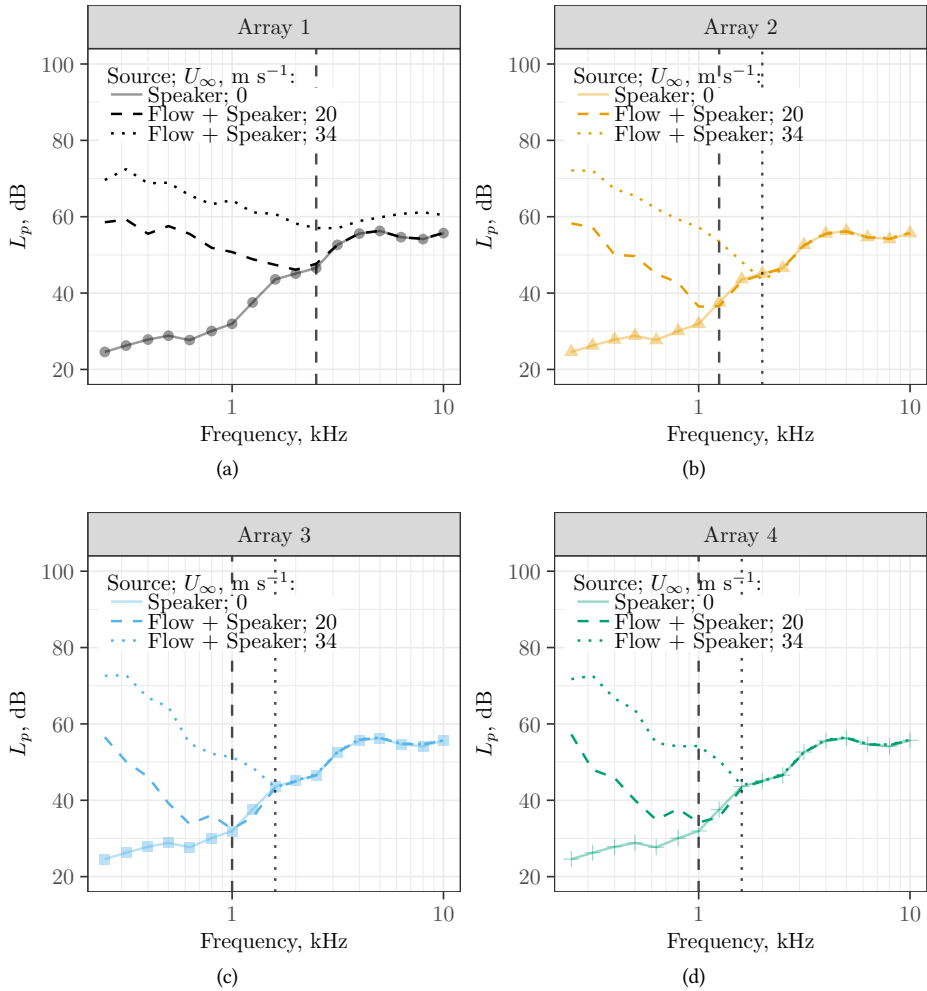Figure 7.11: SNR for each array when using CFDBF and for the single microphone baseline for the $20\,\mathrm{m\,s^{-1}}$ and $34\,\mathrm{m\,s^{-1}}$ cases.

Figure 7.12: Comparison of the one-third-octave band spectra emitted by the speaker with the TBL noise spectra for $U_\infty = 20$ m s^{-1} and $U_\infty = 34$ m s^{-1} with and without the speaker as measured by beamforming at the same source location: a) array 1, b) array 2, c) array 3, and d) array 4. Acoustic calibration from Fig. 7.5b is applied to all cases. Vertical lines are the frequency for each velocity at which the signal is detected.

for the rest of the arrays. This time, arrays 2–4 (Fig. 7.10b-d) offer very similar source maps with the speaker clearly identified at its correct location and with similar sidelobe patterns.

To quantify the SNR increase due to the application of CFDBF, a similar approach as in the previous section was taken. Now $L_{p,\text{signal}}$ is obtained from the integration of the source map for the source only case and $L_{p,\text{TBL}}$ is obtained from the integration of the source map for the flow only case at the same source location. Figure 7.11 highlights the improvement over the single microphone SNR. The application of beamforming improves the SNR by a maximum of 20 dB and the usable frequency range increases significantly. This figure also shows the frequency range in which we can reconstruct the source level from the beamforming plot. For determining these levels, the correction for the acoustic transfer function (Fig. 7.5b) was applied.

Figure 7.12 shows the impact beamforming coupled with different cavity designs has on acoustic measurements for all arrays. This figure also indicates the minimum frequency threshold for being able to reconstruct the correct source level. The signal of interest is represented by the solid lines which are the one-third-octave band spectra emitted by the speaker with no flow ($U_\infty = 0 \text{ m s}^{-1}$). The frequency threshold is defined as the one-third-octave band where the difference between the case with flow and the case without flow is less than 3 dB. These are denoted with a vertical short and long dashed lines, for the cases with $U_\infty = 20 \text{ m s}^{-1}$ and 34 m s^{-1}, respectively. However, near these frequency thresholds, localizing the sound source with beamforming is still challenging due to the fact that the acoustic signal is within 3 dB of the TBL noise. For array 1 (Fig. 7.12a), the sound levels emitted by the speaker are lower than those of the TBL noise for the 34 m s^{-1} case which means the baseline case cannot detect the signal of interest. Array 2 is a clear improvement, detecting the signal after 1.25 kHz for 20 m s^{-1}, and after 2 kHz for the 34 m s^{-1} case. Arrays 3 and 4, with the melamine walls, reconstruct the signal after 1 kHz and 1.6 kHz for the 20 and 34 m s^{-1} cases, respectively. For the low frequencies it is not possible to retrieve the signal of interest for this case due to the low signal levels with respect to the TBL noise levels.

The three cavity geometries enable the source to be measured at a lower frequency threshold, which directly corresponds to a decrease in the measured TBL noise level. Since arrays 3 and 4 reduced the measured TBL noise levels the most, by 40 dB, they are able to identify the source at a lower frequency than array 2. This is despite the fact they slightly attenuate the acoustic signal (Fig. 7.5). The microphone arrays and acoustic imaging techniques allow for the extraction of accurate sound pressure levels even in conditions where a single microphone would have negative SNR values [189, 203]. This ability is, nonetheless, limited to certain SNR values depending on the array geometry and experimental conditions, as well as the number of microphones and data acquisition time [56]. In order to evaluate a more practical case, a distributed acoustic source with higher levels at these low frequencies was investigated in the next section.

7.3.5 Distributed Acoustic Source Measurements

The source maps for the flat plate immersed in a flow with a velocity of 34 m s^{-1} and the 4 kHz one-third-octave band are shown in Fig. 7.13. The flat plate is denoted with cyan lines and the ROI is depicted as a dashed blue rectangle. Similar to the test with the
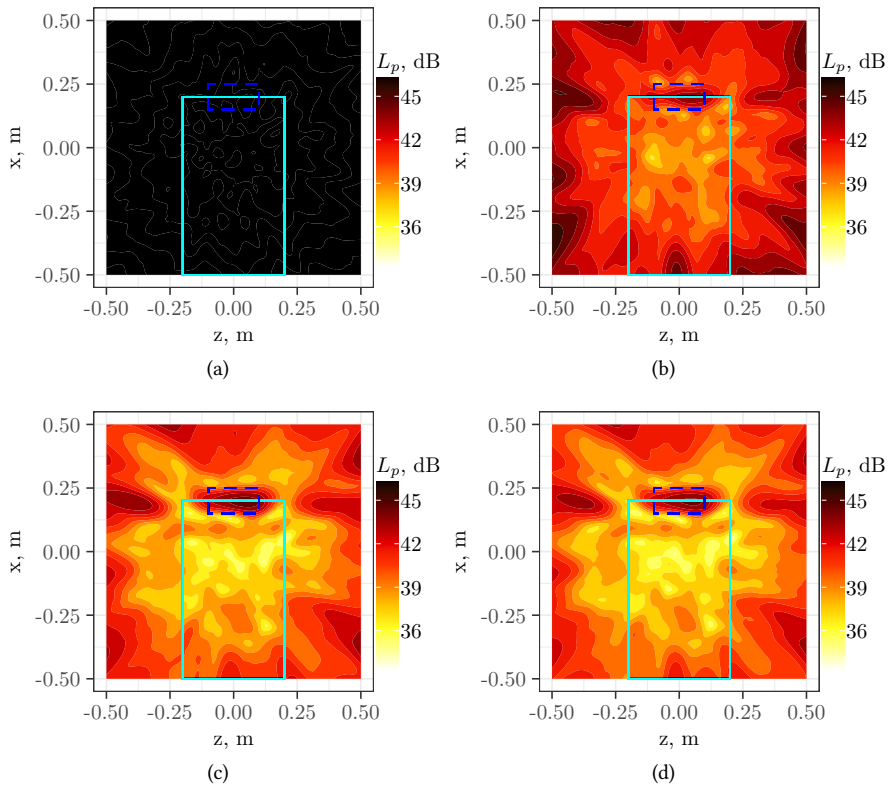
Figure 7.13: CFDBF source maps for the test with the flat plate for the 4 kHz one-third-octave band and $U_\infty = 34$ m s^{-1} for a) array 1, b) array 2, c) array 3, and d) array 4. The flat plate is denoted with cyan lines and the ROI is depicted as a dashed blue rectangle. ΔL_p correction applied.
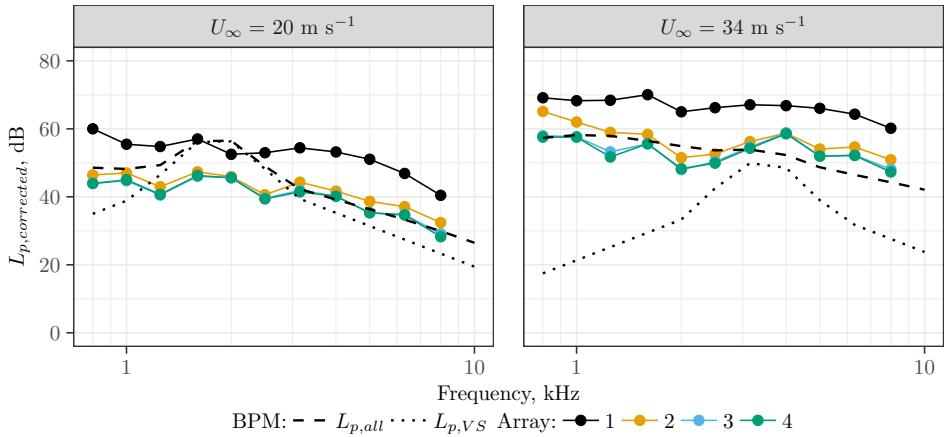
Figure 7.14: One-third-octave band spectra emitted by the trailing edge of the flat plate integrated within the ROI for the four arrays and for $U_\infty = 20 \text{ m s}^{-1}$ and $U_\infty = 34 \text{ m s}^{-1}$ compared with the BPM model. $L_{p,all}$ is the total BPM prediction and $L_{p,VS}$ is the predicted vortex shedding contribution. The L_p values are referred to the baseline of array 1 using the ΔL_p correction shown in Fig. 7.5b.

speaker, array 1 is not able to correctly localize the distributed noise source generated by the flat plate's trailing edge due to the insufficient SNR. Array 2 shows a distributed sound source along the trailing edge, together with the horizontal reflections due to the support side plates as well as their self noise. Arrays 3 and 4 perform similarly, but the distributed source at the trailing edge is more distinct than the array 2 source map.

The one-third-octave band spectra integrated within the ROI covering the trailing edge of the flat plate (see dashed blue rectangle in Fig. 7.13) are depicted in Fig. 7.14 for the four arrays and the two flow velocities. The L_p values shown are referred to the baseline of array 1 using the ΔL_p correction shown in Fig. 7.5b. In addition, the spectra were corrected in order to consider a normalized span of 1 m given that the ROI is 0.3 m wide compared to the 0.4 m wide plate. Additionally, the spectra were reduced by 6 dB to account for the differences between the array and the free-field measurements, see Fig. 7.5b. It can be observed that the spectra of arrays 2 to 4 are in good agreement for the case with $U_\infty = 20$ m s^{-1} (Fig. 7.14a) throughout the whole frequency range. For the case with $U_\infty = 34$ m s^{-1} (Fig. 7.14b), the spectrum measured by array 2 presents L_p values up to 7 dB higher than those by arrays 3 and 4, especially at lower frequencies. This is most likely due to the lower TBL noise attenuation by array 2, compared to arrays 3 and 4 (see Fig. 7.12). Array 1, on the other hand, shows consistently higher values (up to 15 dB higher for some frequency bands) than the other arrays. This is due to the poor SNR of this array, which does not allow for the correct identification of the trailing-edge noise.

The distributed source acoustic measurements are compared against the Brooks, Pope and Marcolini (BPM) semi-empirical model [23]. The model predicts the turbulent boundary layer trailing edge noise and vortex shedding noise contributions among others. The total L_p predicted for the flat plate is in good agreement with that measured by arrays 2–4, as seen in Fig. 7.14. These arrays detected a spectral peak at 2 kHz for the 20 m s^{-1} case and at 4 kHz for the 34 m s^{-1} case. These peaks agree with the BPM predictions for
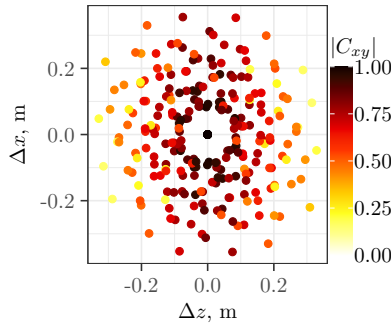
Figure 7.15:   Comparison of the coherence between all cavity locations with respect to all others, sorted by relative distance in the streamwise and spanwise directions. Coherence is calculated for the case with the speaker and flow, $U_\infty = 34 \, \mathrm{m \, s^{-1}}$ for array 4 at 4 kHz.

the vortex shedding contribution. The baseline array, array 1, was unable to identify any vortex shedding. However, these measurements are limited by the high noise levels from the TBL.

7.3.6 Effect of Cavity Geometry on Signal Coherence

CFDBF is based on the phase delays of the arrival of an acoustic wave at different microphones. Therefore losses of coherence, C_{xy}, within the travel time of the sound waves are detrimental for the beamforming results. This is why the effect of cavity geometry on the coherence is important to quantify. The coherence of each microphone signal with respect to that of the center microphone, and with respect to all other microphone signals was calculated using Eq. 2.30.

The aim is to determine how the relative cavity locations, flow conditions, and cavity geometry influence the coherence of the acoustic signals and whether this affects the performance of acoustic imaging. Additionally, in order to determine whether further improvements in beamforming can be achieved, coherence weighting was investigated using the approach discussed in Ref. 192. The reasoning for applying this method is that due to the expected higher coherence of the optimal cavities, more microphones are part of the beamforming process. The microphone signals are multiplied by a weighting factor between 0 and 1 based on their relative coherence with the other microphones. This approach (results not shown here) did not lower the frequency threshold at which the signal could be detected. This is due to the fact that at SNR values near zero, the incoherent noise sources are at a similar level as the coherent sources. The resulting coherence weighting of the microphones reduces the weighting for all microphones and, thus, reduces the measured signal and noise levels equally.

Figure 7.15 depicts the coherence of all cavities compared against all others sorted with respect to their relative distances in the streamwise, Δx, and spanwise, Δz, directions. These results are with flow, $U_\infty = 34 \, \mathrm{m \, s^{-1}}$ and with the speaker for array 4 for the 4 kHz band. This figure is representative of all arrays when the acoustic signal is dominant. When the TBL is dominant, the coherence for all cavities is low, as expected. This representative figure shows that coherence across the array is consistent and that cavity
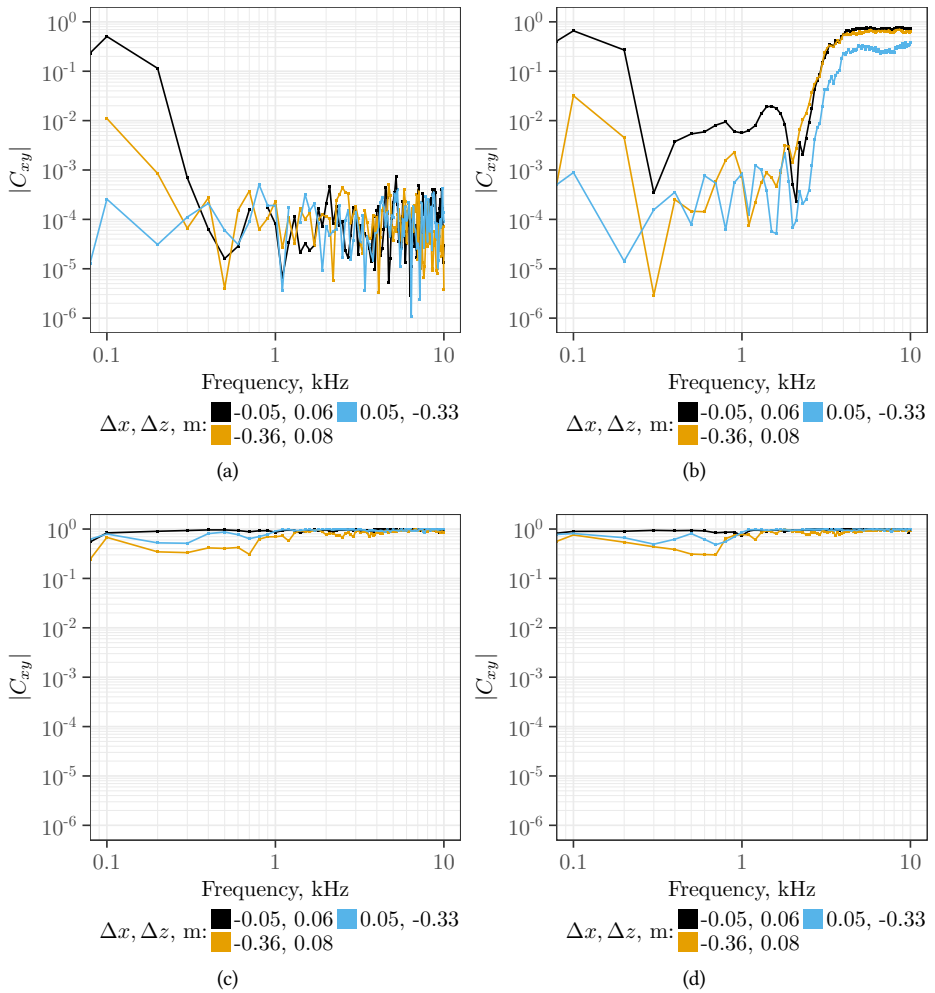
Figure 7.16: Coherence plotted with respect to narrow band ($\Delta f = 25\,\mathrm{Hz}$) frequencies for cavity pairs at three different separation distances. Coherence is calculated for the following cases: a) array 1, with the speaker and flow, $U_\infty = 34\,\mathrm{m\,s^{-1}}$; b) array 4, with the speaker and flow, $U_\infty = 34\,\mathrm{m\,s^{-1}}$; c) array 1, speaker only; and d) array 4, speaker only.

geometry has no detectable influence on the coherence. This behavior is similar for all other arrays. Looking more closely at two representative cases, Fig. 7.16 shows the coherence for array 1, Fig. 7.16a, and array 4, Fig. 7.16b, with respect to frequency for three different microphone pairs for the case with the speaker and $U_\infty = 34 \, \text{m s}^{-1}$. Figures 7.16c and 7.16d are the cases for arrays 1 and 4 respectively with the speaker only and no flow. The selected pairs are the two closest cavities ($\Delta x = -0.05 \, \text{m}$, $\Delta z = 0.06 \, \text{m}$), the largest streamwise distance ($\Delta x = -0.36 \, \text{m}$, $\Delta z = 0.08 \, \text{m}$), and the largest spanwise distance ($\Delta x = 0.05 \, \text{m}$, $\Delta z = -0.33 \, \text{m}$). At 100 Hz, flow noise is dominant and coherence is dependent on the boundary layer coherence lengths for both arrays. For array 4, the coherence values increase only once the TBL noise is 6 dB beneath the acoustic source's signal which occurs for frequencies higher than 2 kHz. Array 1 does not meet this threshold resulting in low coherence, irrespective of frequency. For comparison, the cases with only the speaker, Figs. 7.16c and 7.16d, show coherence values close to 1 for frequencies above 1 kHz. The conclusions drawn from this analysis are as follows:

- The resulting normalized coherence between microphones approaches 1 and is relatively consistent with respect to distance in the streamwise direction for arrays 2, 3, and 4.

- Due to potential three-dimensional flow effects present at the edges of the plate, the cavities near the edge, $|\Delta z| > 0.3 \, \text{m}$ have a reduced coherence value of 0.5.

- The coherence calculations for the cases with the acoustic source and without flow show that irrespective of distance, all cavities have a coherence of ≈ 1.

- Arrays 3 and 4 have higher coherence compared to array 2, which was higher than array 1, for the case with a speaker and flow.

- The trends with respect to relative distance are independent of the type of cavity employed.

Effect of Stainless Steel Cloth Covering
The stainless steel cloth that covers the cavities in arrays 2, 3, and 4 improves the SNR by reducing the influence of the TBL hydrodynamic fluctuations as shown previously in Fig. 7.4. Given the low acoustic impedance of the cloth, 0.15, normalized with respect to air, a negligible change in the acoustic signal's amplitude is expected due to the cloth. Figure 7.16d shows the relative effect of the cavity geometry and cloth on the acoustic signal. Compared with the baseline case, Fig 7.16c, where there is no cloth present, there is no significant change in coherence of the acoustic signal due to the cloth. Both arrays show coherence values close to 1 above 1 kHz and a reduction for lower frequencies where the acoustic signal amplitude is lower and outside of the speaker's intended frequency range. From these results it is concluded that the cloth has a negligible impact on the signal coherence and thus the acoustic beamforming results.

7.4 Summary

This work quantifies the impact of cavity geometry on the SNR, and on the accuracy of acoustic imaging results for microphone arrays. Three cavities, one with a hard–walled

countersink and two conical cavities with melamine walls, all covered with a high thread count stainless steel cloth, are compared with a baseline flush-mounted microphone array. Each array featured 16 microphones in the same layout. These arrays were mounted flush with an open jet wind-tunnel nozzle and used to measure white noise emitted by a speaker mounted outside of the flow and a distributed source from the trailing edge of a flat plate placed within the flow. Conventional frequency domain beamforming with diagonal removal was used to determine the effect cavity geometry has on the acoustic signal, TBL, and resulting SNR.

These cavities reduced the amount of measured TBL noise while minimizing the effect on the acoustic signal, thus increasing the SNR. The cavities with melamine foam (arrays 3 and 4) reduced the TBL noise by up to 40 dB compared to the flush-mounted array. The hard–walled cavity, array 2, reduced the TBL noise by up to 25 dB. However, the hard–walled cavity amplified the signal by 10 dB at certain frequencies due to an acoustic mode, whereas the soft walled cavities caused a reduction between 5 and 10 dB at certain frequencies compared to the flush array. Overall, the SNR was increased due to the TBL being attenuated more than the acoustic signal.

When comparing the hydrodynamic and acoustic transfer functions, the TBL's hydrodynamic phenomena appears to be dominant below 3 kHz. Above 3 kHz, its acoustic component begins to show similar behavior as the acoustic transfer function, seen for the speaker only case. However, the interplay between the TBL's hydrodynamic and acoustic components is complex and requires further study.

The resulting impact on SNR is that the CFDBF has an additional 20 dB improvement over the single microphone for the same cavity geometry. This improvement is seen in the beamforming source maps and integrated L_p where the recessed arrays detected the acoustic signal when the flush-mounted array could not. Moreover, arrays 3 and 4 detected the signal at a frequency threshold 400 Hz lower than array 2.

The coherence of the acoustic signal for all cavity geometries was consistent with respect to the cavity position in the array. The stainless steel covering has minimal impact on the acoustic coherence and, thus, on the beamforming performance. Coherence improves with frequency for arrays 2 to 4 due to the reduction of incoherent TBL noise.

The improvements using the cavities, especially in arrays 3 and 4, are also seen in the flat plate measurements. The source maps using these arrays successfully imaged the trailing edge noise whereas the baseline array did not. Additionally, these arrays identified a spectral peak from vortex shedding that agreed with the BPM model. The baseline case, array 1, was unable to distinguish these peaks from the TBL noise.

These results show that using an appropriately designed microphone cavity augments the acoustic imaging capabilities of a microphone array using CFDBF signal processing. Beamforming with diagonal removal reduces the incoherent TBL noise by up to 20 dB. Adding cavities further improves these measurements by reducing the TBL noise by an additional 40 dB for the melamine cavities. By using optimized cavity geometries with larger diameter microphone arrays with more microphones, even greater improvements to SNR are expected. This approach potentially enables testing of acoustic sources whose sound levels are near the background turbulent boundary layer noise levels. However, more work is needed on understanding the relationship between the hydrodynamic TBL behavior and the cavity geometry to better optimize these cavities.

8

Summary and Outlook

8.1 Summary

Cavities improve the signal–to–noise ratio (SNR) of acoustic array measurements. Increasing this SNR requires the realization of two design goals. First, the pressure fluctuations at the cavity bottom, which are generated by the presence of the TBL at the top of the cavity, must be minimized. Second, it is important to avoid acoustic signal loss and/or distortion as the acoustic wave propagates into the cavity. To address these two goals, this thesis develops a physical acoustic model, empirical models, acoustic finite element method (FEM) simulations, and computational fluid dynamic (CFD) simulations. This development was divided into four research objectives, as outlined in Chapter 1. A summary of these objectives follows:

1. Develop modeling techniques to identify the cavity geometric parameters that influence the attenuation of the turbulent boundary layer noise and affect the acoustic response of the cavities.

Chapters 3, 4, 5, and 6 describe four different modeling approaches to evaluate the TBL attenuation and the acoustic response of the cavity.

Chapter 3, describes a physical model, which decomposed the TBL pressure field modeled using the Corcos model, into a series of orthogonal acoustic modes. The output of this model showed that the TBL attenuation increases with increased aperture size and cavity depth. Furthermore, this model predicted an increase in attenuation when using sound–absorbing melamine as the cavity wall material. These trends agreed with experimental results. However, this model is limited to only cylindrical cavities with a constant cross–section.

The development of two empirical models to describe both the change in spectral energy and the change in SNR due to varying cavity geometries is discussed in Chapter 4. These empirical models were developed using a generalized additive model (GAM) approach applied to the pressure spectra measured at the bottom of twelve cavities, whose aperture sizes, depths, and variation in cross–sectional area, and covering were varied.

These models and the physical model identified the change in TBL attenuation with cavity depth, covering, and increasing aperture size.

Chapter 5 describes a FEM based simulation of the acoustic response of different cavity geometries when subjected to an incident plane. The cavity depth, aperture area, wall angle, countersink depth, presence of a covering, and wall material, were varied in the simulation. The results of this simulation closely matched experimental results.

The VLES CFD simulations, described in Chapter 6, applied the Lattice Boltzmann method to simulate turbulent flow over covered and uncovered cavities. These simulations were used to identify the relationship between cavity geometry, TBL hydrodynamic phenomena, i.e., vortex shedding and convection of turbulence, to the pressure spectra at the bottom of the cavities. The results of these simulations closely agreed with experimental results.

2. Quantify the impact of cavity geometric parameters on acoustic measurements and TBL attenuation.

Chapters 3, 4, and 6 quantified the changes in sound pressure level (L_p) due to varying cavity aperture size, depth, covering, wall angle, and wall material. Covering the cavity, increasing the aperture size, increasing the cavity depth, and forming the cavity out of sound−absorbing materials were shown to reduce the pressure fluctuations at the cavity bottoms. Covering the cavity reduces the energy of the pressure fluctuations by 10 to 20 dB at the bottom, when compared to the same cavity without a covering. Furthermore, these chapters show that the pressure spectral levels decrease with increasing cavity aperture size for covered cavities. Chapters 3 and 6 explain that this trend is because the proportion of TBL energy represented by higher−order cut−off modes increases for larger aperture cavities. These cut−off modes decay with depth as shown in Chapters 3 and 4. Finally, Chapter 3 suggested that sound absorbing melamine foam cavity walls reduce the spectral levels further. This was confirmed experimentally in Chapter 7.

The cavity acoustic response is addressed in Chapter 5. These simulations showed that the depth modes, also referred to as quarter−wavelength acoustic modes, are the dominant acoustic phenomenon present in the cavity, and they amplify the measured acoustic signal at the modes' respective harmonic frequencies. These simulations showed that the amplitude of the acoustic mode, quantified by its quality factor, Q, increases with increasing cavity depth and decreasing aperture size. However, covering the cavity with the stainless−steel cloth and decreasing the wall angle, i.e., to form a conical cavity, reduces the quality factor of the cavities and thus the acoustic response.

3. Identify the acoustic and hydrodynamic phenomena present in the cavities due to the presence of the turbulent boundary layer.

The relationship between the cavity geometry and the acoustic and hydrodynamic phenomena present in both the shear layer and within the cavity are presented in Chapter 6. Both uncovered and covered cavities are studied.

In uncovered cavities, the pressure fluctuations at the bottom are due to a combination of turbulence transported by cavity recirculation and pressure waves generated by impinging vortices. Recirculating flow produces and transports eddies, and is the dominant

mechanism for the production of hydrodynamic pressure fluctuations within uncovered cavities. This recirculation can be reduced with a countersink as its downstream angled wall redirects the recirculating flow away from the cavity bottom, reducing the turbulent pressure fluctuations at the bottom. The vortices shed by the leading edge can also be ingested by the cavity recirculation and transported towards the bottom. These vortices are also a source of acoustic noise because when these vortices impinge on the downstream wall, acoustic waves are produced.

Covering the cavities with an acoustically transparent covering eliminates vortex shedding within the shear layer and prevents flow from entering the cavities. The reduction in recirculation eliminates turbulence generation and transport towards the bottom thus reducing the pressure fluctuations within the cavity. This results in the TBL eddies convecting across the covering being the primary source of pressure fluctuations within covered cavities. When this pressure field is decomposed into orthogonal modes, the resulting modes match the acoustic mode shapes discussed in Chapter 3. These simulations showed that when the cavity is larger than the coherence length, the energy in the TBL pressure field is spread out to higher-order cut–off modes. This results in a greater reduction in pressure fluctuations at the bottom of the larger conical cavity.

4. Quantify the impact of cavities on the SNR when using acoustic imaging post-processing on a microphone array.

Chapter 7 quantifies the difference in SNR between a flush–mounted microphone array and three arrays when measuring an acoustic source with a TBL present over the arrays. Each of the three arrays consists of the following cavity geometries: a hard-walled countersunk cavity, a conical melamine foam cavity with azimuthally distributed ridges, and a conical melamine foam cavity with smooth interior walls. These arrays measured both the acoustic signal produced by a speaker placed outside the free–stream and the signal generated by the trailing edge of a flat plate immersed in the flow. These resulting measurements were post-processed with conventional frequency-domain beamforming (CFDBF).

CFDBF with diagonal removal reduced the TBL noise measured by an array by an additional 20 dB compared to a single microphone measurement from the same array. As a result, beamforming source maps from the cavity measurements detected the acoustic signal where the flush-mounted array could not. This chapter showed that the beamforming techniques to reduce incoherent noise, e.g., the TBL, are complimented by using cavities to attenuate the TBL noise at the microphone location and thus improve the aggregate SNR of acoustic array measurements.
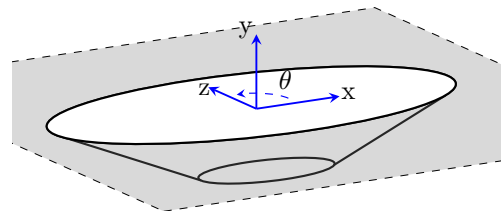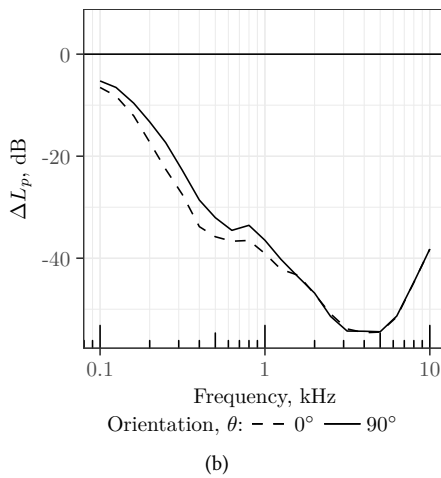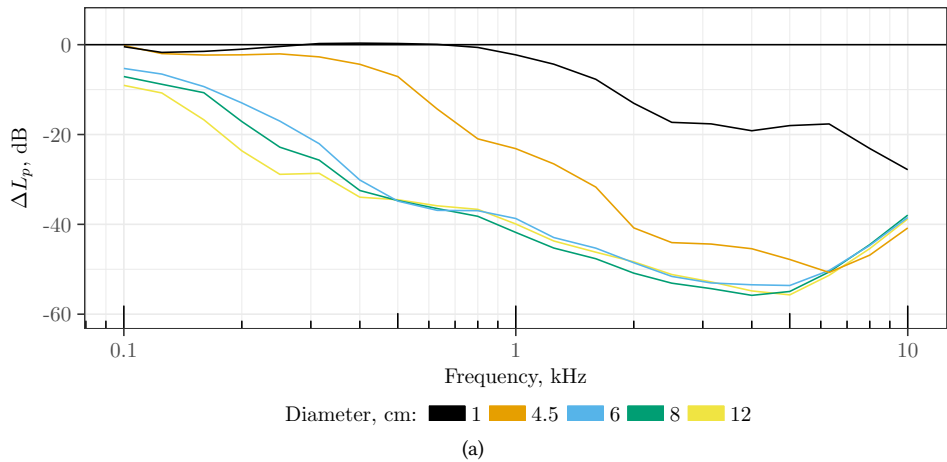
8

(a)

(b)

(c)

Figure 8.1: Measured change in spectra between a flush microphone and a microphone at the cavity bottom. a) ΔL_p due to increasing cavity aperture diameter. b) Effect of orientation for an elliptical cavity. c) Illustration of the elliptical cavity.

8.2 Outlook

8.2.1 Cavity Design

Improving the SNR of acoustic array measurements requires designing the cavity to attenuate the TBL–induced pressure fluctuations while minimizing distortion of the acoustic signal. Covering the cavities with an acoustically transparent material is an important design prerequisite before optimizing the cavity geometry. This covering is necessary because it nearly eliminates all hydrodynamic noise sources, e.g., recirculation of turbulence, within the cavity and thus the pressure field within the covered cavity is predominantly acoustic. Knowing that the pressure field is acoustic is advantageous as it is computationally less demanding to optimize the geometry while solving the acoustic wave equation as opposed to the Navier-Stokes equations. The work presented in this thesis used finely woven stainless–steel cloth, with a thickness of 0.025 mm and a weave opening size of 0.026 mm as the cavity covering. This material was selected because its mechanical properties simplify its installation and because it has a low acoustic transmission loss. While this material was shown to be effective, this work did not investigate alternate materials. Therefore, other materials or combinations of materials, such as Kevlar or thin sheets of foam may further attenuate the TBL pressure fluctuations at the cavity bottom.

The cavity aperture size is a critical design variable that reduces the TBL–induced pressure fluctuations. Larger diameter cavities, when covered, perform better than smaller diameter cavities. This trend is shown in Fig. 8.1a, which depicts the experimentally derived spectral levels decreasing with increasing aperture diameter. This trend is explained by the aperture size increasing relative to the spanwise and streamwise TBL coherence lengths. The pressure field for cavities larger than the coherence length will have multiple regions of positive and negative pressure due to the presence of multiple turbulent eddies above the cover. When this pressure field is decomposed into modes, as described in Chapters 3 and 6, more energy will be contained in higher-order modes. In contrast, cavities whose diameters are smaller than the coherence length have a nearly uniform pressure field. Thus, the decomposition will result in the first mode containing most of the energy. A cavity with more energy present in the higher–order cut–off modes will have lower spectral levels at the cavity bottom than a cavity that has more energy in the cut–on first mode. Thus, the aperture size should be optimized with respect to the TBL coherence lengths. However, Fig. 8.1a shows that, for cavities larger than 6 cm, the improvements due to increasing the cavity size only occur below 500 Hz and are less substantial compared to the improvement from 4.5 to 6 cm. This suggests that there is a limit at which increasing the cavity size is no longer a significant improvement.

Increasing the cavity size is a straightforward approach to improving the performance of cavities. However, since the TBL streamwise coherence length is larger than the spanwise coherence length (Fig. 2.9), the cavity aperture shape does not need to be axisymmetric to improve the attenuation of the TBL. One solution is to use elliptical cross–sectional shapes instead of circular ones. Figure 8.1b shows the spectra at the bottom of an elliptical cavity, illustrated in Fig. 8.1c., at two orientation angles, θ. When the major semi–axis is aligned with the streamwise direction ($\theta = 0°$), the spectrum at the bottom is lower than the spectrum of the cavity rotated 90°. The improved performance of the streamwise aligned ellipse highlights the potential of optimizing the cross–section shape to reduce the TBL pressure fluctuations.
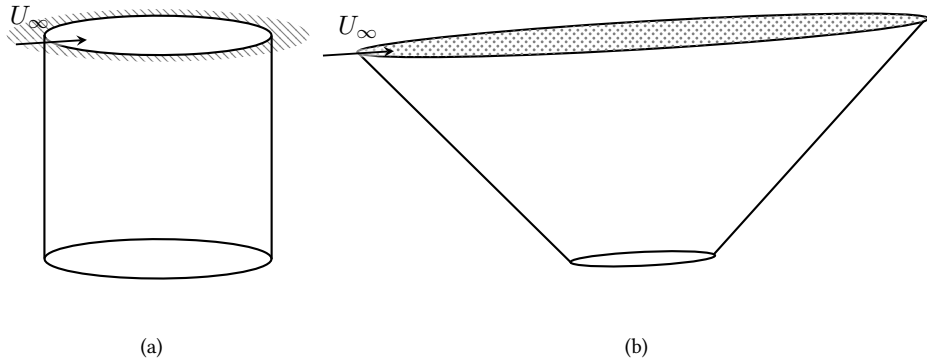
8

Figure 8.2: Comparison of cavity designs a) Original cylindrical cavity design. b) Suggested cavity design.

The depth of the cavities is another important design variable. Yet for depths greater than 1 to 2 cm additional reductions in the TBL induced spectra are minimal. This limited influence of depth occurs because the cut-off modes decay exponentially, and thus beyond 1 to 2 cm their influence is negligible.

The acoustic standing waves distort the acoustic measurements by amplifying the acoustic signal at the standing wave harmonic frequency. Depth–wise (longitudinal) standing waves are typically dominant in this application. While they can not be completely eliminated, their quality factor (amplitude) can be reduced and their harmonic frequency can be shifted to a preferred frequency using the following guidelines: first, increasing the depth decreases the harmonic frequency but increases the standing wave amplitude. Second, covering the cavity reduces the quality factor of these waves. Finally, angled cavity walls, e.g., a countersunk or conical shape, reduces the quality factor of these standing waves. Thus, larger aperture cavities with shallow depths and angled walls, as illustrated in Fig. 8.2b improve the acoustic response of the cavities compared to uncovered hard–walled cylindrical cavities, shown in Fig. 8.2a.

Forming the cavities out of sound-absorbing materials, such as melamine foam, has two benefits. First, it reduces the amplitude of the standing waves as well as the spectral levels of the TBL-induced pressure fluctuations. Second, it enables the cavity geometry to be optimized to minimize the acoustic response to be performed independently of the optimization to maximize the TBL attenuation. When a foam cavity is placed within a holder with hard walls, the acoustic response of the cavity is driven by the holder geometry and not the cavity geometry. Hence, the outer foam holder can be designed to minimize the acoustic response, while the inner foam cavity can be shaped to maximize the attenuation of the TBL pressure fluctuations. Further improvements may also be found by using different sound–absorbing materials to form the cavities. Melamine foam was used in this thesis but other materials or combinations of materials may further improve the attenuation of TBL noise, especially at lower frequencies.

8.2.2 Modeling Approach

Empirical, physical, finite element, and CFD simulations were used to model and identify the cavity geometric parameters that improve the cavity SNR. These modeling approaches give different insights into the physical phenomena that determine the acoustic and hydrodynamic response of the cavities. Additionally, each approach has its respective advantages and disadvantages regarding model fidelity, geometric constraints, and computational requirements.

Figure 8.3 shows the potential modeling approaches and the ones employed in this thesis to model the acoustic and hydrodynamic phenomena. The first branch, on the left, in Fig. 8.3 illustrates the potential modeling strategies for the TBL. Initially, the TBL was modeled with an acoustic physical model (Chapter 3), which identified the relationship between cavity depth, material, aperture size, and the amount of attenuation. Yet, this model is only suitable for specific geometries and does not account for the hydrodynamic phenomena. Thus, a VLES CFD simulation using the Lattice Boltzmann method was employed (Chapter 6). This simulation resolved the turbulent structures, i.e., vortices and eddies, as well as the recirculation patterns that determine the pressure fluctuations at the cavity bottoms. The results of these high fidelity simulations closely matched trends in experimental data. However, these simulations are computationally expensive which is not well suited for optimizing the cavity geometry.

The second modeling branch, on the right, shows the acoustic simulation options for the cavity acoustic response. Simulating the cavity response from the impingement of acoustic waves requires solving the Helmholtz equation, which can be performed with a physical model, a Lattice Boltzmann based simulation, or a FEM approach. The physical model requires that analytical solutions to the Helmholtz equation exist, which restricts which geometries can be studied and thus this approach was not performed in this thesis. The acoustic response can also be simulated using the Lattice Boltzmann method as this method features low dispersion and dissipation errors [204]. This approach was not used due to the computational requirements. Thus, a FEM model was used to solve the Helmholtz equation (Chapter 5), which can solve the wave equation in the frequency domain for geometries and pressure fields that lack analytical solutions.

One finding of this thesis, as discussed in Chapter 6, is that the pressure fluctuations within covered cavities can be modeled as acoustically propagating. This assumption simplifies the model and enables the use of a FEM-based approach. The reduced computational requirement means that the FEM approach is suitable for optimizing the cavity shape and wall material to reduce the TBL-induced spectra at the cavity bottom. This approach requires the imposition of a representative TBL pressure field as a boundary condition at the cavity aperture. Selecting this representative pressure field remains an open research question. One or more candidate cavity designs are the envisioned outcome of the FEM optimization process. The performance of these cavities can then be validated using the LBM CFD approach. Additionally, this approach could incorporate an acoustic source in the simulation to validate the cavity's SNR of acoustic measurements when a TBL is present.
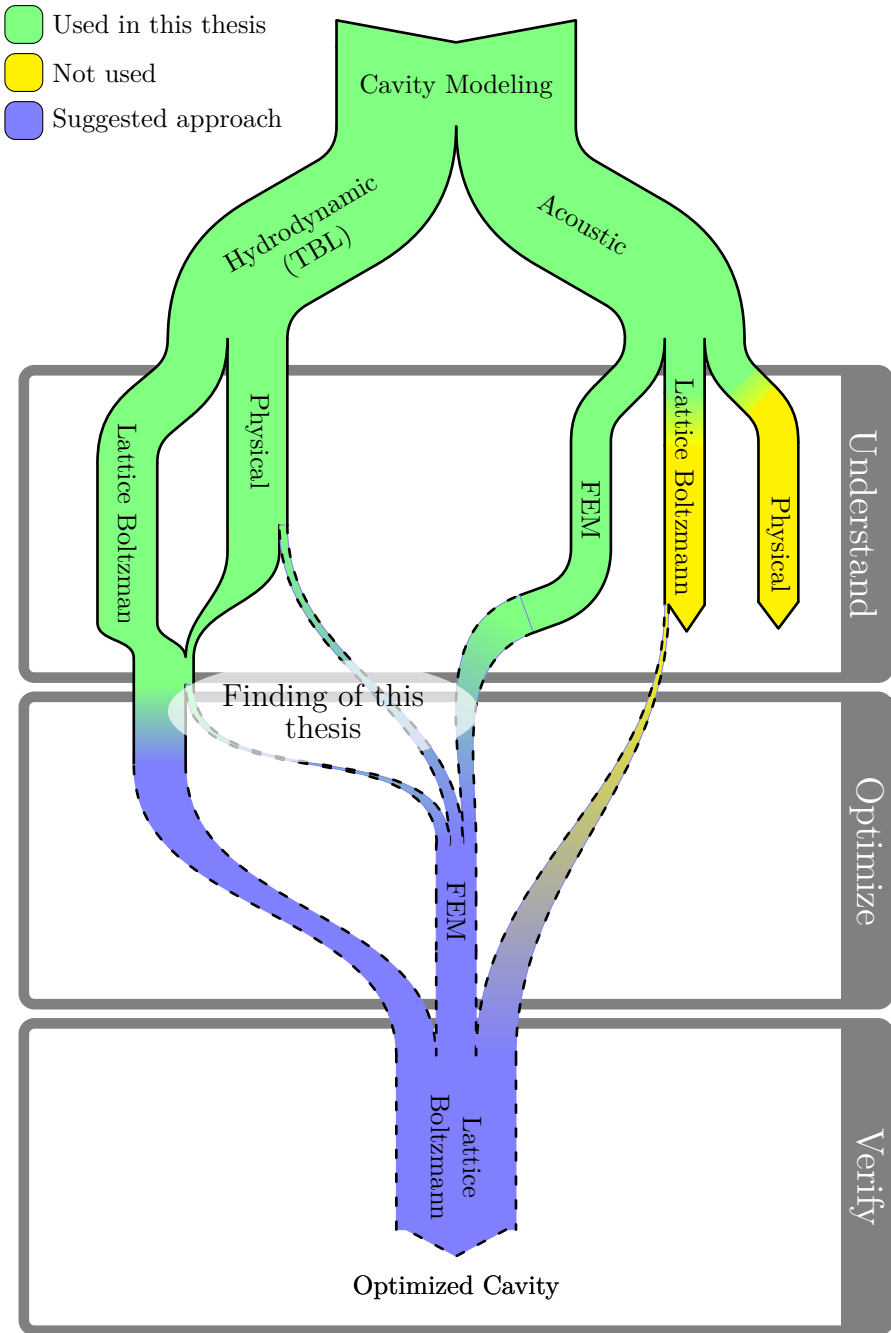
8

Figure 8.3: Modeling approach used in this thesis for the acoustic and hydrodynamic components.

8.2.3 Array Design

The research presented in this thesis establishes a framework to design cavities that improve the SNR of acoustic array measurements in closed test section wind tunnels. The intuitive application of this work is to specify an objective function that produces an optimized cavity with the lowest pressure spectrum at the bottom. Yet, given that the SNR of the array increases with an increasing number of microphones, an objective function can also be defined to optimize the shape to improve the SNR of the cavity while also increasing the number of cavities that can fit within a test section wall. Typically, wind tunnel test sections are longer in the streamwise direction than they are tall. Given that the TBL coherence length is shorter in the spanwise direction, elliptical cavities could be used to increase the number of microphones in the spanwise direction, as shown in Fig. 8.1c. Another variation of the optimization problem is to optimize the cavities in groups, with each group being optimized to reduce the TBL pressure fluctuations within a band of frequencies. Thus, the array could feature cavities optimized for attenuating the TBL at low frequencies and cavities optimized for higher frequencies.

Improving the SNR of cavities at low frequencies is challenging. As Fig. 8.1a shows, increasing the aperture size improves the response at low frequencies. However, the amount of improvement begins to plateau for larger cavities. This suggests that modifying the TBL itself may be necessary to improve the performance of cavities at low frequencies. This work showed that cavities reduce the pressure fluctuations at higher frequencies more than lower frequencies because the TBL eddies are smaller than the cavity aperture at higher frequencies. Large-eddy break-up devices placed upstream of the array, or individual cavities may improve the TBL attenuation by shifting the energy in the TBL from large eddies, which dominate low-frequency TBL noise to smaller eddies, which contribute to higher frequency noise [205]. As this work shows, the larger the cavity is compared to the eddy size, the greater the reduction is in the spectra. Yet, placing these devices in the boundary layer may produce additional noise, which would obviate any improvements to the SNR by reducing the TBL pressure fluctuations. Thus, this trade−off requires additional research.

8

A

Supplemental Details of the LBM Simulation of Turbulent Flow over Cavities

This appendix contains supplementary information relevant to Chapter 6. Within the appendix additional details on the VR voxel sizing, validation of the VR sizing in terms of turbulent kinetic energy (TKE), validation of the computational domain width, and additional visualization of the vortex shedding for the uncovered cavities.

A.1 VR Region Sizing Details

Figure A.1 shows the detailed grid topology of the variable resolution (VR) regions in the computational domain for the uncovered cylindrical cavity and the covered conical cavity. The topology for the uncovered countersunk and conical cavity is similar to the topology of the uncovered cylindrical cavity shown in Fig. A.1a. The covered cavities feature a finer resolution region (VR(-1) and VR(-2)) at the location of the cloth cover, where the porous medium is imposed. Figure A.1b shows the conical cavity topology and the covered cylindrical and countersunk cavities are similar. Table A.1 lists domain and VR dimensions for the cavities.
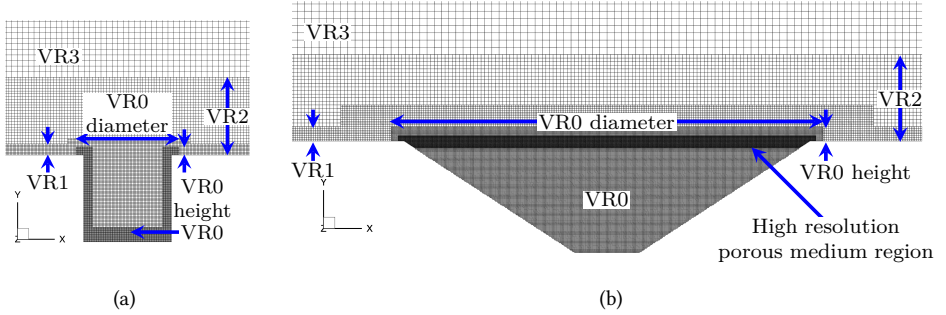
A

(a)   (b)

Figure A.1: Grid topology at the cavities location: a) uncovered cylindrical cavity; b) covered conical cavity.

Table A.1: Dimensions of the domain and of the lattice VR regions. Dimensions shown in cm ($L_{\text{Cylindrical}} = 1\,\text{cm}$).

	Cylindrical		Countersunk		Conical	
	No Cover	Cover	No Cover	Cover	No Cover	Cover
Domain height	136	136	136	136	136	136
Domain length	300	300	300	300	300	300
Domain width	5.12	5.12	5.12	5.12	7.68	7.68
VR5 height	12.08	12.08	12.08	12.08	21.68	21.72
VR4 height	5.68	5.68	5.68	5.68	15.28	15.32
VR3 height	2.48	2.48	2.48	2.48	2.48	2.52
VR2 height	0.88	0.88	0.88	0.88	0.88	0.92
VR1 height	0.08	0.08	0.08	0.08	0.08	0.12
VR1 length	200	200	200	200	200	200
VR0 height	0.08	0.08	0.08	0.08	0.08	0.08
VR0 diameter	1.16	1.16	1.76	1.76	4.66	4.66
VR0 cell size	0.008	0.008	0.008	0.008	0.01	0.01
Porous thickness	-	0.015	-	0.015	-	0.03
VR(-1) thickness	-	0.128	-	0.128	-	0.128
VR(-2) thickness	-	0.032	-	0.032	-	-

A.2 Turbulence Spectra

Figure A.2 shows the PSD of the turbulent kinetic energy (TKE) of the simulated boundary layer at four VR regions, at four values of y^+. The TKE was calculated from the sampled turbulence (u', v', w') upstream of the conical cavity for the medium grid (Table 6.4). The VR1, VR2, and VR3 data were sampled at x = −3.0 cm. This figure shows that the voxel sizes for the VLES simulation are sufficiently small to resolve the turbulent eddies for the frequencies of interest.
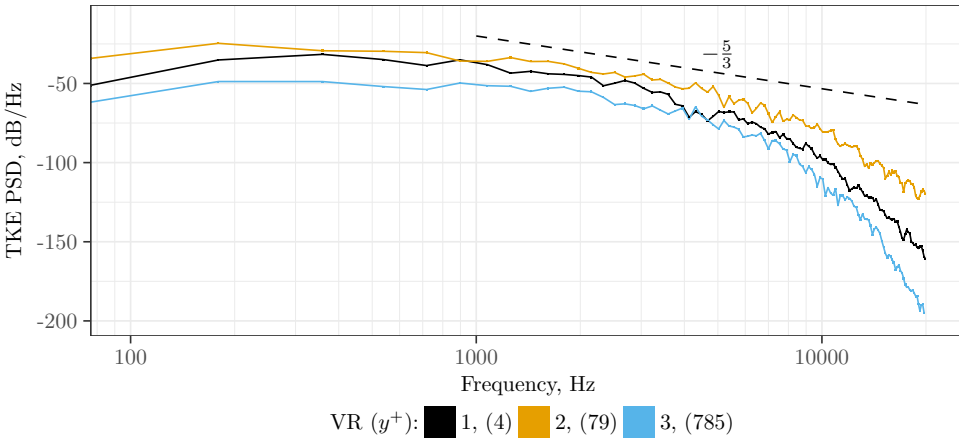
Figure A.2: PSD of the turbulent kinetic energy (TKE) at 3 VR regions over the flatplate, from the uncovered conical cavity simulation.
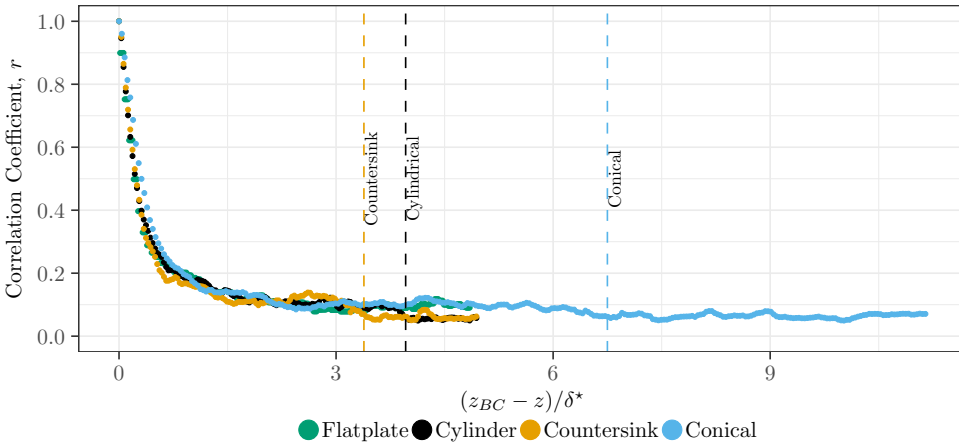
A.3 Computation Domain Width Validation

Figure A.3: Spanwise variation of correlation coefficient for the flatplate and uncovered cavities simulation. The points are sampled at the streamwise center of the domain and at the flatplate surface height, i.e., sampled spanwise along $x = 0$ and $y = 0$. The reference point is the spanwise location of the periodic boundary (positive z). The vertical dashed lines are the spanwise location of the cavity edges.

Figure A.3 shows the spanwise correlation of turbulent pressure fluctuations, sampled along $x = 0$ and $y = 0$, with the pressures sampled at the periodic boundary being the reference point. This figure shows the correlation coefficient, r, for the flatplate and uncovered cavities simulations. The figure also shows that the correlation between pressure fluctuations at the boundary condition and the cavity edge is low with $r = 0.1$. Therefore, the domain's spanwise width is sufficiently wide to minimize the influence of the boundary

A

condition on the cavity flowfield. In wall units, the distance between the periodic boundary condition and the conical cavity edge is $z^+ = 1.4 \times 10^3$. The spanwise distance is one order of magnitude larger than the spanwise extent of the turbulent structures characteristic of high-amplitude pressure peaks, as expected in a zero-pressure gradient turbulent boundary layer, with a similar Re_Θ [206].

A.4 3-D Visualization of Vortex Shedding

Figure A.4 shows the λ_2 isosurfaces and the corresponding pressure contours in an instantaneous streamwise slice at $z = 0$. The λ_2 criterion is used to identify vortices, where $\lambda_2 < -2 \times 10^8$ is used to identify the structures of vortex cores [184]. The streamtraces show instantaneous convection paths for vortices within the cavities. The shedding location of the Kelvin–Helmholtz type vortices [83] is near the spanwise center ($z = 0$) of the upstream edge of the cylinder in Fig. A.4a. For the cylindrical cavity, these vortices are of approximately constant size in the spanwise direction. The vortices are convected within the shear layer until they impinge on the downstream wall, emitting a pressure wave, or are convected towards the cavity bottom. The regions of negative C_p, shown in blue in Figs. A.4a and A.4b for the cylindrical and countersunk cavities, correspond to the vortex cores [83], an example of which is indicated with an arrow in Fig. A.4a. The rarefaction pressure wave from the vortex impingement can be seen within the cylindrical cavity in Fig. A.4a. Unlike the cylindrical and countersunk cavities, the pressure fluctuations within the conical cavity are not substantially influenced by vortex impingement.
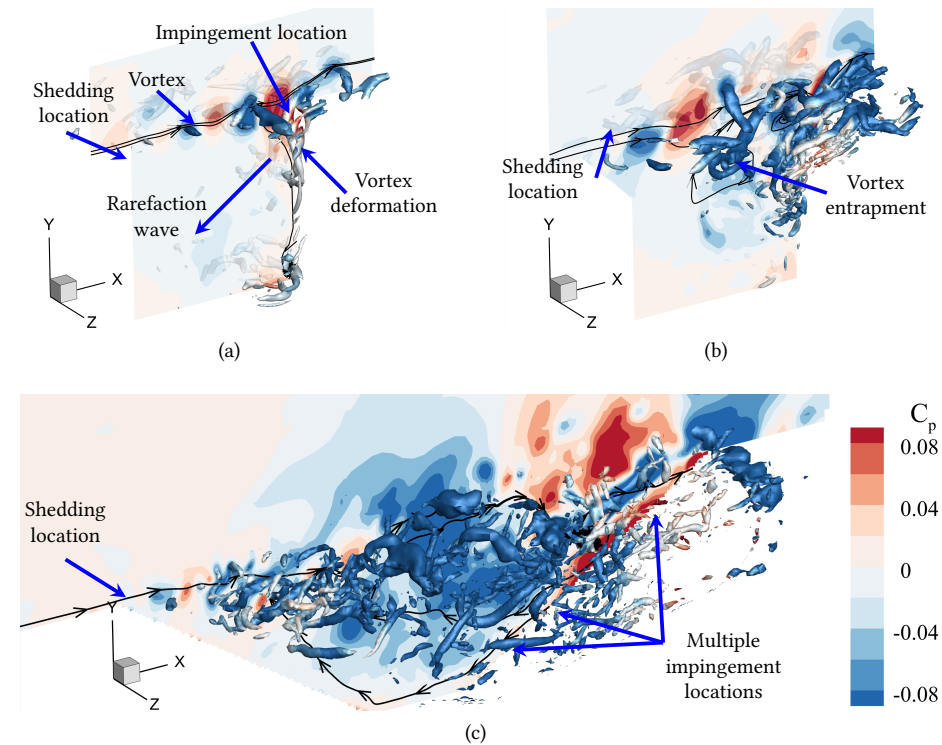
Figure A.4: Instantaneous visualization of the pressure fluctuation contours, p', vortex shedding, and velocity streamtraces. Vortex cores are identified using the λ_2 criterion with the isosurfaces defined by $\lambda_2 < -2 \times 10^8$ for the following cavities: a) cylindrical, b) countersunk, and c) conical.

Bibliography

References

[1] M. Rosenlund, N. Berglind, G. Pershagen, L. Järup, and G. Bluhm, *Increased prevalence of hypertension in a population exposed to aircraft noise,* Occupational and Environmental Medicine **58**, 769 (2001).

[2] T. Münzel, T. Gori, W. Babisch, and M. Basner, *Cardiovascular effects of environmental noise exposure,* European Heart Journal **35** (2014), 10.1093/eurheartj/ehu030.

[3] M. Basner, M. Witte, and S. McGuire, *Aircraft Noise Effects on Sleep–Results of a Pilot Study Near Philadelphia International Airport,* International Journal of Environmental Research and Public Health **16** (2019), 10.3390/ijerph16173178.

[4] J. R. Barber, K. R. Crooks, and K. M. Fristrup, *The costs of chronic noise exposure for terrestrial organisms,* Trends in Ecology and Evolution **25**, 180 (2010).

[5] C. Erbe, R. Williams, M. Parsons, S. K. Parsons, I. G. Hendrawan, and I. M. I. Dewantama, *Underwater noise from airplanes: An overlooked source of ocean noise,* Marine Pollution Bulletin **137**, 656 (2018).

[6] E. Schreurs, E. Verheijen, and J. Jabben, *Valuing airport noise in the Netherlands*, Tech. Rep. 680555005/2011 (RIVM, 2011).

[7] ICAO, *ICAO Revenue Passenger-Kilometers (RPK) Forecasts Scenarios,* (2021).

[8] GWEC, *Global Wind Report 2021,* (2021).

[9] P. Hevia-Koch and H. Klinge Jacobsen, *Comparing offshore and onshore wind development considering acceptance costs,* Energy Policy **125**, 9 (2019).

[10] J. L. Davy, K. Burgemeister, and D. Hillman, *Wind turbine sound limits: Current status and recommendations based on mitigating noise annoyance,* Applied Acoustics **140**, 288 (2018).

[11] S. Oerlemans and P. Fuglsang, *Low-noise wind turbine design,* in *EWEA Workshop* (Oxford, UK, 2012).

[12] E. Fares, B. Duda, and M. R. Khorrami, *Airframe noise prediction of a full aircraft in model and full scale using a lattice boltzmann approach,* in *22nd AIAA/CEAS Aeroacoustics Conference,* (Lyon, France, 2016).

[13] S. Oerlemans, L. Broersma, and P. Sijtsma, *Quantification of Airframe Noise Using Microphone Arrays in Open and Closed wind Tunnels,* International Journal of Aeroacoustics **6**, 309 (2007).

[14] M. Kamruzzaman, T. Lutz, W. Würz, W. Z. Shen, W. J. Zhu, M. O. L. Hansen, F. Bertagnolio, and H. A. Madsen, *Validations and improvements of airfoil trailing-edge noise prediction models using detailed experimental data,* Wind Energy **15**, 45 (2012).

[15] B. A. Fenech, *Accurate aeroacoustic measurements in closed-section hard-walled wind tunnels*, Ph.D. thesis, University of Southampton (2009).

[16] S. Jaeger, W. C. Horne, and C. Allen, *Effect of surface treatment on array microphone self-noise,* in *6th AIAA/CEAS Aeroacoustics Conference and Exhibit* (Lahaina, HI, 2000).

[17] W. Dobrzynski, *Almost 40 years of airframe noise research: What did we achieve?* Journal of Aircraft **47**, 353 (2010).

[18] H. H. Hubbard and K. P. Shepherd, *Aeroacoustics of large wind turbines,* The Journal of the Acoustical Society of America **89**, 2495 (1991).

[19] C. Arce León, *A study on the near-surface flow and acoustic emissions of trailing edge serrations*, Ph.D. thesis, Technische Universiteit Delft (2017).

[20] H. H. Heller and W. M. Dobrzynski, *Sound Radiation from Aircraft Wheel-Well/Landing-Gear Configurations,* Journal of Aircraft **14**, 768 (1977).

[21] B. A. Singer, D. P. Lockard, and K. S. Brentner, *Computational aeroacoustic analysis of slat trailing-edge flow,* AIAA Journal **38**, 1558 (2000).

[22] M. R. Fink and D. A. Bailey, *Airframe Noise Reduction Studies and Clean-Airframe Noise Investigation*, Tech. Rep. NASA-CR-159311 (NASA, 1980).

[23] T. F. Brooks, S. D. Pope, and M. A. Marcolini, *Airfoil Self-Noise and Prediction*, Tech. Rep. (NASA, Langley, VA, 1989).

[24] S. Oerlemans and B. Méndez López, *Acoustic Array Measurements on a Full Scale Wind Turbine,* in *11th AIAA/CEAS Aeroacoustics Conference*, Aeroacoustics Conferences (Monterey, CA, 2005).

[25] A. L. Marsden, M. Wang, J. E. Dennis, and P. Moin, *Trailing-edge noise reduction using derivative-free optimization and large-eddy simulation*, Journal of Fluid Mechanics **572**, 13 (2007).

[26] S. Oerlemans, M. Fisher, T. Maeder, and K. Kögler, *Reduction of wind turbine noise using optimized airfoils and trailing-edge serrations,* in *14th AIAA/CEAS Aeroacoustics Conference (29th AIAA Aeroacoustics Conference)* (Vancouver B.C., 2008).

[27] S. Oerlemans, *Reduction of wind turbine noise using blade trailing edge devices,* in *22nd AIAA/CEAS Aeroacoustics Conference* (Lyon, France, 2016).

[28] M. Azarpeyvand, M. Gruber, and P. F. Joseph, *An analytical investigation of trailing edge noise reduction using novel serrations,* in *19th AIAA/CEAS Aeroacoustics Conference* (Berlin, Germany, 2013).

[29] F. Avallone, W. C. Van Der Velden, D. Ragni, and D. Casalino, *Noise reduction mechanisms of sawtooth and combed-sawtooth trailing-edge serrations,* Journal of Fluid Mechanics **848**, 560 (2018).

[30] C. Arce León, R. Merino-Martínez, D. Ragni, F. Avallone, F. Scarano, S. Pröbsting, M. Snellen, D. G. Simons, and J. Madsen, *Effect of trailing edge serration-flow misalignment on airfoil noise emissions,* Journal of Sound and Vibration **405**, 19 (2017).

[31] A. Rubio Carpio, R. Merino Martínez, F. Avallone, D. Ragni, M. Snellen, and S. van der Zwaag, *Experimental characterization of the turbulent boundary layer over a porous trailing edge for noise abatement,* Journal of Sound and Vibration **443**, 537 (2019).

[32] S. Luesutthiviboon, D. Ragni, F. Avallone, and M. Snellen, *An alternative permeable topology design space for trailing-edge noise attenuation,* International Journal of Aeroacoustics **20**, 221 (2021).

[33] J. D. Revell, H. L. Kuntz, F. J. Balena, C. Home, B. L. Storms, and R. P. Dougherty, *Trailing-edge flap noise reduction by porous acoustic treatment,* in *3rd AIAA/CEAS Aeroacoustics Conference* (Atlanta,GA, 1997).

[34] T. P. Chong and E. Dubois, *Optimization of the poro-serrated trailing edges for airfoil broadband noise reduction,* The Journal of the Acoustical Society of America **140**, 1361 (2016).

[35] T. J. Mueller, *Aeroacoustic measurements,* Experimental fluid mechanics (2002).

[36] E. Sarradj, C. Fritzsche, T. Geyer, and J. Giesler, *Acoustic and aerodynamic design and characterization of a small-scale aeroacoustic wind tunnel,* Applied Acoustics **70**, 1073 (2009).

[37] J. P. Gomes, A. Bergmann, and H. Holthusen, *Aeroacoustic wind tunnel design,* CEAS Aeronautical Journal **10**, 231 (2019).

[38] A. Sahlin and A. V. Johansson, *Design of guide vanes for minimizing the pressure loss in sharp bends,* Physics of Fluids **3**, 1934 (1991).

[39] R. Merino-Martínez, A. Rubio Carpio, L. T. Lima Pereira, S. van Herk, F. Avallone, D. Ragni, and M. Kotsonis, *Aeroacoustic design and characterization of the 3D-printed, open-jet, anechoic wind tunnel of Delft University of Technology,* Applied Acoustics **170** (2020), 10.1016/j.apacoust.2020.107504.

[40] R. M. Martin, T. F. Brooks, and D. R. Hoad, *Reduction of background noise induced by wind tunnel jet exit vanes,* AIAA Journal **23**, 1631 (1985).

[41] E. Duell, J. Walter, S. Arnette, and J. Yen, *Recent advances in large-scale aeroacoustic wind tunnels,* in *8th AIAA/CEAS Aeroacoustics Conference and Exhibit* (Breckenridge, CO, 2002).

[42] G. Wickern, W. Von Heesen, and S. Wallmann, *Wind tunnel pulsations and their active suppression,* in *SAE Technical Papers*, Vol. 109 (2000) pp. 1403–1416.

[43] M. C. Remillieux, E. D. Crede, H. E. Camargo, R. A. Burdisso, W. J. Devenport, M. Rasnick, P. V. Seeters, A. Chou, P. Van Seeters, and A. Chou, *Calibration and Demonstration of the New Virginia Tech Anechoic Wind Tunnel,* in *14th AIAA/CEAS Aeroacoustics Conference (29th AIAA Aeroacoustics Conference)* (Vancouver B.C., 2008).

[44] R. K. Amiet, *Refraction of sound by a shear layer,* Journal of Sound and Vibration **58**, 467 (1978).

[45] R. P. Dougherty, *Turbulent Decorrelation of aeroacoustic phased arrays: Lessons from atmospheric science and astronomy,* in *9th AIAA/CEAS Aeroacoustics Conference and Exhibit* (Hilton Head, SC, 2003).

[46] P. Sijtsma, S. Oerlemans, T. Tibbe, T. Berkefeld, and C. Spehr, *Spectral broadening by shear layers of open jet wind tunnels,* in *20th AIAA/CEAS Aeroacoustics Conference* (Atlanta, GA, 2014).

[47] S. Guidati, C. Brauer, and S. Wagner, *The reflection canceller - phased array measurements in a reverberating environment,* in *8th AIAA/CEAS Aeroacoustics Conference and Exhibit* (Breckenridge, CO, 2002).

[48] S. Radhakrishnan and A. Vakili, *Acoustic measurements and background noise separation in wind tunnels,* in *5th AIAA/CEAS Aeroacoustics Conference and Exhibit*, Aeroacoustics Conferences (Bellevue, WA, 1999) pp. 1123–1132.

[49] W. K. Blake, *Essentials of Turbulent Wall Pressure Fluctuations,* in *Mechanics of Flow-Induced Sound and Vibration, Volume 2*, Vol. 2 (Elsevier, 2017) pp. 81–177.

[50] W. C. Horne and K. James, *Concepts for reducing the self-noise of in-flow acoustic sensors and arrays,* in *5th AIAA/CEAS Aeroacoustics Conference and Exhibit* (Bellevue, WA, 1999).

[51] E. C. Maskell, *Aeronautical Research Council London (United Kingdom)*, Tech. Rep. (1963).

[52] W. J. Devenport, R. A. Burdisso, A. Borgoltz, P. A. Ravetta, M. F. Barone, K. A. Brown, and M. A. Morton, *The Kevlar-walled anechoic wind tunnel,* Journal of Sound and Vibration **332**, 3971 (2013).

[53] C. Allen and P. Soderman, *Effect of freestream turbulence on the flow-induced background noise of in-flow microphones,* in *4th AIAA/CEAS Aeroacoustics Conference*, Aeroacoustics Conferences (Tolouse, France, 1998).

[54] J. Billingsley and R. Kinns, *The acoustic telescope,* Journal of Sound and Vibration **48**, 485 (1976).

[55] B. D. V. Veen, K. M. Buckley, B. D. Van Veen, and K. M. Buckley, *Beamforming: a versatile approach to spatial filtering,* IEEE ASSP Magazine **5**, 4 (1988).

[56] P. Sijtsma, *Accuracy criterion for source power integration with CSM diagonal removal,* in *Berlin Beamforming Conference* (Berlin, Germany, 2020).

[57] H. C. Shin, W. R. Graham, P. Sijtsma, C. Andreou, and A. C. Faszer, *Implementation of a Phased Microphone Array in a Closed-Section Wind Tunnel,* AIAA Journal **45**, 2897 (2007).

[58] L. Koop and K. Ehrenfried, *Microphone-array processing for wind-tunnel measurements with strong background noise,* in *14th AIAA/CEAS Aeroacoustics Conference (29th AIAA Aeroacoustics Conference)* (Vancouver B.C., 2008).

[59] A. Carballo-Crespo and K. Takeda, *An investigation of microphone array installation effects,* in *47th AIAA Aerospace Sciences Meeting*, January (Orlando, FL, 2009).

[60] V. Fleury, L. Coste, R. Davy, A. A. Mignosi, J.-M. M. Prosper, and C. Cariou, *Optimization of microphone array wall-mountings in closed-section wind tunnels,* in *16th AIAA/CEAS Aeroacoustics Conference (31st AIAA Aeroacoustics Conference)* (Stockholm, 2010).

[61] V. Fleury, L. Coste, R. Davy, A. Mignosi, C. Cariou, and J.-M. M. Prosper, *Optimization of Microphone Array Wall Mountings in Closed-Section Wind Tunnels,* AIAA Journal **50**, 2325 (2012).

[62] C. Tam, *The acoustic modes of a two-dimensional rectangular cavity,* Journal of Sound and Vibration **49**, 353 (1976).

[63] A. Rona, *The Acoustic Resonance of Rectangular and Cylindrical Cavities,* Journal of Algorithms & Computational Technology **1**, 329 (2007).

[64] J. P. Dalmont, C. J. Nederveen, and N. Joly, *Radiation impedance of tubes with different flanges: Numerical and experimental investigations,* Journal of Sound and Vibration **244**, 505 (2001).

[65] G. P. Scavone, *An Acoustic Analysis of Single-Reed Woodwind Instruments with an Emphasis on Design and Performance Issues and Digital Waveguide Modeling Techniques*, Doctoral thesis, Stanford University (1997).

[66] P. O. Davies, *Practical flow duct acoustics,* Journal of Sound and Vibration **124**, 91 (1988).

[67] Milton Abramowitz and Irene A. Stegun, eds., *Handbook of Mathematical Functions*, (National Bureau of Standards, Washington D.C., 1964).

[68] S. W. Rienstra, *Fundamentals of Duct Acoustics*, November (Eindhoven University of Tecnology, 2015) pp. 1–50.

[69] S. W. Rienstra and A. Hirschberg, *An Introduction to Acoustics*, Vol. 4825 (2018) arXiv:0521865719 9780521865715 .

[70] J. A. Schetz and R. D. Bowersox, *Boundary layer analysis*, 2nd ed., AIAA education series (American Institute of Aeronautics and Astronautics, Reston, VA, 2011).

[71] F. T. M. Nieuwstadt, J. Westerweel, B. J. Boersma, and J. Westerweel, *Turbulence: Introduction to Theory and Applications of Turbulent Flows*, 1st ed. (Springer, Switzerland, 2016) pp. 1–284.

[72] M. Goody, *Empirical Spectral Model of Surface Pressure Fluctuations,* AIAA Journal **42**, 1788 (2004).

[73] D. M. Chase, *The character of the turbulent wall pressure spectrum at subconvective wavenumbers and a suggested comprehensive model,* Journal of Sound and Vibration (1987), 10.1016/S0022-460X(87)80098-6.

[74] A. Smol'yakov and V. Tkachenko, *Model of a Field of Pseudosonic Turbulent Wall Pressure Fluctuations in Turbulent Boundary Layers,* Sov. Phys. (Acoustics) **37 (6)**, 629 (1991).

[75] M. S. Howe, *Acoustics of Fluid-Structure Interactions* (Cambridge University Press, Cambridge, 1998).

[76] D. M. Chase, *Modeling the wavevector-frequency spectrum of turbulent boundary layer wall pressure,* Journal of Sound and Vibration **70**, 29 (1980).

[77] T. M. Farabee and M. J. Casarella, *Spectral features of wall pressure fluctuations beneath turbulent boundary layers,* Physics of Fluids A **3**, 2410 (1991).

[78] J. E. Ffowcs Williams, *Boundary-layer pressures and the Corcos model: A development to incorporate low-wavenumber constraints,* Journal of Fluid Mechanics **125**, 9 (1982).

[79] K. Ehrenfried and L. Koop, *Experimental study of pressure fluctuations beneath a compressible turbulent boundary layer,* in *14th AIAA/CEAS Aeroacoustics Conference (29th AIAA Aeroacoustics Conference)* (Vancouver, B.C., 2008).

[80] G. M. Corcos, *The structure of the turbulent pressure field in boundary-layer flows,* Journal of Fluid Mechanics **18**, 353 (1964).

[81] W. R. Graham, *A comparison of models for the wavenumber-frequency spectrum of turbulent boundary layer pressures,* Journal of Sound and Vibration **206**, 541 (1997).

[82] D. Rockwell and E. Naudascher, *Self-Sustained Oscillations of Impinging Free Shear Layers,* Annual Review of Fluid Mechanics **11**, 67 (1979).

[83] Y. W. Ho and J. W. Kim, *A wall-resolved large-eddy simulation of deep cavity flow in acoustic resonance,* J. Fluid Mech **917**, 17 (2021).

[84] M. S. Howe, *The Dissipation of Sound at an Edge,* Journal of Sound and Vibration **70**, 407 (1980).

[85] J. Rossiter, *Ministry of Aviation, Aeronautical Research Council Reports and Memoranda*, Tech. Rep. (Aeronautical Research Council, 1964).

[86] Y. Yang, D. Rockwell, K. Lai-Fook Cody, and M. Pollack, *Generation of tones due to flow past a deep cavity: Effect of streamwise length,* Journal of Fluids and Structures **25**, 364 (2009).

[87] P. J. W. Block, *Tech Note D-8351*, Tech. Rep. December (NASA, 1976).

[88] H. H. Heller, D. G. Holmes, and E. E. Covert, *Flow-induced pressure oscillations in shallow cavities,* Journal of Sound and Vibration **18**, 545 (1971).

[89] J. J. Keller and M. P. Escudier, *Flow-excited resonances in covered cavities,* Journal of Sound and Vibration **86**, 199 (1983).

[90] P. Oshkai, T. Yan, A. Velikorodny, and S. Vancaeseele, *Acoustic Power Calculation in Deep Cavity Flows: A Semiempirical Approach,* Journal of Fluids Engineering (2008), 10.1115/1.2907413.

[91] L. Larchevêque, P. Sagaut, T. H. Lê, and P. Comte, *Large-eddy simulation of a compressible flow in a three-dimensional open cavity at high Reynolds number,* Journal of Fluid Mechanics **516**, 265 (2004).

[92] L. F. East, *Aerodynamically induced resonance in rectangular cavities,* Journal of Sound and Vibration **3**, 277 (1966).

[93] M. L. Pollack, *Flow-induced tones in side-branch pipe resonators,* The Journal of the Acoustical Society of America **67**, 1153 (1980).

[94] M. Meissner, *Acoustic modes induced by flow in a pipe with two closed side-branches,* Applied Acoustics **63**, 1071 (2002).

[95] M. Grottadaurea and A. Rona, *Noise sources from a cylindrical cavity,* in *13th AIAA/CEAS Aeroacoustics Conference (28th AIAA Aeroacoustics Conference)* (Rome, Italy, 2007).

[96] O. Marsden, E. Jondeau, P. Souchotte, C. Bogey, C. Bailly, and D. Juvé, *Investigation of flow features and acoustic radiation of a round cavity,* in *14th AIAA/CEAS Aeroacoustics Conference (29th AIAA Aeroacoustics Conference)* (2008).

[97] O. Marsden, C. Bailly, C. Bogey, and E. Jondeau, *Investigation of flow features and acoustic radiation of a round cavity,* Journal of Sound and Vibration **331**, 3521 (2012).

[98] F. R. Verdugo, A. Guitton, and R. Camussi, *Experimental investigation of a cylindrical cavity in a low Mach number flow,* Journal of Fluids and Structures **28**, 1 (2012).

[99] L. Chatellier, *Modélisation et contrôle actif des instabilités aéroacoustiques en cavité sous écoulement affleurant*, Ph.d. thesis, Université de Poiters (2002).

[100] P. N. Shankar and M. D. Deshpande, *Fluid Mechanics in the Driven Cavity,* Annual Review of Fluid Mechanics **32**, 93 (2000).

[101] M. Hiwada, T. Kawamura, I. Mabuchi, and M. Kumada, *Some Characteristics of Flow Patten and Heat Transfer Past a Circular Cylindrical Cavity,* Bulletin of JSME **49**, 1744 (1983).

[102] C. Mincu, I. Mary, S. Redonnet, L. Larcheveque, and J. P. Dussauge, *Numerical simulations of the unsteady flow and radiated noise over a cylindrical cavity,* in *14th AIAA/CEAS Aeroacoustics Conference (29th AIAA Aeroacoustics Conference)* (Vancouver, B.C., 2008).

[103] O. Marsden, C. Bogey, and C. Bailly, *Investigation of flow features around shallow round cavities subject to subsonic grazing flow,* Physics of Fluids **24** (2012), 10.1063/1.4772194.

[104] L. Rayleigh, *XXXI. Investigations in optics, with special reference to the spectroscope,* The London, Edinburgh, and Dublin Philosophical Magazine and Journal of Science **8**, 261 (1879).

[105] Z. Prime and C. Doolan, *A comparison of popular beamforming arrays,* in *Annual Conference of the Australian Acoustical Society 2013, Acoustics 2013: Science, Technology and Amenity* (Victor Harbor, ASTL, 2013).

[106] R. Merino Martinez, *Microphone arrays for imaging of aerospace noise sources*, Ph.D. thesis, Technische Universiteit Delft (2018).

[107] E. Sarradj, *A Generic Approach to Synthesize Optimal Array Microphone Arrangements,* in *Berlin Beamforming Conference* (BeBeC-2016-S4, Berlin, Germany, 2016).

[108] J. R. Underbrink, *Aeroacoustic Phased Array Testing in Low Speed Wind Tunnels BT - Aeroacoustic Measurements,* (Springer, Berlin, 2002) pp. 98–217.

[109] J. Benesty, J. Chen, and Y. Huang, *Microphone array signal processing*, 1st ed., Springer topics in signal processing (Springer, Berlin, 2008).

[110] F. Le Courtois, J. H. Thomas, F. Poisson, and J. C. Pascal, *Genetic optimisation of a plane array geometry for beamforming. Application to source localisation in a high speed train,* Journal of Sound and Vibration **371**, 78 (2016).

[111] A. Malgoezar, M. Snellen, P. Sijtsma, and D. Simons, *Improving beamforming by optimization of acoustic array microphone positions,* in *6th Berlin Beamforming Conference* (Berlin, Germany, 2016).

[112] S. Luesutthiviboon, A. Malgoezar, M. Snellen, P. Sijtsma, and D. Simons, *Improving Source Discrimination Performance by Using an Optimized Acoustic Array and Adaptive High-Resolution Clean-SC Beamforming,* in *Berlin Beamforming Conference* (Berlin, Germany, 2018).

[113] Y. Liu, A. R. Quayle, A. P. Dowling, and P. Sijtsma, *Beamforming correction for dipole measurement using two-dimensional microphone arrays,* The Journal of the Acoustical Society of America **124**, 182 (2008).

[114] A. Brandt, *Noise and vibration analysis : signal analysis and experimental procedures*, 1st ed. (Wiley, Hoboken, N.J., 2013).

[115] P. Welch, *The use of fast Fourier transform for the estimation of power spectra: A method based on time averaging over short, modified periodograms,* IEEE Transactions on Audio and Electroacoustics **15**, 70 (1967).

[116] R. P. Dougherty, *Functional Beamforming,* in *5th Berlin Beamforming Conference* (Berlin, Germany, 2014).

[117] R. Merino-Martínez, P. Sijtsma, M. Snellen, T. Ahlefeldt, J. Antoni, C. J. Bahr, D. Blacodon, D. Ernst, A. Finez, S. Funke, T. F. Geyer, S. Haxter, G. Herold, X. Huang, W. M. Humphreys, Q. Leclère, A. Malgoezar, U. Michel, T. Padois, A. Pereira, C. Picard, E. Sarradj, H. Siller, D. G. G. Simons, and C. Spehr, *A review of acoustic imaging methods using phased microphone arrays Part of the "Aircraft Noise Generation and Assessment" Special Issue,* CEAS Aeronautical Journal **3**, 197 (2019).

[118] T. F. Brooks and W. M. Humphreys, *A deconvolution approach for the mapping of acoustic sources (DAMAS) determined from phased microphone arrays,* Journal of Sound and Vibration **294**, 856 (2006).

[119] P. Sijtsma, *CLEAN Based on Spatial Source Coherence,* International Journal of Aeroacoustics **6**, 357 (2008).

[120] S. Amailland, J.-H. Thomas, C. Pézerat, and R. Boucheron, *Boundary layer noise subtraction in hydrodynamic tunnel using robust principal component analysis,* The Journal of the Acoustical Society of America **143**, 2152 (2018).

[121] B. Arguillat, D. Ricot, C. Bailly, and G. Robert, *Measured wavenumber: Frequency spectrum associated with acoustic and aerodynamic wall pressure fluctuations,* The Journal of the Acoustical Society of America **128**, 1647 (2010).

[122] M. Terracol, E. Manoha, C. Herrero, E. Labourasse, S. Redonnet, and P. Sagaut, *Hybrid methods for airframe noise numerical prediction,* Theoretical and Computational Fluid Dynamics **19**, 197 (2005).

[123] X. Gloerfelt and J. Berland, *Turbulent boundary-layer noise: Direct radiation at Mach number 0.5,* Journal of Fluid Mechanics **723**, 318 (2013).

[124] M. A. Mendez, M. Balabane, and J. M. Buchlin, *Multi-scale proper orthogonal decomposition of complex fluid flows,* Journal of Fluid Mechanics **870**, 988 (2019), arXiv:1804.09646 .

[125] G. W. Stewart, *On the Early History of the Singular Value Decomposition,* SIAM Review **35**, 551 (1993).

[126] C. P. VanDercreek, P. Sijtsma, M. Snellen, D. Ragni, F. Avallone, and D. G. Simons, *Deterministic Model of Acoustic Wave Propagation in a Cavity,* in *25th AIAA/CEAS Aeroacoustics Conference* (Delft, The Netherlands, 2019).

[127] P. Sijtsma, *Phased Array Beamforming Applied to Wind Tunnel And Fly-Over Tests,* SAE Technical Paper Series **1**, 49 (2011).

[128] W. Eversman, *Theoretical model for duct acoustic propagation and radiation*, Tech. Rep. NASA-RP-1258-VOL-2, (NASA, 1991).

[129] N. C. Ovenden, W. Eversman, S. W. Rienstra, A. Member, and A. Professor, *Cut-on Cut-off Transition in Flow Ducts: Comparing Multiple-scales and Finite-element Solutions,* in *10th AIAA/CEAS Aeroacoustics Conference* (American Institute of Aeronautics and Astronautics, Manchester, UK, 2004).

[130] P. M. Morse and K. U. Ingard, *International series in pure and applied physics* (McGraw-Hill, New York, NY, 1968) p. 927.

[131] G. M. Corcos, *Resolution of Pressure in Turbulence,* The Journal of the Acoustical Society of America **35**, 192 (1963).

[132] W. A. Strauss, *Partial differential equations: an Introduction*, 2nd ed. (Wiley, New York, NY, 2008) p. 454.

[133] J. F. Allard and N. Atalla, *Propagation of Sound in Porous Media: Modelling Sound Absorbing Materials*, 2nd ed., Wiley Online Books (Wiley-Blackwell, Oxford, 2009) pp. 1–358.

[134] A. R. Allen and N. Schiller, *Experimental evaluation of equivalent-fluid models for melamine foam,* in *New England NoiseCon-16 Revolution in Noise Control* (Providence, RI, 2016).

[135] C. P. VanDercreek, A. Amiri-Simkooei, M. Snellen, and D. Ragni, *Experimental design and stochastic modeling of hydrodynamic wave propagation within cavities for wind tunnel acoustic measurements,* International Journal of Aeroacoustics **18**, 752 (2019).

[136] M. Kamruzzaman, T. Lutz, W. Würz, W. Z. Shen, W. J. Zhu, M. O. L. Hansen, F. Bertagnolio, and H. A. Madsen, *Validations and improvements of airfoil trailing-edge noise prediction models using detailed experimental data,* Wind Energy **15**, 45 (2011).

[137] S. Oerlemans, M. Fisher, T. Maeder, and K. Kögler, *Reduction of Wind Turbine Noise Using Optimized Airfoils and Trailing-Edge Serrations,* AIAA Journal **47**, 1470 (2009).

[138] R. DeLoach, *Analysis of Variance in the Modern Design of Experiments,* in *48th AIAA Aerospace Sciences Meeting Including the New Horizons Forum and Aerospace Exposition*, Aerospace Sciences Meetings (Orlando, FL, 2013).

[139] A. T. de Jong, *Aeroacoustic Resonance of Slender Cavities: An Experimental and Numerical Investigation*, Ph.d. thesis, Technische Universiteit Delft (2012).

[140] D. Montgomery, *Design and analysis of experiments*, 8th ed. (John Wiley & Sons, Inc., Hoboken, NJ, 2013).

[141] D. Landman, J. Simpson, R. Mariani, F. Ortiz, and C. Britcher, *Hybrid Design for Aircraft Wind-Tunnel Testing Using Response Surface Methodologies,* Journal of Aircraft **44**, 1214 (2007).

[142] T. Morgan-Wall and G. Khoury, *Optimal design generation and power evaluation in R: The skpr package,* Journal of Statistical Software **99**, 1 (2021).

[143] H. H. Bruun, *Measurement Science and Technology*, Vol. 7 (Oxford University Press, 2009).

[144] K. Schoenherr, *Resistance of flat surfaces moving through a fluid,* Trans SNAME **40**, 279 (1932).

[145] D. Bates, M. Mächler, B. M. Bolker, and S. C. Walker, *Fitting linear mixed-effects models using lme4,* Journal of Statistical Software **67** (2015), 10.18637/jss.v067.i01, arXiv:1406.5823 .

[146] S. N. Wood, *Generalized Additive Models: An Introduction with R*, Chapman & Hall/CRC Texts in Statistical Science (Taylor & Francis, 2006) pp. 1–410.

[147] C. P. VanDercreek, F. Avallone, D. Ragni, and M. Snellen, *Simulating the acoustic response of cavities to improve microphone array measurements in closed test section wind tunnels,* The Journal of the Acoustical Society of America **151**, 322 (2022).

[148] P. Sijtsma, R. Merino-Martinez, A. M. Malgoezar, and M. Snellen, *High-resolution CLEAN-SC: Theory and experimental validation,* International Journal of Aeroacoustics **16**, 274 (2017).

[149] K. K. Ahuja and J. Mendoza, *NASA Contractor Report 4653*, Tech. Rep. NASA Contractor Report 4653 (NASA, 1995).

[150] G. Kooijman, A. Hirschberg, and J. Golliard, *Acoustical response of orifices under grazing flow: Effect of boundary layer profile and edge geometry,* Journal of Sound and Vibration **315**, 849 (2008).

[151] A. T. de Jong, H. Bijl, A. Hazir, and J. Wiedemann, *Aeroacoustic simulation of slender partially covered cavities using a Lattice Boltzmann method,* Journal of Sound and Vibration **332**, 1687 (2013).

[152] M. J. Casiano and S. R. Fischbach, *Analytical and Numerical Modeling of Sensor Port Acoustics*, Tech. Rep. TP-20210000024 (NASA Marshall Space Flight Center, Huntsville, AL, 2021).

[153] COMSOL, *Acoustics Module User's Guide,* in *COMSOL Multiphysics® v. 5.5* (COMSOL AB, Stockholm, Sweden, 2019).

[154] N. Kino, T. Ueno, Y. Suzuki, and H. Makino, *Investigation of non-acoustical parameters of compressed melamine foam materials,* Applied Acoustics **70**, 595 (2009).

[155] C. D. Field and F. R. Fricke, *Theory and applications of quarter-wave resonators: A prelude to their use for attenuating noise entering buildings through ventilation openings,* Applied Acoustics **53**, 117 (1998).

[156] F. Silva, P. Guillemain, J. Kergomard, B. Mallaroni, and A. N. Norris, *Approximation formulae for the acoustic radiation impedance of a cylindrical pipe,* Journal of Sound and Vibration **322**, 255 (2009).

[157] H. Yokoyama and C. Kato, *Fluid-acoustic interactions in self-sustained oscillations in turbulent cavity flows. I. Fluid-dynamic oscillations,* Physics of Fluids **21** (2009), 10.1063/1.3253326.

[158] P. Wang, Y. Deng, and Y. Liu, *Vortex-excited acoustic resonance in channel with coaxial side-branches: Vortex dynamics and aeroacoustic energy transfer,* Physics of Fluids **30**, 125104 (2018).

[159] C. W. Rowley, T. Colonius, and A. J. Basu, *On self-sustained oscillations in two-dimensional compressible flow over rectangular cavities,* Journal of Fluid Mechanics **455**, 315 (2002).

[160] L. Larchevêque, P. Sagaut, I. Mary, O. Labbé, and P. Comte, *Large-eddy simulation of a compressible flow past a deep cavity,* Physics of Fluids **15**, 193 (2003).

[161] F. Scarano, M. C. Jacob, R. Gojon, X. Carbonneau, and E. R. Gowree, *Modification of a turbulent boundary layer by circular cavities,* Physics of Fluids **34**, 065134 (2022).

[162] C. Haigermoser, F. Scarano, and M. Onorato, *Investigation of the flow in a circular cavity using stereo and tomographic particle image velocimetry,* Experiments in Fluids **46**, 517 (2009).

[163] S. A. Elder, T. M. Farabee, and F. C. Demetz, *Mechanisms of flow-excited cavity tones at low Mach number,* The Journal of the Acoustical Society of America **72**, 532 (1982).

[164] B. Ruck and B. Makiola, *Flow Separation over the Inclined Step,* Physics of Separated Flows — Numerical, Experimental, and Theoretical Aspects , 47 (1993).

[165] P. W. McCarthy and A. Ekmekci, *Flow features of shallow cylindrical cavities subject to grazing flow,* Physics of Fluids **34**, 27115 (2022).

[166] C. VanDercreek, R. Merino-Martínez, P. Sijtsma, and M. Snellen, *Evaluation of the effect of microphone cavity geometries on acoustic imaging in wind tunnels,* Applied Acoustics **181** (2021), 10.1016/j.apacoust.2021.108154.

[167] C. Teruna, F. Manegar, F. Avallone, D. Ragni, D. Casalino, and T. Carolus, *Noise reduction mechanisms of an open-cell metal-foam trailing edge,* Journal of Fluid Mechanics **898** (2020), 10.1017/jfm.2020.363.

[168] P. L. Bhatnagar, E. P. Gross, and M. Krook, *A Model for Collision Processes in Gases. I. Small Amplitude Processes in Charged and Neutral One-Component Systems,* Physical review **94**, 511 (1954).

[169] C. M. Teixeira, *Incorporating turbulence models into the Lattice-boltzmann method,* International Journal of Modern Physics C **9**, 1159 (1998).

[170] C. Teruna, L. Rego, F. Avallone, D. Ragni, and D. Casalino, *Applications of the Multi-layer Porous Medium Modeling Approach for Noise Mitigation,* Journal of Aerospace Engineering **34**, 04021074 (2021).

[171] C. Teruna, F. Manegar, F. Avallone, D. Casalino, D. Ragni, A. Rubio-Carpio, and T. Carolus, *Numerical analysis of metal-foam application for trailing edge noise reduction,* in *25th AIAA/CEAS Aeroacoustics Conference, 2019* (Delft, The Netherlands, 2019).

[172] G. E. Elsinga and J. Westerweel, *Tomographic-PIV measurement of the flow around a zigzag boundary layer trip,* Experiments in Fluids **52**, 865 (2012).

[173] R. Merino-Martinez, W. van der Velden, F. Avallone, and D. Ragni, *Acoustic measurements of a DU96-W-180 airfoil with flow- misaligned serrations at a high Reynolds number in a closed- section wind tunnel,* in *7th International Conference on Wind Turbine Noise Rotterdam*, May (2017).

[174] R. Merino-Martínez, A. Rubio Carpio, L. T. Lima Pereira, S. van Herk, F. Avallone, D. Ragni, and M. Kotsonis, *Aeroacoustic design and characterization of the 3D-printed, open-jet, anechoic wind tunnel of Delft University of Technology,* Applied Acoustics **170** (2020), 10.1016/j.apacoust.2020.107504.

[175] J. H. M. Ribeiro and W. R. Wolf, *Identification of coherent structures in the flow past a NACA0012 airfoil via proper orthogonal decomposition,* Physics of Fluids **29**, 85104 (2017).

[176] D. Ninni and M. A. Mendez, *MODULO: A software for Multiscale Proper Orthogonal Decomposition of data,* SoftwareX **12**, 100622 (2020).

[177] L. Eça and M. Hoekstra, *Discretization Uncertainty Estimation based on a Least Squares version of the Grid Convergence Index,* Proceedings of the Second Workshop on CFD Uncertainty Analysis, Instituto Superior Tecnico, Lisbon, Oct , 1 (2006).

[178] Q. Zhang and D. J. Bodony, *Numerical investigation of a honeycomb liner grazed by laminar and turbulent boundary layers,* Journal of Fluid Mechanics **792**, 936 (2016).

[179] H. Schlichting and K. Gersten, *Boundary-Layer Theory*, 9th ed. (Springer, 1987).

[180] I. Marusic and G. J. Kunkel, *Streamwise turbulence intensity formulation for flat-plate boundary layers,* Physics of Fluids **15**, 2461 (2003).

[181] K. Mori, H. Imanishi, Y. Tsuji, T. Hattori, M. Matsubara, S. Mochizuki, M. Inada, and T. Kasiwagi, *Direct total skin-friction measurement of a flat plate in zero-pressure-gradient boundary layers,* Fluid Dynamics Research **41** (2009), 10.1088/0169-5983/41/2/021406.

[182] L. T. Lima Pereira, D. Ragni, F. Avallone, and F. Scarano, *Pressure fluctuations from large-scale PIV over a serrated trailing edge,* Experiments in Fluids **61**, 1 (2020).

[183] S. Pröbsting, M. Tuinstra, and F. Scarano, *Trailing edge noise estimation by tomographic Particle Image Velocimetry,* Journal of Sound and Vibration **346**, 117 (2015).

[184] J. Jeong and F. Hussain, *On the identification of a vortex,* Journal of Fluid Mechanics **285**, 69 (1995).

[185] M. J. Czech, J. D. Crouch, R. W. Stoker, M. K. Strelets, and A. Garbaruk, *Cavity noise generation for circular and rectangular vent holes,* in *12th AIAA/CEAS Aeroacoustics Conference*, Vol. 3 (Cambridge, MA, 2006) pp. 1381–1393.

[186] R. Stoker, Y. Guo, C. Streett, and N. Burnside, *Airframe Noise Source Locations of a 777 Aircraft in Flight and Comparisons with Past Model-Scale Tests,* in *9th AIAA/CEAS Aeroacoustics Conference and Exhibit* (Hilton Head, SC, 2003).

[187] R. Merino Martinez, E. Neri, M. Snellen, J. Kennedy, D. Simons, and G. J. Bennett, *Comparing flyover noise measurements to full-scale nose landing gear wind tunnel experiments for regional aircraft,* in *23rd AIAA/CEAS Aeroacoustics Conference* (Denver, CO, 2017).

[188] R. Merino-Martinez, E. Neri, M. Snellen, J. Kennedy, D. G. Simons, and G. J. Bennett, *Analysis of nose landing gear noise comparing numerical computations, prediction models and flyover and wind-tunnel measurements,* in *2018 AIAA/CEAS Aeroacoustics Conference* (Atlanta, GA, 2018).

[189] R. Merino-Martínez, S. Luesutthiviboon, R. Zamponi, A. Rubio Carpio, D. Ragni, P. Sijtsma, M. Snellen, and C. Schram, *Assessment of the accuracy of microphone array methods for aeroacoustic measurements,* Journal of Sound and Vibration **470** (2020), 10.1016/j.jsv.2020.115176.

[190] W. C. Horne and N. J. Burnside, *Development of new wall-mounted and strut-mounted phased microphone arrays for acoustic measurements in closed test-section wind tunnels,* in *21st AIAA/CEAS Aeroacoustics Conference* (Dallas, TX, 2015).

[191] P. Sijtsma, A. Dinsenmeyer, J. Antoni, and Q. Leclere, *Beamforming and other methods for denoising microphone array data,* in *25th AIAA/CEAS Aeroacoustics Conference* (Delft, The Netherlands, 2019).

[192] F. R. do Amaral, C. do Carmo Pagani Junior, and M. A. F. de Medeiros, *Improvements in closed-section wind-tunnel beamforming experiments of acoustic sources distributed along a line,* Applied Acoustics **156**, 336 (2019).

[193] *G.R.A.S. – 40PH CCP Free–field array microphone,* (2020).

[194] *G.R.A.S. – 42AA Pistonphone class 1,* (2020).

[195] Visa, *Visaton – Speaker K 50 SQ – 8 Ohm,* .

[196] Merino-Martinez, P. Sijtsma, and M. Snellen, *Inverse Integration Method for Distributed Sound Sources,* in *7th Berlin Beamforming Conference, March 5 – 6 2018, Berlin, Germany* (Berlin, Germany, 2018).

[197] R. Merino-Martínez, P. Sijtsma, A. R. Carpio, R. Zamponi, S. Luesutthiviboon, A. M. Malgoezar, M. Snellen, C. Schram, and D. G. Simons, *Integration methods for distributed sound sources,* International Journal of Aeroacoustics **18**, 444 (2019).

[198] Y. A. Çengel and J. M. Cimbala, *Fluid mechanics : fundamentals and applications*, 3rd ed. (McGraw Hill, New York, NY, 2014).

[199] A. Rubio Carpio, F. Avallone, D. Ragni, M. Snellen, and S. van der Zwaag, *3D-printed Perforated Trailing Edges for Broadband Noise Abatement,* in *25th AIAA/CEAS Aeroacoustics Conference* (Delft, The Netherlands, 2019).

[200] S. Luesutthiviboon, A. M. Malgoezar, R. Merino-Martinez, M. Snellen, P. Sijtsma, and D. G. Simons, *Enhanced HR-CLEAN-SC for resolving multiple closely spaced sound sources,* International Journal of Aeroacoustics **18**, 392 (2019).

[201] R. P. Dougherty, *Determining Spectra of Aeroacoustic Sources from Microphone Array Data,* in *25th AIAA/CEAS Aeroacoustics Conference*, Aeroacoustics Conferences (Delft, The Netherlands, 2019).

[202] C. VanDercreek, R. Merino-Martinez, M. Snellen, D. Ragni, and D. G. Simons, *Comparison of cavity geometries for a microphone array in an open-jet wind-tunnel experiment,* in *Berlin Beamforming Conference* (Berlin, 2020) pp. BeBeC–2020–D07.

[203] E. Sarradj, G. Herold, P. Sijtsma, R. Merino Martinez, T. F. Geyer, C. J. Bahr, R. Porteous, D. Moreau, and C. J. Doolan, *A Microphone Array Method Benchmarking Exercise using Synthesized Input Data,* in *23rd AIAA/CEAS Aeroacoustics Conference* (American Institute of Aeronautics and Astronautics, 2017).

[204] G. A. Brès, F. Pérot, and D. Freed, *Properties of the Lattice-Boltzmann method for acoustics,* in *15th AIAA/CEAS Aeroacoustics Conference (30th AIAA Aeroacoustics Conference)* (Miami, FL, 2009).

[205] P. R. Spalart, M. Strelets, and A. Travin, *Direct Numerical Simulation of Large-Eddy-Break-Up Devices in a Boundary Layer,* Engineering Turbulence Modelling and Experiments 6 **27**, 679 (2005).

[206] S. Ghaemi and F. Scarano, *Turbulent structure of high-amplitude pressure peaks within the turbulent boundary layer,* Journal of Fluid Mechanics **735**, 381 (2013).

Acknowledgments

Starting a Ph.D. is similar in a lot of ways to spending $20 on a pair of Army surplus skis and signing up for an 8-day ski trek through the Arctic circle via the Kungsleden with limited backcountry skiing experience. Coincidentally, the Ph.D. process and the ski trip both began from a bench in the Arlanda airport waiting for the Arctic Circle night train to Abisko. Many people helped make this stressful, yet rewarding process happen and the following acknowledgments are but an attempt to thank you all.

I would like to thank my promotor Mirjam for her endless support, patience, and insightful suggestions. I would also like to express my appreciation for my co-promotors Daniele and Francesco, whose energetic leadership style and rapid dispensation of expertise helped me immensely. Thank you all for helping me become a better independent researcher.

Pieter Sijtsma, thank you for your help shaping this research and organizing experiments and visits at NLR and Deutsche WindGuard. I would also like to thank you for answering my numerous technical questions. Not only were your answers helpful, but the required research to fully understand the answer improved both my math skills and my knowledge of acoustics. Stefan and Emiel, you were both vital during the wind tunnel experiments that underly the work in this thesis. These experiments would also not have been possible without the rapid and high quality work of Steve and Frank at DEMO.

This work would not have occurred without the support of de Nederlandse Organisatie voor Wetenschappelijk Onderzoek (NWO) via René and the contributions of the THAMES project members. Specifically, thank you to Nicholas and your Deutsche WindGuard team for access to your wind tunnel and for supporting several test campaigns, as well as your feedback that helped shape this work. Marthijn, thank you for providing useful feedback as well as access to your facilities at NLR. I would also like to express my gratitude to Stefan and Wouter for their contributions towards THAMES as well as your technical feedback.

My friends and colleagues within the faculty were indispensable over the past five years. Lisette, you have been immensely helpful in solving my many problems and questions as well as being excellent company at lunch and encouraging the use of Nederlands. Roberto, collaborating with you in the wind tunnel and on our paper was effortless. Furthermore, your experience and knowledge about how to maximize Ph.D. drinks will never be forgotten. Reynard and Victor, I always looked forward to catching up at Ph.D. drinks! Salil, I was fortunate that you started your Ph.D. at (almost) the same time as me. I appreciate your help setting up measurements as well as brewing beer, your help, company, and feedback. Tannaz and Timo, as founding members of the "original" coffee group, thank you for your help identifying the good coffee machines and for your friendship in and out of University. Leo, thank you for the bouldering company. My officemates Alejandro, Ana, and Federica (in order of succession) gracias, obrigado, and grazie for the shared experience. Bieke and Irina, thank you both for always bring the party to work and outside of it. To the next generation and much larger coffee group: Qian, Kathrin, Flavio, Jurri-

Curriculum Vitæ

Colin Paul van Dercreek

21-04-1985   Born in Portsmouth, Virginia USA.

Education

1999 - 2003   Secondary Education
Mount Carmel High School
San Diego, CA USA (1999–2000)

Walter Johnson High School
Bethesda, MD USA (2000–2003)

2003–2008   Bachelor of Science Engineering Mechanics and Astronautics
University of Wisconsin
Madison, WI USA

2008–2010   Masters of Science Aerospace Engineering
University of Maryland
College Park, MD USA

2017–2022   Doctor of Philosophy (Ph.D.) Aerospace Engineering
Delft University of Technology
The Netherlands
Thesis: Improving Acoustic Measurements with Cavities in
Closed Test Section Wind Tunnels
Promotors: Prof. dr. ir. M. Snellen, Dr. D. Ragni

Professional Experience

2007 – 2008   Co-op Engineer
                 Collins Aerospace (formerly Hamilton Sundstrand)
                 Rockford, IL USA

2008 – 2010   Graduate Research Assistant
                 Arnold Engineering Development Center Hypervelocity Tunnel 9
                 White Oak, MD USA

2010–2014   Staff Engineer (Contractor)
                 Defense Advanced Research Projects Agency (DARPA)
                 Arlington, VA USA

2014–2017   Research Associate
                 Institute for Defense Analyses (IDA)
                 Alexandria, VA USA

2022–   Aeroacoustics Engineer
                 CREO Dynamics
                 Linköping, Sweden

List of Publications

Journal Articles

1. H. F. Mourão Bento (co–first) & C. P. VanDercreek (co–first), F. Avallone, D. Ragni, and M. Snellen, Lattice-Boltzmann very large eddy simulations of a turbulent flow over covered and uncovered cavities, Physics of Fluids (2022) accepted for publication

2. C. P. VanDercreek, F. Avallone, D. Ragni, and M. Snellen, Simulating the acoustic response of cavities to improve microphone array measurements in closed test section wind tunnels, The Journal of the Acoustical Society of America 151 (2022), 10.1121/10.0009274.

3. C. P. VanDercreek, R. Merino-Martínez, P. Sijtsma, M. Snellen, R. Merino-Martinez, P. Sijtsma, and M. Snellen, Evaluation of the effect of microphone cavity geometries on acoustic imaging in wind tunnels, Applied Acoustics 181 (2021), 10.1016/j.apacoust.2021.108154.

4. C. P. VanDercreek, A. Amiri-Simkooei, M. Snellen, and D. Ragni, Experimental design and stochastic modeling of hydrodynamic wave propagation within cavities for wind tunnel acoustic measurements, International Journal of Aeroacoustics 18, 752 (2019), 10.1177/1475472X19889949.

Conference Proceedings

1. R. Merino-Martinez, C. P. VanDercreek, and M. Snellen, Evaluation of advanced acoustic imaging methods for microphone–array measurements in closed–section wind tunnels AIAA Aeroacoustics Conference, (Southhampton, UK 2022).

2. C. P. VanDercreek, R. Merino-Martinez, M. Snellen, D. Ragni, and D. G. Simons, Comparison of cavity geometries for a microphone array in an open-jet wind-tunnel experiment, in Berlin Beamforming Conference BeBeC–2020–D07(Berlin, Germany 2020).

3. Colin P. VanDercreek, Pieter Sijtsma, Mirjam Snellen, Daniele Ragni, Francesco Avallone and Dick G. Simons. "Deterministic Model of Acoustic Wave Propagation in a Cavity," AIAA 2019-2425. 25th AIAA/CEAS Aeroacoustics Conference. (Delft, The Netherlands, 2019).

4. Colin P. VanDercreek, Pranav Majunath, Daniele Ragni and Mirjam Snellen. "Design and Evaluation of Microphone Cavity Geometries for Wind-Tunnel Acoustic Measurements," AIAA 2019-1580. AIAA Scitech 2019 Forum (San Diego, CA, 2019).

5. Colin VanDercreek, Michael Smith and Kenneth Yu. "Focused Schlieren and Deflectometry at AEDC Hypervelocity Wind Tunnel No. 9," AIAA 2010-4209. 27th AIAA Aerodynamic Measurement Technology and Ground Testing Conference. (Chicago, IL, 2010).

Included in this thesis.